

**Effects of Creep and Fatigue on the Reliability of SnAgCu Solder Joints in Thermal
Cycling**

by

Mohammed A. Abueed

A dissertation submitted to the Graduate Faculty
of Auburn University
in partial fulfillment of the
requirements for the Degree
of Doctor of Philosophy

Auburn, Alabama
December 12, 2020

Keywords: Solder Joint, Fatigue, Creep, Reliability, Thermal Cycling

Copyright 2020 by Mohammed A. Abueed

Approved by

Sa'd Hamasha, Chair, Assistant Professor of Industrial and Systems Engineering
John Evans, Charles D. Miller Endowed Chair Professor of Industrial and Systems Engineering
Sean Gallagher, Hal N. and Peggy S. Pennington Professor of Industrial and Systems
Engineering

Jia (Peter) Liu, Assistant Professor of Industrial and Systems Engineering

Abstract

The reliability of electronic systems is threatened by the failure of one solder interconnection among thousands connecting several components to the PCB. These joints are exposed to different sorts of harsh circumstances such as vibration, drop, and thermal cycling. Thermal cycling stresses are the most common stimulus that leads to joints failure caused by environmental conditions and the on-off switching cycles of the circuit. Recent studies have shown that the failure mechanism under thermal cycling is caused by both creep and fatigue. Fatigue is dominant during the ramps, while creep is dominant during the dwelling. Such creep and fatigue damages are affected by various parameters such as dwelling time, ramp rate, and temperature range. Therefore, it essential to fundamentally understand the damage mechanisms related to creep and fatigue. Moreover, quantifying the damage under different testing parameters is critical for prediction modeling and material improvement purposes. For decades, lead-free alloys replaced the SnPb alloys in the market share after the lead prohibition, where SAC based alloys are the most common ones. These alloys have exceptional mechanical and thermal properties, but there is a concern about their reliability, especially in harsh applications. Thus, it is vital to investigate the behavior of the SAC-based alloys under these circumstances. Evaluating the reliability of SAC305 solder interconnection under various fatigue and creep conditions at different temperature levels, several stress levels, and dwelling times, quantify them in addition to establish prediction models are the main objectives of this study. This study is divided into two main parts; the first one is to test individual solder joints (spheres) under fatigue and creep at room temperature, where the second part includes testing joints under various temperatures. In the first part, three stress amplitudes; 16,

20, and 24 MPa, and various dwelling times; 0s, 10s, 60s, and 180s are utilized for testing the individual joints. Four levels of temperatures; 25°C, 75°C, 125°C, and -40°C, three stress amplitudes; 16, 20, and 24 MPa, and various dwelling times; 0s, 10s, 60s, and 180s are included in the second part. For creep-fatigue tests, test vehicle includes individual SAC305 solder joints attached to FR-4 glass epoxy boards. The surface finish for all test vehicles is OSP, and SAC305 is the only alloy tested in this research. In the first study, the effect of creep and fatigue on individual solder joints with various stress levels and dwelling times at room temperature is investigated. The second study aims to study the effect of the same parameters of stress and dwelling but at several hot and cold temperature levels. In the previously mentioned studies, both damage mechanisms of creep and fatigue are quantified in addition to the other behavioral and microstructural analysis. There are some differences in the analysis for each part. For part one, the hysteresis loop for each condition is generated where damage parameters, inelastic work per cycle, and plastic strain for each cycle are extracted. Qualitative and quantitative information about the damage experienced by these joints is obtained. These parameters are also utilized in generating the life prediction models and would be helpful in FEA models. The evolution during the life (number of cycles) in term of work per cycle and plastic strain are also observed and provide information about the effect of testing parameters on evolution trends. A two-parameter Weibull plot for each combination is established to examine the reliability under various conditions based on individual life. The evolution in microstructure is also investigated for fatigue and creep tests using SEM and optical microscopes. This study will provide a fundamental understanding of both failure mechanisms of creep and fatigue reliability under the thermal cycling of the SAC305 solder

alloy. Also, modified prediction models based on Coffin-Manson, Morrow Energy, Norris-Landzberg, and Engelmaier will be constructed from the results. The preliminary results show that both creep and fatigue influence reliability, but the creep effect is very significant and remarkably degrade the fatigue life compared to fatigue.

Acknowledgments

Firstly, I'd like to extend my deepest appreciation and gratitude to my advisor, Dr. Sa'd Hamasha, who has supported me throughout my research journey and has essential role in completion this dissertation though his guidance. I am extremely grateful for our friendly discussions during our meetings. There are countless things to remember but things to mention here is the dedicated time to review our documents several times, answering question, responding to emails and many others. He was more than advisor and didn't hold back any time even in personal support.

I'd also like to extend my gratitude to my parents (Adel and Khawla) for their uncountable support and encouragement for pursuing my PhD degree. Their inspiration for this moment was huge and no words could express it. Moreover, I would like to thank my fiancée for her full support and patience. Finally, I would thank my colleagues for their help and assistance.

Table of Content

Abstract.....	ii
Acknowledgments.....	v
Table of Content.....	vi
List of Tables.....	xi
List of Figures.....	xiii
List of Abbreviations.....	xxv
Chapter 1: Introduction.....	1
1.1 Electronic Manufacturing.....	1
1.2 Electronic Packaging.....	2
1.2.1 SMT Components.....	5
1.2.2 Substrate.....	7
1.2.3 Solder Joints.....	9
1.3 Fatigue and Creep Issues of SnAgCu Solders in Real Applications.....	11
1.4 Problem Statement.....	12
1.5 Research Objectives.....	17
1.6 Proposed Dissertation Organization.....	18
Chapter 2: General Background.....	20
2.1 Solder Alloy.....	20
2.1.1 Solder Paste Properties.....	20

2.1.2	Lead-Free Solder Materials.....	23
2.2	Electronics Packaging.....	26
2.2.1	Through Hole Mount Technology (THMT).....	27
2.2.2	Surface Mount Technology (SMT).....	28
2.2.3	Substrate.....	36
2.2.3.1	Substrate Material.....	38
2.2.3.2	Surface Finish.....	40
2.2.3.3	Solder Mask vs. Non-Mask Defined.....	42
2.3	Assembly Process.....	43
2.4	Reliability.....	49
Chapter 3: Literature Review.....		55
3.1	Electronics Reliability.....	55
3.2	Reliability Tests.....	55
3.3	Effect of Fatigue and Creep on Solder Joint Reliability.....	57
3.4	Reliability Models Under Different Fatigue and Creep Conditions.....	65
Chapter 4: Research Methodology.....		76
4.1	Study 1: Effect of Creep and Fatigue on Individual SAC305 Solder Joints Reliability at Room Temperature.....	77
4.1.1	Test Vehicle #1.....	77
4.1.2	Preparation and Assembly.....	78

4.1.3	Experimental Setup	81
4.1.4	Testing Profile and Test Matrix.....	83
4.2	Study 2: Effect of Creep and Fatigue on Individual SAC305 Solder Joints Reliability at Various Isothermal Conditions.....	85
4.2.1	Experimental Setup.....	86
4.2.2	Test Profile and Test Matrix.....	89
4.2.3	Instron 5984 Micromechanical Tester Calibration.....	90
4.3	Study 2: Effect of Creep and Fatigue on Individual SAC305 Solder Joints Reliability at Various Isothermal Condition.....	92
4.3.1	Test Vehicle.....	93
4.3.2	Preparation and Assembly	95
4.3.3	Experimental Setup.....	98
4.3.4	Testing Profile and Test Matrix.....	101
	Chapter 5: Analysis.....	104
5.1	Data Analysis.....	104
5.1.1	Weibull Plots.....	105
5.1.2	Analysis of Variance.....	106
5.1.3	Stress-Strain Analysis.....	108
5.1.4	Trends and Correlations.....	113

5.1.5 Prediction Models.....	118
5.2 Microstructural Analysis.....	119
Chapter 6: The Reliability Modeling of SAC305 Individual Solder Joints During Creep-Fatigue Conditions at Room Temperature.....	126
6.1 Introduction.....	126
6.2 Test Matrix.....	127
6.3 Results and Analysis.....	128
6.3.1 Weibull Plots Analysis and Prediction Modeling.....	128
6.3.2 Stress-Strain Loops Analysis.....	139
6.3.3 The Coffin-Manson and Morrow Energy Models.....	153
6.4 Summary.....	163
Chapter 7: The Degradation Modeling of SAC305 Individual Solder Joints During Creep-Fatigue Loadings at Various Temperatures	164
7.1 Introduction.....	164
7.2 Test Matrix.....	165
7.3 Results and Analysis.....	167
7.3.1 Weibull Plots Analysis and Prediction Modeling.....	167
7.3.2 Stress-Strain Loops Analysis.....	181

7.3.3 The Coffin-Manson and Morrow Energy Models.....	189
7.3.4 The Reliability of SAC305 Joints at Cold Temperature Under Fatigue Condition Compared to Room Temperature.....	197
Chapter 8: Conclusion and Future Works	211
8.1 Conclusions	211
8.2 Future Works	212
References.....	214
Appendices.....	227
Appendix A: Weibull plots of various conditions of stress, dwell time and temperature.....	227
Appendix B: Hysteresis Loop and Work as a function of cycles plots.....	236

List of Tables

Table 4.1: The Test Matrix for Studying the Effect of Creep and Fatigue on Individual SAC305 Solder Joints Reliability at Room Temperature	85
Table 4.2: The Test Matrix for Studying the Effect of Creep and Fatigue on Individual SAC305 Solder Joints Reliability at Various Isothermal Conditions	89
Table 5.1: Applied Shear Loads and Equivalent Stress Amplitudes.....	107
Table 6.1: The Test Matrix for Studying the Effect of Creep and Fatigue on Individual SAC305 Solder Joints Reliability at Room Temperature.....	128
Table 6.2: Fatigue ductility coefficient and fatigue exponent of the Coffin-Manson model.....	157
Table 6.3: Fatigue ductility coefficient and fatigue exponent of the Morrow Energy model.....	161
Table 7.1: The Test Matrix for Studying the Effect of Creep and Fatigue on Individual SAC305 Solder Joints Reliability at Elevated Temperature.....	166
Table 7.2: Constant for stress-life equation at various testing conditions.....	176
Table 7.3: Fatigue results summary.....	177
Table 7.4: Summary of Morrow Energy constants at various dwell times and temperature levels.....	191
Table 7.5: Summary of Coffin-Manson constants at various dwell times and temperature levels.....	195

Table 7.6: Fatigue results summary.....201

List of Figures

Figure 1.1: Different Levels of Packaging.....	3
Figure 2.1: Sn-Ag-Cu Ternary Phase Diagram.....	24
Figure 2.2: THMT vs. SMT Components.....	27
Figure 2.3: THMT Components.....	28
Figure 2.4: Examples of Active Components.....	29
Figure 2.5: Examples of Passive Components	31
Figure 2.6: Schematic of BGA with Pitch Distance.....	32
Figure 2.7: Examples of Plastic Component.....	33
Figure 2.8: Examples of BGA components.....	36
Figure 2.9: Examples of Substrate.....	37
Figure 2.10: Single vs. Multilayer of PCB Design	40
Figure 2.11: Example of Surface Finish- ENIG.....	41
Figure 2.12: Top view of NSMD and SMD pads.....	43
Figure 2.13: Example of Pick-and-Place Machine.....	44
Figure 2.14: Wave Soldering.....	45

Figure 2.15: In-line Vapor Phase Soldering.....	46
Figure 2.16: Reflow Oven Soldering.....	48
Figure 2.17: Bathtub Curve.....	50
Figure 4.1: Test Vehicle for Individual Solder Joints Testing.....	78
Figure 4.2: DEK Galaxy Printing Machine.....	79
Figure 4.3 : 8-zone Pyramax 100N Reflow Oven.....	80
Figure 4.4: Sample Preparation for Individual Solder Joints Vehicles.....	80
Figure 4.5: SAC305 Reflow Profile Schematic.....	81
Figure 4.6: Instron 5948 Micromechanical Tester Setup.....	82
Figure 4.7: Schematic of the Cylindrical Testing Fixture for an Individual Solder Joint.....	82
Figure 4.8: Mechanical Fatigue Only Testing Profile.....	83
Figure 4.9: Mechanical Fatigue Only Testing Profile.....	84
Figure 4.10: Fixture Setup with Chamber for Testing Joints at Different Temperatures.....	87
Figure 4.11: Air Handler with Accessories to Provide Hot and Cold Temperatures.....	88
Figure 4.12: Cooling System: Chiller and Piping.....	88
Figure 5.1: An Example of Weibull Plot.....	106

Figure 5.2: Main Effect Plot	107
Figure 5.3: Interaction Effect Plot levels.....	108
Figure 5.4: Applied Load and Targeted Area Illustration.....	109
Figure 5.5: Stress-Strain or Hysteresis Loop.....	110
Figure 5.6: Hysteresis Loops of Zero Dwelling (Left) and 5s of Dwellings (Right).....	111
Figure 5.7: Hysteresis Loops at Different Stress Levels.....	111
Figure 5.8: Hysteresis Loops and Average Work per Cycle for No Dwelling and 5s of Dwellings Conditions.....	113
Figure 5.9: Fatigue Life of Solder Joint as Function of Cycling Stress Amplitude.....	114
Figure 5.10: Life vs. Stress Amplitudes at Various Dwelling Times.....	115
Figure 5.11: Life vs. Dwelling Times at Various Stress Amplitudes.....	115
Figure 5.12: Life vs. Temperature Levels at Various Stress Amplitudes.....	116
Figure 5.13: Life vs. Temperature Levels at Various Stress Amplitudes.....	116
Figure 5.14: Work per Cycle of Solder Joint Cycled at 16 MPa until Failure.....	117
Figure 5.15: Cleaner, Resin, Hardener (rare line from left to right), Samples and Molds (front line).....	121
Figure 5.16: Grinding (Left) and Polishing Pads (Right).....	121

Figure 5.17: Polishing Alumina Suspension of Various Sizes (First Three from Right) and Colloidal Silica Solution.....	121
Figure 5.18: Automated Grinding-Polishing Machine.....	122
Figure 5.19: ZEISS Axio Imager.M2m Optical Microscope.....	123
Figure 5.20: Cross Polarized Image for As-Reflowed SAC305 Solder Joint with Twin Microstructure.....	123
Figure 5.21: Bright-Field Image for As-Reflowed SAC305 Solder Joint.....	124
Figure 5.22: Hitachi S-2460N SEM.....	124
Figure 5.23: Carbon Coating System.....	125
Figure 5.24: SEM Image of As-Reflowed SAC305 Solder Joint.....	125
Figure 6.1: Weibull distributions for SAC305 joints cycled at different stress amplitudes at no dwelling.....	130
Figure 6.2: The fatigue life of SAC305 solder joints as a function of stress amplitude.....	131
Figure 6.3: Characteristic life as a function of stress amplitude for SAC305 solder joints at No dwelling.....	132
Figure 6.4 a: Weibull distributions for SAC305 joints cycled at different stress amplitudes at 10s dwelling.....	133

Figure 6.4 b: Weibull distributions for SAC305 joints cycled at different stress amplitudes at 60s dwelling.....	134
Figure 6.4 c: Weibull distributions for SAC305 joints cycled at different stress amplitudes at 180s dwelling.....	134
Figure 6.5 a: Weibull distributions for SAC305 joints cycled at different dwellings with 16 MPa stress level.....	135
Figure 6.5 b: Weibull distributions for SAC305 joints cycled at different dwellings with 20 MPa stress level.....	135
Figure 6.5 c: Weibull distributions for SAC305 joints cycled at different dwellings with 24 MPa stress level.....	136
Figure 6.6: Characteristic life as a function of dwell time for SAC305 solder joints cycled with various stress level.....	136
Figure 6.7: Characteristic life as a function of stress amplitude for SAC305 solder joints at various dwellings.....	137
Figure 6.8: Power value (n) as a function of dwell time.....	138
Figure 6.9: Constant (C) as a function of dwell time.....	138
Figure 6.10: The hysteresis loops for SAC305 joints cycled with different stress amplitudes at no dwelling.....	140

Figure 6.11: The hysteresis loops for SAC305 joints cycled with different stress amplitudes at 10s dwelling.....	141
Figure 6.12: The hysteresis loops for SAC305 joints cycled with different stress amplitudes at 60s dwelling.....	141
Figure 6.13: The hysteresis loops for SAC305 joints cycled with different stress amplitudes at 180s dwelling.....	142
Figure 6.14: The hysteresis loops for SAC305 joints cycled at various dwellings with 24 MPa stress level.....	142
Figure 6.15: The hysteresis loops for SAC305 joints cycled at various dwellings with 20 MPa stress level.....	143
Figure 6.16: The hysteresis loops for SAC305 joints cycled at various dwellings with 16 MPa stress level.....	143
Figure 6.17 a: Hysteresis loops; with no dwelling (pure fatigue) and with 10s dwelling (including both creep& fatigue) cycled at 16 MPa.....	144
Figure 6.17 b: Hysteresis loops; with no dwelling (pure fatigue) and with 10s dwelling (including both creep& fatigue) cycled at 20 MPa.....	144
Figure 6.17 c: Hysteresis loops; with no dwelling (pure fatigue) and with 10s dwelling (including both creep& fatigue) cycled at 24 MPa.....	145

Figure 6.18: Inelastic work vs. the number of cycles for SAC305 solder joints cycled at 16 MPa stress amplitude until failure.....146

Figure 6.19: Inelastic work vs. the number of cycles for SAC305 solder joints cycled at various stress amplitudes at no dwelling until failure.....146

Figure 6.20: Inelastic work vs. the number of cycles for SAC305 solder joints cycled at 16 MPa stress amplitudes at various dwelling until failure.....147

Figure 6.21: Inelastic work vs. the number of cycles for SAC305 solder joints cycled at 20 MPa stress amplitudes at various dwelling until failure.....147

Figure 6.22: Inelastic work vs. the number of cycles for SAC305 solder joints cycled at 24 MPa stress amplitudes at various dwelling until failure.....148

Figure 6.23: Hysteresis loops (right) with no dwelling and with 10s dwelling cycled at 16 MPa, and bar chart for average inelastic work for both cases.....149

Figure 6.24: Hysteresis loops (right) with no dwelling and with 10s dwelling cycled at 20MPa, and bar chart for average inelastic work for both cases.....150

Figure 6.25: Hysteresis loops (right) with no dwelling and with 10s dwelling cycled at 20MPa, and bar chart for average inelastic work for both cases.....150

Figure 6.26: Accumulated work until complete failure vs. dwell time at different stress amplitudes.....151

Figure 27: Average Work per Cycle as a function of dwelling times at various stress levels.....	152
Figure 28: Plastic strain per Cycle as a function of dwelling times at various stress levels.....	153
Figure 6.29: Plastic strain per Cycle as a function of dwelling times curves at various stress levels.....	154
Figure 6.30: D-value as a function of stress amplitude.....	155
Figure 6.31: Characteristic life vs. plastic strain for SAC305 joints at various dwelling times on a log-log scale.....	156
Figure 6.32: Characteristic life (Global Coffin-Manson equation) vs. plastic strain for SAC305 joints at various dwelling times on a log-log scale.....	157
Figure 6.33: Inelastic work per Cycle as a function of dwelling times curves at various stress levels.....	159
Figure 6.34: D-value as a function of stress amplitude.....	159
Figure 6.35: Characteristic life vs. inelastic work for SAC305 joints at various dwelling times on a log-log scale.....	161
Figure 6.36: Characteristic life (Global Morrow Energy equation) vs. plastic work for SAC305 joints at various dwelling times on a log-log scale.....	162
Figure 6.37: SEM images for tested joints with dwelling and no dwelling conditions	162

Figure 7.1: Weibull distributions for SAC305 joints cycled at different stress amplitudes under no dwelling at room temperature.....	168
Figure 7.2: Weibull distributions for SAC305 joints cycled at different stress amplitudes under no dwelling at 60°C temperature.....	169
Figure 7.3: Weibull distributions for SAC305 joints cycled at different stress amplitudes under no dwelling at 100°C temperature.....	170
Figure 7.4: The relationship between the characteristic life and stress amplitude SAC305 solder joints in a log-log scale at no dwelling and room temperature.....	170
Figure 7.5: Weibull distributions for SAC305 joints cycled at different temperature levels with 10s of dwelling and 20 MPa stress level.....	171
Figure 7.10: Weibull distributions for SAC305 joints cycled with different dwellings at 25°C and 20 MPa stress level.....	173
Figure 7.11: Weibull distributions for SAC305 joints cycled with different dwellings at 60°C and 24 MPa stress level.....	173
Figure 7.12: Characteristic life as a function of dwell time for SAC305 solder joints cycled with various stress level at 60oC.....	174
Figure 7.13: Summary of fatigue results for all combinations.....	175

Figure 7.14 The characteristic life as a function of stress amplitude at different dwell times and at 60°C testing temperature.....	178
Figure 7.15 The characteristic life as a function of stress amplitude at different testing temperatures and at 10s of dwelling.....	179
Figure 7.16: The full hysteresis loop for the SAC305 solder joints at certain stress amplitude.....	182
Figure 7.17: The evolutions in stress-strain loop for joints cycled with various stress amplitudes at room temperature with no dwelling condition.....	183
Figure 7.18: Stress-strain loop for joints cycled with various stress amplitudes at 60°C with 10s of dwelling condition.....	183
Figure 7.19: Stress-strain loop for joints cycled with 24 MPa stress amplitudes at 25°C with various dwelling periods.....	184
Figure 7.20: Stress-strain loop for joints cycled with 24 MPa stress amplitudes at 100°C with various dwelling periods.....	184
Figure 7.21: The evolution of work long the fatigue life of solder joint cycled with 16 MPa at room temperature.....	185
Figure 7.22: The effect of various stress amplitudes on inelastic work evolution during the joint life while other conditions of dwell time (0s) and temperature levels (25°C) are fixed.....	186

Figure 7.23: The effect of various temperatures levels on inelastic work evolution during the joint life while other conditions of dwell time (0s) and stress amplitude (20 MPa) are fixed.....186

Figure 7.24: The effect of various dwell times on inelastic work evolution during the joint life while other conditions of temperature (60oC) and stress amplitude (24 MPa) are fixed.....187

Figure 7.25: The effect of various dwell times on average inelastic work per cycle and plastic strain for joints tested under various stress magnitudes at 100°C.....188

Figure 7.26: The effect of dwell time levels on average inelastic work per cycle and plastic strain for joints tested under various stress magnitudes with 10s of dwelling.....189

Figure 7.27: The effect of various temperature levels on average inelastic work per cycle and plastic strain for joints tested under various stress magnitudes with 10s of dwelling.....189

Figure 7.28: Morrow energy model for the SAC305 solder joints at room temperature with no dwelling.....190

Figure 7.29: The characteristic life as a function of inelastic work per cycle at different testing temperatures with various dwellings.....192

Figure 7.30: The correlation between the Morrow energy constants and the testing temperature utilizing Arrhenius model.....193

Figure 7.31: Characteristic life vs. plastic strain for joints with no dwelling condition at room temperature.....195

Figure 7.32: The characteristic life as a function of plastic strain at different testing temperatures with various dwellings.....	196
Figure 7.33: The correlation between the plastic strain constants and the testing temperature utilizing Arrhenius model.....	196
Figure 7.34: Weibull distributions for SAC305 joints cycled with various stress levels at -10oC.....	199
Figure 7.35: Weibull distributions for SAC305 joints cycled with various stress levels at -10oC and 25oC.....	199
Figure 7.36: Weibull distributions for SAC305 joints cycled with 16 MPa stress level at -10oC and 25oC.....	200
Figure 7.37: Characteristic life as a function of stress amplitude for both conditions of -10oC and 25oC.....	200
Figure 7.38: Characteristic life as a function of stress amplitude for both conditions of -10oC and 25oC on log-log scale.....	201
Figure 7.39: The evolutions in stress-strain loop for joints cycled with various stress amplitudes at room temperature with no dwelling condition.....	203
Figure 7.40: Full stress-strain loop for joints cycled with 16 MPa stress amplitudes at -10oC and 25oC.....	204

Figure 7.41: Hysteresis loops (right) with no dwelling and with 10s dwelling cycled at 24MPa, and bar chart for average inelastic work for both cases.....204

Figure 7.42: Evolution of inelastic work along SAC305 joints cycled at various stress level at -10oC.....205

Figure 7.43: The effect of various stress levels on average inelastic work per cycle for joints tested at different temperature levels of 25oC and -10oC.....206

Figure 7.44: The effect of various stress levels on plastic strain for joints tested at different temperature levels of 25oC and -10oC.....206

Figure 7.45: Characteristic life as a function of inelastic work per cycle for -10oc.....208

Figure 7.46: Characteristic life as a function of plastic strain for -10oC.....209

List of Abbreviations

BGA	Ball Grid Array
CCGA	Ceramic Column Grid Array
CTE	Coefficient of Thermal Expansion
CPU	Central Processing Unit
CSP	Chip Scale Package
CZ	Czochralski
C4	Controlled Collapse Chip Connection
EDX	Energy Dispersive X-Ray
DIP	Dual In-line Package
DRAMs	Dynamic Random-Access Memory
ENIG	Electroless Nickel Immersion Gold
FR	Flame Retardant
HASL	Hot Air Solder Leveling
ImAg	Immersion Silver
IMC	Intermetallic Compound
IR	Infrared
JEDEC	Joint Electron Device Engineering Council
NSMD	Non-Solder Mask Defined
NCMS	National Center for Manufacturing Sciences
OEM	Original Equipment Manufacturer
OSP	Organic Solderability Preservative
PBGA	Plastic Ball Grid Array
PCB	Printed Circuit Board
PLCC	Plastic Leaded Chip Carrier

RF	Radio Frequency
SAC	Sn-Ag-Cu
SEM	Scanning Electron Microscope
SMD	Solder Mask Defined
SMR	Surface Mount Resistor
SMT	Surface Mount Technology
SOIC	Small Outline Integrated Circuit
SOJ	Small Outline J-Lead
TBGA	Thin Ball Grid Array
THMT	Through Hole Mount Technology
WEEE	Waste Electrical and Electronic Equipment
ZIP	Zig-Zag In-Line Package

Chapter 1: Introduction

1.1 Electronics Manufacturing

Electronics is one of the swiftly evolving and highly pioneering industry which creates fierce and rigorous competition among various companies. Such competition characterized by valuable benefits such as racing in utilizing advancement technology, extend visions towards globalization, and enhance standardization of products and manufacturing machines. Also, the electronics industry is driven by devoting many resources such as money and efforts into research and development for the design and its manufacturability to assure sophisticated products as well as facilitating manufacturing processes. The electronics industry consists of organizations that design, manufacture, assemble, and provide electronic service products. There are vital functions considered the core for the electronics industry, which are product development, manufacturing, supply chain, sales, marketing, customer services, and financing. Electronics manufacturing is the department responsible for transforming product design into real products. In collaboration with the designing team, the manufacturing team is working to investigate the optimum way for production, called the design for manufacturing (DFM) practice. This assures facilitating production in the fastest way and with the minimum operational cost. Also, these teams are working together with supply chain teams to improve manufacturing process performance and efficiency.

The electronics manufacturing industry can be divided into numerous classifications based on function, complexity, and product type. The electronics industry's significant segments are semiconductor supply, which includes all supplies related to semiconductors as an integrated circuit and component supply. Industrial equipment involves various ranges and complexities of equipment from robotics, control systems, and automation, wafer-processing, packaging, and

assembling equipment of semiconductors; communication and computer equipment including all networking hardware like routers, hubs, switchboards, servers, and workstations. Medical devices include diagnostic equipment, X-ray machines, dialysis machines, and monitoring systems; consumer electronics such as home intercommunication, alarm system, TV, mobiles, and others that used home appliances.

Product-based classification is the most common one where products are classified into three main categories: consumer, industrial, and critical products. TV and cell phones are examples of consumer products with a service life of fewer than five years with accompanied low failure cost. Industrial products like telecommunications and electronic office equipment have longer service life than the previous types with higher failure loss. Finally, critical products such as aerospace or medical devices have significant scale characteristics compared to the previous ones of long-term life (more than 20 years) in addition to very costly failure cost up to life-threatening.

Finally, the critical steps in electronics manufacturing are PCB fabrication and assembly, packages manufacturing, and encapsulation. Testing and inspections are vital steps in between: automated optical inspection, in-circuit testing, and functional testing.

1.2 Electronics Packaging

Electronics packaging is the process of placement and assembling many (up to thousands) electronic components in a defined enclosure to provide protection and other functional requirements for the system. There are four primary levels of packaging: the integrated circuit fixed to the silicon chip (level zero), the interconnection between chip and its carrier (1st level), a connection between the chip carrier and printed circuit board (2nd level), and finally the insertion of the card (daughter-board) to the motherboard (3rd level). The zero levels are described by the process of dicing chip from a wafer of silicon, which is fabricated using sequential processes called

the photolithographic semiconductor fabricating process. The subsequent level is referred to as enclosing and connecting silicon chips inside components or directly to the printed circuit board. There are several enclosures and connection options, which will be explained briefly in chapter 2. The second level involves the interconnection of package and printed circuit board. It is defined as placing components on the top of the printed circuit board, considering specific printed circuit board schematic design. Furthermore, it includes the interconnection between the printed circuit board and components that provides the mechanical support for the electrical path with the wiring traces or routes fabricated by the photoetching process at the top of printed circuit board. Finally, the third level is characterized by the connection between the daughter card or printed circuit board to the motherboard. Our interest in this work is the second level represented by the interconnection between components (especially ball grid arrays) and printed circuit boards, which will be explained briefly in the following sections. All levels of packaging are shown in Figure 1.1 [1].

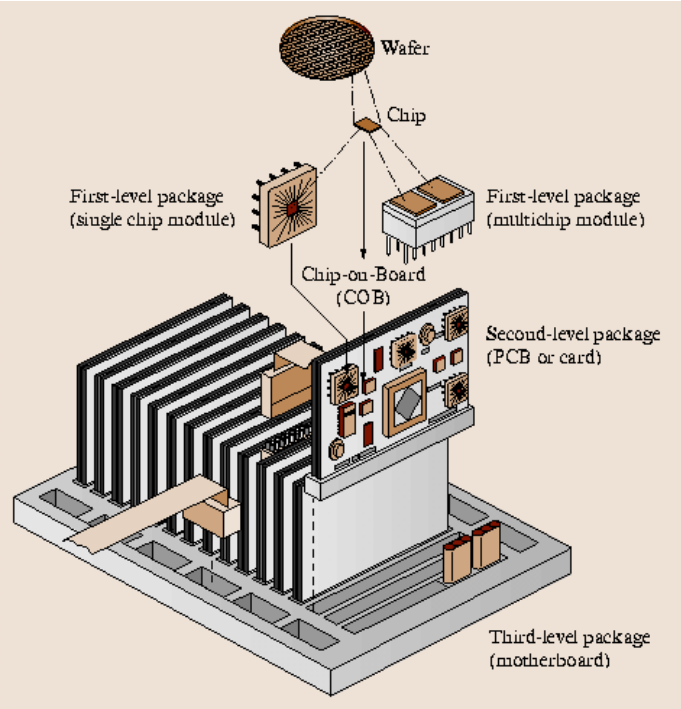


Figure 1.1: Different Levels of Packaging.

The major functions of packaging include: providing mechanical and environmental protection for different levels of packaging, power distribution for various circuits and devices, besides, to manage the input/output (I/O) electrical signals from/to different levels of packaging, also, to offer the heat dissipation generated from these devices. Electronic systems are subjected to various mechanical effects such as vibration, dropping, thermal stresses through transportation, and environmental impacts, including chemicals, radiation, humidity, and dust. Therefore, packaging provides such required protection from these external influences. Signal distribution is essential to perform the critical functions of the electronics system. Different levels of interconnections are responsible for this task by acting as a carrier between several packaging levels. The other substantial part is power. In any electronic system, there are two types of components in terms of activity: active and passive components. The latter lend their electrical properties to the system with no additional active effect. The former requires power to be functional that primarily distributed from a power source through interconnection levels to the desired components. The dilemma of interconnections when performing these two major roles of providing signals and power is the reduction in performance. This would happen due to the noise, propagation delays, and parasitic (undesirable inductive and capacitive) issues related to such kinds of materials [2]. Since there are thousands of active and passive components, heat would be generated due to different processing activities, which negatively impacted the system's performance and function. Also, it would profoundly influence the reliability of different levels of interconnections. Thus, heat management and control techniques, including free and forced convection, should be utilized at the design phase of the electronics system to assure the optimum (considering the cost) heat dissipation. Reliability engineers should consider this issue as the most critical challenge during system operation.

1.2.1 Surface Mount Technology (SMT) Components

Generally, chip and its carriers are classified into three main groups according to the connection method to the printed circuit board: direct chip attachment, through-hole (THMT), surface mount technology (SMT). In this section, surface mount technology components will be explained briefly, especially solder ball connection, while others are clarified in chapter 2. As the name implies, surface mount technology chip carriers are mounted on the top or surface of printed circuit board via leads, unleaded, or solder ball connections. Leads of various types (J, S, L) are utilized in such types to connect to the substrate using solder paste, which printed on specific areas within the substrate called metal pads. Each lead with the printed solder paste acts as a joint and connected to the substrate after reflowed. This lead is connected directly with silicon chip through the component mold from its other side. The second type is the leadless ones where grooved terminations usually plated with gold called castellations are deployed within the component side and positioned directly on specified places within the substrate. Compared to the previous one, the advantage of these types is the shorter path with fewer signals of parasitic and noise problems. The led (especially J-type) ones are more reliable than others due to the absorption of deformation-strain by leads generated by mechanical shock and vibration influences. The last part is the ball-grid arrays (ball grid array), where solder balls are utilized over the bottom area of the chip carrier to provide both mechanical and electrical connections. Since this type of joints is used in this work, further details are clarified. JEDEC guidelines are followed during the ball grid array manufacturing to standardize this process and make trading worldwide easier. Typical grid spacing is 32, 40, 50, 60 mils, and finer pitches are also fabricated. The body size range is between 7 and 50 mm, with pin counts varying from 16-2400, while 200-500 is the universal pin range. These balls might be used in both; first and second levels. Within the first level, it is called Controlled

Collapsed Chip Connection (C4) and connects the silicon die to the component, whereas balls in the second level called ball grid array. Our interest in this work, including all mechanical tests, relates to ball grid array only. Ball grid array packages include two types of materials; ceramic and plastic, where each has its pros and cons. Plastic types are mostly used in consumer electronics due to their lower price compared to ceramic ones. Also, since the popular substrate material is glass epoxy, connecting plastic components with such substrate is more reliable than ceramic ones due to better match of the coefficient of thermal expansions (CTE) between substrate and component, especially during thermal cycling conditions. On the other hand, ceramic ones are hermetically sealed so, by itself, is more superior in function and performance. The drawbacks of such type are the significant higher prices compared to plastic ones and the remarkable coefficient of thermal expansions mismatch between this type and epoxy substrate. The solution is to have a ceramic substrate to reduce the coefficient of thermal expansions mismatch and enhance the reliability drastically, but this would add more cost to the system. Therefore, such ceramic types are introduced in military and aerospace applications where high reliability is a vital concern. Compared to other types of led and leadless, ball grid array has several advantages. First, it has higher I/O capacity compared to others due to more balls (joints) to be deployed with the bottom part of the chip carrier compared to other types. The previous advantage makes the ball grid array, for a specific footprint, of higher circuit density. Since the package is comparably smaller than others, less weight, size, and cost will be offered, and more chips could be enabled on the same printed circuit board. The shorter interconnection of ball grid array s enhances the inductance and resistance performance and makes it preferable in high processing applications like CPU compared to leaded ones. Also, the improved heat dissipation controls make it better for various applications. There are other benefits in terms of manufacturing, such as a reduction in coplanarity problems,

self-alignment during the reflow process, less bridging during paste printing, and higher yields during assembly. Meanwhile, ball grid arrays have some drawbacks; hard to rework individual joints, impossible visual inspection for joints located in the central areas, and higher possibility of failure under thermal cycling due to high rigidity of both joints chip carrier [1, 2, 3]. Chip scale package (CSP) is a modified version of ball grid array with many similarities. The main difference is in the area of the chip relative to the area of the package. The ratio is only 1.2 times in chip scale package compared to 4 times in other ball grid arrays for any pitch size and has a lower I/O count.

1.2.2 Substrates

The substrate or printed circuit board is an integral part of any electronic system due to its mechanical and electrical vital functions. It is a thin board fabricated mostly from laminates, glass materials, and epoxy materials. From a mechanical perspective, printed circuit board is the primary surface used for mounting most of the components for their entire life in a fixed position by different attachment methods; direct attachment, through hole mount technology, and surface mount technology. It involves metal (mostly copper) soldering pads with various sizes and arrays of landing patterns that are fabricated using a lithographic process. These pads considered as anchor points that provide mutual connections via solders materials after the reflow process. On the other hand, the metalized footprint facilitates the electrical paths between different connection levels. printed circuit board also contains all required wiring channels, conduits, and strip lines, which acts as a conductor for transferring both; power and signals to connect various types of packages. From the design for maintainability prospective, it is required for the printed circuit board to be a field replaceable. Thus, printed circuit board is the testing bed and should have accessible testing points for the electronic system circuits via testing probes. Another major function of printed circuit board is to act as a marking surface during assembly. printed circuit

board specifies all the components identifications in addition to positions for placement. Based on the degree on circuit density and number of connections mounted on top of boards surfaces, printed circuit boards are divided into three common types: single-sided, double-sided, and multilayered printed circuit board. Also, printed circuit boards are classified according to the types of components fixed on top of it; Type I (surface mount technology Only), Type II (surface mount technology & through hole mount technology), and Type III (through hole mount technology Only). This classification is the most common because it is important in determining the unique assembly sub-processes related to each type. The material utilized to fabricate any PCB might be either polymeric laminates, flexible organics, or ceramic. There are many factors considered when choosing the fabrication materials: cost, electrical and mechanical properties. A further explanation for this topic and other design aspects of printed circuit board, such as routing methods and algorithms, footprint design, and others, are available in chapter 2. The most excellent and common option in consumer electronics considering the previous classification is the combination of the multilayered and glass-epoxy substrate material. Its characterized by cheaper options with higher circuit density and excellent mechanical properties compared to other options. Multilayer printed circuit board includes several layers of copper and laminates of polymeric composites. Layers are initially prepared in a sandwich of a pre-preg partially polymerized glass epoxy sheet. After stacking layers on top of each other's, it heated and laminated together to become as one part, including all wiring plans. Finally, multilayer printed circuit board is ready for drilling the vias of different types that connect different circuits of each layer to the components, where other vias might be utilized to fix through hole mount technology components. After the printed circuit board is fabricated, electrochemical deposition or plating of a thin layer of different materials is implemented on the top (metallic) or vias surfaces to protect the metal parts of printed circuit board

from environmental effects. This plating is employed during various manufacturing steps and called surface finish. The typical surface finishes are organic solderability preservatives (OSP), Electroless Nickel Immersion Gold (ENIG), Immersion silver (ImAg). There are others deployed depends on the application and cost considerations. In this work, printed circuit boards with OSP surface finish are utilized in all experiments. This is important to eliminate the variability due to surface finish from all tests since it has a significant impact on reliability results under various testing conditions. OSP is water-based organic compounds (Benzimidazoles, Alkylimidazoles, and many more) that are employed over Cu surfaces and provide an organic-metallic layer to prevent Cu oxidation. The coating thickness ranges between 0.7-1.0 μm .

1.2.3 Solder Joints

Solder joints are the linkage between the printed circuit board and ball grid arrays components, which provide the electrical/power connection and mechanical support. The primary mechanical requirement for joints is to absorb strains caused by various environmental and operational conditions. In the past (the 2000s), the most common materials were Tin-Lead (SnPb) eutectic (63%Sn37%Pb), near eutectic, in addition to other doped Tin-Lead material. This is due to their low melting point, exceptional solderability, high reliability, and favorable mechanical properties. This maintained until its harmful effect on health and environment discovered. Therefore, extensive research by the electronics industry and educational parties was conducted over the last three decades to develop new environment-friendly material and replace it with Tin-Lead based alloys. The issue is that the failure of an individual solder joint would cause the rundown of the entire electronic system. Therefore, there are several aspects to consider for the newly developed alloy to make this transition. Mechanical and chemical properties, cost, wettability, reliability, availability, manufacturability are examples of these factors. SnAgCu (SAC) alloy or one of its

eutectics with different chemical compositions was the best alternative for Tin-Lead alloy even it has a little higher melting temperature of 217°C for ternary eutectic SAC compared to 63Sn37Pb for 183°C. This creates a sort of challenge during the assembly, especially during the reflow process, but adopted rapidly after extensive research on the reflow profile. Also, the peculiar thing about this alloy is that changing the percentage of any of these elements (Sn, Ag, Cu) would change the mechanical behavior remarkably. Nevertheless, there are many groups based on elements percentages where SAC305 is an example of the SACN05 group. Even there are many other lead-free alloys such as Sn-In, Sn-Bi, Sn-Zn. SAC-based alloys found to be the optimum one to replace the SnPb based alloys due to their superior mechanical properties and best option for the design for manufacturability and assembly. Initially, the solder paste material is printed on the footprints, and the BGA components with its balls are placed on the top of PCB, then reflowed in the oven. During the reflow process, the temperature of reflow reaches up to 240°C for SAC alloys (which is above liquidus) for the 40s then cooled down with a constant rate of 4°C. At the end of cooling, intermetallic compounds (IMC) between SAC elements are formed, and the IMC layer is responsible for the mutual connection between printed circuit board and components. Types of formed intermetallic compounds alter the alloy's mechanical properties due to its superior mechanical properties compared to the bulk material. For SAC alloys, there are three possible compounds: Ag_3Sn , Cu_6Sn_5 , and Cu_3Sn . The latter found mostly near the Cu pads because it requires high Cu content. In the last decade, tiny amounts of elements such as Bi, In, Sn, etc. called dopants are added to SAC-based alloys. This found to enhance reliability, improve the mechanical properties, and facilitate the manufacturability and assembly.

1.3 Fatigue and Creep Issues of SnAgCu Solders in Real Applications

As mentioned earlier, electronic packaging includes different materials at various levels. The first level, for example, consists of silicon die enclosed in polymeric or ceramic packages. Also, there are several materials involved in the second level: ceramic or glass-epoxy substrates, copper traces, and different materials of various components. The issue is that each material has its unique thermal and mechanical properties, and their response to external effects such as temperature is different as well. Solder interconnection is the softest part of the packaging system since it is influenced by various reactions of different parts to such effects. Generally, CTE determines the rate of expansion or contraction for a particular material upon exposure to variable temperatures. Since each part of the electronic packaging system has its own CTE, it responds differently from others under a certain temperature level. This would generate stress or thermal stress (since it is related to temperature) on the interconnection of different levels. Since the stress is coplanar with material cross-section, it is called shear stress. Under harsh applications, electronic packaging is induced to severe thermal cycling conditions from few up to hundreds of times every day. Consequently, solder interconnections are exposed to numerous shear stresses during cycling between extremes. The frequent application of shear stress is called fatigue shear stress, and since it occurs due to temperature effect, it is metaphorically named as thermal shear fatigue stress or simply "thermal fatigue". Creep is another damage mechanism that is experienced by solder interconnections under harsh conditions, especially at elevated temperatures. Due to creep, the material is deformed under constant stress as a function of time. Such a mechanism is exacerbated when the operating temperature is high compared to alloy melting temperature. For SAC alloys, room temperature is considered to be elevated, since it is considered as an elevated homologous temperature; it is the ratio of operation/melting temperatures in Kelvin. Creep is activated when

homologous temperature above 0.5, which is the case for most lead-free alloys that exceed 0.5 even at room temperature. Thus, under harsh applications of thermal cycling that is usually ranging between - 40°C to +125°C, the corresponding homologous temperature ranges between 0.48 - 0.80. Therefore, the effect of creep should be considered as a dominant deformation mechanism under such conditions.

Accelerated tests are used to predict the life of interconnections under different operating conditions due to related difficulties of cost and time to perform tests under normal conditions. The idea of accelerated testing is to simulate the normal operating conditions but significantly reduce the time (accelerated) under harsh conditions with getting the same failure modes as normal conditions. This would be implemented by rising; stress levels, cycling frequency, dwell time, ramp rate, or testing temperature range to generate failures rapidly. On the other hand, test parameters should be modified carefully to avoid misleading outcomes. The test should simulate the normal operating conditions and generate the same failure mode induced at long term conditions. Then, fatigue life models for normal conditions are generated from accelerated test results, and related accelerated factors and reliability models are established accordingly. Moreover, accelerated data might fit one of the conventional fatigue models, and related constants are attained after that.

1.4 Problem Statement

Solder interconnection is defined by the solder sphere, solder paste, and surface finish, where each part has a critical impact on reliability. Typically, solder interconnection between PCB and components provides electrical connection and mechanical support. The latter function is characterized by absorbing the mechanical displacements induced once exposure to various conditions. Even the deformation is accommodated by solder interconnection and other joint parts,

component, and PCB, solder interconnection responds visco-plastically while other parts deform elastically. The reason behind that is the influence of the solder joint by the supported load according to other parts compliance. Since these parts are fabricated from different materials, and each has unique mechanical properties, especially CTE, they respond uniquely when subjected to the temperature. In harsh thermal applications (-40°C to $+125^{\circ}\text{C}$), the joint is exposed to alternating shear stress due to expansion and contraction displacements of the solder joint system throughout cycling between both extremes of high and low temperatures. This thermomechanical stress is driving the damage accumulation over time until fatigue failure occurred eventually. Therefore, various parties concerned in harsh applications such as consumer electronics, aerospace companies, Department of Defense, automotive corporations, and many other industries launched several massive projects to understand the fatigue failure mechanism. Electronic systems are an integral part of thousands of critical applications in various fields, and the failure of one solder joint would result in overall system failure and catastrophic consequences in terms of high-cost and human being life-threatening. Therefore, business and research parties realized the importance of investigating the effect of fatigue mechanism on solder interconnection reliability. The beginning was in the late 60s with many research projects on SnPb based alloys.

The project's target was to investigate the effect of fatigue on solder interconnections reliability under different thermal conditions; isothermal [4] and thermal cycling [5] ones. The effect of different parameters; strain range [6], ramp rate [7], hold time [8], and temperature [9] on the fatigue life was also explored. Projects involve metallurgic studies and microstructure analysis using SEM and EDX technologies. For decades, the world switched to lead-free solders and the research project as well. Research projects are studying the effect of different factors related to thermal and mechanical fatigue mechanisms on solder joint reliability. The research group at

Auburn University explored the fatigue effect broadly under various circumstances on SAC-based alloy's reliability. Their studies implemented under thermal and isothermal conditions including several stress levels [10], surface finishes [11], varying amplitude [12], aging conditions [13], ramp rates [14] in addition to others related to investigate the mechanical properties; shear strength [15], creep [16], and tensile strength [17]. Other researchers performed similar studies with various other geometries [18] and conditions; thermal extremes [19], aging circumstances [20], etc. on SAC-based alloys. Findings were consistent with Auburn group results.

On the other hand, creep found to have a large impact on the reliability under harsh conditions. The low homologous temperature (ratio of operating/melting in °K) of SnPb and SAC based alloys considered room temperature as elevated temperature. In general, creep effect is induced even at lower homologous temperature (T_h) but activated when $T_h > 0.5$, which is the case for SnPb ($T_h=0.65$) and SAC-based ($T_h=0.6$) alloys at room temperature. This impact is exacerbated at dwelling periods of elevated temperatures of harsh thermal cycling conditions like automotive and aerospace. This requires considering the creep as the dominant failure mechanism in harsh applications. Several studies found that solder interconnection failure under thermal cycling is combined with creep and fatigue [21]. Fatigue is dominant during ramps [8], while creep is dominant during dwelling, especially at elevated temperatures [9]. Creep noticed to have a minor effect during dwelling at low extreme [9]. Creep is different from stress relaxation; creep is the deformation of a material under constant stress, while stress-relaxation was the reduction in stress when strain held constant. During dwelling periods, the joint is crept and/or relaxed (stress relaxation) and subjected to plastic and elastic, time-dependent, and independent changes in stress and strain simultaneously. This combined process is called creep-relaxation [9]. Despite creep and relaxation are distinguished from each other in the mechanism, it was demonstrated that related

plastic flow and microstructural changes are identical based on stress-strain data [8]. Several research studies were implemented on SnPb-based alloys to discover the effect of creep on solder fatigue life under different temperatures and holding times [6]. Other researchers also studied the evolution of creep and tensile properties under various temperatures and aging conditions [22]. Over the last 20 years, SAC-based alloys found to be the best replacement of SnPb ones due to its exceptional solderability and superior mechanical properties. Therefore, scientists executed broad research to examine the effect of creep on fatigue life under isothermal and thermal conditions with various parameters as elevated temperature [23], holding time [21], temperature extremes [24], and geometries [25]. While others investigated creep properties using nano-indentation tests [26]. There is no study investigated solder material behavior under combined effects of creep and fatigue in one experiment, especially for SAC-based alloys.

Most of the research utilized bulk samples (dog-bone, lap-type, uniaxial tension specimens) to investigate the creep and fatigue properties under different conditions and their effects on solder joint reliability. The fabrication procedures almost the same for all types with some differences in molds. The solder material is melted and poured in these molds under vacuum and solidified. Then, samples are reflowed with the same defined profile for that composition. Results from bulk samples are misleading compared to actual solder joints due to many reasons. The primary issue is that actual joints have IMC layer, few (one, two, or three) grains microstructure, specific precipitate distribution, unique geometry, and sizes that are entirely different from bulk ones which don't have IMC primarily. This would result in different modes of failure, microstructure evolution, and damage accumulation. Other essential factors, such as surface finish, which affect interconnection reliability, can't be examined. Thus, utilizing bulk samples in reliability tests, especially for critical applications, wouldn't reflect precisely results about solder joints, and it's all

related mechanical properties and microstructure evolution. Instead, it would be useful in tracking general trends and behavior under different conditions. There is a gap in research about employing actual solder joints in the reliability tests to investigate the joint's behavior and microstructure evolution at different temperature levels.

The reliability models or prediction models are generated from accelerated tests results under various conditions. Data is fitted using appropriate distribution to obtain a prediction model for solder joints. A Weibull distribution with its main parameters, scale (θ), and shape (β) is the most common method to represent the reliability data. The location parameter is related to Weibull distribution as well but rarely used in such work. Also, data are fitted to common fatigue models as Coffin-Manson and Morrow Energy models, where related constants are determined simultaneously. When testing at different temperature levels, a new term should be included called the Arrhenius model to involve the temperature effect. Most research in this area investigated the effect of fatigue or creep on bulk solders' reliability under isothermal conditions. Whereas, few studies performed such tests on SAC-based individual solder joints at various isothermal conditions. For thermal cycling tests, a full system of components, PCB, and interconnection are utilized. Weibull distribution is primarily employed in qualitative comparisons between different interconnection alternatives based on scale parameter or early failure (B10) parameter. There are other models employed to predict life under thermal-cycling conditions such as Norris- Landzberg and Engelmaier models. Extensive research is performed to predict the lives of solder assemblies under different thermal cycling conditions of different based alloys of SnPb [5,27-28] and SAC [29-31]. Also, the effect of various parameters as dwell time [32], ramp rate [33], and temperature range [34] on fatigue life were explored. Few studies included all these factors together and

conclude to modified versions of prediction models to represent the fatigue life under service conditions.

Most research work doesn't involve sufficient testing parameters, conditions, and systematic research studies to understand the fatigue life of solder joints fundamentally. The uniqueness of this work is to test an individual SAC305 solder joints once at a time under fatigue and creep-fatigue conditions at various testing temperatures. In this work, three extensive research studies are planned to be implemented systematically. This includes various testing conditions and profiles, isothermal and thermal cycling conditions, temperatures levels, multiple setups, and interconnection levels. The first study involves testing individual solder joints under the effect of creep and fatigue at room temperature. The second one includes examining individual solder joints under various cold and elevated temperature levels. The third one consists of three sub-studies: typical thermal cycling test of BGAs, air to air thermal shock, liquid to liquid thermal shock. The last study's objective is to investigate the different dwelling times and ramps on fatigue life reliability. Prediction models for all these studies will be generated simultaneously. Finally, extensive metallurgical analysis is performed to explore the microstructure evolution under various testing conditions. This would provide a better understanding of failure mechanisms and determine the related failure modes with these failures.

1.5 Research Objectives

The purpose of this research work is to investigate the effect of both fatigues and creep on solder joints reliability under various testing conditions. Also, damage due to fatigue and creep is distinguished by quantifying related damage parameters such as inelastic work per cycle and plastic strain. Prediction models for solder joints under different real service conditions are

generated accordingly. To achieve such objectives, the following targets are to be attained from the study:

- Establish detailed procedures including test vehicles design and assembly, experimental setups, testing profiles, and testing conditions to examine solder joints fatigue reliability of solder joint interconnection under different conditions.
- To understand the combined effect of both fatigue and creep on solder joint reliability, and quantifying the damage related to each one.
- Develop reliability models of individual solder joints to predict the fatigue life influenced by various parameters of temperature, stress levels, and dwell time.
- Study the effect of different thermal cycling test parameters, dwell time, ramp rate, and temperature ranges on thermal fatigue life reliability of solder joints.
- Develop reliability models of solder joints to predict the thermal fatigue life induced by various parameters of temperature, ramp rates, and dwell time.
- Perform an extensive metallurgical analysis using SEM and EDX technologies to explore the microstructure evolution with time. Also, it includes determining the failure modes after tests are completed and providing a better understanding of each mechanism.

1.6 Proposed Dissertation Organization

This proposal involves seven chapters. The first chapter includes a brief introduction about the electronics manufacturing and packaging, description of solder joints issues in real service conditions, and concludes with research objectives. Chapter two spots extensive information about electronics manufacturing, packaging, and assembly process. Research works related to this study in the world are pointed out in chapter three. Chapter four describes in detail all materials and methods involved in each test, including test vehicle preparation and assembly, experimental tools

with setup and testing profile, data acquisition, and finally, microstructure analysis. Chapter five addresses the effect of creep and fatigue on individual SAC305 solder joints reliability in isothermal conditions. The effect of creep and fatigue on individual SAC305 solder joints reliability at different cold and elevated temperatures is covered in Chapter six. Finally, the effect of different thermal cycling parameters on SAC305 solder material thermal fatigue reliability is elaborated in chapter seven.

Chapter 2: General Background

2.1 Solder Alloys

Solder alloys are metallic material utilized to unite two different pieces in a process similar to welding but at lower temperature ranges. It includes melting the alloy above its liquids phase and cool it down to obtain a rigid connection. In electronics, wide ranges of alloys are utilized to connect various parts of electronics systems. For decades, Tin-lead alloys were dominant the market share of alloys due to its low price, sophisticated properties, and easy manufacturability. When it was prohibited for commercial use, governments worldwide were looked for a replacement through several funded projects performed by military, industry, and academia. SAC alloys were the best candidate for this purpose due to many reasons such as availability, relatively low cost, superior properties compared to other alternatives, and excellent manufacturability. Therefore, it's essential to explore the properties of these alloys. This section discusses two main parts: various general properties of solder pastes in addition to a thorough description of the lead-free alloys.

2.1.1 Solder Paste

Paste composes of metal powder particles suspended in thickened flux. After the determination of paste composition, fine particles are formed molten solder is chilled on a rotating wheel under inert conditions to avoid oxidation. Solder bars are another type utilized to prepare the paste for wave soldering. The cost is higher for the former process due to precise quality requirements, extra scrap solder, and addition of solvent and fluxes to paste.

The metal composition is a critical parameter that must be determined based upon application. Several factors play a crucial role in defining the composition of paste. The type of PCB and

components used in the assembly is the most critical factor. This is due to the melting temperature of the used paste; ceramic packages could withstand high reflow temperatures, but degradation problems appear if the same profile is utilized for reflowing the plastic ones [3]. Since the paste is printed on pads, it is critical to check the compatibility of solder with the PCB metallization. The application is no less significant than the previous issues. There is another major factor related to the metal composition, which is the content of the metal. This is due to its role in defining the fillet size. It increases as the metal content percentages increase at specific viscosity. This is explained by the higher thickness achieved during reflow with higher metal content [3]. Solders with high strength of shear and tensile are recommended at high-temperature applications [2,3]. Cost is to be considered when determining the metal composition since there are variances in metal costs. Silver (Ag), for example, is costly compared to other elements and should be optimized with reliability when involved in the final composition. Finally, environmental condition is a significant concern due to its impact on the universe. Elements as Pb proved to have severe effects on human health and atmosphere.

Particle shape and size are primary properties that specify the powder oxide content and paste printability. Particles with regular shape and low surface areas are recommended rather than others. The former is critical to avoid screen and stencil blockage, whereas the latter is essential to void excess oxidation. For these reasons, spherical is preferred among the elliptical ones. There are six types (1-6) of powder sizes according to Joint Electron Device Engineering Council (JEDEC) standards. The ranges of sizes for different types are 75-150 μm for type 1 and 5-15 μm for type 6. When choosing particle size, the general guideline is a ratio between stencil aperture width and powder size not to exceed 4.2 [2-3].

Particle shape and size are primary properties that specify the powder oxide content and paste printability. Particles with regular shape and low surface areas are recommended rather than others. The former is critical to avoid screen and stencil blockage, whereas the latter is essential to void excess oxidation. For these reasons, spherical is preferred among the elliptical ones. There are six types (1-6) of powder sizes according to JEDEC standards. The ranges of sizes for different types are 75-150 μm for type 1 and 5-15 μm for type 6. When choosing particle size, the general guideline is a ratio between stencil aperture width and powder size not to exceed 4.2 [2-3, 5, 8, 11].

Primarily, solder paste is a viscoelastic material, which means that its general behavior is between viscous and elastic. The science that deals with the change of material form and flow are called Rheology. It describes the material elasticity, plasticity, and viscosity properties. Since the paste is printed on printed circuit board, it is critical to study its fluidity on the board. This is due to its fundamental relationship with the final assembly quality, reliability, manufacturability, and printability. Also, it is influenced by paste composition and powder paste, suspension agent, flux, solvents, etc. There are three main rheological properties, viscosity, slump, and tackiness. Viscosity defined as the internal friction of the fluid due to molecular reaction causing the material resistance to flow. The central unit is Poise, and it is in direct relation to temperature and stress. There are various classifications based on viscosity where solder paste is considered as a thixotropic fluid which deforms under applied stress. Paste viscosity also is negatively affected by particle size. In the electronics manufacturing industry, it is essential to measure the paste viscosity to avoid printing complications. The two common types are Brookfield and Malcom viscometers. Slump is the paste's ability to spread out on the surface after being deposited. The paste with less slump is better to avoid excessive spreading on the lands. Paste slump is about the metal content of the solder. The slump test is executed on varying land patterns pitches to check for the desired

thickness. The paste considered to be failed if bridging is found with adjacent lands. The ability of paste to hold SMT components on double-sided PCB after flipped during reflow is called tackiness. Tackiness is an indication if paste working life has passed by or not. Nevertheless, there are testers to check for the tackiness of the paste where the required force to remove standard weight from the standard size of dumped solder [1-3,5].

2.1.2 Lead-Free Solder Materials

SnPb-based alloys were dominated the market share of solder paste materials until the early 2000s. It has a low melting temperature in addition to superior mechanical properties such as ductility and reliability. SnPb alloys have excellent manufacturability as wettability and compatibility with other PCB and components materials [1, 3]. In the 2000s, RoHS considered Pb as a toxic element, and it was prohibited from trading worldwide. It's found that it has a seriously harmful effect on human health and the atmosphere as well. Moreover, Waste of Electrical and Electronic Equipment (WEEE) regulations banned the use of Pb in any electronic components, and it should not be recycled. All these decisions were the prime mover for the electronics industry to look for alternatives of Pb to Pb-free alloys. With the help of research and governmental parties like NCMS, the electronics industry launched projects to find the best replacement. There were many aspects to consider, such as toxicity level, availability, feasibility, reliability, manufacturability related issues like wettability and printability. The following step was to adapt the manufacturing and assembly process simultaneously due to some differences. The main project aimed to choose the best, and 3 out of 79 alloys were recommended Sn-58Bi, Sn-3.5Ag-4.8Bi, and Sn-3.5Ag.

Among lead-free alloys, Sn-Ag-Cu (SAC) based alloys were the best-fit candidate and showed promising results as paste material. This is due to the low melting temperature, outstanding mechanical properties, and compatibility with other assembly parts. Also, SAC alloys, especially.

SAC105, 305 were utilized as interconnection solder balls in packaging for BGAs. The International Printed Circuit Association (IPC) proposed that these two alloys will be the most selected in the future. SAC based alloys have preferences among other Sn-Ag ones due to their relatively low temperature and excellent mechanical properties. On the other hand, eutectic SAC has a melting temperature of 217°C, which is relatively high compared to the eutectic SnPb of 183°C. The issue is high reflow temperature above liquids up to 240°C and its negative impact on assembly parts such as PCB warpage and components popcorn effect in addition to other reliability problems.

SAC alloys are the most widely in the market share even though it is not identified as a replacement for all applications. There are many groups; SACN05 series as SAC105, 305, SACN05 series, or near eutectic, in addition to ones utilized for high-temperature applications, drop, and vibration optimization like SAC3810, SAC3595 and SAC107. The advantage of SAC compared to the binary eutectic SnAg alloys is the lower melting temperature and better mechanical properties. Figure 2.1 below shows the near-eutectic region for SAC alloys. Most of these alloys are located near the eutectic region. The eutectic and near eutectic melting temperature are specified around 217°C, where the exact eutectic point is not identified [1-3].

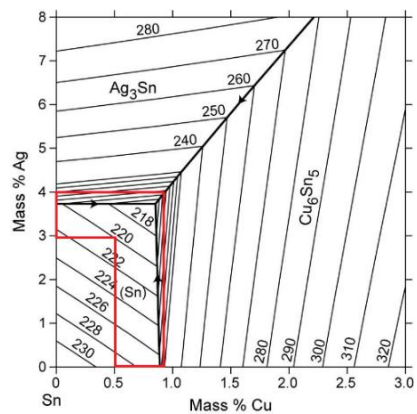


Figure 2.1: Sn-Ag-Cu Ternary Phase Diagram

Another essential characteristic of SAC is the related intermetallic compounds (IMC). IMC is formed between different elements Sn, Ag, and Cu, and has improved properties than original elements. IMC is essential to provide soldering between pad and paste, but excessive thickness leads to the brittle layer and influences the reliability harmfully. The major IMCs that might be formed during soldering are Ag_3Sn , Cu_6Sn_5 , and Cu_3Sn . Ag_3Sn is formed due to reaction between Ag and Sn, where Cu_6Sn_5 is formed due to reaction between Cu and Sn, and both can be found in bulk solder or near the IMC layer. The last one, Cu_3Sn , is formed only at high temperatures with a high content of Cu. That is why it's mainly existed near Cu pads, not in the bulk area. Since there is no reaction between Ag and Cu, there is no IMC particles. As mentioned earlier, IMC particles enhance the mechanical properties significantly due to their role in lattice distortion and block the dislocation movement, which reflects on the strength of the alloy. The SAC alloys reported having 3-4 times fatigue properties than eutectic SnPb solders. This is due to the existence of IMC, Ag_3Sn and Cu_6Sn_5 particles. With all these, it's questionable if SAC alloys could completely replace the SnPb in all conditions due to reliability issues at harsh applications. Moreover, it was found that aging exacerbates the life degradation of these alloys, especially at high temperatures. With all these drawbacks, the potential is shown to substitute SnPb alloys with lead-free alloys with the doping. Doping is the addition of small amounts of certain elements (called dopants) such as Bi, Ni, Co, La, Mg, Mn, Ce, Ti, Fe, In, B, etc. found to improve the reliability and the mechanical and manufacturability properties remarkably. Each element has an extraordinary influence on SAC alloy, depending on the application and, for example, adding a small amount of Bi to SAC alloys found to enhance the strength material significantly [1-2] in addition to lower the melting temperature. Also, doping with Ni found to stabilize the microstructure of SAC alloy and reduce the metal consumption from pads in addition to increase the reliability [35-37]. There are other

elements called rare-earth metals introduced to enhance the wettability and improve the ductility. Today, SAC-X solders have been widely used in the market due to its impact on the overall properties. The key with doping is the percentages of dopants added, which demonstrated to be very sensitive to the material properties and behavior.

2.2 Electronic Packaging

As mentioned earlier, the main objective of electronic packaging is to provide both mechanical support and electrical connections between PCB and component. There are different levels of packaging where the second level, which is between the chip carrier, and the PCB, will be discussed extensively in this study. The critical point is the rapid demand for new generations of products. This means more electronic systems of smaller sizes, lower power consumption with high efficiency and performance. Consequently, serious challenges were revealed by reliability issues, thermal management, and new packaging technologies related to a reduction in size.

Typically, there are four levels of packaging from zero to three. The zero level includes silicon die or semiconductor device processing. Czochralski (CZ) is the production method of silicon crystal ingots. Using the diamond saw, ingots are sliced into thin wafers and polished, then sent for the photolithographic process [2-3] to produce integrated circuits or nano transistors. The first level is prepared by packaging the dice into specific packages. These packages have several functions: mechanical support, protect the active circuit, thermal management, and dice handling. The second level is explained briefly in the next session, including the two main types (mounting-based) of electronic components; THMT and SMT (as shown in Figure 2.2), substrate material, elements, and manufacturing process in detail, and finally, the potential of the new packaging technologies. There is one type of packaging won't be included, which is the direct chip attachment to PCB due

to their limited use. A direct attachment could be implemented via chip and wire bonding or flip-chip option. The third level is generally referring to attaching the daughter to the motherboard.

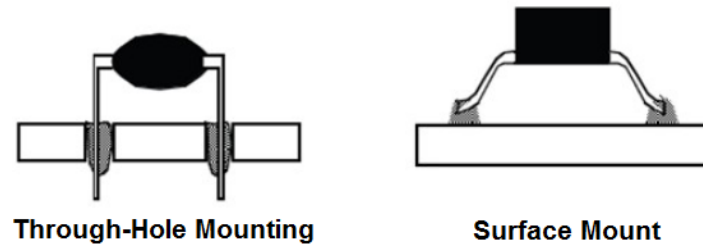


Figure 2.2: THMT vs. SMT Components

2.2.1 Through-Hole Mount Technology (THMT)

The concept of bonding in this type is the insertion of components leads to plated-through holes existed within the PCB. Then, leads are clinched and cut to as a fastening technique before soldering. Solder joints after wave soldering provide electrical connection and mechanical support. This is the first type of component, but it has few I/Os connections and required a sizeable real state area on the PCB. On the other hand, it has extraordinary reliability compared to SMT ones. Dual in-line packages (DIPs) are the oldest type. It is about two rows of leads or pins arranged on 100 mils pitch centers along the longer sides of the package. With these specifications, no more than 8-10 pins (I/O) for each package with a large cross-section of these leads. The advantage is robustness in addition to the advantage of automatic and smoothing assembly. After insertion, it is clinched and passed through a wave of molten solders. The final standoff of the final DIP is massive compared to other packages that facilitate cleaning the flux to avoid corrosion. Quality assurance performs testing for DIP by connecting lead to wire bonding to assure its functionality before assembly. The last step in assembly is to plate the leads to prevent storage-related problems like corrosion. Cases might be plastic or ceramic, where the latter have better hermeticity for high-

reliability applications. The main disadvantages of this type are low real-estate efficiency, limited I/O up to 64 pins for the largest one, and poor wire-ability. Zigzag in-line (ZIP) is another type of THMT carrier but has ZIP packages employed basically to reduce the pitch effectiveness and increase the area efficiency. Pin-grid-array is utilized as a substitution of DIP when higher I/O is necessary up to 940 pins. In a ceramic related type of this assembly, which utilized for reliable application, a heat sink is employed with design modifications. The related problem is the elevated cost for both the ceramic package and the compatible PCB. Figure 2.3 shows some examples of THME components [2,4].

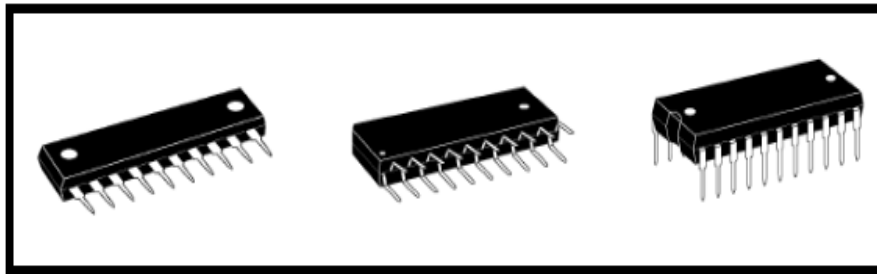


Figure 2.3: THMT Components

2.2.2. Surface Mount Technology (SMT)

MT chip carriers are classified based on types of connection with PCB into four main groups: leaded, leadless, BGAs, and chip-scale packages. SMT packages are mounted on PCB rather than penetration as through-hole types. The critical characteristic of SMT is the capability to offer excellent packaging density that reflects on real-estate savings. This reduction in size positively affects other electrical characteristics, such as less parasitic losses of inductance and conductance. On the other hand, SMTs have several concerns. Package bodies are exposed to high temperatures during reflow, causing many warping issues and moisture cracking failures. Also, packages are very close to PCB, which impact negatively on the flux cleanliness process. Although bodies are

exposed to high temperatures due to their closeness to the PCB, the leads are not. This means more rigorous in solderability requirements. There are passive and active SMT packages. The former lends its electrical properties to the circuit with no additional control. Resistors, capacitors, and inductors are examples of passive packages. Active components are characterized by having logical or control functions affecting the circuit. Other types of packages are examples of active components such as BGAs, DIP, SOT, QFN, etc. Active or passive components might be either THMT or SMT type. Figure 2.4 shows examples of these components of such active components.

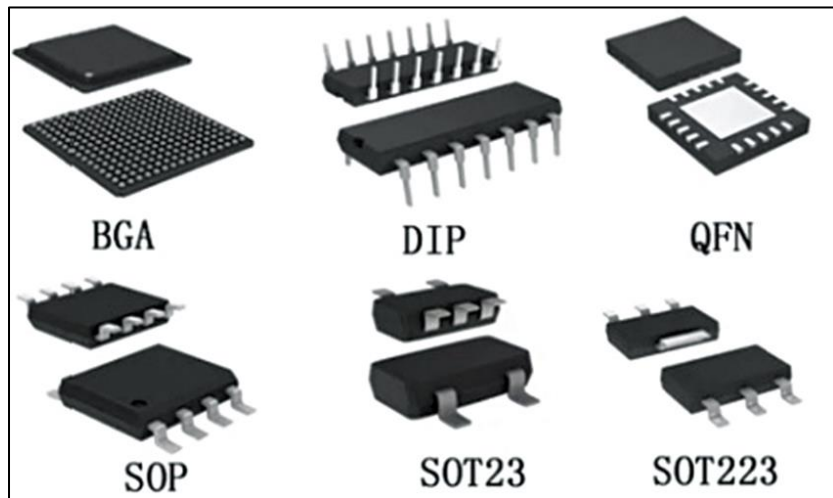


Figure 2.4: Examples of Active Components

Passive components like; monolithic ceramic capacitor, tantalum capacitor, and thick film resistor are the most common types of components. Such packages have wide ranges of sizes that could be either rectangular or circular, and they are small relative to SMT. Also, their weight is ten times lower leaded one with termination utilized to be mounted rather than leads. Terminations offer better design benefits of shock and vibration, with a significant reduction in parasitic losses. The circular or tubular types are less in cost but have some reliability and material handling challenges. Two types of terminations are available: wraparound and flat terminations, where the former is

commonly used due to its better solderability. Solder-dipped and Nickel plating are the two types of finishes for terminations, where the latter found to have extra benefits in placement and dissolution prevention. Due to their lower weight, such packages have challenges in misalignment and tombstoning during reflow soldering [1-2, 6-7].

Moreover, it has parts leaching problems during wave soldering. There are two types of resistors: discrete and the network one. Thick and thin films are the two main types of discrete. The resistors manufacturing process is almost the same, and the core one is screening a resistive film, usually ruthenium dioxide, on a flat alumina substrate surface. This is where resistance value is obtained and might be adapted based on the deposited resistive film. A passivation layer is utilized to cover the resistive layer for protection and heat dissipation purposes. Terminations usually consist of three layers: adhesion layer, Nickel barrier, and solder coating arranged from inside to outside, respectively. Thick film ones are the most common due to their low cost, but the thin film is utilized when precise tolerances (less than 1% compared up to 20% for thick ones) are required. Resistors have several watt ratings for different sizes. Zero resistors are used, which called a "jumper." There are many similarities between resistors and capacitors in design and manufacturing. Capacitors' primary function is to regulate the output voltage of components. It could be made of ceramic or tantalum. Ceramic majorly utilized for high-frequency applications like DRAMs while tantalum could be used for large volumetric ones. Due to the sensitivity of such applications where ceramic capacitors are utilized, leads or termination must be minimized to avoid related parasitic losses. Generally, capacitors used for decoupling and frequency control applications, and it's the most considerable component that could be found in any electronic system. The number of dielectric layers determines the capacitor value; the more the layers, the larger the capacitance value.

With all these benefits for a capacitor, there is a challenge in harsh applications, including thermal cycling. A severe problem is demonstrated due to mismatch in CTE of various parts that cause early failures. Tantalum capacitors are fit for high volume and reliability applications. Instead of termination, tantalum ones have other configurations: welded sub contacts, and warp under lead contacts. The latter has some concerns during placement in addition to the gold terminations that could embrittle joints. Commonly, capacitance value ranges between 0.1 to 100 μ F. Figure 2.5 illustrates examples of passive components.

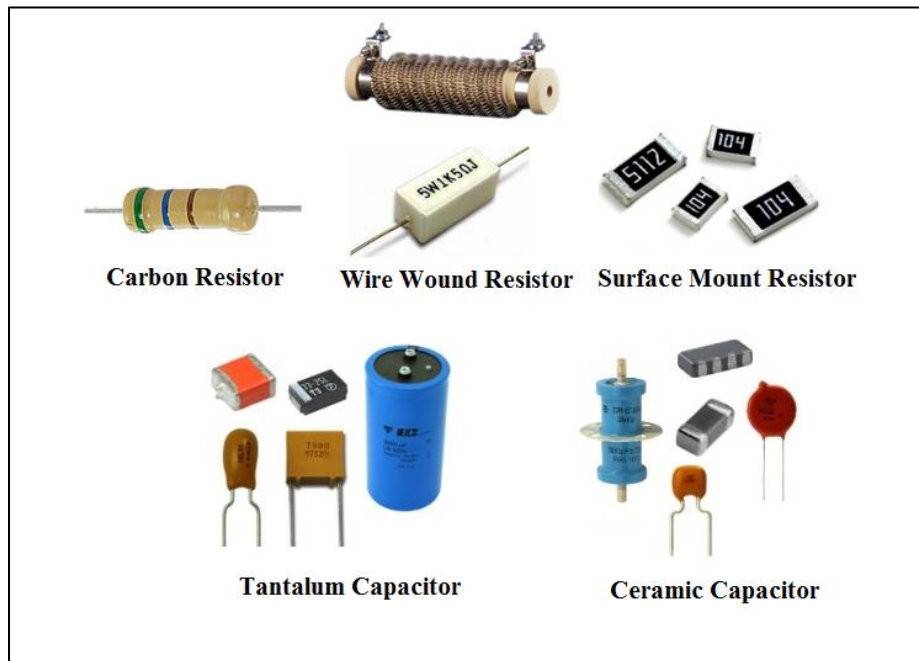


Figure 2.5: Examples of Passive Components

There are many configurations based on size, type, and design for the SMT active packages. Ceramic packages with leadless ends are utilized mainly in military applications due to their hermeticity, which provides high circuit performance and superior package reliability. The drawback is the mismatch in CTE with glass epoxy boards, which causing joint cracking and reduces the reliability. This problem is solved by employing a ceramic substrate, which impacts

with higher cost. Leadless ceramic chip carriers are mainly used in the military due to their capability to sustain harsh operating temperatures between -55°C to 125°C . Leads are replaced by gold-plated, grooved terminations called castellations. This design provides shorter contact and fewer signal paths, which means fewer losses.

The standard pitches are 40 and 50 mils with other few options for fine pitches. Schematic for BGA is shown in Figure 2.6 illustrating the pitch distance. There are many designs and lid orientation which provide more options for connection and heat dissipation purposes. Leaded options are also available with two connecting options of pre-leaded and post led. The difference between these types is that preloaded type supplied to assembly plant with attached lead, wherein the latter one, assembly plants internally attach leads to packages [1, 3]. There are many types of leads: J, L, S, or gull-wing shape. Due to the new process of attachment, leaded ceramic packages are not used generally where the most common ones are leadless ceramic and plastic packages.

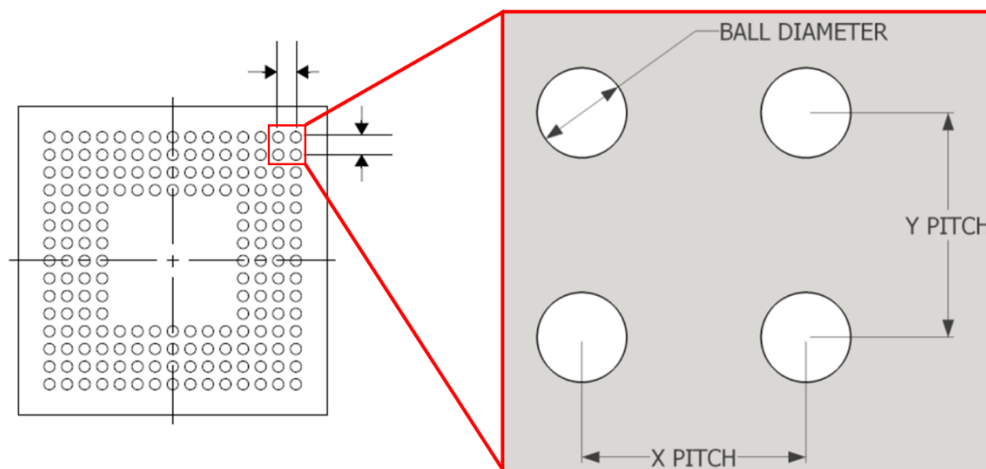


Figure 2.6: Schematic of BGA with Pitch Distance

On the other hand, plastic component is the typical type in the industry and consumer electronics. Unlike the ceramic one, they are compatible with glass epoxy substrate due to their close CTE

matching, which benefits with cost-effectiveness and high-reliability interconnection. In contrast, there are few drawbacks shown up when utilizing plastic packages during the reflow process. Unlike ceramic packages, plastic ones are susceptible to moisture. The three main factors that influence the cracking susceptibility are the size of the die, plastic thickness, and moisture content in surroundings. Simply, the cracking mechanism starts when the moisture content in the package exceeds the threshold limit; crack is initiated due to moisture expansion caused by reflow temperature. The most common packages used are small outline transistor (SOT), small outline diodes (SOD), small outline integrated circuit (SOIC), small outline J-lead devices (SOJ), and plastic leaded carrier (PLCC) [1-3, 9]. Examples of plastic components are shown in Figure 2.7

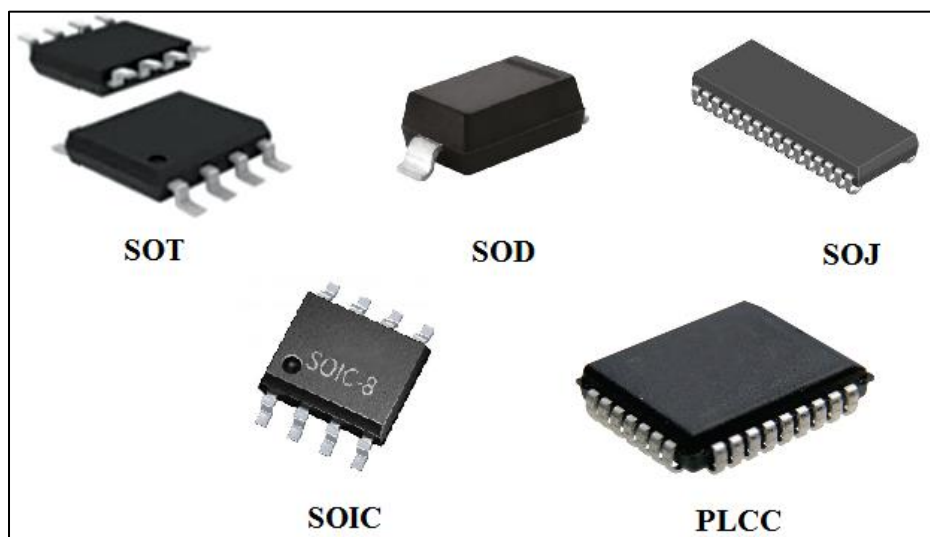


Figure 2.7: Examples of Plastic Components

SOT is one of the predecessors in electronics, among other active devices. They are ones with three leads: SOT23, SOT 89, or with four lead as SOT 143 devices. SOD group has two connecting configurations; gull wing and leads bent under the package. The three leads are the most widespread, but the four leads utilized mainly in RF applications transistors. Dual diodes and Darlington transistors are examples of these packages. These devices are attached using wave or

reflow soldering. SOICs are shrinkage model of DIP but with smaller pitches (0.05 inch) and could house larger IC than is SOT packages. Gull wings are the most common type of connection with PCB, where it's hard to inspect compared to other lead types. Theoretically, these packages suffer from serious reliability issues due to their CTE mismatch between its plastic package and alloy-42 or Kovar leads. Fortunately, the industry overcomes this concern by utilizing Cu leads and enhance the plastic mold properties to reduce the mismatch in CTE. Plastic lead carrier considered as the compulsory replacement of DIP, especially with 40 pins. It has several leads counts for different applications. The leads in PLCC aims to take up excessive joint stress and prevent joints from cracking. Coplanarity is a frequent problem for PLCC, and planarization is a suggested method but not recommended to solve the problem. Elegant pitch packages are introduced to the industry because of the necessity to higher counts (I/O) with small real-state.

Also, larger packages have challenges to keep coplanarity during reflow, and fine pitches were the solution for this issue. Fine pitches have corner bumpers, which extends 2 mils beyond the leads for extra protection during handling. Pitches could be 0.5, 0.4, or 0.3 mm and different pins up to 576 pins—the standoff heights for these packages ranging from 0-25 mils in all standards. Components like SOIC and PLCC are soldered using convection or vapor phase reflow process.

Fine pitch packages solve the problem of less I/Os by utilizing more pins with less pitch distance. This requires precise, and windows tighten processes, but it lowers the package yield due to fragile leads during handling. High cost for these packages is another concern in addition to challenges of handling and rework. As a result, BGAs showed promising characteristics to solve several of the problems mentioned above related to fine pitch components. BGAs provide high density with significant yield improvement. Also, they have short leads, which imply less parasitic losses and signal propagation delay. BGAs could be either ceramic or plastic-type. The most remarkable

characteristic about BGAs is its self-alignment during reflow even when misplaced by up to 50%. BGAs arrays might be perimeter or full array, with ball pitches 40,50, and 60 mils and pin count varying from 16-2400. Unlike the plastic ones, Ceramic BGAs (CBGAs) are hermetic and tightly sealed, which results in zero water or vapor absorption. The result is the elimination of the popcorn effect that occurred due to moisture absorption. Their standoff is measured by ball diameter, which is commonly 35 mils, and its proofed to be adequate for rework. The drawbacks of CBGAs are the high thermal mass and CTE mismatch with glass-epoxy substrates. The former issue causes some difficulties in the reflow profile, where the later threatened the reliability. This problem could be solved by utilizing a ceramic substrate but increase the cost significantly. Another version of CBGAs is the ceramic column grid array (CCGA), where columns replace balls with a diameter of 20 mils and height ranging between 0.05-0.087 inch. The extra height improves reliability because more stress could be taken up due to mismatch in CTE [1, 4].

On the other hand, taller joints reduce the electrical performance and add more cost to package profile with more susceptible to handling damage. Plastic BGAs (PBGAs) is widespread in the industry due to its lower cost. Its internal connection might be either wire bond or flip-chip interconnection. Heat slug could be utilized within the package to enhance thermal performance. Resins form part of the mold, which enhances the stability performance for these packages by reducing the mismatch with PCB. Generally, PBAGs are low in cost, but it could be increased if fine pitches are utilized.

The reason is due to the high cost of fine line PCBs and high-temperature resins. There are other concerns about PBGAs, which are difficult to work and warpage during reflow at high temperatures. Unlike the CBGAs, these packages are sensitive to moisture where mold package crack and die delamination are the most common related failures. The component sizes, solder ball

diameters, and pitches are almost the same as ceramic type. There are other types of BGAs: tape BGAs (TBGAs) and chip-scale packages (CSPs). The latter is a modified version of BGAs, but the significant difference is the higher ratio of dying to overall package dimensions. The percentages of the bare area around the silicon die are no more than 20%. CSPs have two main concerns, which are larger package size and lower electrical performance compared to BGAs. Figure 2.8 shows examples of BGA family.

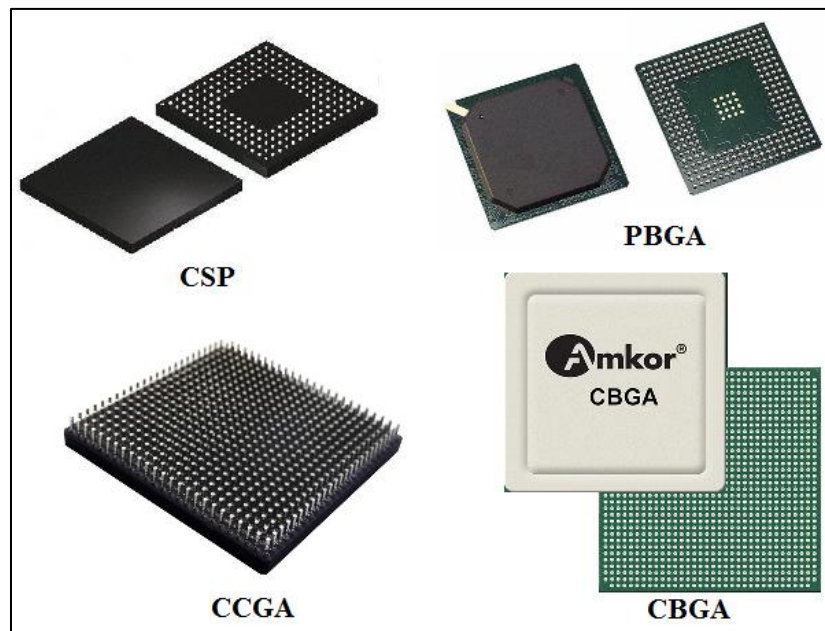


Figure 2.8: Examples of BGA Components

2.2.3 Electronic Substrate

The substrate is the support structure for packaging and interconnections and plays a vital role in providing electrical, mechanical, and thermal support. Substrate selection depends mainly on the application of either military or industry. For military applications, ceramic packages are utilized due to its hermiticity, where two types of substrates could be employed. If high reliability is required, a ceramic substrate is used to reduce the mismatch in CTE with trade-off the cost. There

is another approach that is developing a substrate with a surface layer to absorb the stress. Even this method proves to enhance the reliability of solder joints, but problems were shifted to surface layer vias and traces, and it is not utilized in industry. The last option is to use leaded packages rather than leadless ones, which improve the reliability of joints but not eliminate related issues. This option could employ PCBs of epoxy type with acceptable reliability. Figure 2.9 shows an example of the substrate [1, 5, 8].

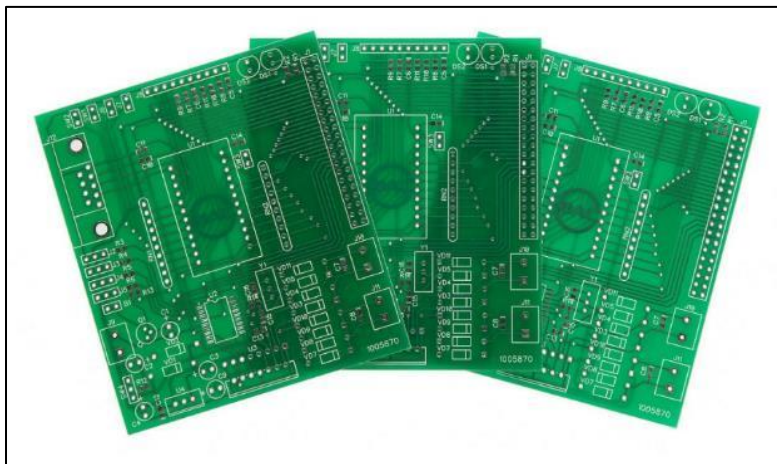


Figure 2.9: Examples of Substrates

The glass transition temperature is another characteristic that is considered seriously during selection. It is a property for polymers that describes the change of substrate physical structure from hard to soft, rubbery phase with temperature. If the reflow temperature exceeds the transition temperature, many reliability issues will show up. At high temperature and rubbery phase, any small force could deform the PCB easily and cause the warpage, which impacts the reliability. This problem is found only in polymer-based substrates like epoxy but not in ceramic ones—the glass transition temperature for epoxies like FR-4, almost 120°C, and about 230°C for polyimide.

The thermal expansion coefficients in three dimensions of X, Y, and Z are of great importance. The issue is that the glass laminate expands greatly, but the resin has some sort of constraints. Even

the three-dimensional expansion is for the same material; the magnitudes are different due to anisotropic (direction independent) property. The problem is exacerbating when there is a different combination of materials. In X and Y direction, laminate thermal expansion is constrained by many elements within the PCB of all layers; glass fibers, copper traces, pads, barrel, or vias plating.

On the other hand, Z-direction expansion isn't constrained by any previous elements except the plating of the vias. As a result, large (almost ten times) expansion is expected in Z-direction compared to other directions. It's found that in X-Y direction has CTE about 12-16 ppm/°C, where its 100-200 ppm/°C in Z-direction. That is why it is essential to consider the thickness of the substrate as it causes serious reliability issues due to vias cracking under thermal stress [1-2].

2.2.3.1 Substrate Materials

Ceramic substrates are the most used substrates in military applications due to CTE matching with ceramic components but with an added cost. The two main manufacturing processes for ceramic PCBs are thick and thin-film processes. The thin-film process is a subtractive method utilized to determine the elements such as conductors and resistors on the substrate. Naturally, the process is as following; resistive materials are deposited in vacuum followed by gold plating. Then, gold is removed from areas at desired resistors locations. Copper replaced the gold to avoid joint embrittlement due to IMC formation related to gold. This process is expensive but utilized for very narrow widths of about two mils. Thick film technology is capable of producing 4 mils, but the standard widths are ten mils. The process starts with screen printing various layers of conductance, resistance, and insulation. Then, its volatiles removed by drying and finally fired. Firing ceramic substrates occurred at 1500°C.

Glass-epoxy is the most utilized PCB material in consumer electronics and commercial applications. As the name implies, it consists of two parts: epoxy and glass fibers. Glass fibers are the base material that provides laminate stability. Epoxy or resin gives the laminate the ductility property. The composite material is preferred due to its ability to combine properties of different materials in one structure. For instance, glass is stiff and brittle under bending while adding sturdy material such as resin improves ductility. Glass fiber has no difference in processing than any other glass process. Sand is melted at high temperature; then, the molten glass is extruded in various diameters. Small diameters are formed into bundles or yarns and tied together as one piece. Epoxy resin is injected within the glass cloth and holds everything together. The resin contains chemicals such as curing agents, flame retardants, and other adhesion additives added to improve the properties. Curing agent improves the cross-linking of epoxy chains. Flame retardants are added to enhance safety by making the PCB self-extinguishing. Adhesion elements promote the connection between cloth and epoxy resin. Many types are depending on the laminate polymer and resin systems used. Phenolic, epoxy, polyester, and polyimide are examples of resin systems. However, paper and glass fibers are examples of the base material. The substrate might be single or multilayer (as shown in Figure 2.10), where the most common types are G-10 and FR-4 since they are cheap and the process only. Multilayer PCB is processed by utilizing partially cured material called prepreg [3, 6, 8].

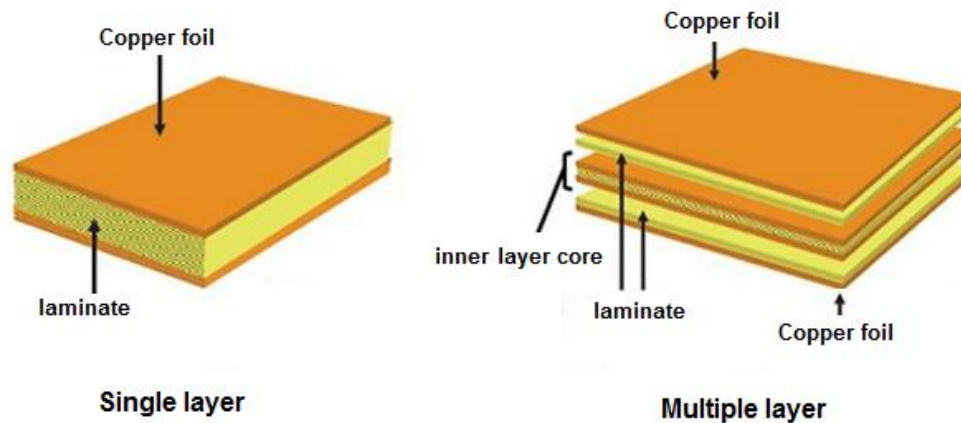


Figure 2.10: Single vs. Multilayer PCB Designs

2.2.3.2 Surface Finishes

Surface finish defined as the layer of coating between bare board and components. Surface finish is applied to enhance the solderability and protect Cu parts from environmental effects. Surface finish is mainly provided by the plating process, which has two main types: electroplating and electroless plating. The former type is the deposition of metal molecules in an electrolytic chemical solution using electricity as a prime mover for moving molecules to the target. The electroless process is also a chemical composition but requires a reducing agent to move metal out of the chemical path to the target. Plating is a critical process and determines many PCB characteristics such as quality in addition to other mechanical properties such as fatigue and shear strength. Plating may involve several metals such as copper, nickel, silver, gold, etc. Plating mechanism is almost the same in concept for all processes; solution containing metals is the source, while plating occurs when positive ion incorporating with a negative electron from the source. The plating process might be for the copper pads, traces vias, etc. The first plating was Hot Air Solder Leveling (HASL), which typically performed by applying flux to PCB and dipped it into Tin/Lead solder

pot. The final coating is a thin layer of solder protecting the Cu. There are many challenges with this type of rough surface, PCB warping, and vias damages. Since Pb is prohibited from using, it's no more used in the field. An example of surface finish within the electronic package is shown in Figure 2.11.

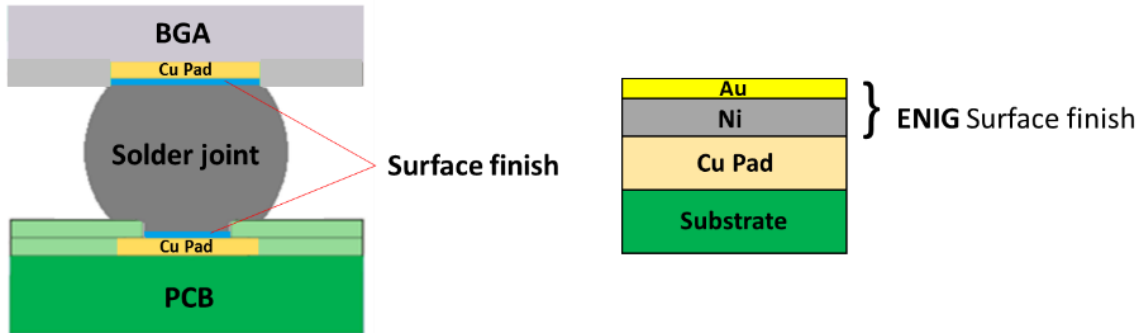


Figure 2.11: Example of Surface Finish- ENIG

Organic solderability preservative (OSP) is one most common types of surface finish utilized in PCB manufacturing. It's a water-based, anti-tarnish coating made from organic compounds over the Cu surface to avoid oxidation and corrosion. There are various types of compounds utilized as benzotriazole, imidazole, etc. The bonding provides the protective layer between the organic compounds with the Cu layer on pads. This layer provides protection and keeps the Cu solderable. It has other advantages that make it preferable for the electronics industry; it has low cost, flatten the surface compared to other alloys, is lead-free, and has fewer effects on the environment. There are two classifications for the coating based on the thickness: thick and thin. Thick type ranges between 0.2-0.5 μm , where the thin one ranges between 0.1-0.2 μm . There are some concerns about OSP, especially its robustness. Also, some issues of de-wetting might occur in thin layers and caused the exposition of Cu. The other drawback of this type is the incompatibility with specific flux and paste types, which causes improper soldering fillets. Due to its weakness compared to

other metals coating, OSP finish may suffer from reliability issues specifically under thermal cycling. Electroless Nickel Immersion Gold (ENIG) is a metal type coating used to protect the Cu pads from different kinds of corrosion. Nickel is first applied using electroless coating, followed by depositing a layer of gold. This type of finish impacts the finish with both layers' benefits; nickel to provide a flat, smooth surface, and Au enhances the wettability. There are two issues related to this finish: IMC embrittlement and black pads. Previous study [38] has shown brittle interface fracture for this type of finish. Gold diffuses into the bulk sample, and IMC becomes thicker and weaker. Black pad is the black corroded spots or layer of nickel lefts on the Cu pads causing open circuit and failure. Immersion Silver (ImAg) is another typical finish utilized for coating PCB. It helps to enhance the solderability and reduce with low cost compared to ENIG. The IMC near the interfacial contact or even in bulk is different and related to the surface finish. In OSP type, the common IMC is related to joint material, no effect or migration, or even interaction between them. Therefore, Cu_6Sn_5 and Ag_3Sn are observed. Since there is Au in ENIG, new IMCs are formed, such as AuSn_4 and the other IMCs. For the ImAg, Ag_3Sn is the common related one in addition to Cu_6Sn_5 . There is another IMC; Cu_3Sn , which doesn't form except with high content of Cu like near the Cu pads. These interfacial IMC grows with time (aging), get thicker and more brittle. So, it becomes a critical point that threatens the joint. Aging at elevated temperature due to harsh applications exacerbates the problem [1-3, 9, 12-14].

2.2.3.3 Solder Mask

Solder mask defined as a gloss-like layer made out of polymer (commonly Acrylate and Epoxy) applied on the PCB to protect the Cu traces on the top of it. The main goal is to protect the copper traces from oxidation and prevent solder bridging. The pads might be either solder mask defined, or non-solder mask defined. In the former type, the area in which the solder ball is attached is

called the solder mask defined area. However, the NSMD is the solder mask area that does not cover the Cu pad. SMD is weaker than NSMD due to less contact area because the mask area is far away from the pads. SMD and NSMD areas are shown in Figure 2.12.

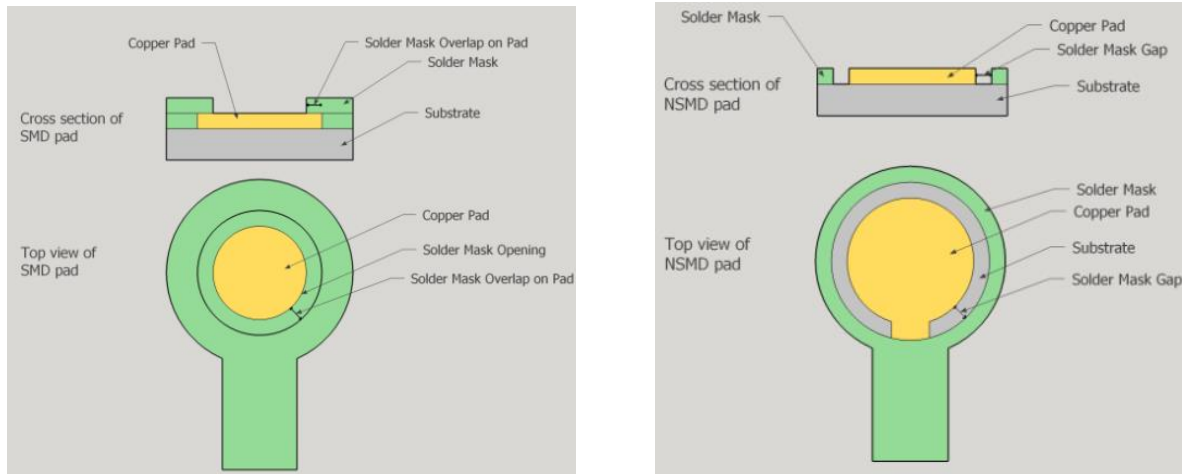


Figure 2.12: Top view of NSMD and SMD pads

According to the images shown above, the SMD has overlapped the Cu pad area and provides less area than the original Cu pad. On the other hand of NSMD, there is space between the Cu pad and mask, so the soldered area covers the whole pads. Therefore, NSMD showed higher resistance of thermo-mechanical fatigue due to better stress distribution among the contact area than the one of SMD [1-3].

2.3 Assembly Process

Components are placed on the board using pick-and-place machines. At the beginnings, this step was done manually for prototyping purposes with the aid of a microscope. Nowadays, automated pick and place machines are utilized. The utilized machine depends mainly on the application, assembly size, placement rate, feeder's capacity, type, and required placement rate and accuracy. Feeders might be of the wafer, tray, bulk, tape type, or combination of any of these. Placement is

the other essential parameter for choosing the pick-and-place machines. This includes many aspects as a way to pick components, positioning, and placement. An example of a pick-and-place machine is shown in Figure 2.13.



Figure 2.13: Example of Pick-and-Place Machine

After the components are placed on top of boards, the assembling process takes place by soldering them to the boards. Soldering is the same as welding but occurred at lower temperature ranges. There are two main ways to perform soldering: wave soldering (Figure 2.10) or reflow soldering (Figure 2.11). Wave soldering is utilized for different purposes: soldering components terminations for THMT and soldering discrete components such as resistors, capacitors, diodes, etc. Typically, the most critical factor in wave soldering is wave geometry. It includes directions (uni or bi), how many waves (single or double), types of waves (vibration or turbulent), and others. The primary classification for wave geometry is dual and vibration waves. For dual wave, there are two waves: smooth and turbulent. The first is turbulent, which ensures the best distribution of solders among the board surface, whereas the laminar or smooth one eliminates the bridging. Oil

is introduced as a thin-film layer mainly reduces the oxide formation. The turbulent wave oscillates perpendicular to the PCB back and forth many times either from multiple tiny nozzles or one nozzle only where the tiny ones are better to assure narrow, precise jetting and printing. Vibration is another type of wave soldering by either oscillation wave from nozzles or ultrasonic vibrating waves called the OMEGA wave. The latter is commonly employed due to its higher capability of controlling the waving process and its related targets. The frequency for this wave ranges between 50 or 60 Hz. This process is performed under an inert environment like N₂ to reduce the outgassing and solder skips. Many studies showed that the vibration method is more efficient and sophisticated than dual wave one. For the double-sided PCBs, there are many scenarios of two steps of bonding the small components and soldering them via wave or reflow soldering on the second side and reflow the SMT heavy components on the first side. There might be many related problems shown up like adhesion problems with temperature, adhesion curing, etc. Even the process might be of one step; it will take more time for adhesion dispensing and curing. Figure 2.14 shows the process of wave soldering [1, 4-5, 13].

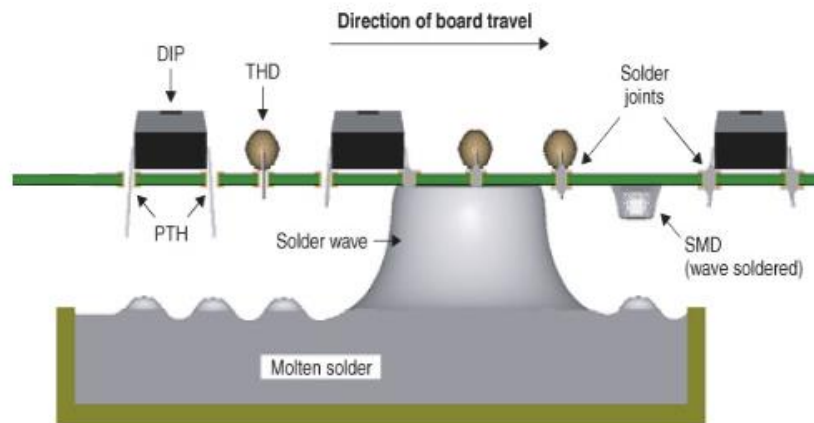


Figure 2.14: Wave Soldering

The reflow process for the SMT heavy components options are either vapor phase or infrared reflow oven. Vapor Phase Soldering (VPS) produces many defects, and it's used only for specified applications. On the other hand, it has precise heat distribution through different components and higher efficiency. The concept of this process is to use the latent heat of vaporized liquid to provide heat for soldering. The liquid is spread on the solder joint, and as its vaporized, it lends its latent heat to the joint and vaporizes. Since the maximum temperature for the system is the boiling point of the liquid, no component will reach that, resulting in better heat distribution and eliminating the related warping issues. Perfluorocarbon is the primary type of these liquids with boiling points around 215°C. The severe problem of this type is the solder wicking. Since both Cu pads and joints are heating up with different rates, leads reach the high-temperature 16s before the land causing the solder to wick to the leads and create an open joint.

There was a suggestion to reduce it by preheating the whole system, but this doesn't eliminate it. Another way is to employ different compositions of paste with a higher melting point, so the paste will wait to heat up with PCB simultaneously. Examples of in-line vapor phase soldering are shown in Figure 2.15.

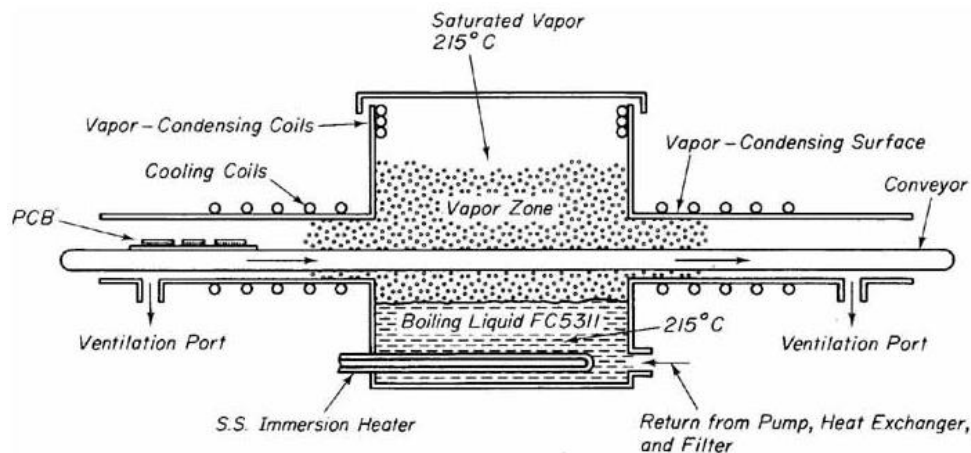


Figure 2.15: In-line Vapor Phase Soldering

Reflow ovens weren't popular at the beginnings due to critical issues shown up, such as PCB burning, charring, and discoloration. The leading cause was the improper reflow profiles that have been utilized. There are three main types of systems; radiant IR, Convection IR, and convection only type based on the type of heat of convection and radiation and heat mechanism. Each one has its applications and preferences, and there is no perfect IR or convection. Even in IR convection systems alone, there is no full IR or convection since both effects exist with less than 20% of the other source. For the typical case of IR and convection, the effect of both is almost equal in amount with 60% for the convection. Typically, convection ovens have separate, controlled, multiple heat zones between 3-20 monitored continuously by thermocouple system or thermal profiler. Gradual heat is required to avoid any thermal shocks, and it would help drive off the volatile elements rather than trapped within solders. PCB is moved between zones via conveyor where each zone has fans to circulate air to have steady-state, uniformly heat distribution within the oven. The oven must have three main zones of preheating, soaking, and cooling [1-2].

Preheating majorly dry off the paste's volatiles, soaking assures the uniform elevated temperature distribution among the PCB, where the cooling to cool down the joints and end the soldering process. Any additional zones for any of these types are recommended to achieve the best-related profile for that region smoothly. IR ovens have the radiation mechanism where the convection oven used the convection mechanism. The difference is that radiation doesn't require any physical contact since its mandatory to have different temperatures of both bodies to radiate energy between them. On the other hand, there must be physical contact between the fluid and the solid in the convection ovens. The issue with radiation ovens is the low radiant required between bodies to avoid firing. This means lower temperature and a longer wavelength, which would result in more reflection and shadow effect. The challenge would be to find the best profile considering various

variables: heat level, wavelength, and shadow effect. Since the convection oven depends on convection heat transfer, it could be enhanced by increasing the temperature or convection transfer coefficient. The former has limitations due to solder paste melting points and other defects related to high temperature. The second factor is the convection coefficient, which is influenced by the flow rate and angle of attack. The higher the flow rate, and the more vertical the angle, the higher coefficient of convection. That is why their fans are added on vertical directions of the joints within the oven. One of the main benefits of convection solder is that the air temperature limits the solder temperature. Also, this process is enhanced by employing inert gases during different reflow zones. The combined convection/IR has some benefits of both types, such as minimizing the shadow effect and PCB coloring problem. On the other hand, incomplete paste curing occurs due to severe skin formation resulting from circulating air. This skin would explode, causing splattering during reflow. Recently, convection ovens dominate the market due to difficulties associated with IR ones with new BGAs joints, which is the impermissibility of radiation to the inner joints of these packages. Example of solder reflow oven including inert gas blanketing is shown in Figure 2.16.

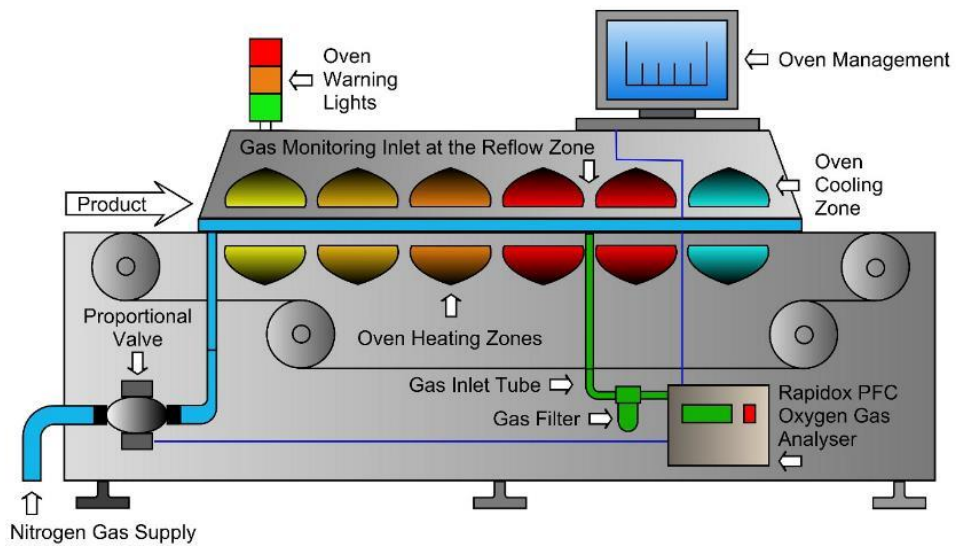


Figure 2.16: Reflow Oven Soldering

2.4 Reliability

Reliability is defined as the probability of not failing for specific products during lifetime operation. The goal of reliability science is to increase the process performance by reducing the failures and machine downtimes. Also, it includes the failure root cause investigation, analyzing, and characterization. Reliability is a probability-based art due to the differences like operational processes and conditions that could generate many results where it's time-dependent and degrades with time. Failure data collected from different accelerated tests and fitted to particular distribution are utilized to generate failure distributions for time accordingly. Least square or maximum likelihood methods are mainly applied to check for best parametric estimation. The most common distribution employed in reliability is Weibull distribution.

Failure rates could be decreasing, constant or increasing with time and could be modeled by and characterized by the hazard rate function of the form power function:

$$\lambda(t) = at^b \dots\dots\dots (2.1)$$

Where $\lambda(t)$ is the instantaneous hazard rate or failure rate function, t is time, a, b are constants. The function $\lambda(t)$ increases for both $a>0, b>0$ and decreases for $a>0, b<0$. Basically, failure rate with its three main categories could be presented in Bathtub curve. It summarizes the three behaviors for any product. The first portion of the curve is the early failure, or it's called infant mortality. The second and the third parts are called random failure and wear out curve respectively. The summation of the all these curves together is referred to bathtub curve as shown in Figure 2.17.

Failure could be expressed in other form of Weibull distribution:

$$\lambda(t) = \frac{\beta}{\theta} \left(\frac{t}{\theta}\right)^{\beta-1} \dots\dots\dots (2.2)$$

$$\theta > 0, \beta > 0, t \geq 0$$

Where β is the shape parameter and θ is the scale parameter. Once the hazard rate function $\lambda(t)$ is known, reliability function could be derived by using equation

$$R(t) = \exp \left[- \int_0^t \lambda(t') dt' \right] \dots \dots \dots (2.3)$$

Substituting $\lambda(t)$ in equation above, we get

$$R(t) = \exp \left[- \int_0^t \frac{\beta}{\theta} \left(\frac{t'}{\theta} \right)^{\beta-1} dt' \right] = e^{-\left(\frac{t}{\theta}\right)^\beta} \dots \dots \dots (2.4)$$

And the probability of failure $F(t)$ is defined as:

$$F(t) = 1 - R(t) = 1 - e^{-\left(\frac{t}{\theta}\right)^\beta} \dots \dots \dots (2.5)$$

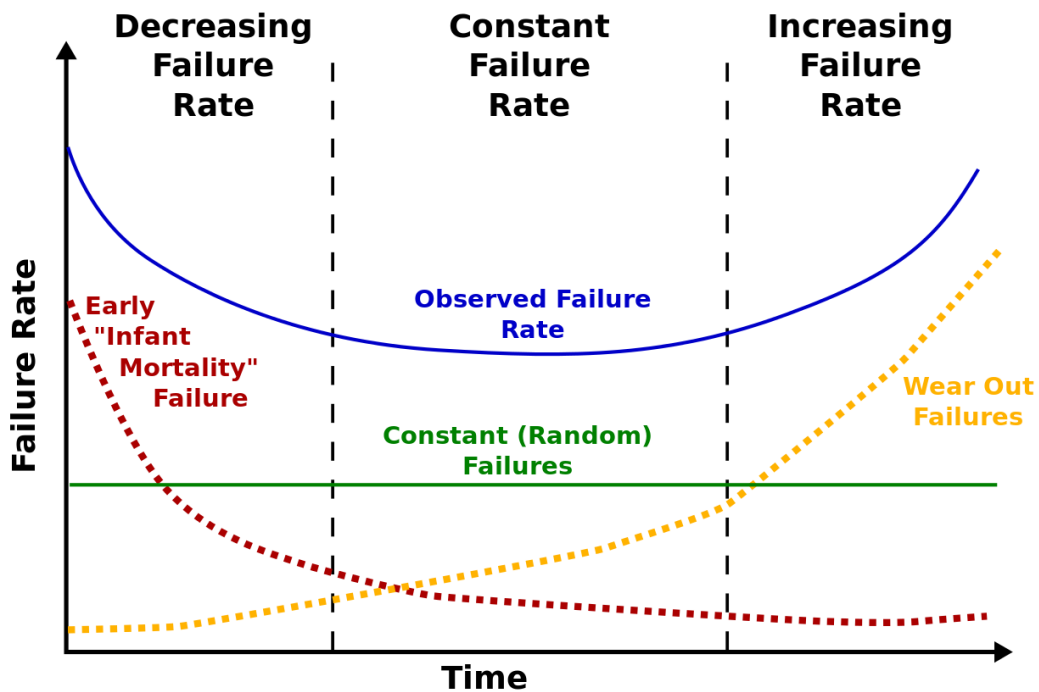


Figure 2.17: Bathtub Curve

In this research, accelerated life tests are useful for predicting the various components' life under different conditions. However, other tests were implemented for other purposes, such as burnin, screen, qualifications, and sequential tests [6-8]. Accelerated life tests are performed to assess the reliability of packaging components under operating conditions in the field. The idea beyond that is the infeasibility of implementing actual tests to assess the reliability under actual operating conditions due to the long time required to perform these tests. Accelerated test conditions simulate what happened in actual operating conditions but in an accelerated manner. This is a critical issue since different failure modes would be generated if accelerated conditions were not employed carefully, and misleading results are obtained. In terms of data, there are seven types of accelerated tests: Type I censoring, Type II censoring, Type III censoring, Type I k multiply censoring, Type II k multiply censoring, Type I replacement, Type II replacement. There are differences in the objectives for these tests. In the three types of censoring, for example, the types of collected data might be different; requires failure for all test samples in the first type, data is collected whatever it's once the test cycles or time is finished for the second type, and finally the third type which aims to terminate the test once a certain number of failure generated. Types I and II k similar for second and third types, respectively, but the difference is in removing samples rather than collecting failures. In types I and II replacement, the main characteristics of these tests are replacing the failed samples during the test or finishing it after a certain number of replacements.

In accelerated tests, harsh conditions are applied to enhance the occurrence of the failure within a shorter time compared to normal operating conditions. This could be happened by employing one or different harsh conditions such as applying a higher number of cycles per time unit (frequency), increasing the stress amplitudes compared to one in the field, applying elevated temperatures ranges, harsh vibration amplitude, and so on. Consequently, adapted equations are generated,

including actual life cycles relevant to accelerated test cycles with specific multiplier termed accelerated factor.

There are different models utilized for different test purposes and research objectives, including accelerating factors. In this particular research work, there are plenty related to various testing parameters as constant stress, work per cycle, strain, elevated temperatures, and thermal cycling profiles in addition to others. Constant-Stress model is a standard model employed to estimate life under constant stress. The mechanism showed that the same behavior is followed when stress level changes with the same mode of failure. It's a linear relationship between operational life relates to testing life with acceleration factor according to the equation below

$$t_n = AF * t_s \dots\dots\dots (2.6)$$

Where t_n , t_s are the life at both normal and testing conditions respectively. AF is the acceleration factor.

Arrhenius model is utilized when elevated temperature is part of the test conditions. Accelerated factor is generated according to the following equation

$$AF = \exp [B (\frac{1}{T_1} - \frac{1}{T_2})] \dots\dots\dots (2.7)$$

Where B is constant, T_1 and T_2 are the temperatures in Kelvins for the both actual operation and testing conditions respectively. Other model called Eyring model include a combined effect of both temperature and stress. Such factor is presented by below equation

$$AF = (\frac{T_2}{T_1})^A \exp [B (\frac{1}{T_1} - \frac{1}{T_2}) e^{C (S_2 - S_1)}] \dots\dots\dots (2.8)$$

Where A, B, C are constants, T₁ and T₂ are the temperatures in Kelvins for the both actual operation and testing conditions respectively. S₁ and S₂ are the stress for the both actual operation and testing conditions respectively. Coffin-Manson model is a common model utilized to simulate the stress cycling at different temperature levels according to the following equation

$$AF = \frac{N_L}{N_H} = \left(\frac{\Delta T_H}{\Delta T_L}\right)^b * \left(\frac{f_L}{f_H}\right)^{-a} * \exp\left[\left(\frac{E_a}{K}\right) * \left(\frac{1}{T_{KH}} - \frac{1}{T_{KL}}\right)\right] \dots\dots\dots (2.9)$$

Where a is cycling exponent, b is temperature range exponent, where E_a is the activation energy constants. N_L and N_H are the number of cycles required to initiate the crack at low and high stress level, respectively. ΔT_L and ΔT_H are the number of cycles required to initiate the crack at low and high stress level, respectively. f_L and f_H are the number of cycles per day for low and high stress level, respectively. T_{Kh} and T_{Kl} are the maximum absolute temperature (K) for high and low stress level, respectively. For thermal cycling, there are two common models: Norris-Landzberg and Engelmaier models. The former was the first model established to relate the life of interconnects under various thermal cycling conditions according to below equation

$$\frac{N_{Lab}}{N_{Machine}} = \left(\frac{\Delta T_M}{\Delta T_L}\right)^2 * \left(\frac{f_L}{f_M}\right)^{0.5} * \Phi(T_{max}) \dots\dots\dots (2.10)$$

Where f_L and f_M are the frequencies of cycles per day under lab and machine conditions, respectively. ΔT_L and ΔT_M are the testing temperatures under lab and machine conditions, respectively. The last term is an empirical factor related to temperatures between peak temperatures during the test. Many other modified versions of these models were established and due to various varying test conditions, such as materials and its properties, different geometries utilized in different applications, several operational conditions, etc. Engelmaier model is a

modified version of Coffin-Manson model for thermal cycling and power cycling operation conditions according to the following equations

$$N_f = \frac{1}{2} \left(\frac{\Delta\gamma}{2\varepsilon_f} \right)^{\frac{1}{c}}, \dots\dots\dots(2.11)$$

$$c = -0.442 - 6 * 10^{-4} T_s + 1.74 * 10^{-2} \ln(1 + f) \dots\dots\dots (2.12)$$

Where N_f is the mean cycles to failure, $\Delta\gamma$ is cyclic shear strain, ε_f is the fatigue ductility coefficient, c is the fatigue exponent, T_s is the mean cyclic solder joint temperature in °C, f is the cyclic frequency.

Finally, it is critical to mention the importance of failure mode analysis. Failure mode or model is part of physical family models utilized in reliability tests to determine the root cause of the inevitable failure and the mechanism that leads to it. This would help in generating a sophisticated mathematical model based on physics phenomena. The constructed model includes mathematics correlation and parameters related directly or indirectly to other critical factors such as material properties, test sample geometry, environmental conditions, testing profiles, and circumstances. Other factors as dependency on time should be clarified due to its direct relation with reliability functions. To construct such models, specific procedures should be followed to bring up a robust model. First, identify the failure mechanism and modes, and then develop the deterministic model, followed by predicting the reliability under both conditions of actual operational and testing ones with all related test materials, samples, circumstances, etc. Finally, calculate the fatigue life with design suggestions to enhance the service life, material microstructure, and accelerated reliability testing profiles [2-5, 8-9].

Chapter 3: Literature Review

3.1 Electronics Reliability

It is vital to study the reliability of different electronics systems' levels due to the expected occurrence of failure at any of them, especially under harsh conditions. These systems may exist in critical applications such as airplanes, automobiles, and space shuttles, where such failures may threaten lives. Also, the cost and amount of work for fixing such reliability issues are increasing drastically as moving further in the customer chain. For example, repairing early failures for assembled components costs a few cents if discovered at OEM plants, whereas such amounts jump to few hundreds under service conditions. Moreover, the amount of work and effort to find the faulty component and repair it or replace it is tripled. Unfortunately, the failure of an individual solder joint causes breakdown for the entire system and generates problems mentioned before. Therefore, it is essential to investigate the reliability of such systems at the necessary levels of the electronic system, which is the joint level. In this chapter, reliability under vibration, corrosion, and drop is spotted among various studies in the literature. The effects of creep and fatigue on joints reliability under thermal and isothermal conditions are discussed briefly from literature research studies. Several reliability models generated for various tests under different conditions are discussed.

3.2 Reliability Tests

In this section, reliability studies under vibration, corrosion, and drop tests under various circumstances are highlighted. Vibration is defined as the periodic, repetitive motion or displacement of the body from specific reference. Cars under-the-hood suffers from vibration

hundreds of times every day. Moreover, aging has a severe effect on reliability and exacerbates the problem, especially at high temperatures.

Vijayakumar et al. [39] investigated the reliability of SnPb, SAC105 and SAC305 BGAs of various geometries (10, 15, 19 mm) under vibration conditions of 55°C aging temperature and 6, 12, and 24 months aging times. They found that aging at more extended periods (e.g., 12 and 24 months) reduces the reliability significantly compared to the short term of aging (6 months) at 55°C. For SAC alloys, microstructure analysis showed intermetallic failure mode, while the mode is shifted to the component side in SnPb results. Lall et al. [40] studied the reliability of SAC 105 and 305 alloys under combined effects of both vibration and elevated temperatures in automotive applications. Their study includes various testing conditions of vibration G-amplitudes (5g, 10g, and 14g) and temperature level (25°C, 55°C and 155°C) for CABGA packages. Components were aged for two months at 150°C. Also, FEA models were generated for comparison purposes. Results showed that increasing operating temperatures would both reduce and shift the natural frequency. Components exposed to higher amplitudes (nearby the source) failed faster than others far from the source of vibration. Failure founds to be near the IMC layer from the components side. The higher the G-level, the larger the hysteresis loop or inelastic work per cycle and plastic strain generated per cycle. Many vibration studies had been performed, including various testing conditions of short-term aging [41] and random vibration at high temperatures [42-44]. Other research groups have worked on generating prediction models under such conditions [22, 45-46].

Corrosion is another type of damage that affects reliability. There are many forms of causes for corrosion, such as humidity, sulfur [47], environment, and contaminants. The impact of corrosion may be noticed by reducing different electrical performance aspects of an electronic system such as resistivity, conductivity for various parts of the system, PCB, components like resistors [48],

joints [49], and Cu traces and vias. However, many studies look for a suggested solution like isolation with passivation, protective films, and coatings to reduce the influence of corrosion [50].

Drop is another common failure in packaging consumer electronics, especially cell phones. SAC-based alloys showed reliability concerns, particularly with aging compared to SnPb alloys. However, SAC-Doped based alloys show a dramatic increase in reliability results with Bi, Ni, and others compared to SAC only alloys. Cai et al. [51] investigated the effects of doping in enhancing the reliability and mechanical properties of SAC alloys under different aging temperatures (50, 75, 100, and 125°C) and durations (0-6 months). SAC-based alloys and others with dopants were tested to investigate the effect. Also, SnPb alloys were included for comparison purposes. Results show that increasing aging temperatures and periods degrades the reliability and mechanical properties drastically due to microstructure evolution. On the other hand, adding dopants blocks the movement of slip-planes and decreases this effect dramatically. Other researcher studied other conditions of drop tests including several dopants [37], failure mechanisms [35], related prediction models [36], assembly levels [52].

3.3 Effect of Fatigue and Creep on Solder Joint Reliability

The reliability of electronic systems is threatened by a failure of one out of thousands of solder joints connecting several types of components. This is critical because electronic system parts are working together to run a particular logic function under the car hood or at the space shuttle. Since these electronic systems are switching on and off many times every day, the board and attached components are expanding and contracting accordingly. Such a cycle is occurred due to environmental and operating conditions. During this thermomechanical cycling, stresses are generated on the joints connecting boards and its related components due to the mismatch in CTE

between them. Since the temperature difference drives stresses, and it occurred cyclically, it is called thermomechanical fatigue stresses. Researchers try to fundamentally understand this phenomenon by testing on the basic level represented by solder joints under various conditions, geometries, materials, testing specimens, and testing parameters in an accelerated manner. They tried to simulate the joints behavior under real-life conditions to extract more information about failure mechanisms and their unique behavior. In this section, the fatigue and creep failure mechanisms, in addition to related research studies from literature, are introduced briefly.

Coombs V. D. [6] investigated the performance of the fatigue life for the Lap-Type solder joint of different materials; pure Tin, Pure Lead and, Eutectic Tin-Lead. He implemented two types of testing: torsion and lap shear fatigue tests. Torsion tests were performed on a hollow cylinder specimen at different temperature ranges to examine the influence of temperature. On the other hand, lap shear would provide the effect of solder layer thickness on the solder fatigue at room temperature. He found that fatigue behavior for tin-lead and pure tin independent of test temperature with no creep rupture process happened, whereas strong relation was recorded for pure lead materials. In the lap shear test, he found that there is a negative relation between strain range and the cycles to failure at room temperature. Since he used two different types of samples, bulk in torsion test and solder ones in lap shear test, different parallel lines were generated but still in the typical ranges of the strain fatigue behavior. One main reason is due to differences in testing specimen's geometries, which found to be of huge effect on the test results.

Rathore et al. [4] investigated the fatigue behavior of SnPb based alloys doped with different dopants in flip-chip applications. Cantilever solder material specimens were tested at different conditions. The tested temperatures were 25, 85, 120, and 150°C. Two frequency ranges were employed: high of 1800 CPM (cycle per minute) and low of 1800 and 450 CPD (cycle per day).

The strain range was between 0.1-5.0 percent of 200 samples in total. Increasing the temperature found to enhance the damage localization at grain boundaries significantly and cause early failure. With a high strain range of 2.2-5.0 percent, strain range become the dominant failure criteria is the strain range and not the temperature or the strain rate. Finally, a gradual decrease in load amplitude is recorded as a result of stress relaxation.

KARIYA et al. [53] studied the mechanical fatigue properties (fatigue and tensile strength) of different lead-free Sn-3.5Ag-X alloys with referenced to Sn-3.5Ag binary alloy under isothermal conditions. Dopants include Bi, Cu, In, and Zn with various samples of different weight percentages (Wt. %) in dog-bone shape. Results show a significant increase in tensile strength, especially for increasing percentages of Bi. However, a reduction in ductility is observed through the load drop curve, which responsible for lowering fatigue life. Moreover, fatigue behavior with or without the X element still follows the Coffin-Manson relation, and life is dominated by the alloy ductility.

Xu et al. [54] explored the fatigue properties of SAC and SnPb based alloys under isothermal fatigue conditions. PBGAs were used in this test with a shear fatigue profile to check the reliability with various strain ranges. Fatigue constants generated from the Coffin-Manson model provide data about material behavior, reliability, and mechanical properties. At certain strain ranges, SAC305 shows better fatigue reliability than SAC105 and SnPb but not for all strain ranges.

Paradee et al. [21] studied the fatigue behavior and creep relaxation of dog bone SAC305 alloys was explored under different testing conditions. Results showed that increasing the stress would result in more elongation of Sn precipitates. Also, lowering the testing frequency enhances the

separation of different IMC from Sn precipitates and coarsening. Other researchers have been utilized bulk samples in their work and generate similar results [19-20, 23-25, 55].

Sinan et al. [14] investigated the fatigue properties of individual SAC-based doped spheres with Bi, Ni, and Sb and various surface finishes of OSP, ENIG, and ImAg. Shear and shear fatigue tests were performed to identify these properties. It is found that the higher the Ag content, the superior fatigue and shear strength obtained.

The effect of microstructure on reliability was explored by Pang et al. [56] under a various shear rate of 0.0005, 0.005, 0.05, and 0.5 mm/min. results were matched with one in [14,21] that lowering the shear rate would reduce the life significantly.

Hamasha et al. [12] studied the reliability of SAC-based alloys under varying conditions. It's found that the characteristic life of joints varies with stress amplitude with a factor of -6.5 as ductility exponent. The reliability of SAC305 doped alloys with Ni was studied by El-Daly et al. [57]. They noticed superior strength material compared to SAC305 alloys.

Al Athamneh et al. [10] compared the fatigue behavior of SAC305 and SAC-Bi solder joints with aging thoroughly. Regardless of the stress and aging conditions, SAC-Bi shows superior behavior compared to SAC305. For certain alloy, increasing the stress amplitude and aging levels (duration and temperature) decreases fatigue life, mainly for SAC305. Also, Al Athamneh et al. [13] investigated the effect of aging on the fatigue and shear strength of SAC305 joints under various stress levels (16 MPa, 20 MPa, and 24 MPa) and aging times (0, 10, and 100 hrs.) and temperatures (100°C and 150°C). Hysteresis loop and plastic strain were obtained. Results show that increasing the stress magnitudes generating larger loops and plastic strain values, which means larger damage

per cycle. Moreover, harsh aging conditions of longer duration and elevated temperatures lead to fatigue life reduction remarkably.

Others [15, 18, 58] studied fatigue properties for SAC-based bulk samples under several stress amplitudes and different aging conditions: temperatures and durations. Generally, results follow the same behavior under various conditions but with inaccurate estimations for the properties. This is expected due to the different microstructure between actual joints and bulk ones. Other researchers explored the evolution of microstructure of SAC-based alloys under fatigue conditions.

Chowdhury et al. [59] investigated the effect of mechanical cycling on microstructure evolution and damage accumulation for bulk SAC305 samples. Samples were cycled for different periods and removed accordingly for microstructure analysis using SEM. Quantification of several mechanical properties provides useful information about the material degradation. Aggravating grain boundary sliding noticed from intergranular cracking leads to a high creep strain rate.

Others [26, 60-64] studied the microstructure evolution of SAC-based alloys under various aging conditions, including the degradation effect of aging on mechanical properties. There are other mechanical behaviors affected by aging, including creep response [65-67], fatigue life [68-70], and thermal cycling reliability [11, 70-74].

Creep deformation is a significant damage mechanism that causes joints failure as well. It's considered as the essential failure mechanism during thermal cycling. It's defined as the time-dependent deformation of a material exhibited to a constant load. Stress relaxation is similar in damage to creep, but it's defined as the damage flow or stress reduction (relaxation) of material under constant strain. Both mechanisms have the same plastic flow and microstructure changes. Also, stress-strain curves for curves found to be identical [8]. Under thermal cycling, both

mechanisms have existed, and time-dependent stress and strains occurred simultaneously. Commonly these combined mechanisms called stress-relaxation mechanisms. Creep happened at low temperatures but enhanced at elevated homologous temperature. For most SAC-based or even SnPb alloys, room temperature is high due to related large homologous ratio above 0.5, where creep becomes the dominant failure mode [75]. This is due to the low melting temperature of alloys ranging between 185°C for SnPb ones and up to 217°C for most SAC-based alloys. During thermal cycling, failure occurs due to the mismatch in CTE between chip and component or component and PCB due to thermomechanical stresses. It's a combined effect of creep and fatigue where fatigue is existed during the ramps and creep during the ramps. Since test duration is mostly above room temperature, creep is dominant during thermal cycling, primarily at room temperature [9]. Basically, the constant load is applied in the creep test, and deformation is measured and recorded with time. The higher the load and the temperature applied, the larger the deformation obtained. Typically, creep curve divided into three regions: primary, secondary, and tertiary regions. The primary region begins with high strain rate deformation due to strain hardening with a steep slope and reduces with time during the steady-state, then finally steeped again after the crack initiation and propagation. The secondary creep is named as steady-state creep due to the dynamic balance between strain hardening and recrystallization. This strain rate within this region utilized by researchers in FEA that used to predict the joint's reliability under various conditions. The last region is related to the rapid increase of strain rate due to crack. There are different mechanisms of creep to take place; dislocation glide, dislocation creep, grain boundary diffusion, and lattice diffusion [76-77] dependent on applied or suffered conditions. In the case of dislocation glide, dislocations move along the slip planes at higher stress levels over the whole homologous temperature range [78]. Dislocation creep is noticed during the high homologous temperature of

0.5 and above with intermediate stress amplitude. It's a high-temperature deformation mechanism caused by the controlled diffusion of dislocation movements, and they climbed away from the barriers. The grain boundary-based diffused creep had been investigated by Coble R. L. [79]. It begins with the atomic or ionic diffusion along with grain boundaries under low stress and temperature range levels. The last type is the lattice creep, Nabarro-Herring Creep, or called bulk diffusion creep. The failure mechanism involves the migration of interstitial atoms and lattice vacancies along the grain boundary gradient in the reverse direction under tension or compression stress [80]. During the case of no pressure, interstitial atoms and lattice vacancies are in-continuous migration, which proportion to gradient concentration. On the other hand, lattice deforms and tends to move in the direction of relieving the stress in the existence of pressure. Both movements will eventually cause creep.

Fahim et al. [81] investigated the evolution of microstructure, including IMC of SAC-based alloys at elevated temperatures using nanoindentation testing. This is due to its high-volume fraction compared to the reduced size of the package. SAC joints pulled out from aged BGAs components for six months at 125°C and tested consequently. ENIG surface finish for PCB was utilized, and both interfaces, Cu pad-IMC layer, and IMC layer-bulk region, had investigated using SEM/EDX techniques. The indentation study involved exploring the mechanical properties such as modulus of elasticity, creep, and hardness. The test conditions include indenting spheres at room temperature and several elevated temperatures; 50, 75, 100, and 125°C. SEM/EDX results showed significant degradation in mechanical properties at elevated temperatures compared to room temperature. The total indentation movements had calculated continuously during the constant load and fitted to the empirical hyperbolic tangent model. The creep rate found to increase with temperature. In a following study, Fahim et al. [17] studied the nanomechanical evolution of IMC

in lead-free alloys. The IMC's mechanical behavior, in addition to its layers, was explored using nanoindentation under the same testing conditions. Other parameters, such as hardness, time-dependent creep, and tensile properties, were investigated. As previously discovered, the increasing temperature would significantly reduce the mechanical properties, especially at 125°C. SEM/EDX images show less coarsening and IMC growth in SAC-based dopant alloys.

Alam et al. [16] investigated the mechanical behaviors of tensile and creep properties for lead-free alloys at high temperatures. Several solder alloys: SAC305, SAC_Q, SAC_R, and Innolot had been tested at high temperatures ranges between 125-200°C (e.g., 125, 150, 175, and 200°C). with a strain rate of 0.001/s. The high-temperature data stress-strain data or hysteresis had been fitted reasonably to the old Anand constitutive model generated from data ranges between 25-125°C. Moreover, the creep and tensile behaviors were explored and compared for different alloys. Generally, results showed that increasing the temperature would remarkably reduce the mechanical properties of lead-free alloys; degradation percentages were almost 50% for SAC305. A high increase in creep rate was recorded as well. Also, SAC-based alloys with dopants as Bi, Ni, and Sb showed better mechanical properties compared to SAC- only alloys. Ahmad et al. [82] continue the study of [16] by implementing extensive study for the effect of high temperature on mechanical properties evolution of SAC-based alloys using the nanoindentation technique. Tested spheres size was 0.46 mm and were obtained from PBGA carefully to void the effect of grain orientation, which proved to have a huge impact on the reliability according to literature. Therefore, only single grain orientation spheres were picked for testing. The same temperatures as in the previous study were utilized with fixed loads for 900s, while the creep was monitored continuously. Some indentations were done after aging. It was found that high temperatures and aging drastically degraded the material properties, especially when both extreme conditions

applied to high temperatures (100-125°C) and longtime aging periods of one day. Also, a higher creep strain rate was observed up to 100X compared to room temperature.

Wu et al. [83] explored the microstructure evolution of SAC305 alloys under the effect of aging for short and long terms. In the former study of short aging, the evolution in microstructure had been monitored in specific regions every one hour using SEM. For the long-term aging, samples were observed every 250 hours. Ag₃Sn, in addition to others, had been observed with aging. Aging found to alter the number of IMCs with its total area, particle average area, and diameter, in addition to normalized diameter. Results showed that IMC particles number reduced while its diameter increased drastically with aging. Also, the remarkable evolution in microstructure found to be within the 250 hours of aging and then almost become negligible.

Fahim et al. [84] extended their study for mechanical characterization and evolution, including aging. Samples were aged for six months at 125°C. All components have an ENIG surface finish. Samples were aged, then spheres were extracted, molded, prepared, and indented for microstructure analysis. In their work, they analyzed several mechanical properties, including elastic modulus and hardness for different IMC precipitates; Ag₃Sn, Cu₆Sn₅, (Cu_{1-x} Ni_x)₆Sn₅. The latter showed the highest modulus and hardness quantities. Generally, aging found to reduce the mechanical properties, especially with long term aging at high temperatures. SEM/EDX techniques were utilized for analyzing the data.

3.4 Reliability Models Under Different Fatigue and Creep Conditions

Over the years, scientists tried to predict the life of different electronic parts such as joints and components under different conditions. It is precious and vital to come up with such reliability models in order to predict the life of these parts under the machine or during realistic field

conditions. This would help in reducing the cost related to failures significantly. Also, it would provide a better idea about the life of electronics systems in general. Therefore, researchers commenced to study the effect of different conditions on the component's reliability and developed reliability models for several sizes of components and joints. Moreover, various types of solder materials were tested under different conditions of temperature ranges, dwelling periods, and ramp rates. Such research was thoroughly implemented for solder materials of SnPb based, but since it was prohibited, most of the research was moved to SAC based paste.

Norris and Landzberg [27] were ones who started early developing the reliability models of SnPb. They studied the reliability of SnPb controlled chip collapsed interconnections under different accelerated thermal cycling conditions. They consider the effect of strain, time, and temperature factors. The strain is introduced through the Coffin-Manson equation with some level of modifications on the original equation to become

$$N (\Delta T)^2 = \text{Constant} \dots \dots \dots (3.1)$$

The effect of time or frequency found to be significant with a factor of 1/3, which is close to results in [4]. Their experimental tests included four groups of 35 bumps tested at different temperature ranges and cycling conditions of -60-150°C with three CPH, 0-150°C with two CPH and, 30-110°C with 30 CPH. Each group was tested for at least 50% failure. Data were fitted and regression analysis was implemented, and log-normal lifetime model was used to predict the failure rate which found to be

$$F.R = \frac{1}{R(t) \sigma t (2\pi)^{0.5}} \exp \left\{ \frac{-1}{2} \left[\frac{\ln(t) - \ln(t_{50})}{\sigma} \right]^2 \right\} \dots \dots \dots (3.2)$$

Where R(t): the reliability function of the distribution, t₅₀: time at 50% failure occurrence.

Engelmaier W. [5] studied the fatigue life of SnPb based CCC joints during power cycling and generated models to predict the life based on the Coffin-Manson Model. He clarified the best way to simulate the acceleration tests for power cycling application and its deviation of thermal cycling because of the effect of warpage and transient strains that occurred under environmental conditions. CCC with different PCB options was utilized at different testing temperatures profiles. He developed a modified version model of Coffin-Manson including the effect of temperature and cycling frequency:

$$N_f = \frac{1}{2} \left(\frac{\Delta\gamma}{2\varepsilon_f} \right)^{1/C} \dots\dots\dots (3.3)$$

Where $C = -0.442 - 6 * 10^{-4} T_s + 1.74 * 10^{-2} * \ln(1 + f)$, $2\varepsilon_f \approx 0.65$, $\Delta\gamma$ is the cyclic shear strain, f is the frequency.

Vayman S. et al. [85] investigated the reliability of low tin solders alloys under different isothermal fatigue conditions, including extensive temperature range (5-150°C), hold times (seconds-hours), strain ranges (0.1-1 percent), frequencies ($10^{-2} - 1$ Hz) and environmental conditions (vacuum-air). The study also includes determining the failure mechanism and failure modes for each condition in addition to the life prediction model. Results showed different failure fatigue mechanisms for 96.5Pb3.5Sn according to testing conditions. At high frequency (>0.2 Hz), the intergranular crack was observed at a low strain range (0.3) and mixed of intergranular and transgranular at high strain range. Holding times reduce life significantly even after a few seconds, and its effect is way more significant than the ramp time effect. The effect of temperature found to be substantial for low strain range and negligible for high strain range, which is similar in [5]. Empirical reliability model was developed for holding time and ramp time factor as following:

$$Nf = \frac{C+D (tht+thc)}{2tr+tht+thc} \dots\dots\dots (3.4)$$

Where N_f is the life, t_{ht} is the holding time during tension, t_r is the time during ramps, t_{hc} is the holding time during compression, C, D are constants.

The effect of the environment with its related consequence on reliability results and models had been examined by Engelmaier W. [33] due to its importance in design for reliability for different electronics assemblies. Also, it has a critical effect on planning the accelerated tests. His study includes thermal cycling conditions, mechanical fatigue cycling, various frequencies, and hold times in addition to strain ranges for both leaded and leadless components. The fatigue life for certain failure probability X for SM attachment is

$$N_f (x\%) = \frac{1}{2} \left(\frac{F}{2\varepsilon_f} \frac{LD \Delta\alpha T_e}{h} \right)^{\frac{1}{c}} \left(\frac{\ln (1-0.01 x)}{\ln (0.5)} \right)^{\frac{1}{\beta}} \dots\dots\dots (3.5)$$

Where $C = -0.442 - 6 * 10^{-4} T_s + 1.74 * 10^{-2} \ln (1 + \frac{360}{td})$, L_D is the distance to neutral point, $\Delta\alpha$ is the difference in coefficient of thermal expansion, T_e is the equivalent cycling temperature swing, h is the solder joint height, β is the shape parameter.

The previously mentioned correlation is the generic formula and modified ones for different conditions are generated accordingly. Following this study, Engelmaier [7] suggested acceleration transformation utilized for comparison purposes among data from different tests by normalizing data to one condition. The acceleration factor between operating conditions and accelerated conditions is described below

$$N_f (2) = \frac{1}{2} [(2N_f(1))^{c1} \left(\frac{\Delta\gamma_2}{\Delta\gamma_1} \right)^{\frac{1}{c2}}] \dots\dots\dots (3.6)$$

Where $N_f(2)$ is the fatigue life in operating condition 2, $N_f(1)$ is the fatigue life in an accelerated test (condition 1), C_1 is the fatigue exponent in condition 1, and C_2 is the fatigue exponent in condition 2.

Kanchanomai and Mutoh [29] proposed a prediction model for low cycle fatigue life for bulk SnAg solder samples under various levels of temperatures (20°C, 85°C, and 120°C) and frequencies (10⁻³ Hz, 10⁻² Hz, and 10⁻¹ Hz). Three common models have been utilized in this study: Coffin–Manson model, Smith–Watson–Topper (SWT) model, and Morrow energy model. Previous studies showed that these models are temperature and frequency dependent. The fatigue ductility increases at a higher frequency and lower temperatures. Flow stress and frequency dependent modifications were involved in these models to provide better correlation. Results showed that material behavior could be described by the Coffin-Manson model shown below within temperature range 20-120°C and frequency range 10⁻³ to 10⁻¹:

$$(N_f v^{k-1})^\alpha \Delta \epsilon_p = \theta \dots \dots \dots (3.7)$$

Where N_f is the fatigue life, ϵ_p is the plastic strain, v & k are the frequency and frequency exponent, respectively, α is the fatigue ductility exponent, and θ is the fatigue ductility coefficient. Unfortunately, this model failed to describe behaviors under the influence of temperature. Other models showed the same material behavior under similar conditions. On the other hand, Smith–Watson–Topper (SWT) and Morrow energy model have achieved consistent results for prediction fatigue life under various temperatures and frequency levels. Smith–Watson–Topper (SWT) model is directly related to stress and the total strain range as a function of temperature as shown in the equation below:

$$(\sigma_{\max} \Delta \epsilon_T) N_f^n = d \dots \dots \dots (3.8)$$

Where σ_{\max} is the maximum stress, $\Delta \epsilon_T$ is the total strain range, n is the fatigue ductility exponent, and d is the fatigue ductility coefficient. Morrow Energy or Plastic Strain Energy Density–Life Model have correlated the frequency and plastic strain with correspondence to the total energy density as below

$$(N_f v^{k-1})^m W_p = C \dots \dots \dots (3.9)$$

Where v and k are the frequency and frequency exponent evaluated from the fatigue life–frequency relationship, respectively. C is the fatigue coefficient, W_p is the plastic strain energy density, and N_f is the fatigue life. There is another researcher [86-87] described the fatigue life with modified frequency, flow stress and modified Morrow models together in a temperature and frequency dependent models shown below

$$(N_f v^{k-1})^m \frac{W_p}{2\sigma_f} = C \dots \dots \dots (3.10)$$

Solomon H. [28] suggested a low cycle fatigue model that predicting the fatigue life as a function of plastic strain for eutectic alloys under various temperature; -50, 35, 125, and 150°C.

$$\Delta \gamma_p N_f^\alpha = \theta \dots \dots \dots (3.11)$$

Where $\Delta \gamma_p$ is the plastic shear strain range, α and θ are constants. As stated in the literature, the damage is highly activated by creep, especially at elevated temperature. Syed A. [30] combined two common equations to provide life model, which are Monkman–Grant equation for creep rupture [88] and Miner rule [89]. In Monkman–Grant equation, there is an inverse correlation between time to rupture and strain rate of steady-state creep. With this understanding, he predicts

the life under stress for one cycle of creep and utilized Miner rule to calculate the accumulation damage for multi cycles according to the following equation:

$$N_f = \left(\frac{E_1}{C_1} + \frac{E_2}{C_2} \right)^{-1} \dots\dots\dots (3.12)$$

Where E is the accumulated creep strain for the whole cycle, constants are determined as 50 and 15.87 for C_1 and C_2 respectively. Later to this study, Syed [86/31] utilized creep strain and creep strain density quantities to predict the life for two different SnPb and others doped with Au. The equations are

$$N_f = (C^I \epsilon^I_{acc} + C^{II} \epsilon^{II}_{acc})^{-1} \dots\dots\dots (3.13)$$

$$N_f = (W^I w^I_{acc} + W^{II} w^{II}_{acc})^{-1} \dots\dots\dots (3.14)$$

Where N_f is the number of cycles to failure for both equations. C^I and C^{II} represent the constants related to the creep strain-based model, respectively. ϵ_{acc} represents accumulated creep strain per cycle for each creep mechanism. W^I and W^{II} represent constants related to dissipated creep energy density-based model, respectively. w_{acc} represents accumulated creep energy density per cycle for each creep mechanisms.

Osterman et al. [90], proposed a life assessment model for lead-free interconnectors based on strain range. CLCC packages soldered to PCB by SAC405 alloy had been tested under thermal cycling with a fixed range of 100°C. The midpoint temperature was located between 25-75°C with dwell time varying between 15-75 mins. Numerical regression was used to relate the data between strain range to life model proposed by [5]. Test results showed a reduction dwell time effect at higher temperatures extremes. Pan et al. proposed [34] acceleration model for SAC alloys under various thermal cycling conditions. Different thermal cycling profiles were utilized in this study including

various temperature range (0-100 °C, 0-60 °C, 40-100 °C, -25-125°C), dwell times (10, 35, 60 mins) and cyclic frequency. Also, several geometries, CBGAs, CSPs, and TSOPs were investigated. A modified Norris-Landzberg model was generated to fit the thermal cycling results. The model is shown below in equation

$$AF = \frac{N_o}{N_t} = \left(\frac{\Delta T_t}{\Delta T_o} \right)^{2.65} \left(\frac{t_t}{t_o} \right)^{0.136} \exp \left[2185 \left(\frac{1}{T_{max, o}} - \frac{1}{T_{max, t}} \right) \right] \dots\dots\dots (3.15)$$

Where ΔT_t , ΔT_o are the temperature ranges for testing and operating conditions, respectively. t_t and t_o are the dwell times for testing and operating conditions, respectively. $T_{max,t}$ and $T_{max,o}$ are the maximum temperature for testing and operating conditions, respectively. Various testing parameters were investigated. Based on the temperature range, the ratio between characteristics life for different packages were compared at constant T_{max} and dwell time and found to be centered around 3.7. The effect of dwell time is also explored but indirectly since dwell times were different for several tested packages. Finally, the effect of T_{max} is studied and found to have a huge impact on solder reliability when comparing at certain dwell times and temperature ranges. The relation of the three parameters was utilized to fit within the Norris-Landzberg equation to bring out the final equation shown above. The relations of different effects are shown below.

$$AF \propto \left(\frac{\Delta T_t}{\Delta T_o} \right)^a, AF \propto \left(\frac{t_t}{t_o} \right)^b, AF \propto \exp \left[c \left(\frac{1}{T_{max, o}} - \frac{1}{T_{max, t}} \right) \right] \dots\dots\dots (3.16)$$

Salmela O. [96/91] investigated several acceleration factors proposed by others [27,34] for lead-free material under different thermal cycling conditions. The idea is to recalibrate such models proposed previously for SnPb and adapt them for lead-free alloys. Three thermal cycling profiles were utilized to examine the test vehicles of aluminum substrate attached via SAC387 to FR-4 PCB. Profiles include fixed ramp rates, 15 mins dwelling at extremes and a total cycle of 80 mins.

The tests were terminated after 1000 cycles. After analysis, the acceleration factor was proposed and found to be

$$AF = \frac{N_{test}}{N_{field}} = \left(\frac{\Delta T_{test}}{\Delta T_{field}} \right)^{1.662} \left(\frac{f_{field}}{f_{test}} \right)^{1/3} e^{\left[\frac{E_a}{k} \left(\frac{1}{T_{max,field}} - \frac{1}{T_{max,test}} \right) \right]} \dots\dots\dots (3.17)$$

Where N_{test} and N_{field} are the fatigue lives, ΔT_{test} and ΔT_{field} are the temperature ranges, f_{test} and f_{field} are the frequencies, $T_{max,test}$ and $T_{max,field}$ are the maximum temperatures for testing and field conditions respectively. Since frequency not changed, the frequency exponent found to be the same as the Norris-Landzberg model where $E_a=0.092$ eV is the activation energy, but it should be higher for SAC-based alloys. Also, he included a correction factor to compromise for material and geometry. The correction factor is as follows

$$Corr(\Delta T) = A \cdot \ln(\Delta T) + B \dots\dots\dots (3.18)$$

Where ΔT is the temperature difference, A and B are constants. Dalton et al. [32] investigated the effect of induced strain on the reliability of new generations of SAC-based alloys with high Ag and the fatigue behavior under thermal cycling. Typically, the third generation is designed to enhance the toughness of IMC, where solid solution compensates for the loss in strength due to precipitate coarsening. Two thermal cycling profiles are utilized in this study; 0/100°C and -40/125°C. Four alloys were tested; SAC387, Innolot, Castin (Sn-Ag2.5-Cu0.8-Sb0.5) in addition to SnPb for comparison purposes. Results showed that crack propagation occurred along the package side due to higher stress levels, but it might be found on the PCB side. The higher strain levels represented by large temperature range resulted in a drop in characteristics life between 60-83%. Almost the same life (76%) is predicted by the Coffin-Manson equation. Maxim et al. [92] proposed a prediction model for lead-free alloys of LEDs on metal cores. The study utilized a semi-analytical model to predict life under thermal cycling. Strain energy is introduced as a

damage parameter calculated by combining interfacial stiffness and material properties. Two different alloys were tested: SAC305 and another one with high creep resistance. Researchers fitted their data to a modified version of the Norris-Landzberg equation to correlate the plastic and creep strain suffered under testing conditions. Creep strain energy is calculated from the temperature-dependent package and solder properties.

$$N_f(63.2\%) = C_1 (W_{\max})^{-C_2} \left(\frac{LN(1-0.01x63.2\%)}{LN(0.5)} \right)^{1/\beta} \dots\dots\dots (3.19)$$

Where $N_f(63.2\%)$ is the fatigue life, W_{\max} is the accumulated maximum energy, L is the distance to the neutral axis, β is the shape parameter, C_1 , and C_2 are constants. Lall et al. [93], proposed a decision support model for lead-free flip chips reliability under harsh applications. The model included mathematical formula, accurate guidance for making decisions about packaging geometries, and perturbing to reduce the reliability risks related to utilizing the new technologies. Sensitivity analysis is also included in this study to assess the various designs, material in addition to other applications conditions. A combination of statistical tools and fundamental understanding of the failure mechanisms, including damage mechanics and related constitutive behaviors, are used to bring out the model. Data is generated from the CAVE3 database for harsh thermal cycling tests. Various profiles were employed with different test vehicle geometries. Models from both aspects, statistics and failure mechanics-based, are generated respectively according to equations and validated with actual ATC failure data.

$$t_{63.2\%} = a_1 + b_1(\text{Die Size MM}) + b_2(\text{Ball Count}) + b_3(\text{Under fill ID}) + b_4(\text{Solder Comp ID}) + b_5(\text{Ball Dia MM}) + b_6(\text{Pad Type ID}) + b_7(\Delta T) \text{ [Statistical Model]}$$

$$t_{63.2\%, \text{ joint}} = N_0 + \frac{a}{da/dN} \dots\dots\dots (3.20)$$

$$N_0 = K_1 (\Delta W)^{k_2} \dots\dots\dots (3.21)$$

$$(da/dN) = K_3 (\Delta W)^{k_4} \dots \dots \dots (3.22)$$

Where $t_{63.2\%}$ is the time at which 63.2% of components are expected to fail, a_1 and parameters b_i , for $i = 1$ to 7 represent the sensitivities of reliability to the respective parameters, a is the joint diameter at the interface, N_0 is the number of cycles for crack initiation, and da/dN is the crack propagation rate, K_1 , K_2 , K_3 and K_4 are constants.

Pierce et al. [94] suggested a methodology to predict the life of lead-free interconnects under thermal fatigue conditions. Isothermal fatigue data were generated by employing a double lap shear test assembly. Also, stress-strain and creep data had generated. SAC396 alloys were tested under various conditions of thermal cycling and isothermal fatigue. For fatigue data, a correlation between empirical and FEA analysis is performed where the general fatigue life model is generated basically from a unified creep plasticity damage model, and its used to predict the fatigue cracks. Both FEA and failure and damage mechanics are connected together to generate the model. Also, the model was validated upon experimental thermal cycling results. PBGAs were testes in thermal profile with temperature extremes ranging between -55 to 125°C and ramp rate 10°C/min for 200-4000 cycles. Microstructure analysis was implemented to investigate the crack growth in detail. They proposed a model as a foundation for crack growth shown in the equation below where its related parameters were determined from results

$$a = \int_0^{W^{pl}} \left(\frac{da}{dW^{pl}} (T, a) \right) dW^{pl} + a_0 \approx \sum_{i=1}^{N_{CS}} \left(\frac{da}{dW^{pl}} (T, a) \right)_i \Delta W^{pl}_i + a_0 \dots \dots \dots (3.23)$$

where T is the temperature, a is the crack length, a_0 is an initial crack length, da/dW^{pl} is the rate of crack growth per increment of plastic work, and dW^{pl} is a differential increment of volume-averaged plastic work at a specific temperature which is summed over the complete fatigue.

Chapter 4: Research Methodology

This research aims to understand the damage of both creep and fatigue under thermal-cycling conditions and quantifying each one. Thus, various methods, different test vehicles and, unique experimental setups are used to achieve this goal. This includes the research studies with detailed testing matrix, testing conditions and parameters, the testing vehicle components, experimental setup, and the testing profile/profiles employed in each research study.

The components for each testing vehicle, how the sample is prepared and assembled are clarified in detail. Two different test vehicles will be utilized to accomplish the goals for this research work. The first one includes coupons with actual solder joints to be tested individually. The other will be aboard with multiple assembled components on its top to be tested as a whole unit under various thermal tests. In both cases, a brief procedure of board fabrication is mentioned.

This chapter discusses in details the experimental tools that address the setups and testing profiles to be employed in both tests. The experimental setup including the design of the setup, specification, and capabilities in addition to the required accessories are identified for each study. Two different setups are demonstrated to implement our methods. A customized fixture is used for the first two methods to examine the reliability of individual solder joint under mechanical fatigue and combined creep-fatigue tests at various temperature levels: room, elevated and, cold temperatures. Two distinguished testing profiles are included to perform the tests mentioned above. The other setup is for the thermal cycling test, which is a chamber with a unique data acquisition system. A standard testing profile is used with several parameters of ramp rates and dwelling times. At the end of this section, microstructure analysis is discussed. Also, detailed testing conditions and parameters for each study are identified. This is demonstrated by establishing the testing matrixes or experimental layouts for each study.

4.1 Study 1: Effect of Creep and Fatigue on Individual SAC305 Solder Joints Reliability at Room Temperature

The first study includes investigating the effects of creep and fatigue on SAC305 solder joints reliability under various stress levels and dwell times at room temperature. Mechanical fatigue tests with no dwelling and combined of creep-fatigue are employed with three stress levels (16, 20, 24 MPa). In the creep-fatigue test, four dwelling times (5, 10, 60, 180s) are examined. Accelerated shear fatigue test on individual solder joints is employed to simulate dwelling times and stress amplitudes on fatigue performance. Mechanical shear fatigue test is performed to investigate the effect of pure mechanical fatigue on joints reliability. On the other hand, a combined test of creep-fatigue provided a combined effect of both damage mechanisms. With these related quantities, the effect of creep is separated and quantified. Two damage parameters: inelastic work per cycle and plastic strain are investigated to quantify these effects.

4.1.1 Test Vehicle #1

This test vehicle is utilized for mechanical fatigue and the combined fatigue-creep tests at room temperatures. The tests are implemented on individual solder joints for assessing the reliability of such joints under various conditions. This would help to understand the behavior at the joint level under fatigue and fatigue-creep conditions. Moreover, it would help to deliver damage quantification of these effects. The test vehicle consists of a PCB substrate and individual solder joint assembled on the top of it. The PCB is a substrate made of FR-4 glass epoxy material with full array (10 x 12 = 120 coupons) of small test coupons where. The dimensions of this board are 100mm x 120mm. Each coupon is separated from the other via v-scoring divisions. Each test coupon consists of a full array of 30 mils SMD SAC305 solder joints with 10mm x 10mm. The pitch distance is 3 mm, and only solder mask defined pads were used with an opening of 22 mils.

Each PCB has OSP surface finish. Figure 4.1 shows the actual full testing board with a schematic for testing coupons as well.

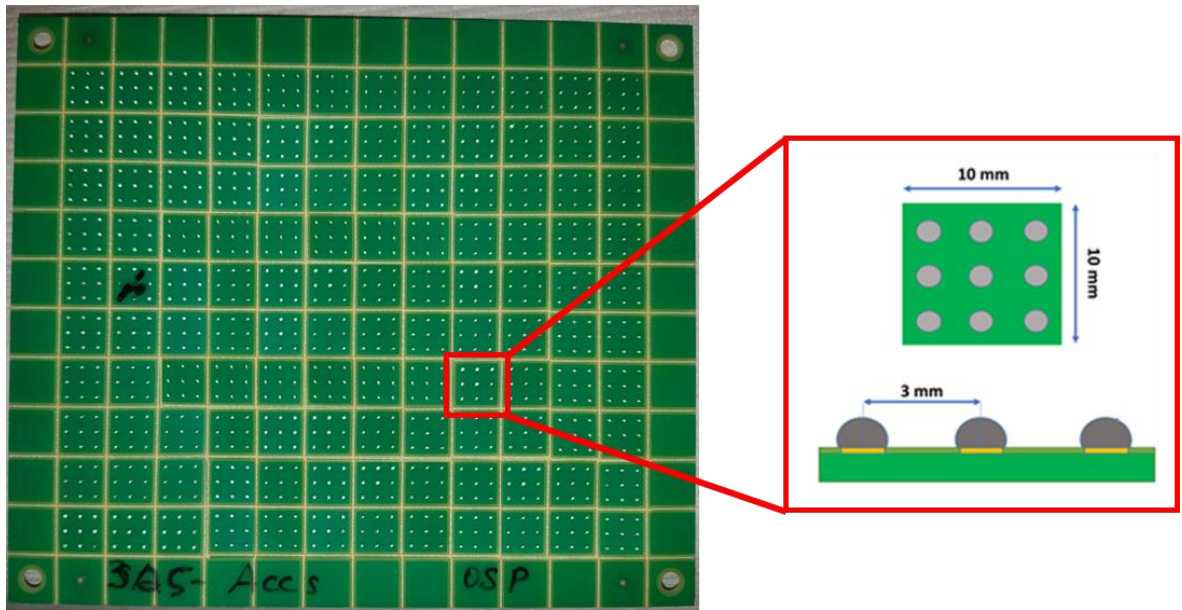


Figure 4.1: Test Vehicle for Individual Solder Joints Testing

4.1.2 Preparation and Assembly

Accurus (solder paste company) provided the solder joint material; then, sample preparation was implemented at Universal Instruments Corporation labs. The process is as follows; (1) stencil #1 with four mil thickness was aligned on the top of the PCB. Then, (2) tacky flux was printed using a stencil printing machine, DEK Galaxy (Figure 4.2). After flux is printed, (3) this stencil was removed, and flux was left on the top of the copper pads. Next, (4) another stencil with six mil thickness and wider aperture is placed on top of the PCB. Then, (5) SAC305 solder spheres were populated manually using a brush to fill the apertures. After tacky flux printing and spheres spreading steps, the inspection process is performed to assure flux quality and that spheres are placed in their defined locations. Finally, (6) the board reflowed at eight zones Pyramax 100N reflow oven (Figure 4.3) within the N₂ environment according to SAC305 typical reflow profile with preheat time of 200s, the peak temperature of 235°C, 40s above the liquidus and cooling rate

of 4°C/sec. The reflow profile was monitored during the reflow process to assure the joints wettability without board damage. The advantage of this process is that there is no issue when losing spheres since individual solder joints are tested. A stencil that used to prepare the samples is shown in All the processes mentioned above are shown in Figure 4.4. Also, a reflow profile for SAC305 is shown in Figure 4.5.



Figure 4.2: DEK Galaxy Printing Machine



Figure 4.3 : 8-zone Pyramax 100N Reflow Oven

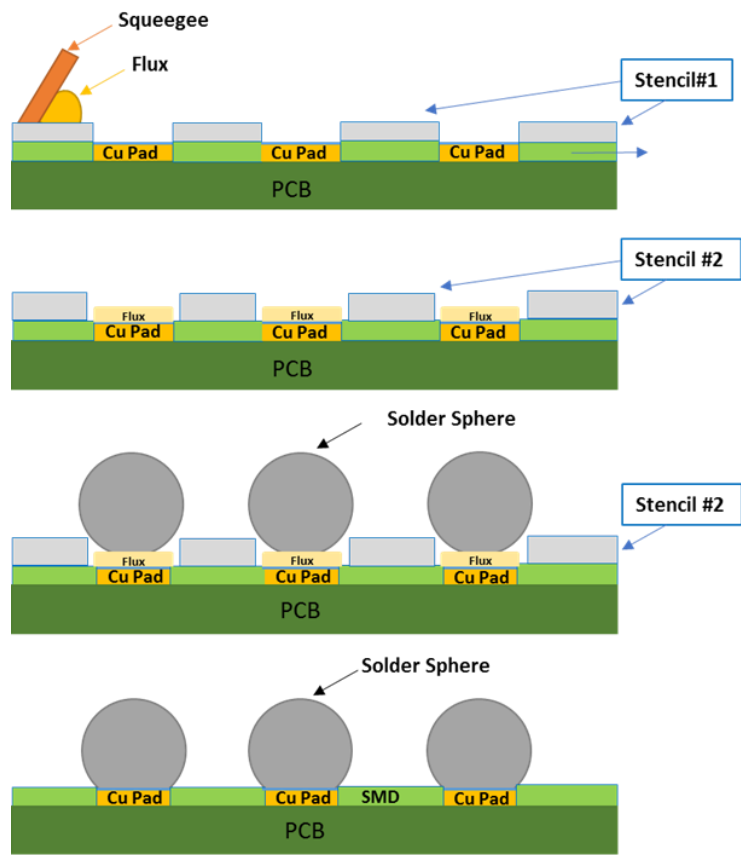


Figure 4.4: Sample Preparation for Individual Solder Joints Vehicles

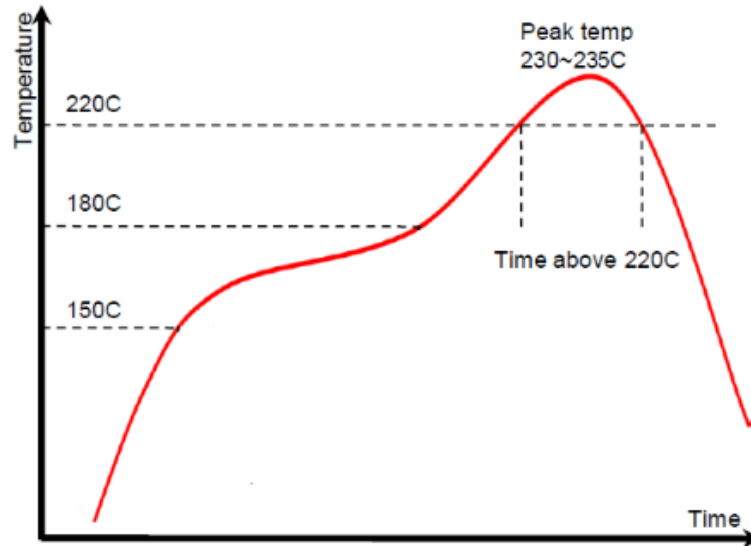


Figure 4.5: SAC305 Reflow Profile Schematic

4.1.3 Experimental Setup

In this test, where individual solder joints are tested, Instron 5984 micromechanical tester with a customized fixture is used. Our machine can perform tensile, compression, shear, and cyclic fatigue tests. The drive system specification of this multifunction tester precision is 94 nm in displacement and applied load range between 2mN and 2KN. The driver of the micro-position controller is of screw-type with an optical encoder of 20 nm resolution in displacement. In this research study, 10N and 2KN load cells are used to measure the load. Since our test is unique, including testing individual solder joints rather than bulk typical samples, a fixture is customized for this purpose. Two parts are introduced: sample holder and testing fixture.

Testing coupons are fixed on the sample holder and control the Z and X-axis of the joint movement. The Z-axis movement is used to control the standoff distance for the shear fatigue cycling test, between 10-25% of the solder diameter (30 mils). In our case, the standoff or shear height is 0.05mm. Test coupons are fixed on the stage holder by a particular type of glue with a shear strength of 0.1 N/mm². On the other hand, a tip with a circular shape and 1mm in diameter is

fastened to the drive system and controls the Y-axis movement. The perfect intersection of these three movements will adapt the insertion of solder joints within the middle of the tip with the accurate standoff height. Finally, failure is defined when the solder joint is taken off the test vehicle. Figure 4.6 shows the Instron micromechanical tester setup. Also, a schematic diagram for this setup is shown in Figure 4.7.

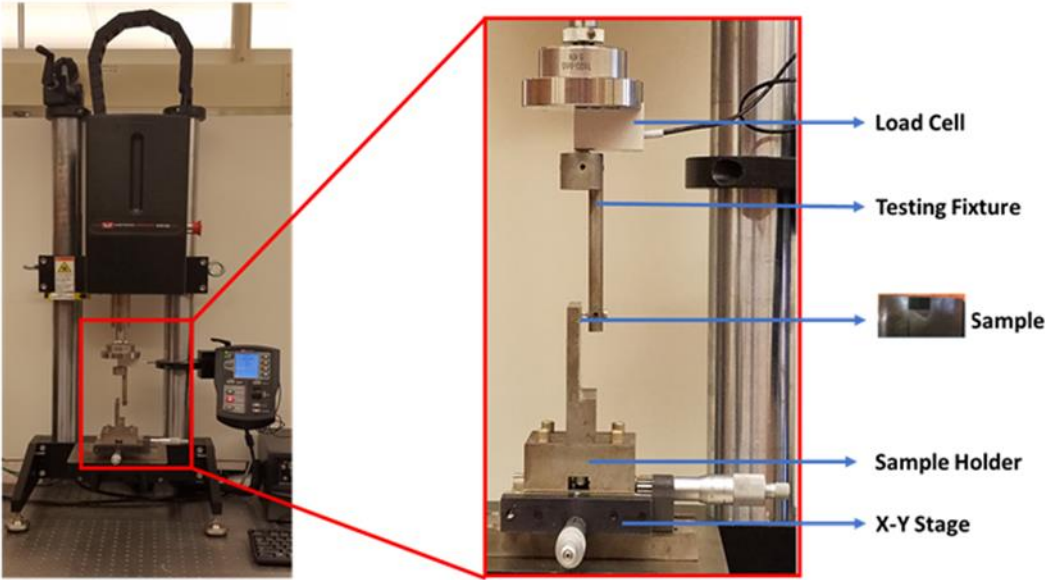


Figure 4.6: Instron 5948 Micromechanical Tester Setup

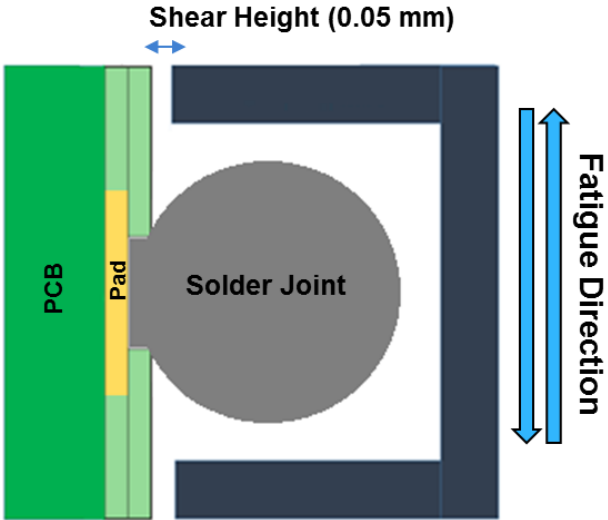


Figure 4.7: Schematic of the Cylindrical Testing Fixture for an Individual Solder Joint

4.1.4 Testing Profile and Test Matrix

In creep-fatigue tests, there are two profiles examined at different temperatures: room, elevated and cold temperatures. The first one is utilized for mechanical fatigue tests only. As shown in Figure 4.8, the test started by cycling the solder joint from its position or zero position up with fixed ramp rate of 0.1 mm/s until reached defined stress as a control parameter, then it switched and cycled in the other direction down until reaches the negative value of same defined stress and hold for a moment. It switches and cycled back to other defined positive stress values and so on back and forth between extremes until complete failure. The definition of one cycle is the completion movement between the two extremes and pass its original position. Load and displacement data are recorded continuously every 0.01s. Hysteresis loops, which are stress-strain loops, will be generated for each cycle. Average stress is calculated by dividing the load value by the pad area. Shear strain is calculated by dividing the measured displacement by the distance between the center of the solder joint and the pad surface.

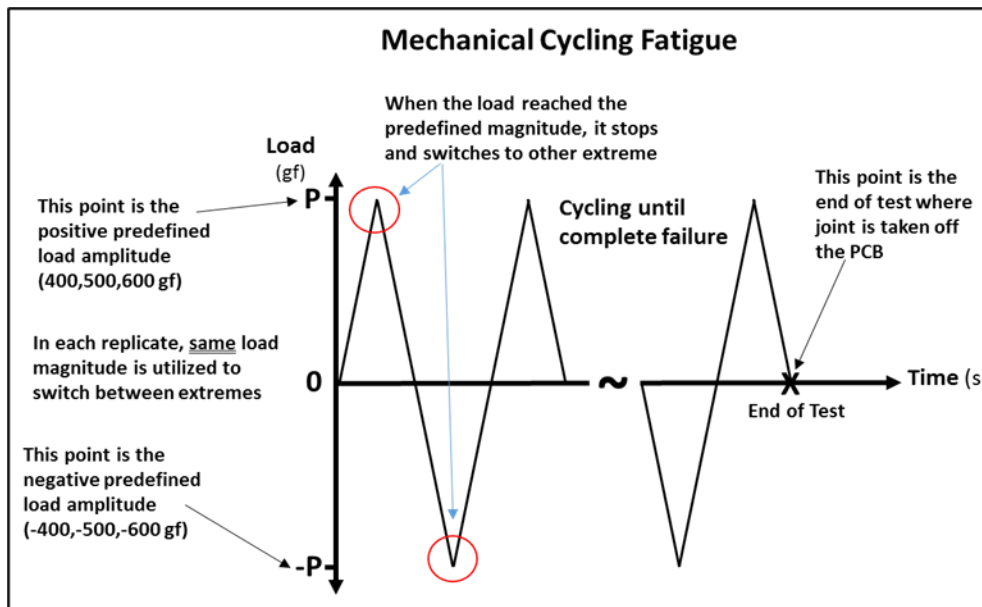


Figure 4.8: Mechanical Fatigue Only Testing Profile

On the other hand, there is a combined test of creep and fatigue, as shown in Figure 4.9. The first part will be the same as in the fatigue test. It starts from zero position, ramps it up with a fixed rate of 0.1 mm/s until it reaches defined stress as a control parameter. Then, the strain is held for a particular dwelling time, and the stress is relaxed for a smaller amount of amount depending on the dwelling period, the longer the dwelling time, the more relaxed in stress. Once the defined dwelling time is finished, it switched to another extreme of negative stress, hold the strain for the same dwelling time which experienced during the positive side, and stress is relaxed. Once dwelling time is over, the cycle is repeated until complete failure. The definition of one cycle is the same as the previous test.

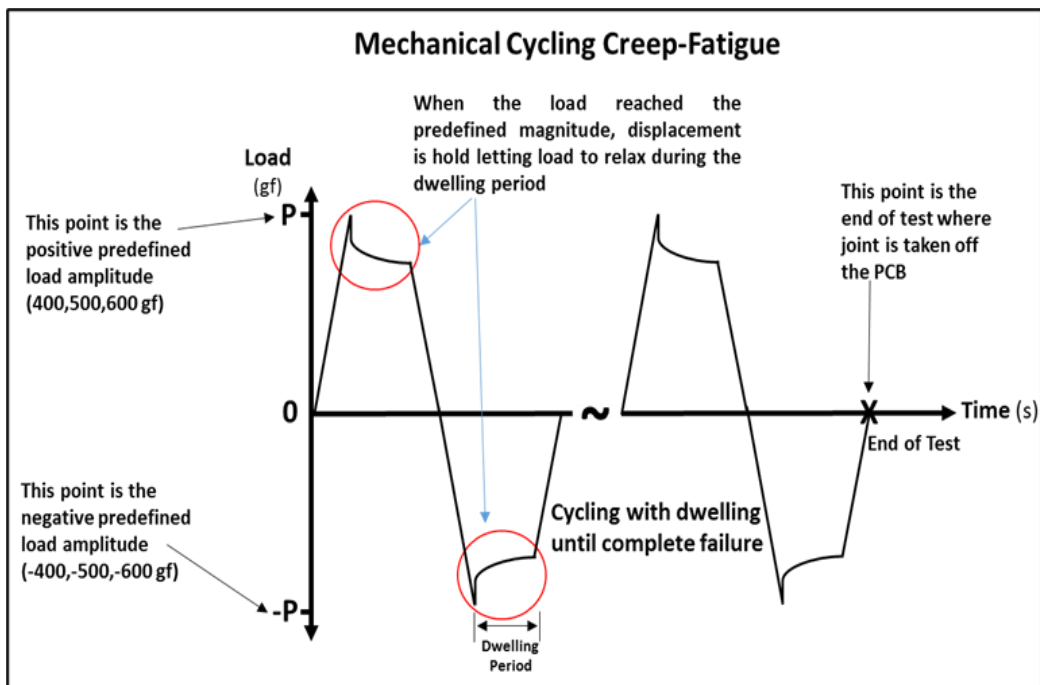


Figure 4.9: Mechanical Fatigue Only Testing Profile

Based on the previously mentioned profiles, test matrix is generated. In fatigue only test, seven replicates of testing individual joints are implemented with each stress level of 16, 20, and 24 MPa at room temperature. In combined creep-fatigue test, seven joints are cycled until complete failure

for each condition of various stress amplitudes: 16, 20, and 24 MPa and several dwelling periods: 5, 10, 60, 180s. The test matrix is tabulated in Table 4.1.

Table 4.1: The Test Matrix for Studying the Effect of Creep and Fatigue on Individual SAC305 Solder Joints Reliability at Room Temperature

Stress Amplitude (MPa)	Fatigue Only Test	Creep-Fatigue Test			
	0s dwell	5s dwell	10s dwell	60s dwell	180s dwell
16 MPa	7 samples	7 samples	7 samples	7 samples	7 samples
20 MPa	7 samples	7 samples	7 samples	7 samples	7 samples
24 MPa	7 samples	7 samples	7 samples	7 samples	7 samples

4.2 Study 2: Effect of Creep and Fatigue on Individual SAC305 Solder Joints Reliability at Various Isothermal Conditions

In the previous study, joints are failed due to the effects of creep and fatigue, and each is quantified to study the contribution of each mechanism. In this study, involving temperature complicating things. This study simulates the dwelling conditions that occurred at both thermal cycling extremes. Effects of creep and fatigue on individual solder joints under different ranges of temperature levels, stress amplitudes, and dwelling periods are addressed. It is expected to have a higher creep effect in this study because it is a strong temperature-dependent parameter, specifically at high homologous temperature. The same testing profiles are employed but at various temperature levels. OSP surface finish is used only as well. A fixed ramp rate (between extremes) of 0.1 mm/s is utilized for all replicates. Elevated temperatures of 75, 125°C, and one cold

temperature of -40°C are the temperatures to be included in this study. The accelerated test is applied to assess the reliability of individual solder joints at various temperature levels. Same preparation and assembly procedures in the first study are followed since same test vehicle is utilized for testing.

4.2.1 Experimental Setup

The previously mentioned setup in the first study is utilized to test individual joints at room temperature. This study includes mechanical fatigue and creep-fatigue tests at various temperatures. The same setup is used with some modifications, as shown in Figure 4.10. Due to elevated and cold temperatures, challenges are shown up. First, the chamber is added and fixed via bolts and hangers to the mainframe of the machine. At high elevated temperature, thermal management is required to handle the heat transfer effect. Part of the fixture is passed through the chamber from up and down, so special fillings are used to avoid the heat loss out of the chamber. This would assure the steady-state temperature among the chamber volume since any heat loss would disturb the system stability. In this test, a 2KN load cell is used with a completely different geometry than the previous one and placed at the bottom of the setup to record data. Heat is transferred via conduction through fixtures plates, and this causes severe problems for the load cell at the bottom of the system driver at the top. Therefore, a new design of a hollow cylindrical fixture is utilized to circulate chilled water within the setup passing through the critical areas that might heat up and in contact with these critical components to control their temperature. Various testing temperatures are provided via an air handler with a built-in heater for elevated temperature and liquid N_2 for cold temperatures. A controller for temperature and fan speed is utilized as well. Isolation hoses are used for connecting the air handler to the chamber, as shown in Figure 4.11. A refrigerator chiller shown in Figure 4.12 is used to control the temperature of the circulated water.

The chiller flow rate is 20 L/min and works on a wide temperature range between -25 to +100°C. The piping system includes PVC plastic material hoses, hose clamps used at each contact point with metals and, rubber gaskets between any metal contacts. Centering the solder joint is more comfortable in this test compared to the previous one for both directions. The upper plate that included the tip can move in Y-direction, and it could easily adjust this direction due to proper machine resolution. The sample is fixed on the lower plate of the fixture that is attached to the load cell. Its placed at the center of the plate width, which determines the X- position of the sample. The Z-direction will be controlled by a slot that is allowed the tip to slide through, and there are side screws to fix it in certain positions. All positions are known and adjusted due to load cell reading, which considered as an indication of the tip touching the solder joint.

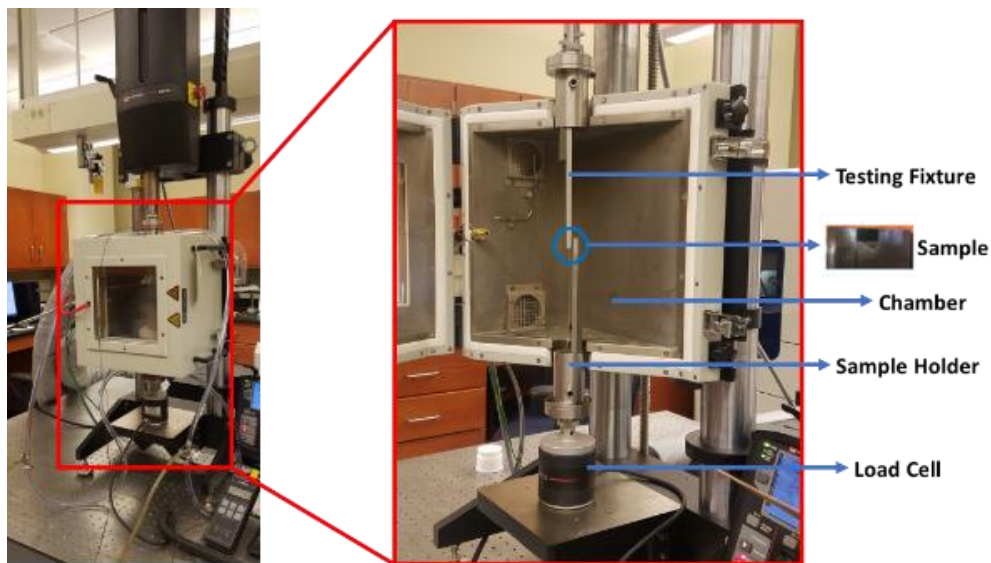


Figure 4.10: Fixture Setup with Chamber for Testing Joints at Different Temperatures

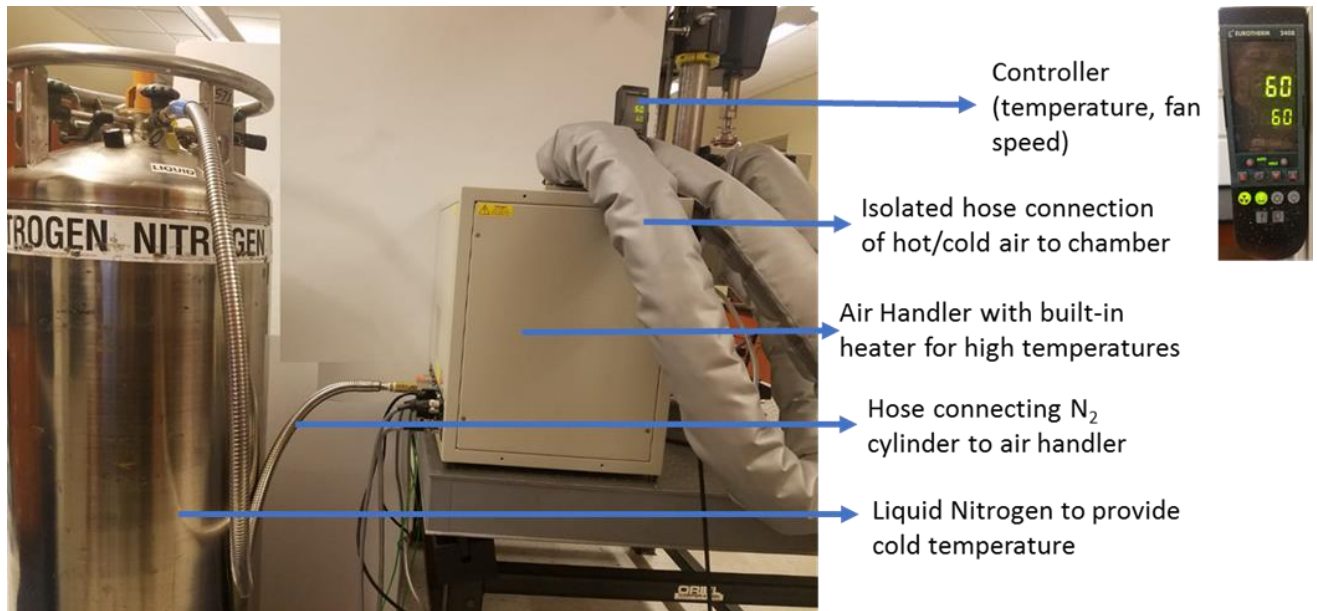


Figure 4.11: Air Handler with Accessories to Provide Hot and Cold Temperatures



Figure 4.12: Cooling System: Chiller and Piping

4.2.2 Testing Profile and Test Matrix

Testing profiles employed in this study are precisely the same as in the previous one. Fatigue only profile is performed on seven individual solder joints for each condition of stress amplitude and temperature level. Also, same number of replicates (seven) are employed in creep-fatigue tests. Seven solder joints are cycled at each condition of stress amplitude, temperature levels, and dwelling times. Stress amplitudes are 16, 20, and 24 MPa, temperature levels are -40, 75, and 125°C, whereas the dwelling periods are 5, 10, 60, 180s. The test matrix is tabulated in Table 4.2.

Table 4.2: The Test Matrix for Studying the Effect of Creep and Fatigue on Individual SAC305

Solder Joints Reliability at Various Isothermal Conditions

Temperature Level (°C)	Stress Amplitude (MPa)	Fatigue Only Test	Creep-Fatigue Test			
		0s dwell	5s dwell	10s dwell	60s dwell	180s dwell
-40	16 MPa	7 samples	7 samples	7 samples	7 samples	7 samples
-40	20 MPa	7 samples	7 samples	7 samples	7 samples	7 samples
-40	24 MPa	7 samples	7 samples	7 samples	7 samples	7 samples
75	16 MPa	7 samples	7 samples	7 samples	7 samples	7 samples
75	20 MPa	7 samples	7 samples	7 samples	7 samples	7 samples
75	24MPa	7 samples	7 samples	7 samples	7 samples	7 samples
125	16 MPa	7 samples	7 samples	7 samples	7 samples	7 samples
125	20 MPa	7 samples	7 samples	7 samples	7 samples	7 samples
125	24 MPa	7 samples	7 samples	7 samples	7 samples	6 samples

The last point to highlight is the randomization principle when implementing the various tests. Seven replicates or simple seven solder joints are tested at each combination. However, we still apply randomization among our experiment by performing fatigue test or combined creep-fatigue test for one replicate only and test another joint but at different test combination without certain or defined order. Therefore, its assured to have randomization in all our test combinations.

4.2.3: Instron 5984 Micromechanical Tester Calibration

All replicates in the previous studies are implemented using Instron 9584 micromechanical tester shown previously. This tester provides precise capability to test small geometries and specimens under shear, fatigue, tension, compression, and others including wide rang of loads from milli-newtons up to 2000N. This carried out by utilizing ultra-high-level precise drive system with superior accurate load measurement. Micro-position displacement obtained using preloaded ball-screw drive system that is equipped with both a rotary encoder and a 10nm resolution encoder.

Basically, calibration is required for all machines under frequent operation or even after long term ignorance to assure its operating limiting tolerances. This involves validation of machine accuracy for load and displacement measurement particularly. Universal machines or instruments specially the critical ones should be calibrated frequently according to defined schedule to guarantee results within tolerances. Calibration is implemented by comparing the results from machine or instrument with either calibrated or standard devices or piece depending on the usage of the machine. There are many standards such as ASTM utilized for calibration purposes for as strain and load rate as in ASTM E2309, speed and displacement as in ASTM E2658, and measurement of dynamic force as in ASTM E467, torque as in ASTM E2624, tension and compression as in ASTM E4.

Only ASTM E2309 and ASTM E2658 calibration standards are employed in this work. Our procedures started by calibrating the displacement and time pieces with calibration devices of digital linear scales and displacement measuring transducers. The combined estimate of uncertainty for the calibration devices shall be equal to or less than 0.333 of the allowable error for the measuring system, whereas confidence level of 95% is the estimated uncertainty of the calibration devices. It is important to minimize any misalignment between the calibration device and testing device before to the calibration. This would assure to optimize the result. However, temperature needs to be closely monitored. Five minutes is waiting time which required for the component to be energized. Also, this would allow all the devices to be thermal stable. The testing machine needs to be corrected to its maximum verification displacement to ensure that the maximum displacement can be achieved during the calibration. Moreover, the machine should have adequate space for the calibration device. The calibration device must be installed in the testing machines and aligned together closely to eliminate the errors.

Based on ASTM E2309 standard, the method for displacement calibration devices is followed through the ‘follow-the-displacement’ method. However, “the displacement reading on the calibration device is followed until the testing machine reaches a nominal graduation on the displacement readout scale of the measurement system” according to the standard. After that, the displacement is recorded. Then, suitable displacement increments are selected, to obtain a zero reading for both; the machine and the calibration device and adjust the testing machine slowly and smoothly for all verification measurements. The percentage uncertainty for displacement range values should not exceed the required classification criteria of the displacement measuring system. Also, the method for using speed calibration device is through the ‘stop and start method’ where: “the displacement at where the verification run will start or stop will be firstly determined based

on the verification standard for material testing speed ASTM E2658. Later, start moving the crosshead, start the displacement calibration device readout and time calibration device once the preset start displacement is reached. The time crosshead achieved the defined stop displacement as indicated by the displacement calibration device, stop the crosshead from moving. Finally, “compute the indicated speed error in percentage”. Repeat the verification run to acquire the second run for the repeatability. The percent error for the speed indication shall not exceed the required classification criteria. Finally, the calibration/verification interval needs to be reviewed by supplier technical team. It is highly recommended not to exceed 12 months without calibration for normal operating conditions. However, calibration should instantly performed after any repair or any other reason requires double check the accuracy of the measuring device.

Chapter 5: Analysis

This chapter illustrates the two types of analysis: data and metallurgical analysis that are used in this research. Data analysis discussed the followed procedures used to interpret analytical results. This includes plots that are utilized to fit collected data, analysis of variance, stress-strain analysis, and other trends among different parameters to determine relations between them. Also, this would help not only in extracting and establishing numerous correlations accordingly but will provide a clear understanding of material behavior with time. Data analysis will assist in forming or modifying prediction and reliability models based upon common models in the literature. Metallurgical or microstructure analysis is demonstrated to determine the modes of the failure; it might be through the IMC layer, bulk joint, pada cratering, etc. Moreover, it would help in fundamentally understanding the behavior of the material during the testing conditions.

5.1 Data Analysis

In this Section, various analysis methods are discussed. Weibull plots are utilized to fit the reliability data generated from various tests. Also, analysis of variance for thermal cycling data, including primary and interaction plots, are considered. Stress-strain analysis, including details about hysteresis loops, is also investigated. Several technical details and calculations that are related to individual solder joints are explained thoroughly. Then, various trends and relations between several parameters are explored to explain the behavior of solder materials under different conditions. Finally, results will be fitted to some conventional prediction models to check its validity for these models with some modifications due to various applied conditions. This would be valuable in generating models that predict life under the same circumstances in real applications.

5.1.1 Weibull Plots

Two parameter Weibull analysis is utilized to investigate the distribution of the failure data according to the equation 5.1:

$$R(t) = e^{-\left(\frac{t}{\theta}\right)^\beta} \dots\dots\dots (5.1)$$

Where R(t) is the reliability at time ‘t’, β is the shape parameter which represents the slope of plot, θ : is the characteristic life; the time at which 63.2% of the samples are expected to fail.

Figure 5.1 shows an example of Weibull plot for three different conditions. Weibull distribution plot is generated for each case to represents failure distribution for the data. Each point in the plot represents one replicate tested at that condition. Shape and scale parameters for each plot are determined. Scale parameter or characteristic life represents the 63.2% probability of failure. The shape parameter represents the variability in the data. Weibull distribution plots are constructed using Minitab Software for each stress level considering the maximum likelihood estimation method as the parametric estimation method. This type of analysis will be introduced in all data generated from various tests of all studies since all of them considered to be reliability data.

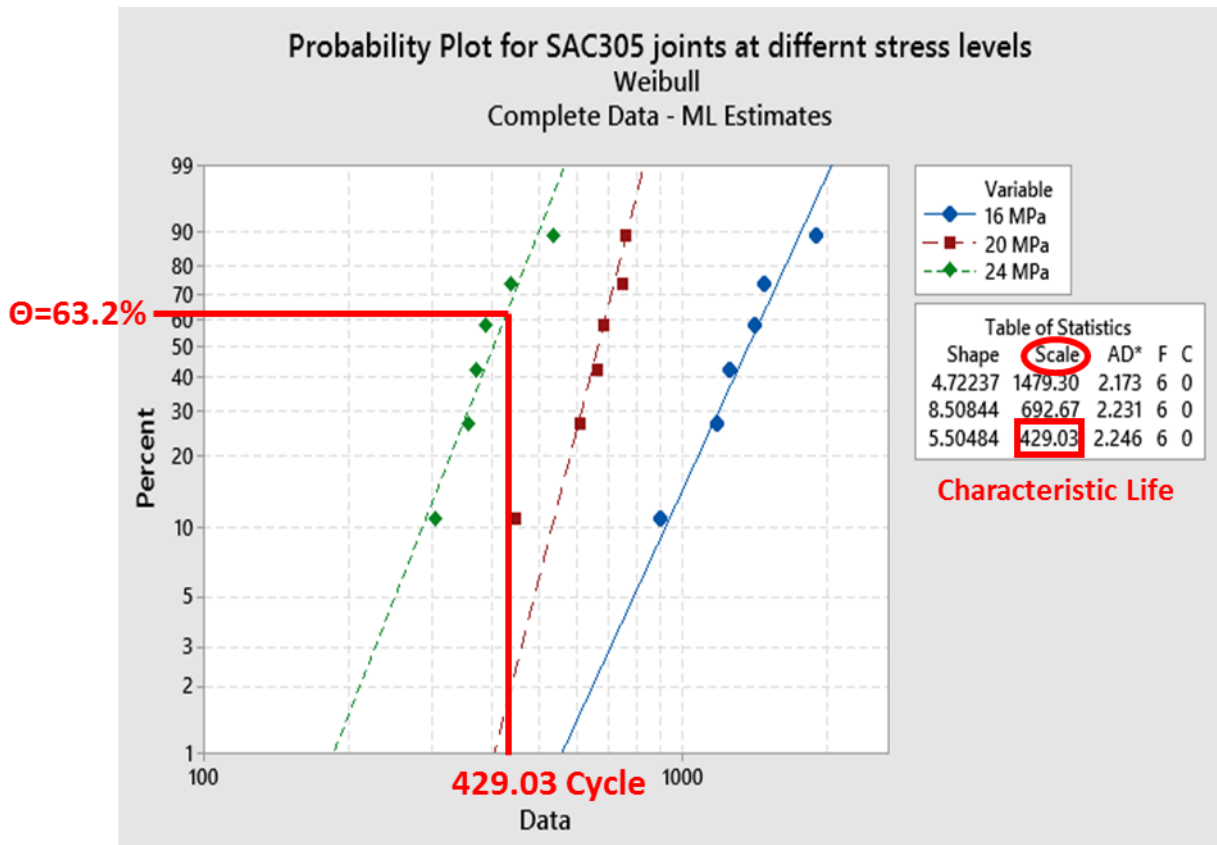


Figure 5.1: An Example of Weibull Plot

5.1.2 Analysis of Variance

Analysis of variance or ANOVA is defined as a collection of statistical models in addition to their correlated estimation techniques utilized to examine and analyze the differences or variations among various tested groups. It includes statistical hypothesis testing such as null hypothesis test, T-test, F-test, etc. and used extensively as exploratory data analysis approach. Also, there is two other analysis which is part of ANOVA called main and interaction effect analysis. These effect analyses are performed to determine the influential factors among several testing parameters. The main effect plot used to examine each factor's effect separately when there are several testing factors. Such a factor is found to be main when there is a significant effect of that factor on the response is observed when applied at different levels. The interaction effect considered various

combined factors which affects the response if they applied together. This will help assess the relationship between two or more variables to see if one factor's impact depends on the other factor's level. This analysis is considered for thermal studies to see the substantial effects of various testing parameters. The main effect and interaction effect plots are shown in Figures 5.2 and 5.3, respectively. The main effect plot concluded that surfaces drastically affect the Mean since the slope is steep. On the other hand, solder alloy found to have no significant effect on the mean since the line slope is almost horizontal. The interaction effect plot determines the influential negative or positive effect on the response. For example, the Mean is positively affected or higher for OSP surface finish when the sphere alloy is SAC105.

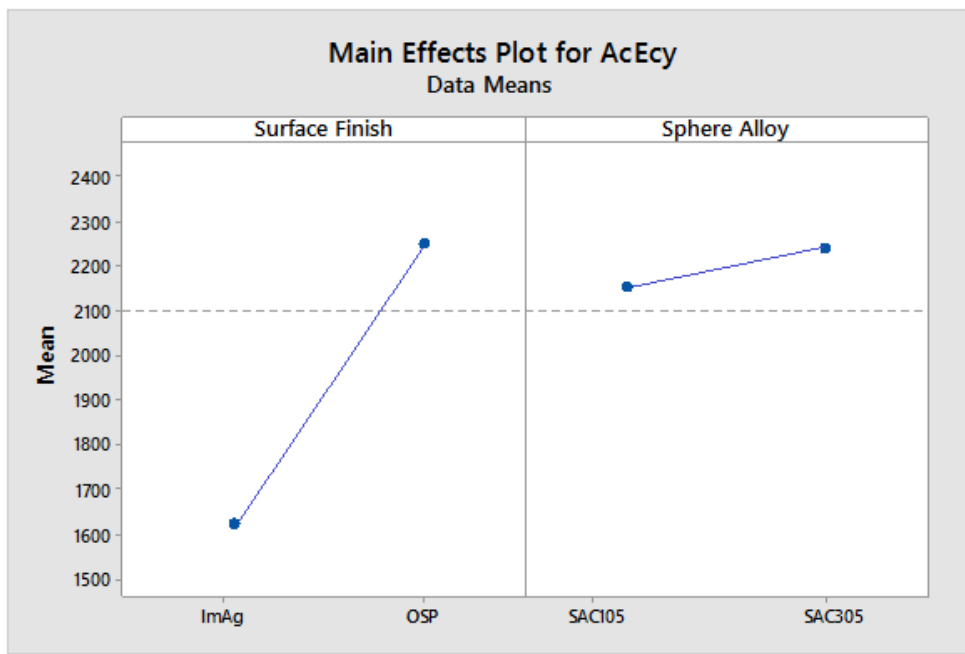


Figure 5.2: Main Effect Plot

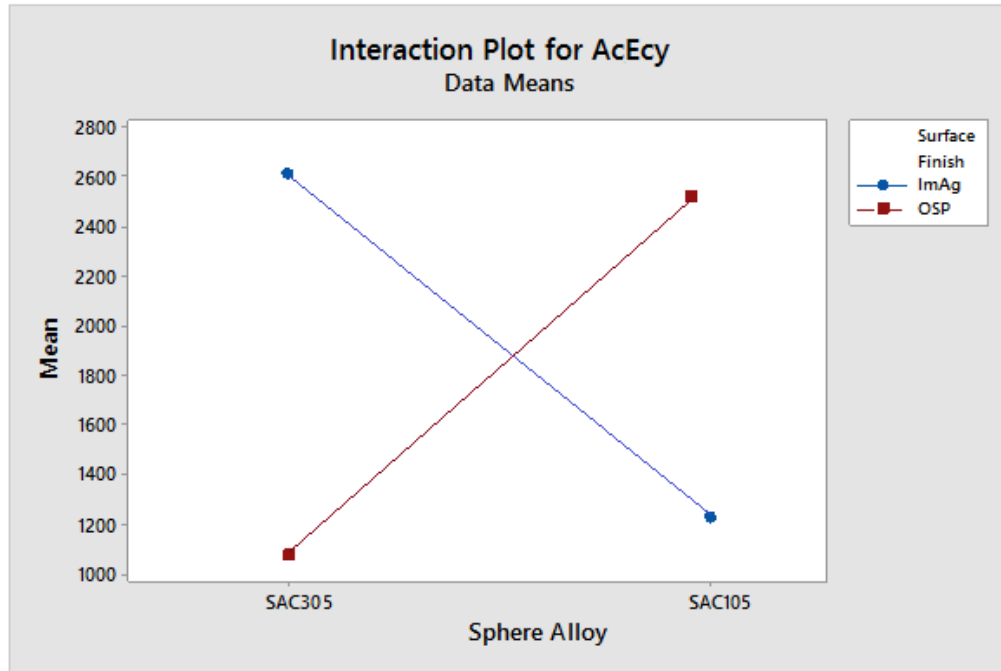


Figure 5.3: Interaction Effect Plot

5.1.3 Stress-Strain Analysis

This Section is essential because it discusses and explains various technical aspects of each experiment and physics behind it. In the first two studies specifically, individual solder joints are tested or sheared using round tip under specific load applied by The Instron 5948 MicroTester. The load cell that is attached to the Instron machine capture the load, and the machine itself capable of capturing the displacement with high resolution up to 20 nm. The data acquisition software is capable of recording the load-displacement continuously. These two parameters of load and displacement are essential in our analysis and are transferred to stress-strain data accordingly. Generally, the shear stress is defined as a force tending to deform a material along a plane parallel to the imposed load. It can be calculated by dividing the applied force to the sheared area. The force is applied by the tip on the solder joint in a direction parallel to the PCB plane, as shown in Figure 5.4.

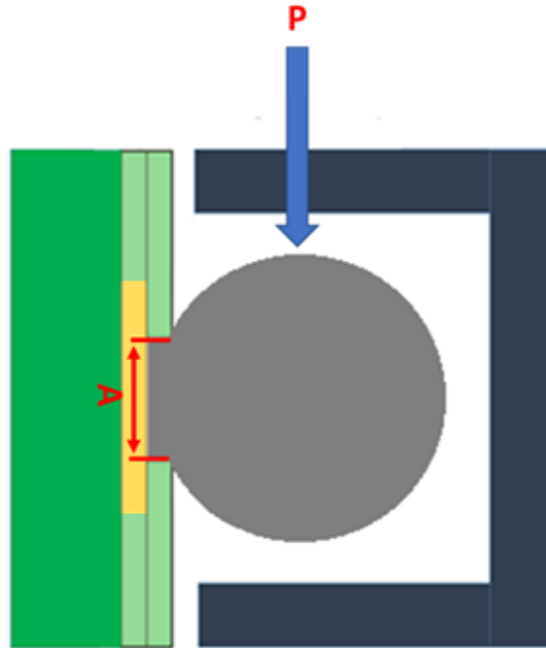


Figure 5.4: Applied Load and Targeted Area Illustration

The applied loads in our case are 400, 500, and 600 gram-force. The sheared area (A) is the SMD opening area. SMD diameter is 22 mil \approx 0.559 mm, and the total area is around 0.245 mm². Therefore, the equivalent shear stress in each case is obtained by dividing the shear load by the SMD according to table 5.1. In a real application, the maximum shear stress suffered by an individual solder joint is 3 MPa. Therefore, the stresses, as mentioned above of higher magnitude, are applied for the accelerations shear testing. Strain or Engineering strain is defined as the ratio of deformation relative to the original dimension. Shear strain is defined as the displacement of the surface directly in contact with the applied shear load or stress from its original position. In our joints, the deformation or is the measured displacement by Instron, where the original position is the radius of the solder joints.

Table 5.1: Applied Shear Loads and Equivalent Stress Amplitudes

Load (gf)	400	500	600
Stress (MPa)	16	20	24

The corresponding values of stress and strain for each cycle are plotted together, and the result is a loop called the stress-strain loop or hysteresis loop. Stress is on Y-axis, and Strain is the X-axis. The importance of such loops is characterized by the area within these loops, which represents the plastic work (damage) for that cycle—also, the difference in a strain which along X-axis at zero amplitude is called plastic or inelastic strain. Plastic strain and average work per cycle are essential parameters to provide valuable information about the joint properties and their behaviors. Also, "plastic strain" and the "average inelastic work per cycle" are utilized in various prediction models for life prediction purposes. These loops are plotted under various conditions of stress amplitudes, temperature levels, and dwelling times for comparison purposes. Figure 5.5 illustrates the concept of stress-strain or hysteresis loop.

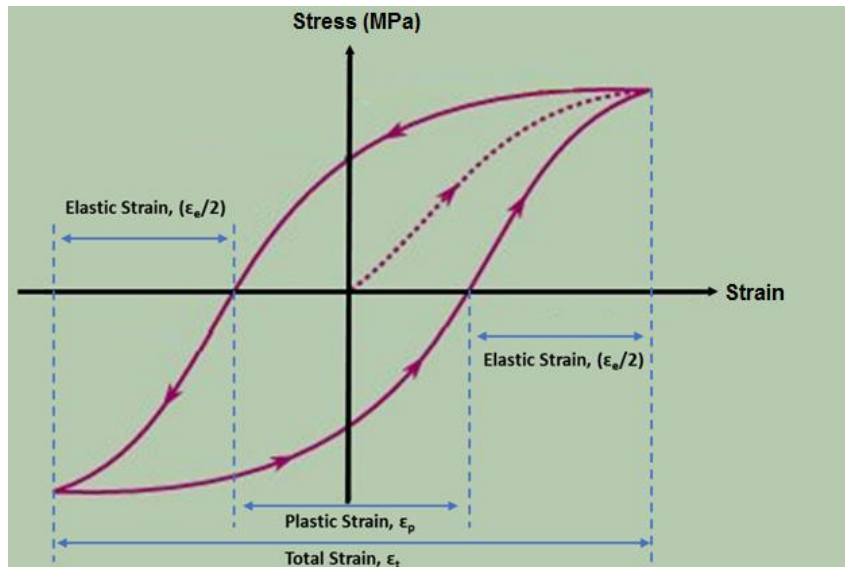


Figure 5.5: Stress-Strain or Hysteresis Loop

As mentioned earlier, hysteresis loops are vital to determine the damage generated per cycle as well as the average damage during the life. Therefore, it is employed for damage comparison purposes between various testing parameters and conditions such as dwelling periods or stress levels by comparing the area (the average plastic work) for each case as shown in Figures 5.6 and 5.7, respectively.

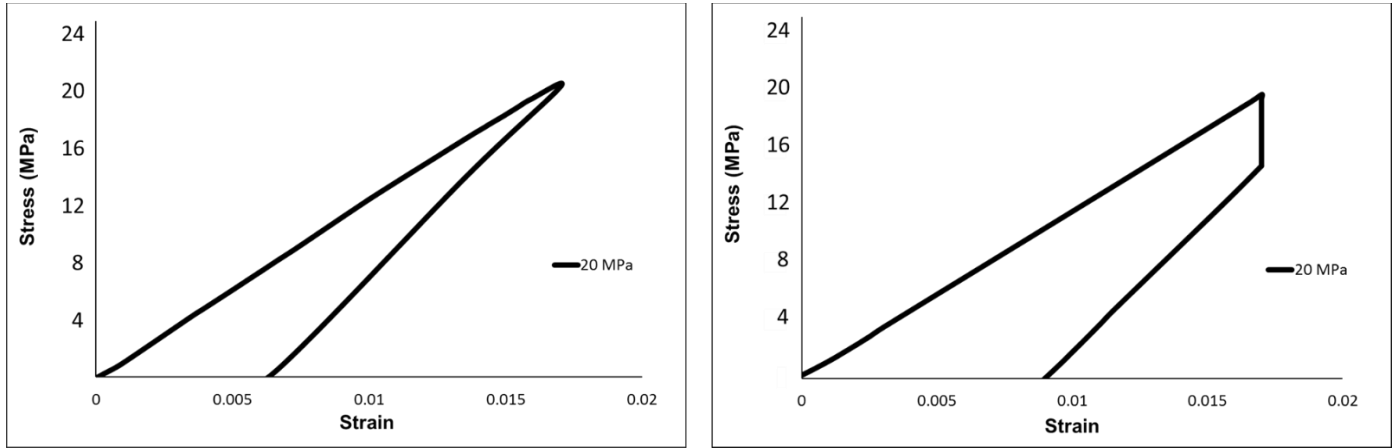


Figure 5.6: Hysteresis Loops of Zero Dwellings (Left) and 5s of Dwellings (Right)

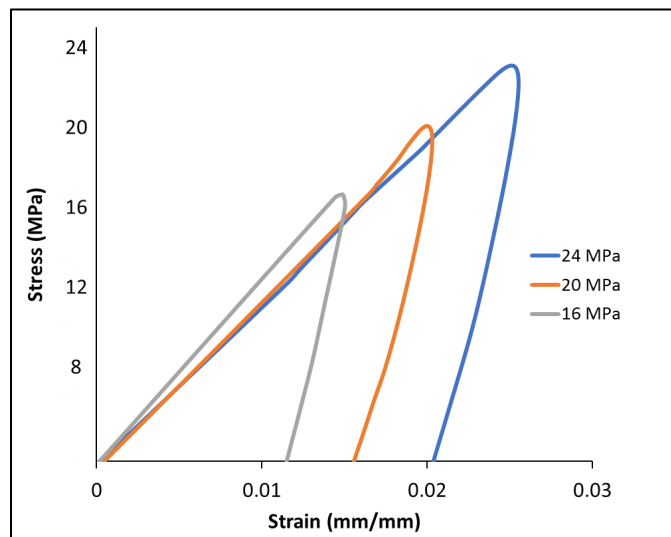


Figure 5.7: Hysteresis Loops at Different Stress Levels

In the first two studies, one of the study objectives is to distinguish effects of creep and fatigue from each other's and quantify them as well. Thus, hysteresis loop is valuable to provide such

quantities. Figure 5.8 illustrates the importance of such quantities. On the left side of the image is the hysteresis loops for two conditions of dwellings: zero (fatigue only) and 5s of dwelling. Just to reminder that the area within the loop represent the damage work. The blue area represents the damage due to fatigue only, where the whole yellow area represents the damage due to creep and fatigue. Consequently, the gray area represents the subtraction of these two conditions which is the damage due to creep. The assumption in our hypothesis is no creep effect is considered during the fatigue only test and all the damage is due to fatigue only. This is reasonable due to the relative high strain rate of 0.1 mm/s which do not allow the creep effect. On the other hand, combined test of creep-fatigue assumed to have a combination of both effects, where fatigue is dominant between ramps and creep is dominant during dwellings. Scientifically, both creep and stress-relaxation are two different processes that happened during the dwellings of the combined test. Creep is noticed when stress is constant, while relaxation in stress is observed when strain is held constant. To be very precise, damage due to each process must be distinguished from each other since one of variables is controllable. However, in both cases of creep and relaxation, it was found that the plastic flow and, microstructurally, same things happen. Also, comparing curves that related stress to strain (hysteresis loop) found to be identical for both processes of creep and stress-relaxation.

In real life application and even in our test, time dependent changes in stress and strain by joints are experienced concurrently. Thus, both damages are considered as a single damage called “creep-relaxation” or simply creep.

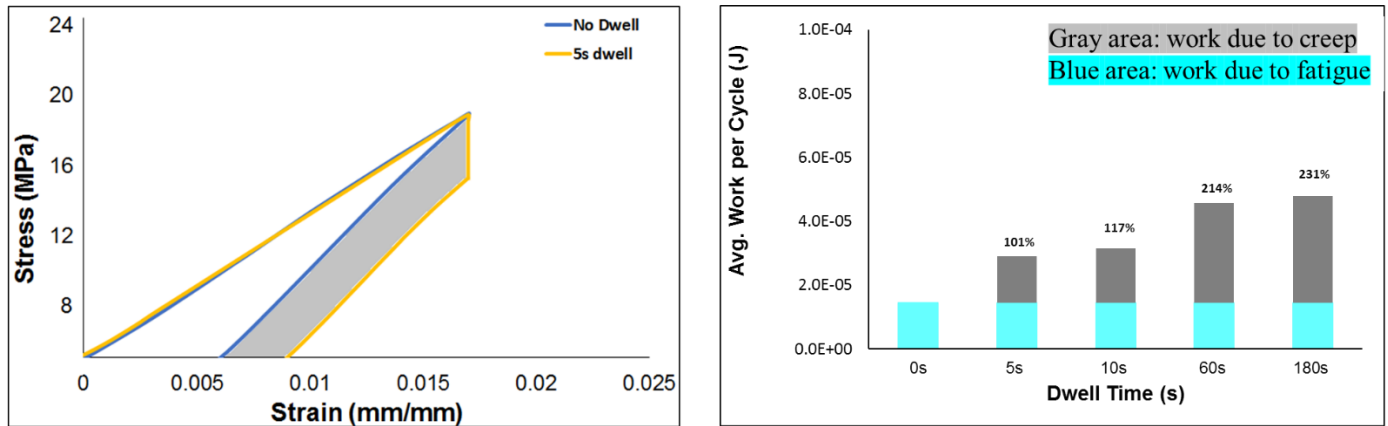


Figure 5.8: Hysteresis Loops and Average Work per Cycle for No Dwelling and 5s of Dwellings Conditions.

5.1.4 Trends and Correlations

In the first two studies, there are various testing parameters and conditions such as pure fatigue, combined fatigue and creep, several stress amplitudes, various temperatures levels, and numerous dwelling periods. Also, multiple damage parameters, such as plastic work per cycle, and plastic strain, are extracted. Life is the key parameter to establish related reliability relations. Its concluded that there are many correlations to be plotted among the previously mentioned testing parameters, conditions, damage parameters, and responses. These relations are valuable in investigating the various trends or behaviors of joints, microstructure evolution with time through damage mechanism, and in establishing various prediction models based on these parameters. Life as a function of stress that is shown in Figure 5.9 is of great importance. To illustrate, the number of cycles to failure (N) as a function of stress amplitude (S) or simply N - S curve shows the relation of fatigue life as a function of stress amplitude on a log-log scale. This correlation could be used to predict life as a function of stress amplitude by fitted it to a power equation.

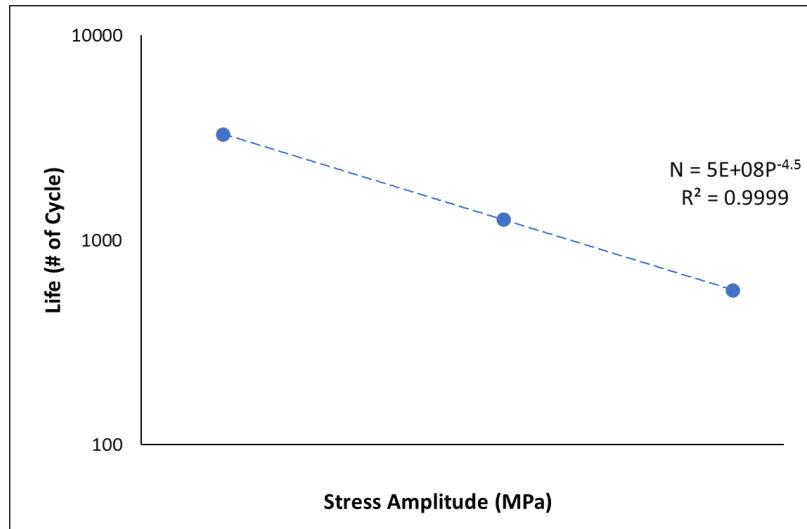


Figure 5.9: Fatigue Life of Solder Joint as Function of Cycling Stress Amplitude

Figures 5.10 to 5.13 show various correlations and trends of life and average work per cycle as a function of multiple parameters (temperature, dwelling times, stress levels) with various conditions are plotted. Each plot provides informative information about the effect of that particular parameter on joints life considering other parameters. For example, Figure 5.10 shows the effect of stress amplitude on joints life under various dwelling times. This general conclusion is crucial to provide trend or behavior of joints under such actual similar circumstances in addition to propose a research question behind such phenomena if reason is unknown and might end up with another full independent study.

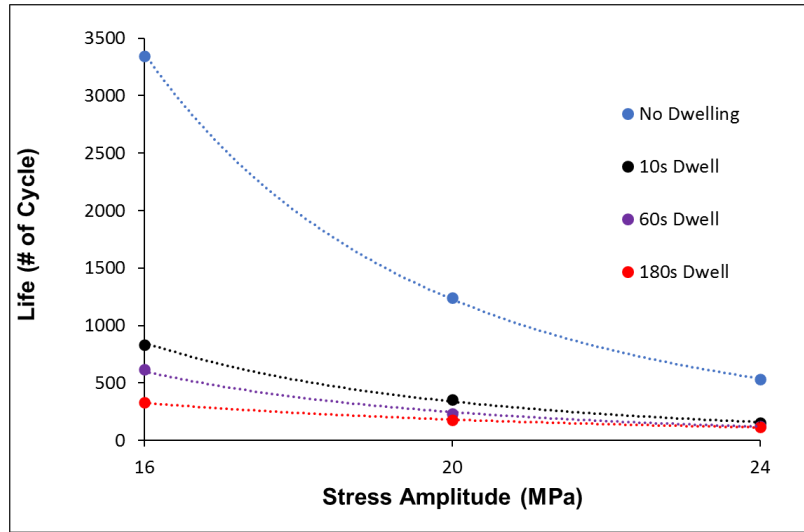


Figure 5.10: Life vs. Stress Amplitudes at Various Dwelling Times

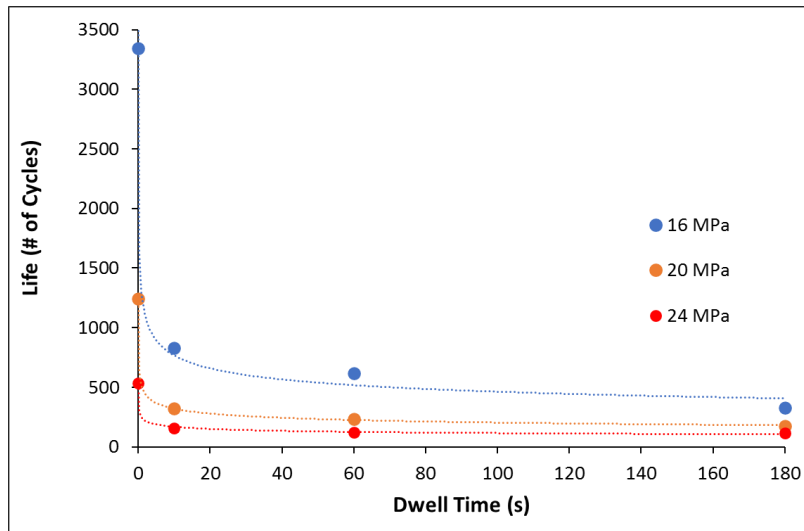


Figure 5.11: Life vs. Dwelling Times at Various Stress Amplitudes

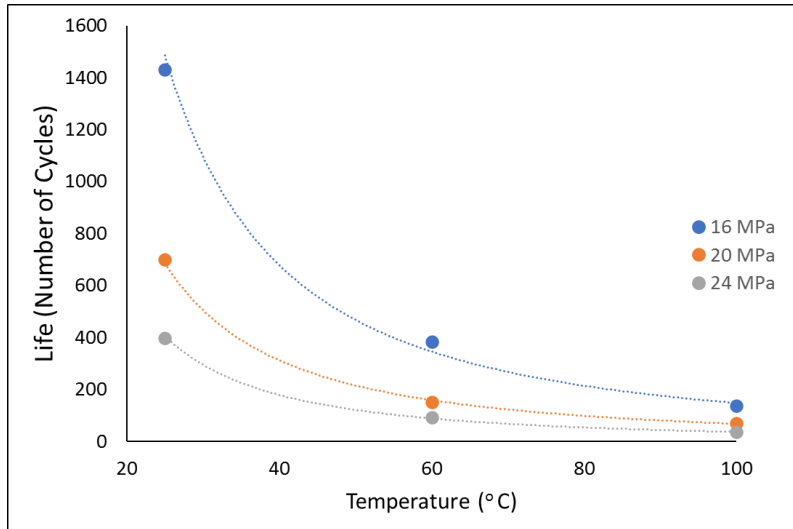


Figure 5.12: Life vs. Temperature Levels at Various Stress Amplitudes

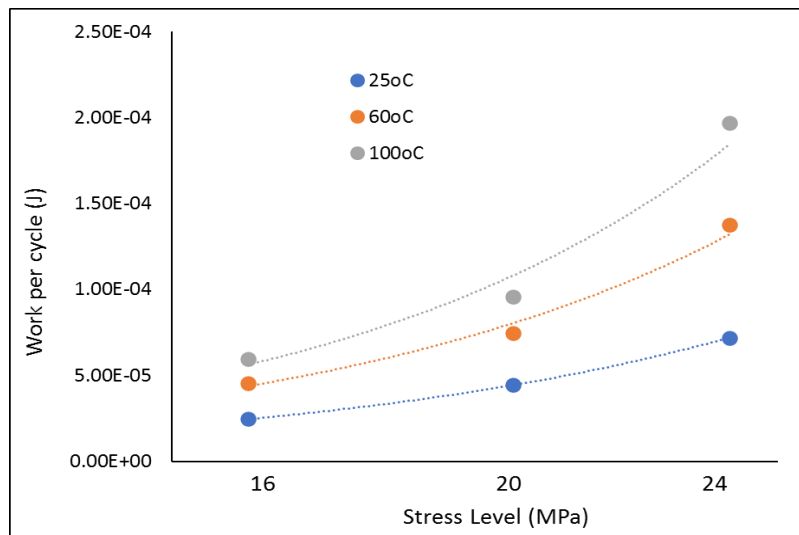


Figure 5.13: Average Work per Cycle vs. Stress Levels at Temperatures Levels

To demonstrate the joints microstructure evolution during the joint's lifetime, a critical plot is generated for all testing combinations, which is the average work per cycle as a function of the number of cycles, as shown in Figure 5.14. The evolution in damage within joints lifetime is examined by checked the evolution in plastic (damage) work per cycle. Such a plot provides critical information about the damage alternation in joint lifetime under several combinations of

testing conditions. It's clarified in the literature that solder joint fatigue life under mechanical cycling fatigue conditions is characterized by three regions: decreasing, constant, and increasing rate of dissipated work per cycle. The first region is the strain hardening, which occurs due to the changes in the dislocation structure. It keeps decreasing until it levels off. The second region is the constant or steady-state region, where the rate of work per cycle remains almost constant. This region represents around 90% of the fatigue life. The last region is the crack initiation and propagation. In this region, the work per cycle increases exponentially until complete failure. The next question: is this behavior remains the same under different testing conditions of dwelling times or even elevated temperatures. The full answer to this question will be provided at the end when such a graph is generated for all combinations of testing conditions. FEA is an easy and fast way utilized to generate life models and predict life. Unfortunately, in FEA, the average work per cycle and plastic strain considered to be constant during the lifetime, which is not true according to our results. So, the significance of such a plot is to provide exact information about various damage parameters during a joint's lifetime.

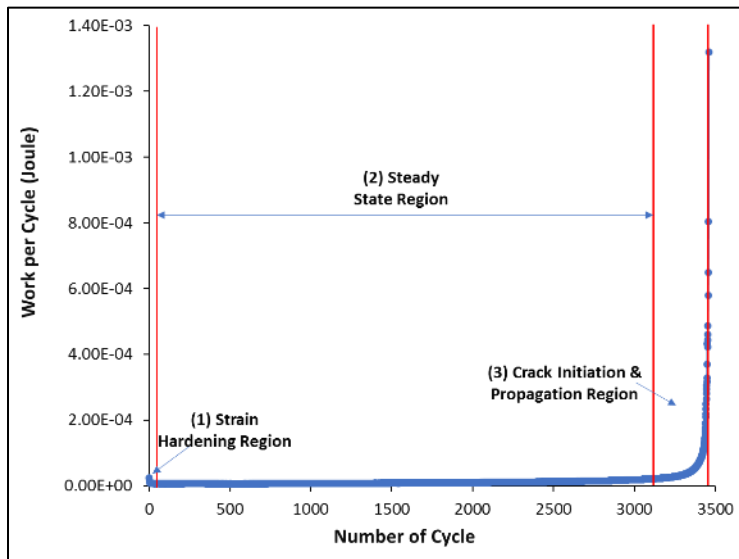


Figure 5.14: Work per Cycle of Solder Joint Cycled at 16 MPa until Failure

5.1.5 Prediction Models

This is the main objective for each study, which is to establish a prediction model from extracted data. Prediction models are valuable tools that are generated based on statistics utilized to predict the life of the electronics system running under certain circumstances in an accelerated manner. So, instead of waiting five years until checking the failure of joints in automotive applications, for example, a fair estimate for such a system's lifetime can be predicted in few months, which saves time and cost. Also, this method is more convenient than FEM one which has many approximation and assumptions that is required to achieve such models. The value of this work is to combine both physics and statistics to determine various prediction models.

Power Equation model is the first model utilized to fit our data. The relationship between the characteristic life and the cyclic stress amplitude is established by utilizing a power equation like equation 5.2

$$N_f = D * P^{-c} \dots\dots\dots(5.2)$$

Where N_f is the characteristic life, P is the stress amplitude, D and c are the material constants of ductility index and coefficient, respectively. Results of first and second studies will be fitted to this model and check for its adequacy.

Coffin-Manson model is the second model to be introduced in our work due to importance. Basically, the relationship between the characteristic life and the plastic strain is generated by fitting results to the equation 5.3

$$(N_f)^\alpha \Delta \epsilon^p = \theta \dots\dots\dots(5.3)$$

Where N_f is the characteristic fatigue life of the solder joints, ϵ_p is the plastic strain, α and θ are constants. Result in first and second test are fitted to this model and will be checked for its adequacy.

Morrow Energy model is the third model to be introduced in this work. The relationship between the characteristic life and the plastic work is established by utilizing a power equation in equation 5.4:

$$(N_f)^m \Delta W_p^c = \theta \dots \dots \dots (5.4)$$

Where N_f is the characteristic fatigue life of the solder joints, ΔW_p is the plastic work, m and c are constants. Result in first and second test are fitted to this model and will be checked for its adequacy.

Since the second study is mainly performed at various temperatures, therefore, Arrhenius Approach is introduced. A factor named “K” which represents the process rate is considered and its with direct relation with temperature according to equation 5.5

$$K = A e^{-\frac{B}{T}} \dots \dots \dots (5.5)$$

Where K is the process rate, T is the absolute temperature (in kelvins), A and B are constants.

5.2 Microstructural Analysis

As mentioned previously, this analysis is vital to determine the failure modes within joints. Also, it helps in explaining the failure mechanisms of the test. In thermal cycling, for example, the basic failure mechanism started by inhomogeneous deformation and coarsening among the microstructure, followed by recrystallization. Finally, material softening, crack initiation, and propagation. So, after thermal cycling, microstructure should show such recrystallization effects

for comparison purposes and test verification. Even testing individual solder joints at elevated temperatures would show some certain recrystallization. This explained by the fact of recrystallization initiation if the temperature is above a defined threshold point, which may be the case in our test at elevated temperature.

Standard procedures are followed in our lab for sample preparation. Depending on the test vehicle, either component or solder joints coupons, a targeted element is mounted within plastic mold made from resin and hardener with a fixed ratio between resin to hardener of 6:1 in weight. Element is placed and fixed within the mold by holder clips and cured for 24 hours at room temperature. Examples of liquids and accessories to prepare the samples is shown in Figure 5.15. Next, the sample is pulled out of the mold, and by that time, it is ready for grinding and polishing procedures, respectively. Grinding paper with 120, 400, 600, 800, 1000 and, 1200 grit is used in sequence with 120 is the roughest and 1200 is the finest. Grinding is stopped with the 120 paper once the middle of the solder joint appears. During switching between different grit sizes, the sample is rotated by 90° after each grit. This would guarantee that cuts made by the previous paper are removed by the following finer one. After each grinding grit, samples are checked using a microscope to check cuts from the previous process. Polishing is started immediately once the grinding is done. Four stages of polishing solutions include 3 μm, 1 μm, 0.05 μm, and 0.02 μm. The first three solution are alumina base particle or suspension while the fourth one is a colloidal silica base material. Each polishing stage lasts between 15-30 minutes to make sure that scratches from the previous stage are eliminated. An ultrasonic cleaner is utilized to remove residuals from the polishing process. Grinding and polishing pads are shown in Figure 5.16. Also, polishing solutions of different sizes are shown in Figure 5.17. All grinding and polishing procedures are performed using semi-automated grinding machine shown in Figure 5.18.



Figure 5.15: Cleaner, Resin, Hardener (rare line from left to right), Samples and Molds (front line)



Figure 5.16: Grinding (Left) and Polishing Pads (Right)



Figure 5.17: Polishing Alumina Suspension of Various Sizes (First Three from Right) and Colloidal Silica Solution



Figure 5.18: Automated Grinding-Polishing Machine

After that, samples are ready for analysis using the optical microscope. Sophisticated ZEISS Axio Imager.M2m optical microscope with an Axiocam 503 color microscope camera and ZENCore software is used to analyze the sample and determine the failure mode. Polarized images are generated to check for recrystallization as well. Interface software has the capability of saving the data for future analysis. ZEISS microscope with a camera is shown in Figure 5.19. Typical cross polarized and bright field images for SAC305 solder joints are shown in Figures 20 and 21, respectively.

Furthermore, Scanning Electron Microscope (SEM) photos might be generated for further analysis and determining the composition of the intermetallic compound using Energy Dispersive X-Ray (EDX) analysis. IMC layer is measured either by this microscope or the previous one since it has such an option. Since conductive samples could be used with this microscope and epoxy ones are not, it's coated using carbon or gold and can be used with this microscope for the mentioned

analysis. SEM and carbon coating devices are shown in Figures 5.22 and 5.23, respectively. A typical SEM image for SAC305 solder joint is shown in Figure 5.24.

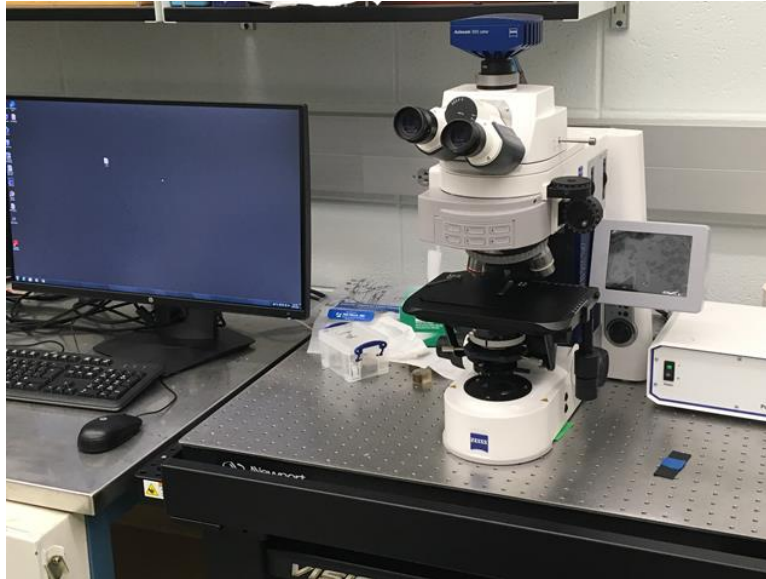


Figure 5.19: ZEISS Axio Imager.M2m Optical Microscope

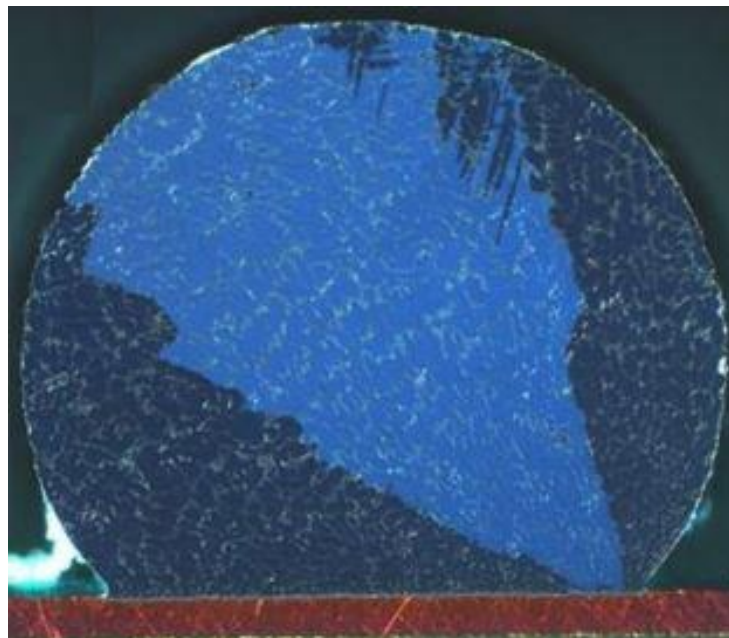


Figure 5.20: Cross Polarized Image for As-Reflowed SAC305 Solder Joint with Twin Microstructure

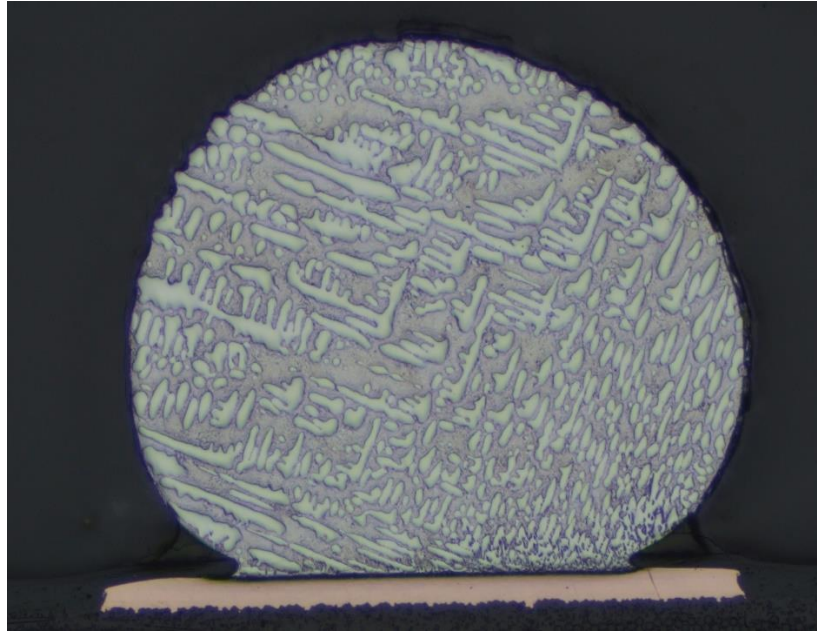


Figure 5.21: Bright-Field Image for As-Reflowed SAC305 Solder Joint



Figure 5.22: Hitachi S-2460N SEM



Figure 5.23: Carbon Coating System

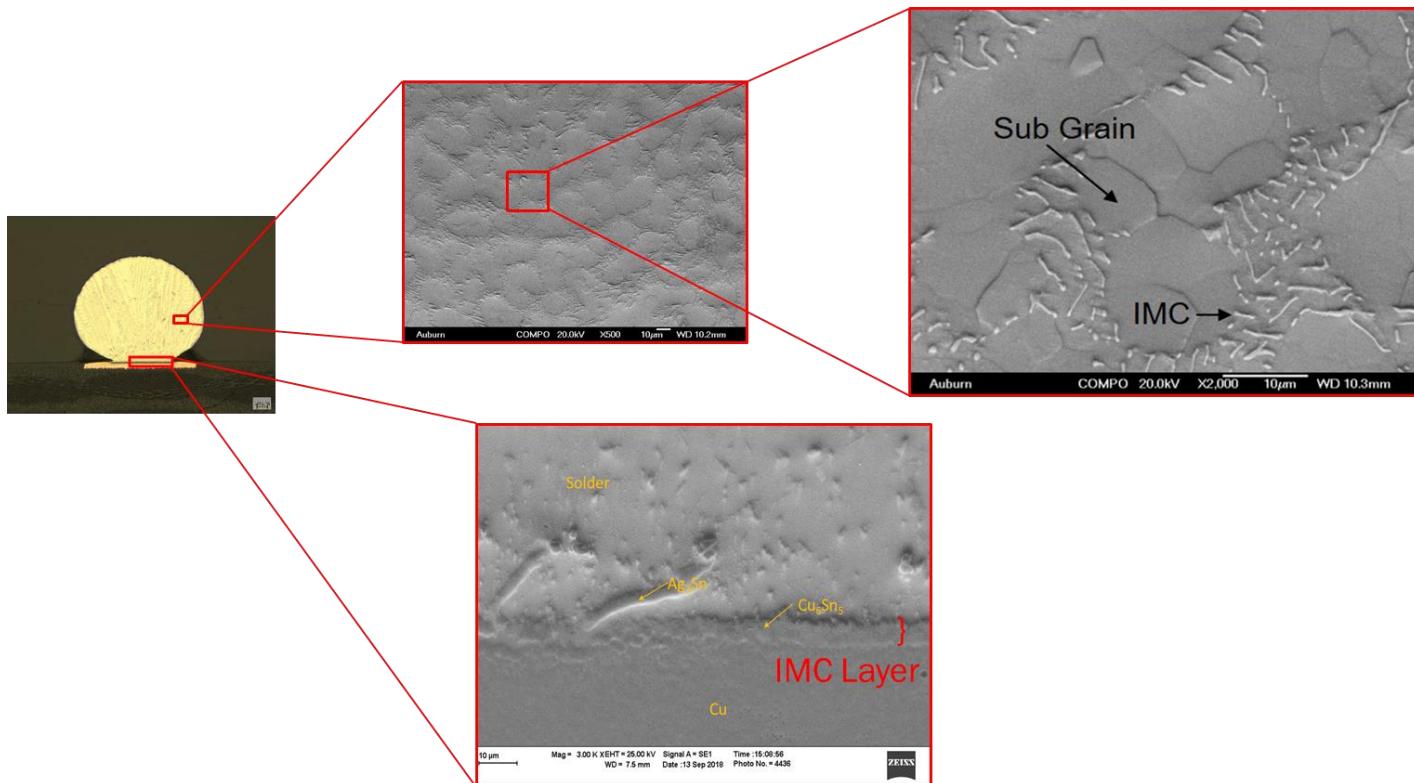


Figure 5.24: SEM Image of As-Reflowed SAC305 Solder Joint

Chapter 6: The Reliability Modeling of SAC305 Individual Solder Joints During Creep-Fatigue Conditions at Room Temperature

6.1 Introduction

The robustness of electronic assemblies is determined by the mechanical integrity of solder joints against various degradation influences. Thermal alteration between temperature extremes considered as a major trigger which leads to degradation in joints life under realistic applications. Switching of on-off cycles for electronics systems as in power cycling in addition to the exterior sources of elevated temperature from surroundings are examples of thermal cycling cases. The behavior of solder joints under thermal cycling is complicated due to its influence by damage mechanisms of creep, fatigue, and the interaction of both mechanisms. Creep is dominant during dwelling periods, while fatigue is influential between ramps. Other factors such as oxidation, microstructure evolution, and phase changes are of great importance as well. Essentially, the failure of joints under thermal cycling occurs due to the mismatch in coefficient of thermal expansions (CTEs) of PCB and components. As temperature alternating between extremes, a cyclic shear stresses on joints are generated and cause failure.

In this study, the reliability of individual solder joints is explored under both effects of both creep and fatigue at room temperature using accelerated shear fatigue tests. The effects of stress amplitudes and dwell times are studied. Three stress amplitudes with various dwelling times are applied in this study. At each testing condition, Two-parameters Weibull distribution is generated to describe the fatigue life of solder joints. A numerical reliability model is developed as a function of stress amplitude and dwelling time. The evolution in stress-strain loops is observed for each testing condition. The damage due to fatigue is characterized from creep by quantifying related damage parameters as plastic work per cycle and plastic strain at various testing conditions. Coffin-

Manson and Morrow Energy models are utilized to examine the relations between plastic strain and plastic work respectively with fatigue life. Finally, general reliability models as a function of plastic strain and plastic work are established.

6.2 Test Matrix

Accelerated shear fatigue tests and combined tests of creep-fatigue are performed to assess the reliability of individual solder joints at room temperature. The tests include cycling individual SAC305 joints under various dwelling times and stress amplitudes. Three stress amplitudes of 16, 20, 24 MPa with various dwelling times of 0, 10, 60, and 180 seconds are applied in this study. Originally, the plan was to include 5s of dwelling in the combined creep-fatigue test, but it was excluded considering it as a short dwell time. Essentially, accelerated reliability test designs are considered as good/high rank if and only if the stored damage mechanisms during the test were similar to the realistic applications or conditions. Consequently, the developed model would predict the component life more accurately. Creep deformation and anelastic recovery are the dominant mechanisms stored for solder materials near or above room temperature during the holds in the cyclic test. According to previous study [22], deformation is initiated by anelastic strain, anelastic recovery during the relaxation time, followed by creep deformation. It was found that if dwell or hold time is in the range of 3-9s (short), the anelastic strain acts to retard the creep deformation from being the dominant damage mechanism. Therefore, 5s of dwelling was excluded from the test. Room temperature is the only temperature included in this research study. Other cold and elevated temperatures are utilized in the next research study, where results to be compared for correlated purposes. Seven individual solder joints are tested at each combination. Table 6.1 shows the test matrix for this study.

Table 6.1: The Test Matrix for Studying the Effect of Creep and Fatigue on Individual SAC305
Solder Joints Reliability at Room Temperature

Stress Amplitude (MPa)	Fatigue Only Test	Creep-Fatigue Test		
	0s dwell	10s dwell	60s dwell	180s dwell
16 MPa	7 samples	7 samples	7 samples	7 samples
20 MPa	7 samples	7 samples	7 samples	7 samples
24 MPa	7 samples	7 samples	7 samples	7 samples

6.3 Results and Analysis

In this part, the results and its related analysis are explained including the reliability modeling part. First, Weibull analysis for both mechanical fatigue and creep-fatigue tests is introduced for all testing conditions. This include Weibull plots for under testing conditions of various stress amplitudes and dwelling times in addition to establish a general reliability model as a function of dwell time. Second, the evolution in hysteresis loops for all testing combination is demonstrated. Related damage parameters of plastic strain and inelastic work are explored. Creep effect is quantified in combined creep-fatigue test comparted to fatigue only test. The last section contains general reliability models are generated based on Coffin-Manson and Morrow Energy Models.

6.3.1 Weibull Plots Analysis and Prediction Modeling

In this section, the Weibull plots for mechanical fatigue test is introduced followed by prediction modeling section. Then, Weibull plots for combined creep-fatigue test in addition to related prediction modeling is presented.

Mechanical Fatigue Condition

Weibull Plots

Two parameters Weibull plots are generated for each testing combination to describe the fatigue behavior of solder joint. To demonstrate the degradation in fatigue life or joints reliability, a two-parameter Weibull equation [48] is applied as shown in equation (6.1)

$$R(t) = e^{-\left(\frac{t}{\theta}\right)^\beta} \dots\dots\dots(6.1)$$

Where R(t) is the reliability at time t (the probability of not fail), t is the time or number of cycles, θ is the scale parameter or characteristic life and β is the shape parameter.

Figure 6.1 shows the Weibull plot for joints cycled according to the mechanical fatigue profile (No Dwelling) with various stress amplitudes. A significant reduction in joints reliability is observed at higher stress levels. Weibull distribution plots were constructed using Minitab Software for each stress level, considering the maximum likelihood estimation method as the parametric estimation method. The variability of data is low according to the shape (β) parameter values.

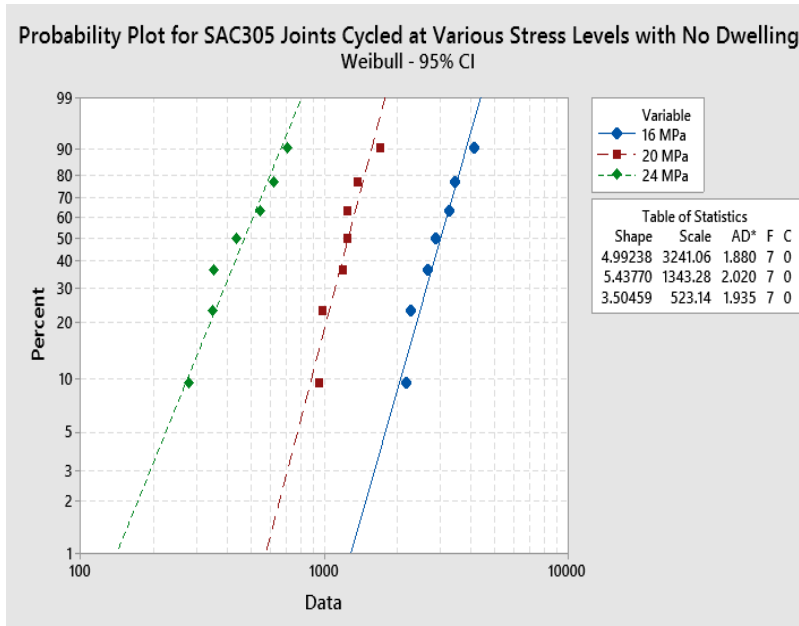


Figure 6.1: Weibull distributions for SAC305 joints cycled at different stress amplitudes at no dwelling

Prediction Modeling

The characteristic life and stress amplitude are related according to power equation [48] shown in equation (6.2)

$$N_{63} = C * P^{-n} \dots\dots\dots (6.2)$$

Where N_{63} is the characteristic life, P is the stress magnitude, C , n are constants. n is called the ductility factor where lower value implies higher ductility.

Figure 6.2 illustrates the fatigue life as a function of stress amplitude. Seven solder joints are cycled until complete failure with each stress level. The fatigue life is reduced drastically at higher stress levels.

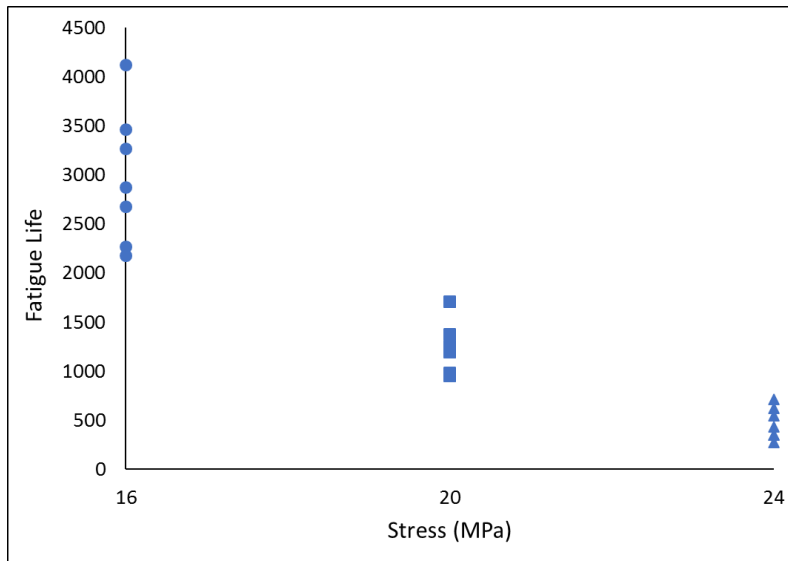


Figure 6.2: The fatigue life of SAC305 solder joints as a function of stress amplitude

Characteristic life is a vital parameter to define reliability as a function of stress level according to equation (6.1). Therefore, the characteristic life of SAC305 joints as a function of stress amplitude at the “No Dwelling” condition is plotted, as shown in Figure 6.3. Data were fitted to a power equation which found satisfactory to describes the characteristic life of joints as a function of stress amplitude according to equation (6.2). It is concluded that the power value for the generated power equation is -4.5 , which reflects the fatigue ductility exponent coefficient of the material. Also, decreasing the stress value by a factor of 2 will lead to life reduction by a factor of 19. Similar results were found by others [12].

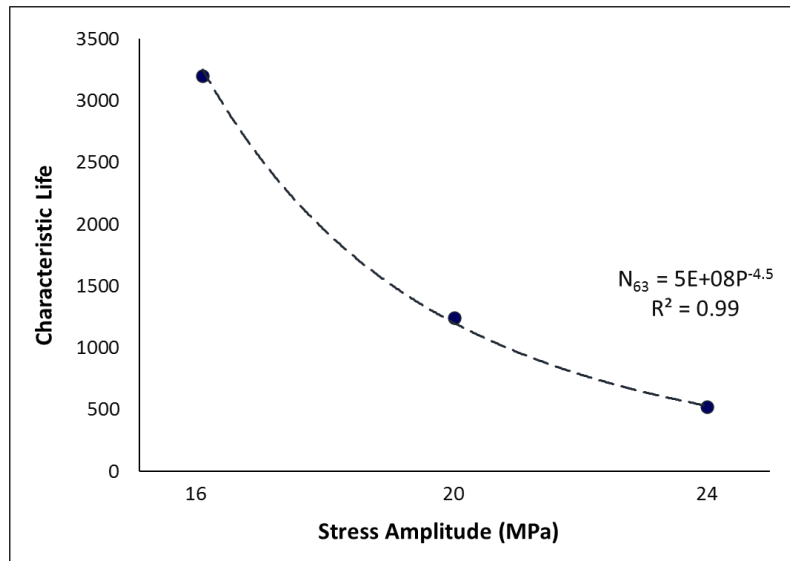


Figure 6.3: Characteristic life as a function of stress amplitude for SAC305 solder joints at No dwelling

Dwelling (Creep-Fatigue) Condition

Weibull Plots

In order to examine the effects of dwelling on the fatigue life of the solder joints at different stress conditions, individual solder joints were tested at amplitudes of 16, 20, and 24 MPa with different dwell times of 0, 10, 60, and 180s at 25°C. The shape and scale parameters of the Weibull distribution were obtained for all combinations. In Figures 6.4 (a, b, c), the Weibull plots for each dwelling level is generated. At certain dwelling times, increasing the stress amplitude leads to substantial fatigue life reduction. Moreover, at a certain stress level, the fatigue life is decreased extremely with dwellings of 10s. Life remains to decrease with longer dwellings but in a less amount. Results are shown in Figures 6.5 (a, b, c).

In Figure 6.6, characteristic life as a function of dwell time for various stress amplitude is plotted. Creep effect (due to dwelling) found to be substantial. There are some results for less life of lower stress and higher dwelling conditions than ones cycled with higher stress and shorter dwellings.

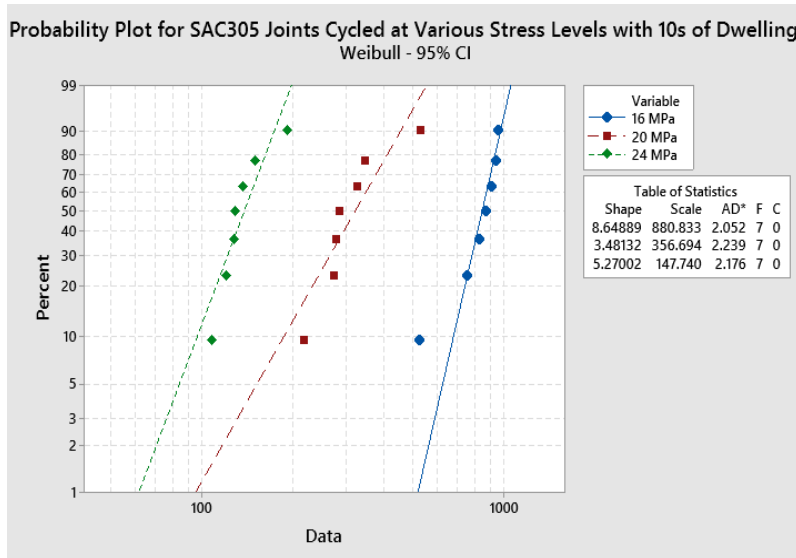


Figure 6.4 a: Weibull distributions for SAC305 joints cycled at different stress amplitudes at 10s dwelling

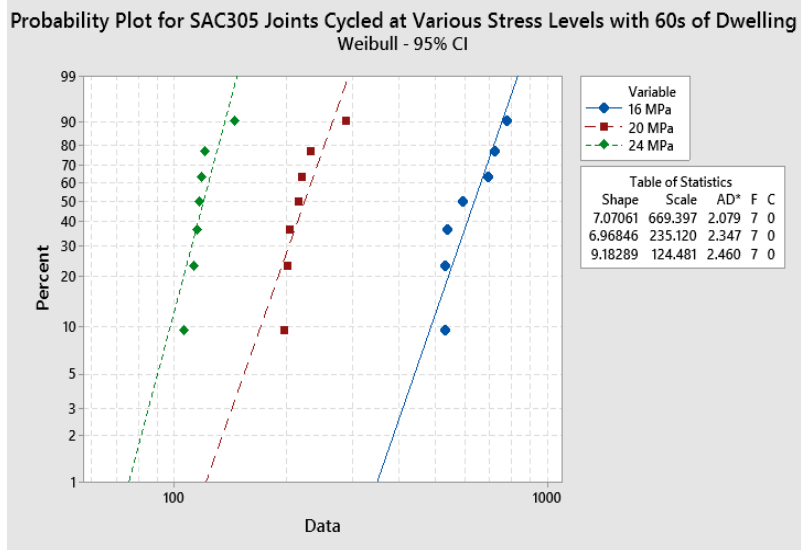


Figure 6.4 b: Weibull distributions for SAC305 joints cycled at different stress amplitudes at 60s dwelling

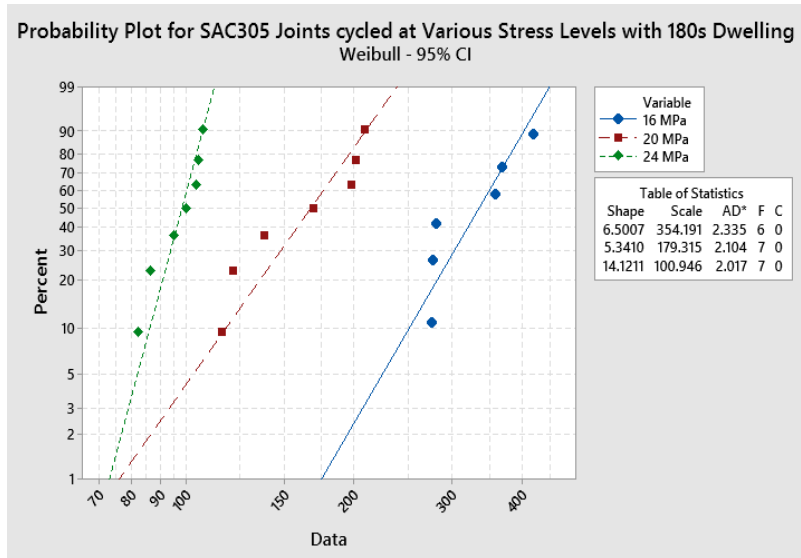


Figure 6.4 c: Weibull distributions for SAC305 joints cycled at different stress amplitudes at 180s dwelling

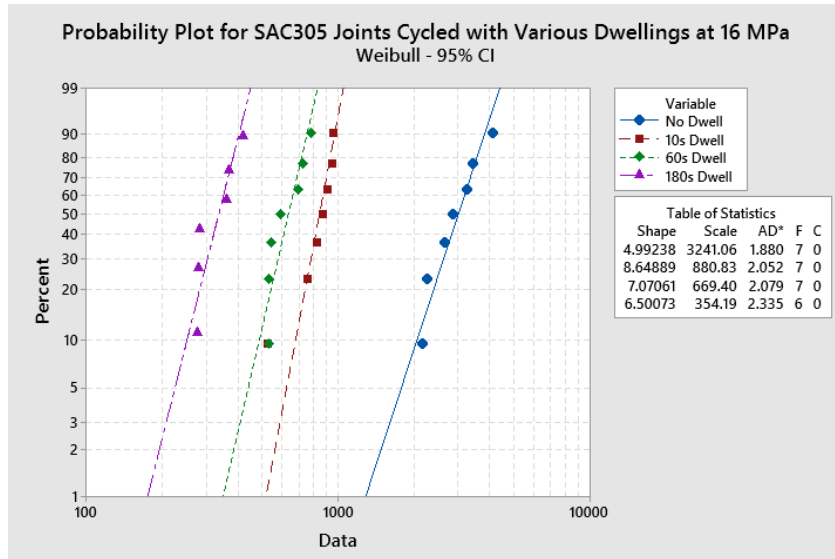


Figure 6.5 a: Weibull distributions for SAC305 joints cycled at different dwellings with 16 MPa stress level

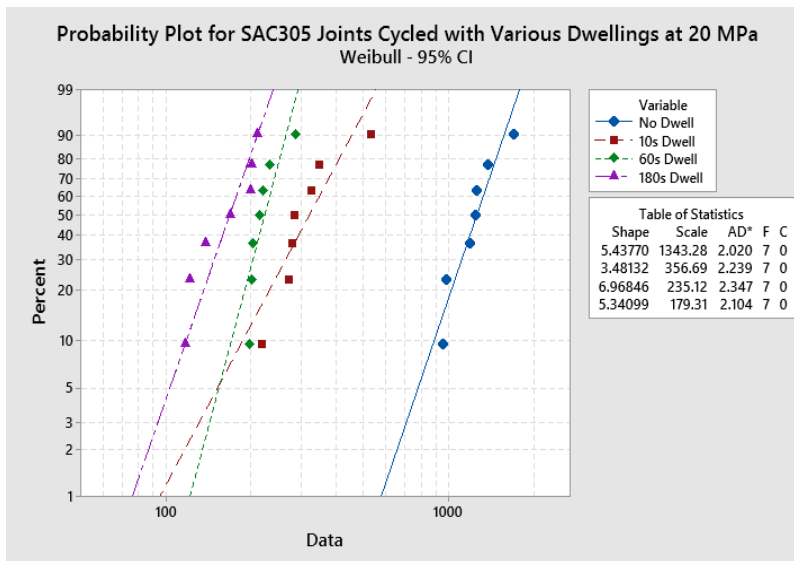


Figure 6.5 b: Weibull distributions for SAC305 joints cycled at different dwellings with 20 MPa stress level

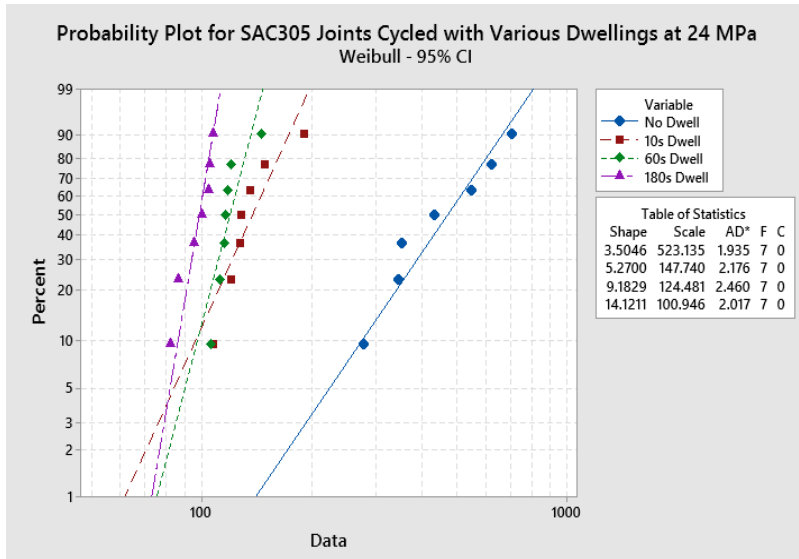


Figure 6.5 c: Weibull distributions for SAC305 joints cycled at different dwellings with 24 MPa stress level

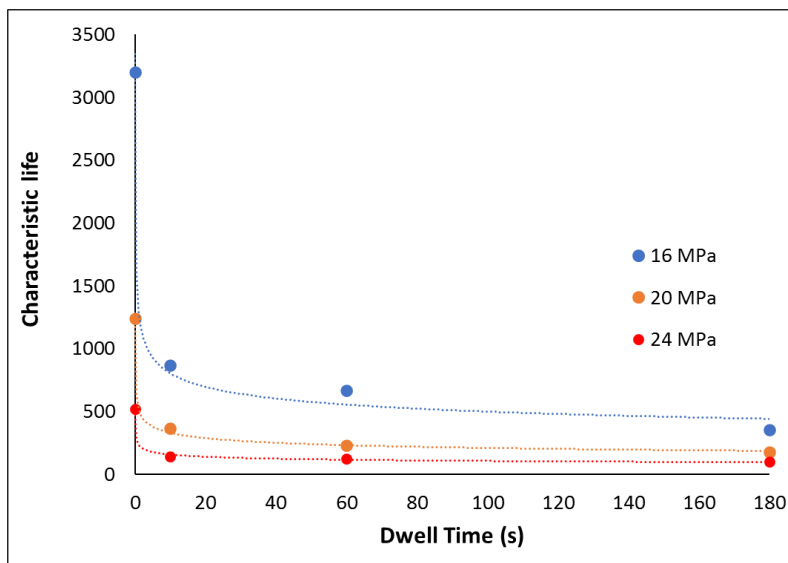


Figure 6.6: Characteristic life as a function of dwell time for SAC305 solder joints cycled with various stress level

Prediction Modeling

To characterize the reliability model as a function of dwelling, the relationship between characteristic life and stress amplitudes for joints cycled with various dwelling are plotted as shown in Figure 6.7 where data are fitted to power equations for each dwelling periods. A decreasing trend for the power value (the material ductility exponent) is identified when the dwell time is increased. However, the constant C observed to decrease with dwelling. The R-square values are above 99% for all fitting lines.

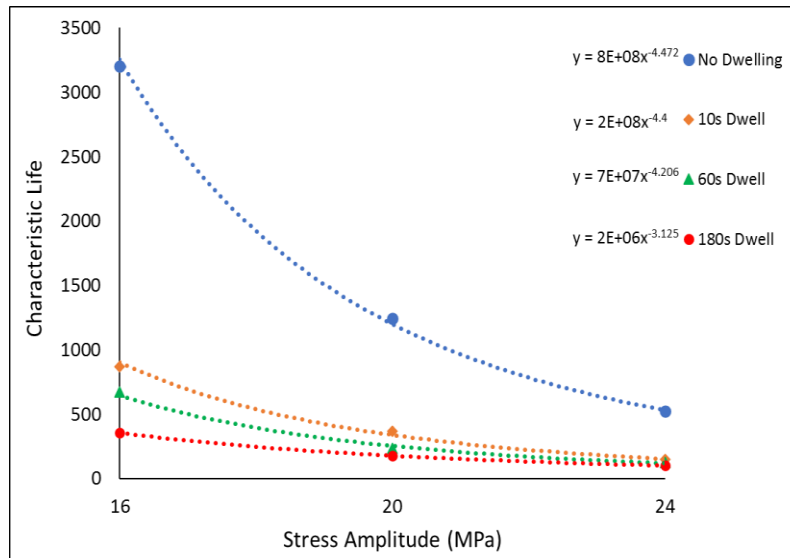


Figure 6.7: Characteristic life as a function of stress amplitude for SAC305 solder joints at various dwellings

To predict the reliability as a function of dwell time and stress amplitude; the correlation between n and C values as a function of dwell time (t_d) must be identified. Correlations to predict the power values of n and C value as a function of dwell time are shown in Figures 6.8 and 6.9.

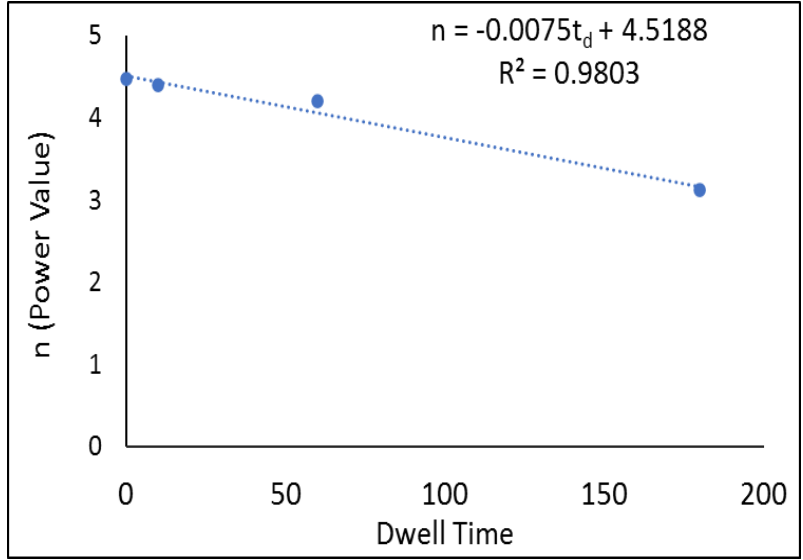


Figure 6.8: Power value (n) as a function of dwell time

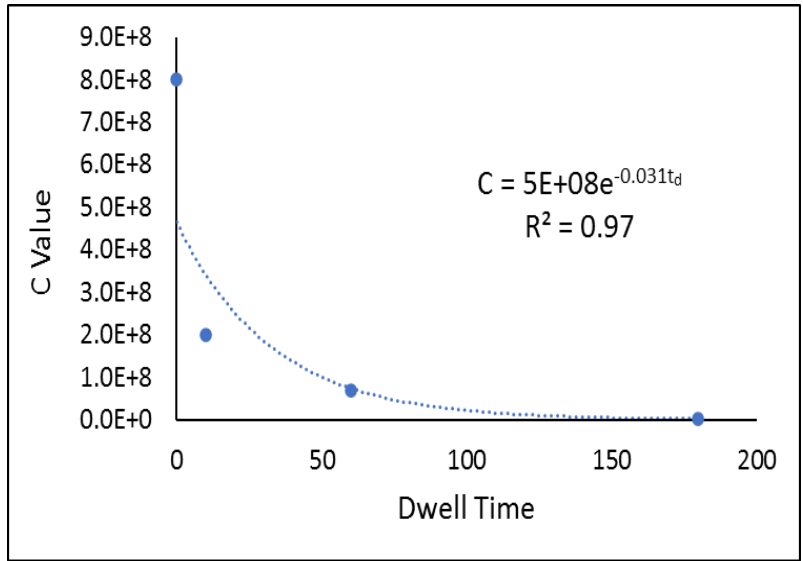


Figure 6.9: Constant (C) as a function of dwell time

From equation (2), the characteristic life is predicted as a function of stress amplitude and dwell time as shown in equation 6.3

$$N_{63} = 5 \cdot 10^8 \cdot e^{(-0.031t_d)} \cdot P^{-(-0.0075t_d + 4.5188)} \dots\dots\dots (6.3)$$

Where N_{63} is the characteristic life, P is the stress amplitude, t_d is the dwell time. To find out the general reliability model of solder joints as a function of dwell time, parameters in equation (1) must be determined. In our case, there is no observed trend for the shape parameter of the Weibull plot at different dwell times and stress amplitudes. The shape parameter values were found between 3.5 and 14 with an average of 6.66. For the scale parameter (θ); the finding of characteristic life from equation (6.3) is substituted in equation (6.1). As a result, the general reliability model as a function of dwell time is established as shown in equation (6.4)

$$R(t) = e^{-\left(\frac{t}{5 \cdot 10^8 \cdot e^{-(0.03 \cdot t_d)} \cdot P^{(0.0075 \cdot t_d + 4.5188)}}\right)^{6.66}} \dots \dots \dots (6.4)$$

6.3.2 Stress-Strain Loops Analysis

Stress-strain loop or Hysteresis loop is essential to determine the damage parameters for each cycle represented by the inelastic work and plastic strain per cycle. These parameters are directly related to the accumulated damage through the life of the joint. The loop area represents the inelastic (damage) work per cycle where its width along x-axis represents plastic strain. In this section, the evolution in hysteresis loops at all testing combination of mechanical fatigue and combined creep-fatigue tests is demonstrated and evaluated. Also, damage work due to creep effect is quantified by subtracting the inelastic work per cycle for a certain combined test from the corresponding one with mechanical fatigue without dwelling. Its justified that creep and stress-relaxation effects are negligible during the mechanical fatigue only test due to the fast ramp rate which prevent creep damage to occur. Results for the accumulated work, average work per cycle and plastic strain are plotted and explained briefly in the last part of this section.

Figure 6.10 shows the average hysteresis loops for joints cycled with various stress levels at no dwelling. Both inelastic work (area inside the loop) and the plastic strain are obviously increased with higher stress amplitude.

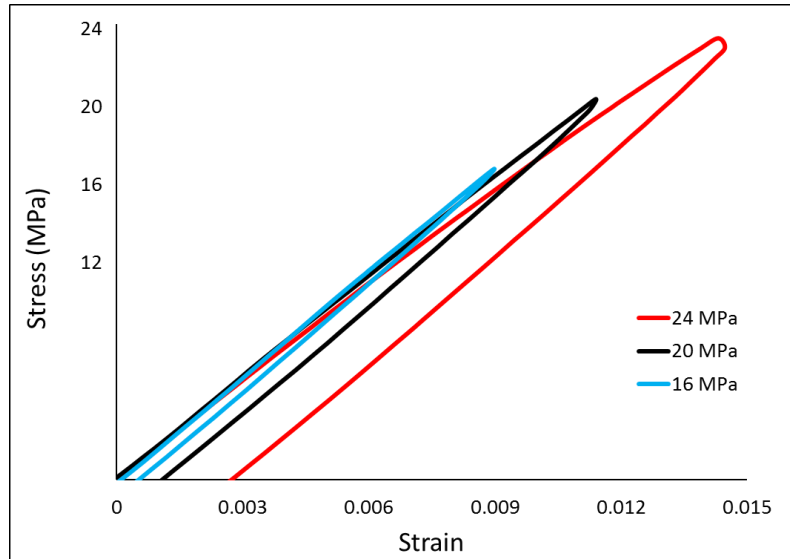


Figure 6.10: The hysteresis loops for SAC305 joints cycled with different stress amplitudes at no dwelling

In Figures 6.11 to 6.13, average hysteresis loops are generated for various dwelling periods. At specific dwelling, the same trend is observed; the hysteresis loop is enlarged drastically at higher stress levels. Moreover, more stress-relaxation is noticed with higher stress magnitudes. The enlargement of hysteresis loops is due to a massive increase in accumulated damaged work due to the creep effect in addition to fatigue damage. Consequently, evolution in hysteresis loops is generated for various dwelling times at certain stress levels, as shown in Figures 6.14 to 6.16. Similar behavior is noticed for the plastic strain parameter. The higher stress or more prolonged dwelling would cause more plastic strain to be accumulated at a particular dwelling or stress levels,

respectively. Figures 6.17 (a, b, c) show full hysteresis loops for joints cycled at various stress levels at fixed dwellings (no dwelling and 10s dwelling).

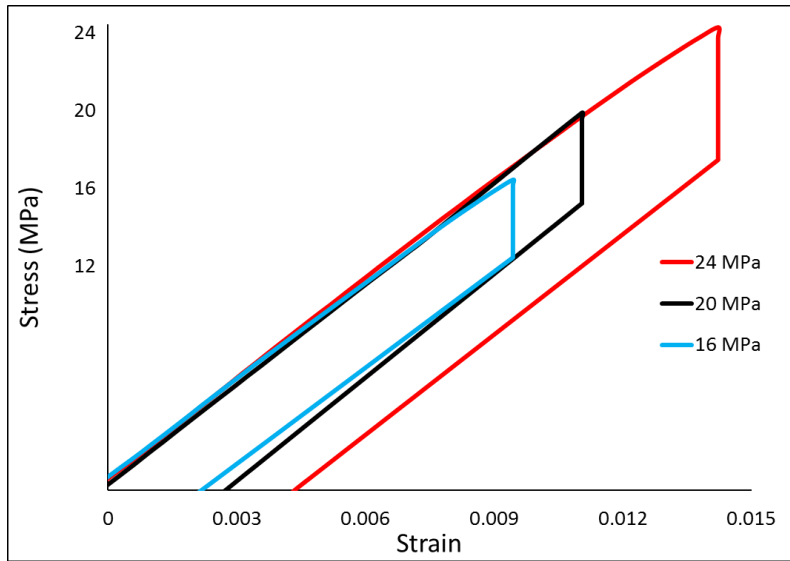


Figure 6.11: The hysteresis loops for SAC305 joints cycled with different stress amplitudes at 10s dwelling

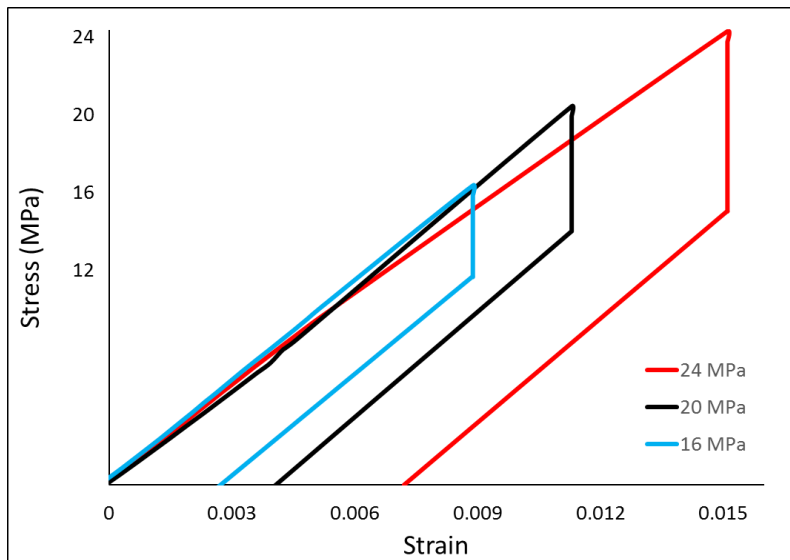


Figure 6.12: The hysteresis loops for SAC305 joints cycled with different stress amplitudes at 60s dwelling

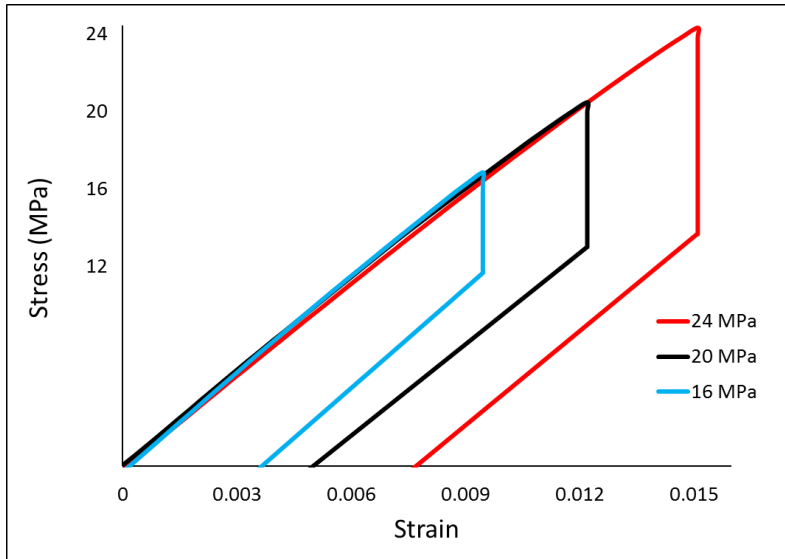


Figure 6.13: The hysteresis loops for SAC305 joints cycled with different stress amplitudes at 180s dwelling

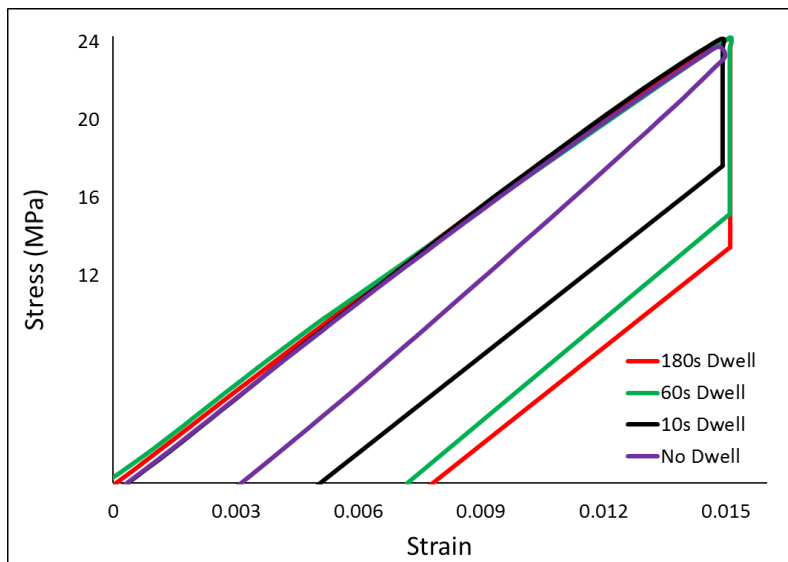


Figure 6.14: The hysteresis loops for SAC305 joints cycled at various dwellings with 24 MPa stress level

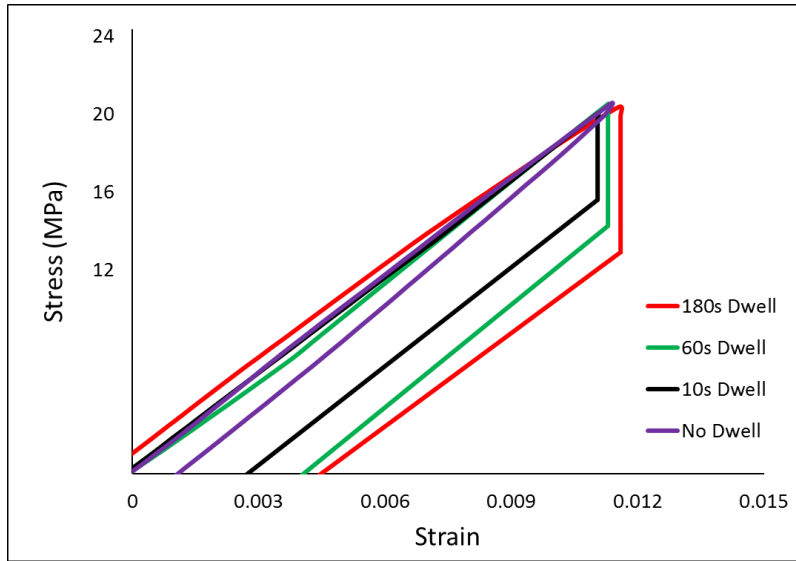


Figure 6.15: The hysteresis loops for SAC305 joints cycled at various dwellings with 20 MPa stress level

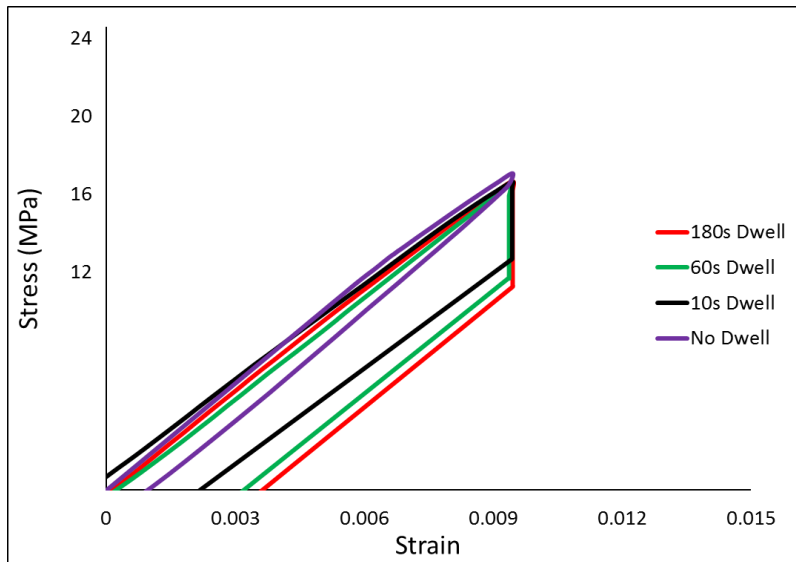


Figure 6.16: The hysteresis loops for SAC305 joints cycled at various dwellings with 16 MPa stress level

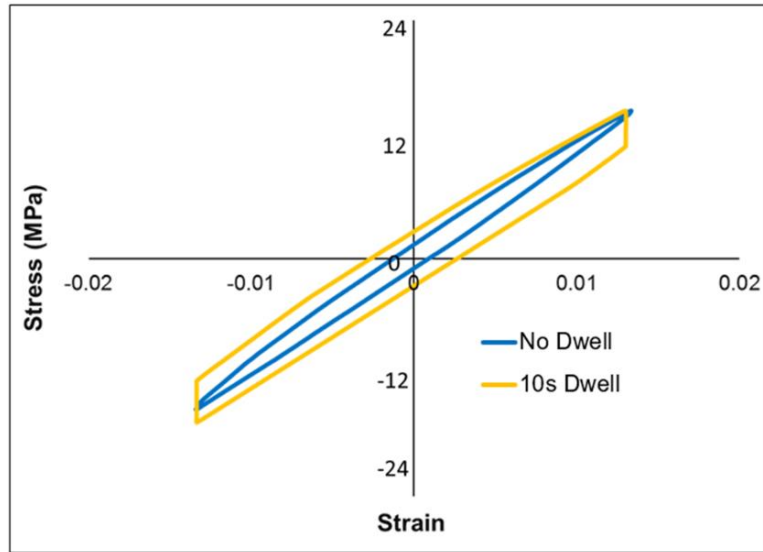


Figure 6.17 a: Hysteresis loops; with no dwelling (pure fatigue) and with 10s dwelling (including both creep& fatigue) cycled at 16 MPa.

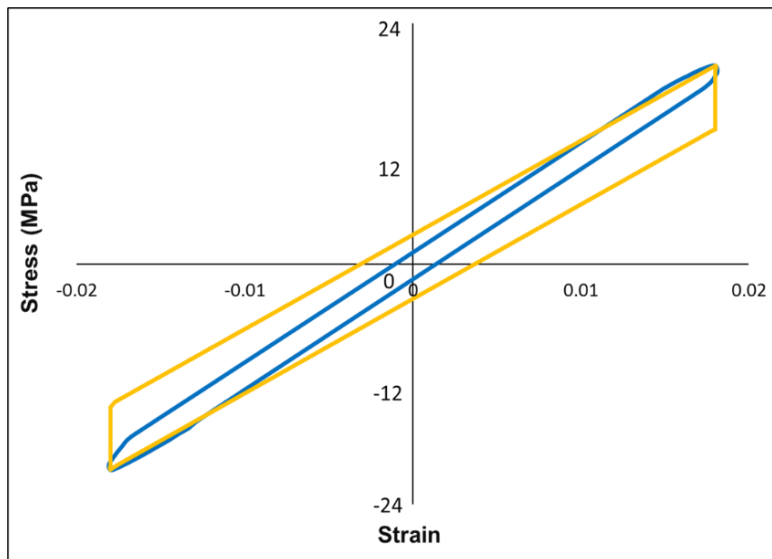


Figure 6.17 b: Hysteresis loops; with no dwelling (pure fatigue) and with 10s dwelling (including both creep& fatigue) cycled at 20 MPa.

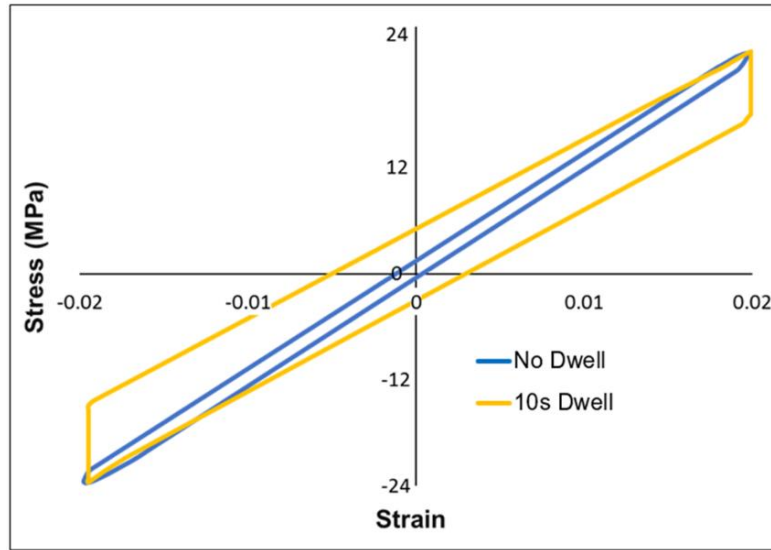


Figure 6.17 c: Hysteresis loops; with no dwelling (pure fatigue) and with 10s dwelling (including both creep& fatigue) cycled at 24 MPa.

The evolution in the hysteresis loop is directly related to the damage parameters; inelastic work, and plastic strain per cycle. Therefore, it is essential to examine the progression of such parameters during the joint lifetime to explain the evolvement of stress-strain loops. Figure 6.18 represents the typical development of inelastic work during the joint's life. This would provide an understanding of such behavior. The evolution is divided into three regions; the first region is the strain hardening, and it lasts for a few cycles. The second region includes the constant or steady-state region, which represents most of the joint life. The last phase is the crack initiation and propagation. The same behavior is noticed for all combinations of dwellings and stress levels, as shown in Figures 6.19 to 6.22.

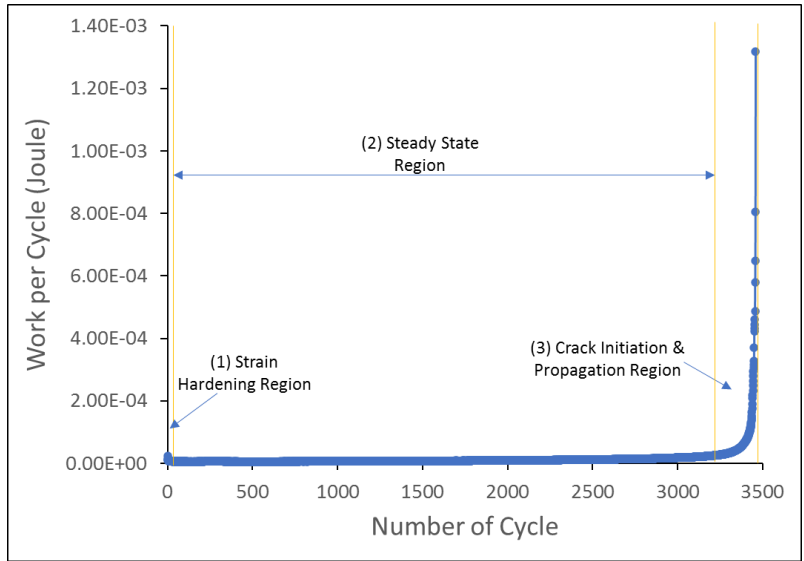


Figure 6.18: Inelastic work vs. the number of cycles for SAC305 solder joints cycled at 16 MPa stress amplitude until failure

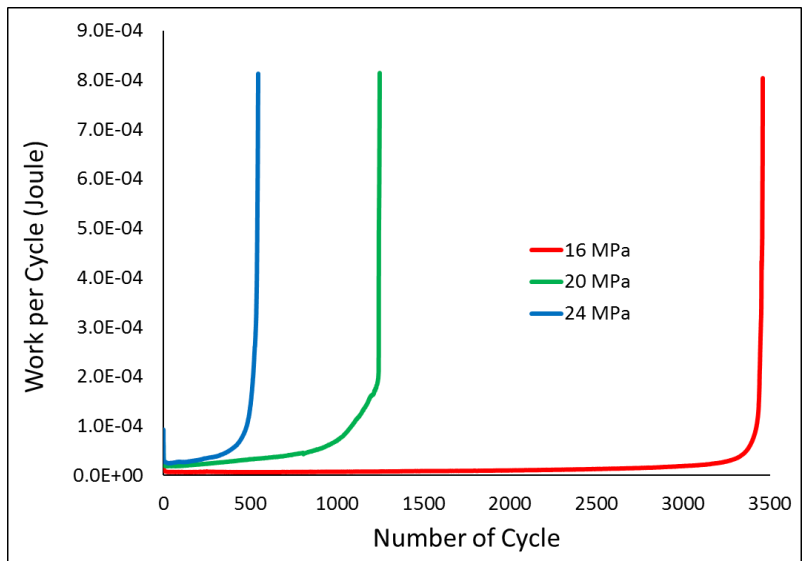


Figure 6.19: Inelastic work vs. the number of cycles for SAC305 solder joints cycled at various stress amplitudes at no dwelling until failure

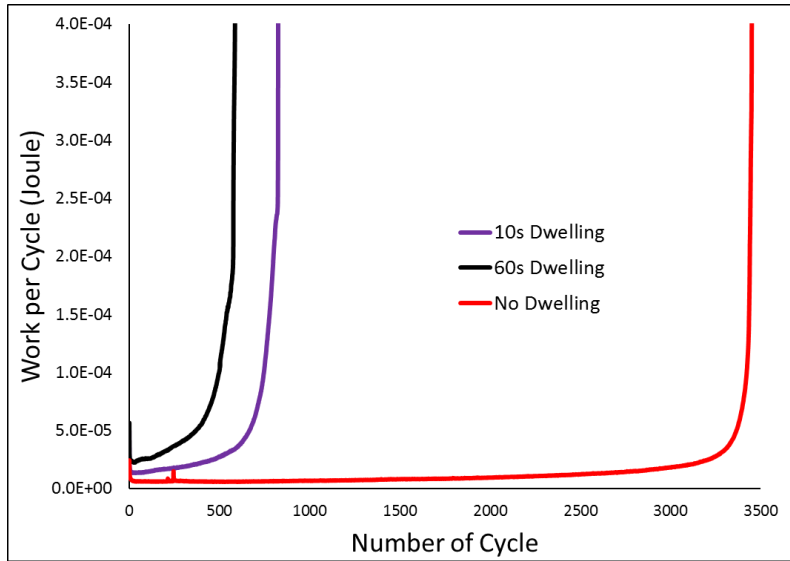


Figure 6.20: Inelastic work vs. the number of cycles for SAC305 solder joints cycled at 16 MPa stress amplitudes at various dwelling until failure

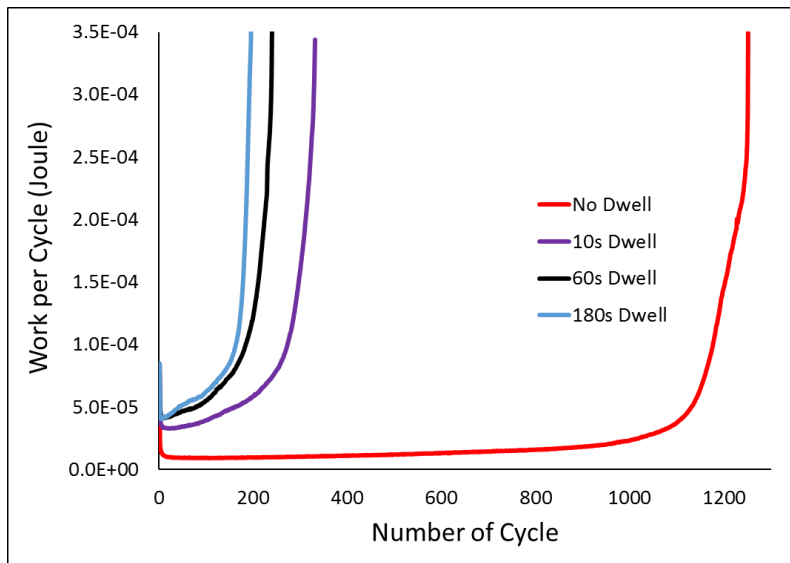


Figure 6.21: Inelastic work vs. the number of cycles for SAC305 solder joints cycled at 20 MPa stress amplitudes at various dwelling until failure

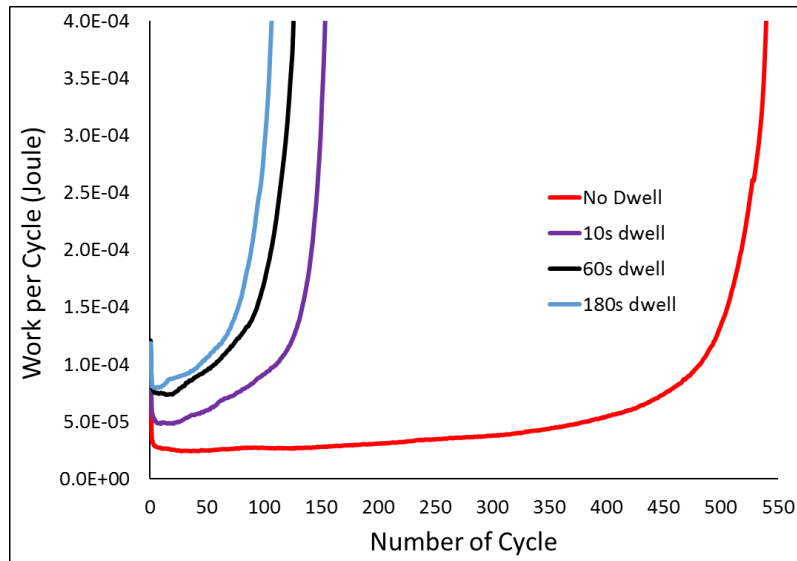


Figure 6.22: Inelastic work vs. the number of cycles for SAC305 solder joints cycled at 24 MPa stress amplitudes at various dwelling until failure

Creep Effect

In this study, the creep effect is demonstrated by evaluating the damaged work per cycle and compare it for both conditions of no and 10s of dwelling. At no dwelling conditions, the damaged work is related to cyclic fatigue only since the only effect is mechanical fatigue. The creep effect is considered negligible due to the fast ramp rate employed. This would not allow a considerable creep effect to take place between ramps. However, the damage due to creep is dominant during the dwelling, and the damage due to fatigue is acquired between ramps in the case of a combined creep-fatigue test. According to above, it is assumed that inelastic (damaged) work is caused by fatigue only in the cyclic fatigue test with no dwelling, and inelastic (damaged) work due to creep-fatigue is generated due to combined effects of creep-fatigue at dwelling conditions. Consequently, the damaged work due to creep is determined approximately by subtracting damage due to fatigue only (at no dwelling) from the one generated in the dwelling experiment. Figure 6.23, for example, shows the hysteresis loops for both conditions of no dwelling (green colored) and with 10s of

dwelling (yellow colored) in addition to bar chart summarizing the damaged work generated for both cases. For more clarification, the damaged work due to fatigue is colored as green in the bar graph, and the damage due to creep is added accordingly for each case with more extended dwelling periods. Results show that work due to creep is increasing with longer dwelling times, where the related damage on a life reduction basis is reflected obviously. Despite the amount of inelastic work due to creep almost similar to fatigue in the case of 10s dwelling, but the reflection on life reduction is massive by reducing life by a factor of 3. Same trends are shown in Figures 6.24 and 6.25 for other stress levels with higher damaged work is noticed due to more damaged created due to higher stress.

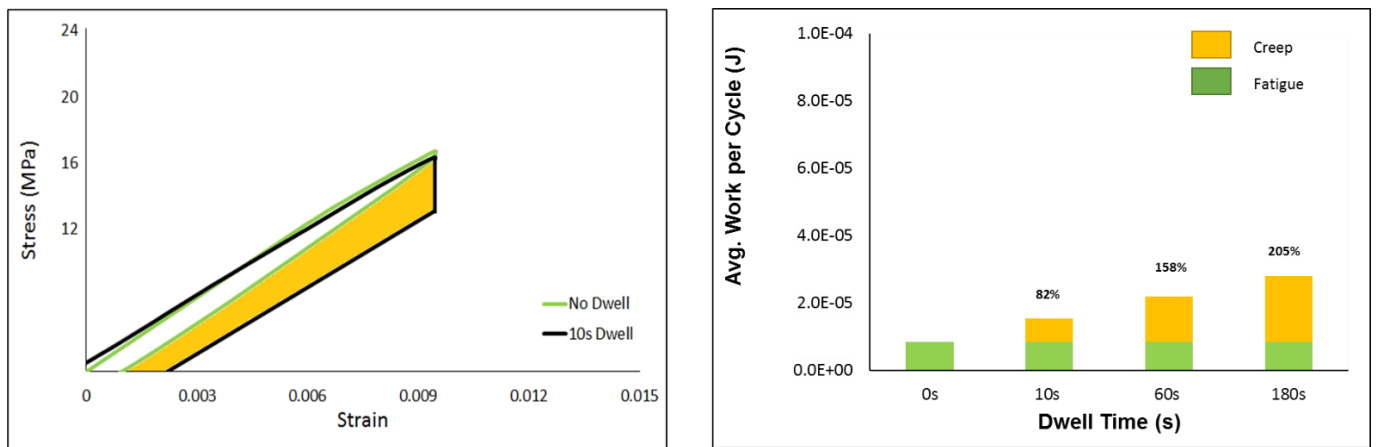


Figure 6.23: Hysteresis loops (right) with no dwelling and with 10s dwelling cycled at 16 MPa, and bar chart for average inelastic work for both cases

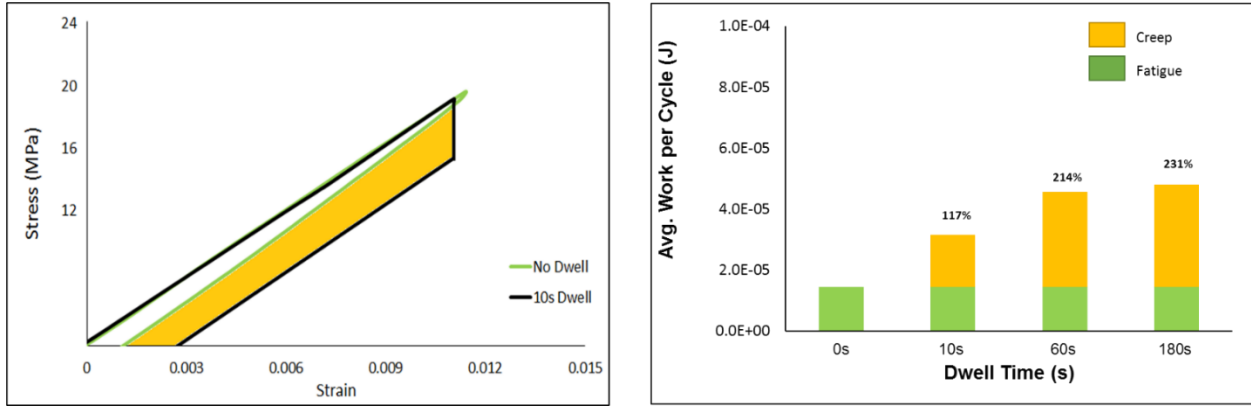


Figure 6.24: Hysteresis loops (right) with no dwelling and with 10s dwelling cycled at 20MPa, and bar chart for average inelastic work for both cases

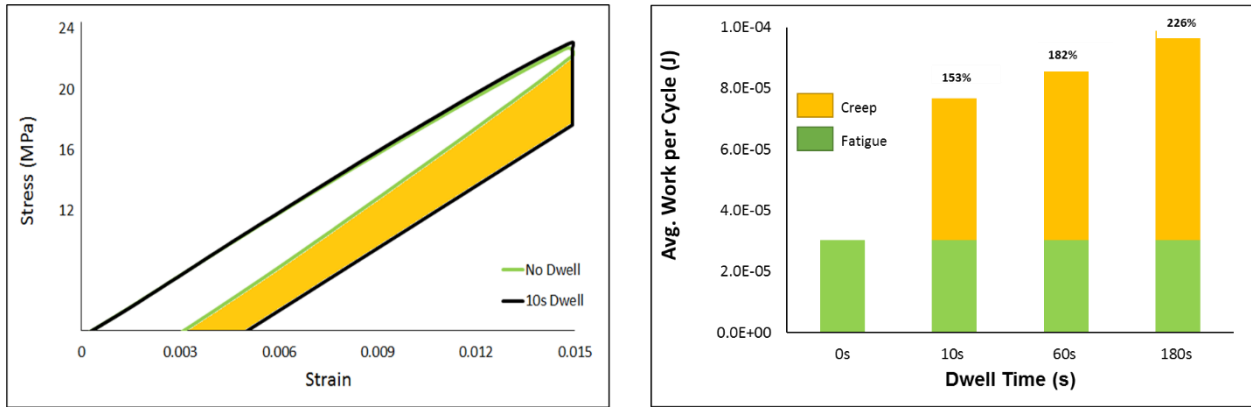


Figure 6.25: Hysteresis loops (right) with no dwelling and with 10s dwelling cycled at 20MPa, and bar chart for average inelastic work for both cases

Figure 6.26 illustrates the average accumulated work until complete failure for SAC305 joints as a function of the dwell times time for different stress levels. For a certain stress level, it is noticed that increasing dwelling periods generates lower accumulated work until complete failure. This can be explained by the less amount of cycles observed until complete failure for extended dwellings which accompanied with less accumulated work. Accumulated work includes other

types than the damaged or plastic work, which might be work due to friction or generated heat accompanied with each cycle.

The trend is different during the dwellings. At no dwell, 10s and 60s of dwellings, the lower the stress level generates more accumulated work than higher stress ones due to the significant additional cycles (accompanied with more accumulated work) observed until complete failure. On the other hand, the non-significant difference in the number of cycles until complete failure at 16MPa stress level compared to the other stress levels of 20 and 24MPa causes to have less accumulated work at 180s of dwelling. Also, the number of cycles until complete failure for 20 and 24MPa are close together, but more accumulated work is generated in the case of 24MPa due to the higher average damage work during the 180s. That is why it shows more accumulated damage work in case of 24 MPa.

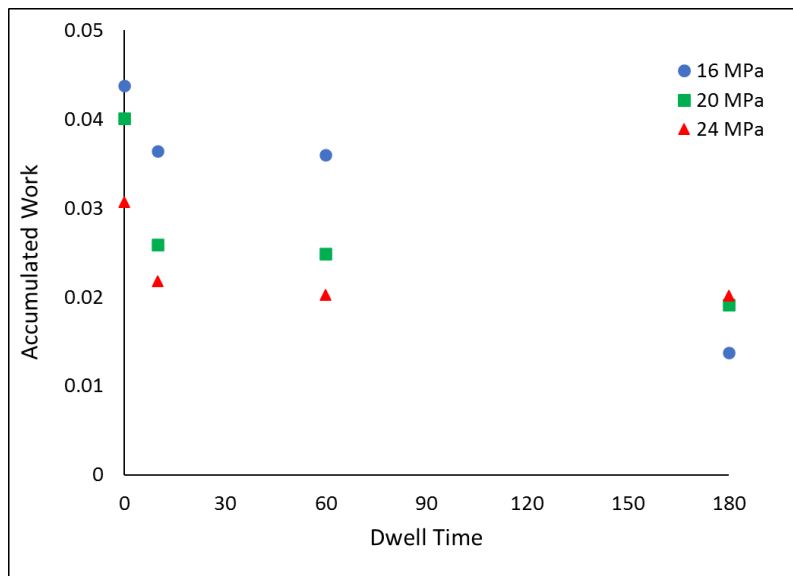


Figure 6.26: Accumulated work until complete failure vs. dwell time at different stress amplitudes

Figures 6.27 and 6.28 illustrate the average inelastic work per cycle and plastic strain as a function of dwell time, respectively. Both, the average work per cycle and the plastic strain observed to increase with higher stress levels at specific dwellings drastically. This can be explained by the more damage accumulated with higher stress levels at fixed dwelling and generates more inelastic work and plastic strain. Also, the longer dwelling would produce more inelastic work and plastic strain at a specific stress level. This is due to creep damage accumulated with extended dwellings. However, the creep effect might be substantial on both quantities of inelastic work and plastic strain compared to the stress level. In many cases, inelastic work and plastic strain are higher at lower stress levels with longer dwellings than higher stress amplitude with shorter dwell time.

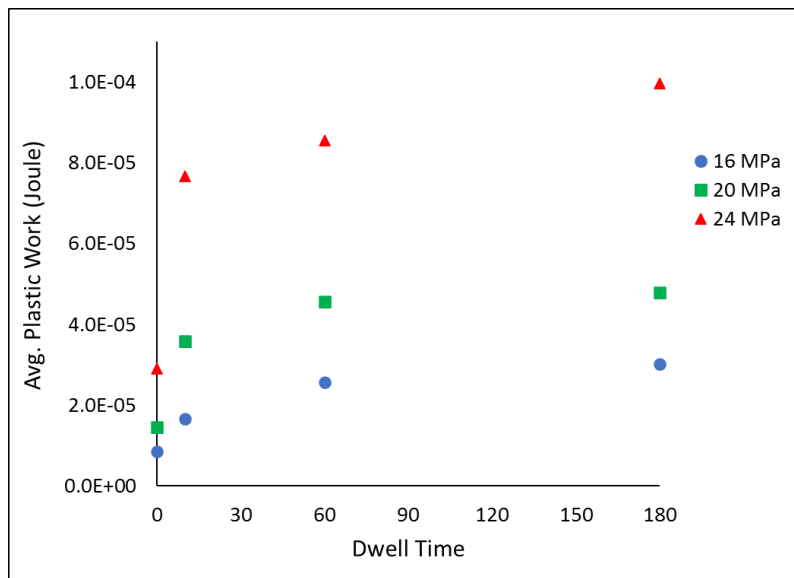


Figure 27: Average Work per Cycle as a function of dwelling times at various stress levels

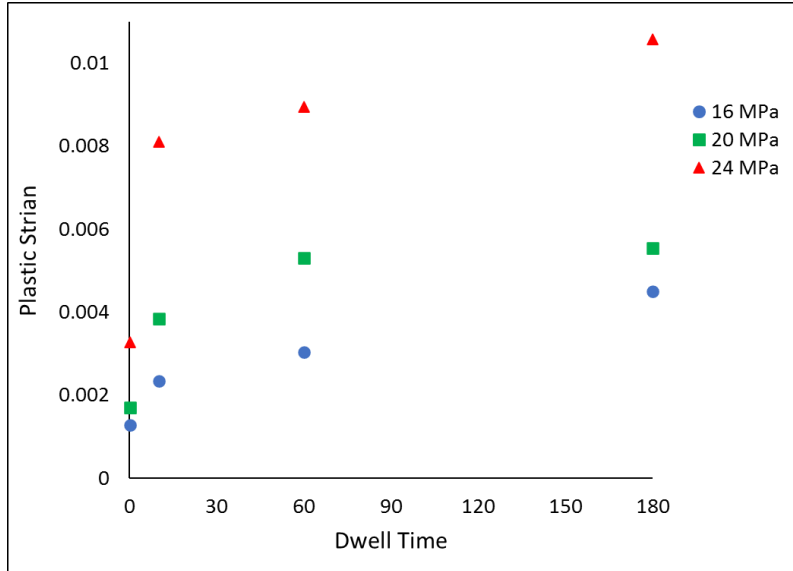


Figure 28: Plastic strain per Cycle as a function of dwelling times at various stress levels

6.3.3 The Coffin-Manson and Morrow Energy Models

Coffin-Manson and Morrow Energy are the most common models to predict the fatigue life as a function of plastic strain and inelastic work, respectively. Typical increment trend is observed in plastic strain and inelastic work with higher stress magnitude or longer dwell time. A general reliability model is established accordingly as a function of either plastic strain or inelastic work if a correlation is demonstrated.

Coffin-Manson Model

Figure 6.29 describes the plastic strain as a function of dwell time. It is clearly shown that there is a trend of plastic strain as a function of dwell time at various stress amplitudes. With high R-square for all curves, data are fitted to a power equation so the plastic strains can be predicted as a function of dwell time according to equation (6.5).

$$\gamma = D * t_d^{0.119} \dots\dots\dots (6.5)$$

Where γ is the plastic strain, D is constant, t_d is the dwell time. The D-value could be also formulated as a function of stress amplitude according to Figure 6.30. Thus, equation 6 can be expressed as shown in equation (6.6).

$$\gamma = 0.0003e^{0.1248 P} * t_d^{0.119} \dots\dots\dots(6.6)$$

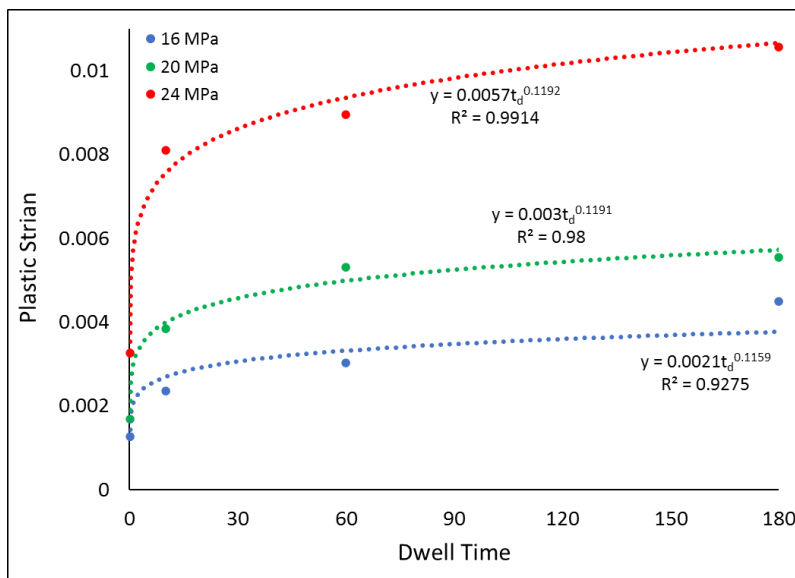


Figure 6.29: Plastic strain per Cycle as a function of dwelling times curves at various stress levels

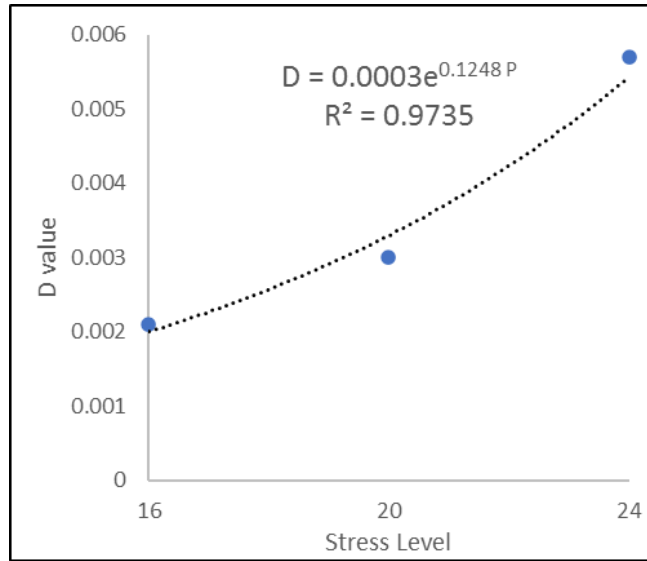


Figure 6.30: D-value as a function of stress amplitude

Coffin Manson is one of the most common models employed for fatigue life prediction as a function of plastic strain. The correlation between the fatigue life and the plastic strain is illustrated in equation (6.7):

$$N_{63} = S^{\frac{1}{\alpha}} \gamma^{\frac{-1}{\alpha}} \dots\dots\dots (6.7)$$

Where N_{63} is the characteristic fatigue life, γ is the fatigue ductility coefficient, S is the plastic strain, and α is the fatigue exponent. Based on the Coffin-Manson equation, the general reliability model as a function of plastic strain could be developed under certain conditions. If there is no clear trend for the coefficient of fatigue ductility (γ) and the fatigue exponent (α) at various dwellings, this implies that dwelling does not affect the Coffin-Manson equation. Also, data points for all conditions should have a similar trend (slope) to be fitted to a global Coffin-Manson equation no matter what the dwelling time is. To establish such a model; the characteristic life as a function of plastic strain (Eq. 6.7) must be obtained. Then, the new equation is substituted in Eq. 6.1 to obtain the reliability model.

To examine the model applicability in our case, the stated above conditions must be checked. Figure 6.31 demonstrates the characteristic life as a function of plastic strain for various dwelling periods. Data points have the same trend (slope) and could be fitted to a global Coffin-Manson equation. The values for Coffin-Manson equation constants at various dwellings are generated accordingly, as shown in Table 6.2. It is obviously shown that there is no clear trend in these constants regardless of the dwelling time. This means dwelling has no effect on the Coffin-Manson model, and a general model could be developed. The values of the Coefficient of fatigue ductility (γ) and the Fatigue exponent (α) for the global equation are 0.19 and 0.646, respectively. Moreover, the global Coffin-Manson model is illustrated as shown in Figure 6.32.

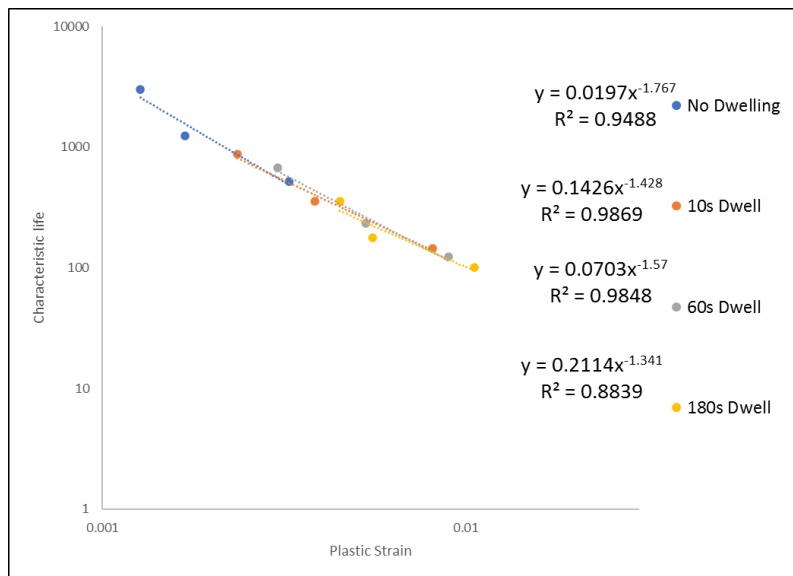


Figure 6.31: Characteristic life vs. plastic strain for SAC305 joints at various dwelling times on a log-log scale.

Table 6.2: Fatigue ductility coefficient and fatigue exponent of the Coffin-Manson model

Dwelling time	Fatigue ductility (C)	The fatigue exponent (m)
0	0.108	0.565
10	0.255	0.7
60	0.185	0.636
180	0.313	0.745
Global	0.19	0.646

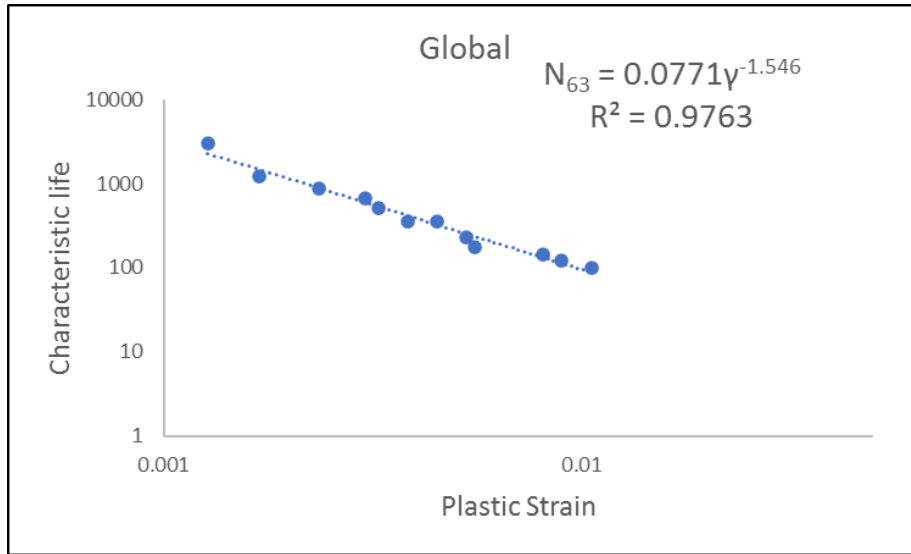


Figure 6.32: Characteristic life (Global Coffin-Manson equation) vs. plastic strain for SAC305 joints at various dwelling times on a log-log scale.

Finally, the characteristic life equation as a function of plastic strain (Eq.6.7) must be obtained and substituted in the reliability equation (Eq.6.1) to develop the reliability model as a function of plastic strain. The characteristic life as a function of plastic strain is obtained from Figure 6.32 as shown in equation (6.8):

$$N_{63} = 0.0771\gamma^{-1.546} \dots\dots\dots(6.8)$$

Substituting equation 6 in the reliability equation (Eq.6.1) and considering the average shape parameter for all combinations as the defined shape parameter, the general reliability model is developed as shown in equation (6.8)

$$R(t) = e^{-\left(\frac{t}{0.0771 * \gamma^{-1.456}}\right)^{6.66}} \dots\dots\dots(6.8)$$

Where γ is the Plastic Strain, t is the number of cycles.

Morrow Energy Model

Inelastic work is another parameter considered to measure the damage, where Morrow Energy equation is the common related model. Figure 6.33 illustrates the inelastic work as a function of dwell time for various stress levels. It shows a trend in inelastic work as a function of dwell time at various stress amplitudes. With high R-square for all curves, data are fitted to a power equation, so the inelastic work is predicted as a function of dwell time according to equation (6.9)

$$W = D * t_d^{0.12} \dots\dots\dots(6.9)$$

Where W is the inelastic work, D is constant, t_d is the dwell time. On the other hand, the D -value could be also formulated as a function of stress amplitude according to Figure 6.34. Thus, equation 6.9 can be expressed as shown in equation (6.10)

$$W = (-5.0^{-6} * P - 7^{-05}) t_d^{0.12} \dots\dots\dots(6.10)$$

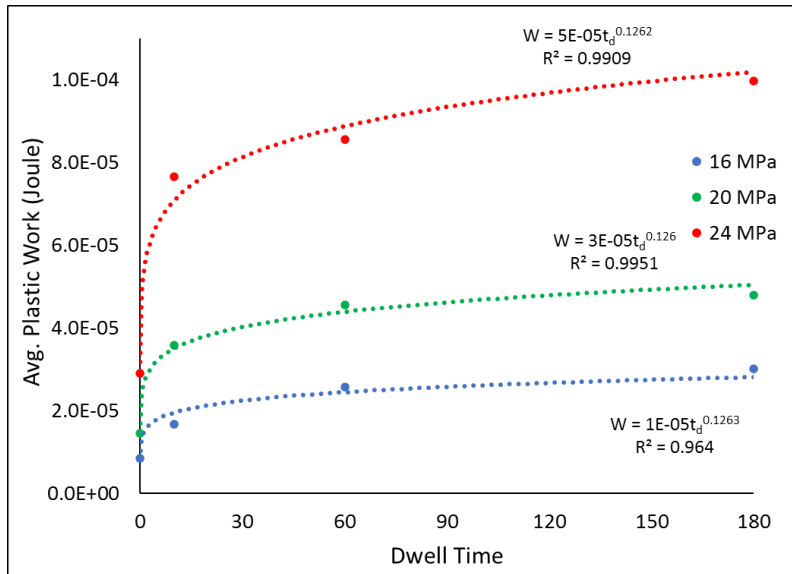


Figure 6.33: Inelastic work per Cycle as a function of dwelling times curves at various stress levels

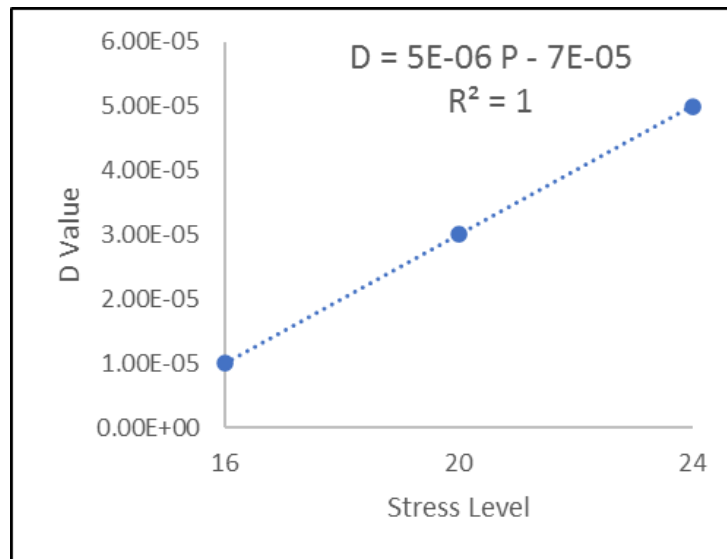


Figure 6.34: D-value as a function of stress amplitude

Morrow Energy is a common model used to predict the life as a function of inelastic work as shown in equation 6.11

$$N_{63} = C_m^{\frac{1}{m}} W_m^{-\frac{1}{m}} \dots\dots\dots (6.11)$$

Where N_{63} is the characteristic fatigue life, C is the fatigue ductility coefficient, W is the inelastic work, and m is the fatigue exponent. In the same way with the Coffin-Manson model, the reliability model as a function of inelastic work based on the Morrow Energy model could be established under similar circumstances defined above. Our data show that fatigue ductility and fatigue exponent have no clear trend at various dwellings, as shown in Figure 6.35. Furthermore, the data points on a log-log scale demonstrate to have a similar trend (slope) and could be fitted to the global Morrow Energy equation. The fatigue ductility and the fatigue exponent constants for all dwellings are specified accordingly, as shown in Table 6.3. It is obviously shown that there is no clear trend in these constants regardless of the dwelling time. This means dwelling has no effect on the Morrow Energy model, and the global model could be developed. Figure 6.36 shows the global model for Morrow Energy equation considering that the global constants for Fatigue ductility coefficient and fatigue exponent are 0.0025 and 0.737, respectively.

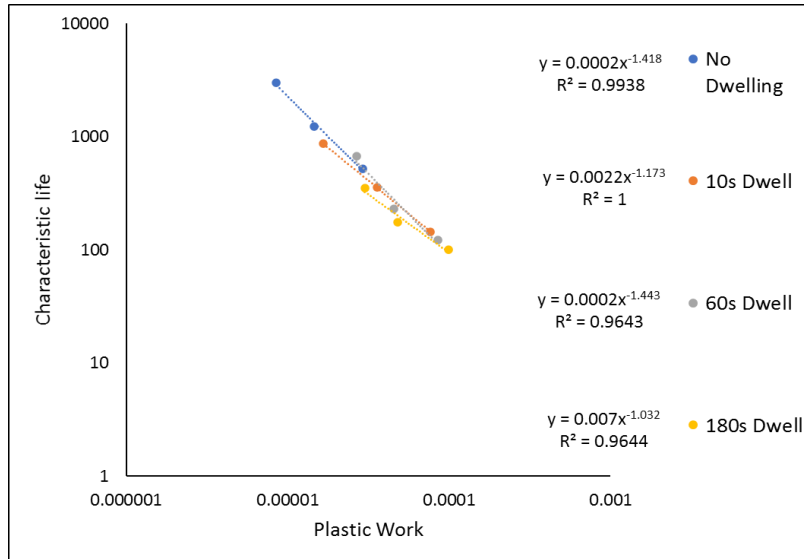


Figure 6.35: Characteristic life vs. inelastic work for SAC305 joints at various dwelling times on a log-log scale.

Table 6.3: Fatigue ductility coefficient and fatigue exponent of the Morrow Energy model

Dwelling Time	Fatigue Ductility (C)	The Fatigue Exponent (m)
0	0.0023	0.713
10	0.0055	0.85
60	0.0028	0.69
180	0.0085	0.96
Global	0.0025	0.737

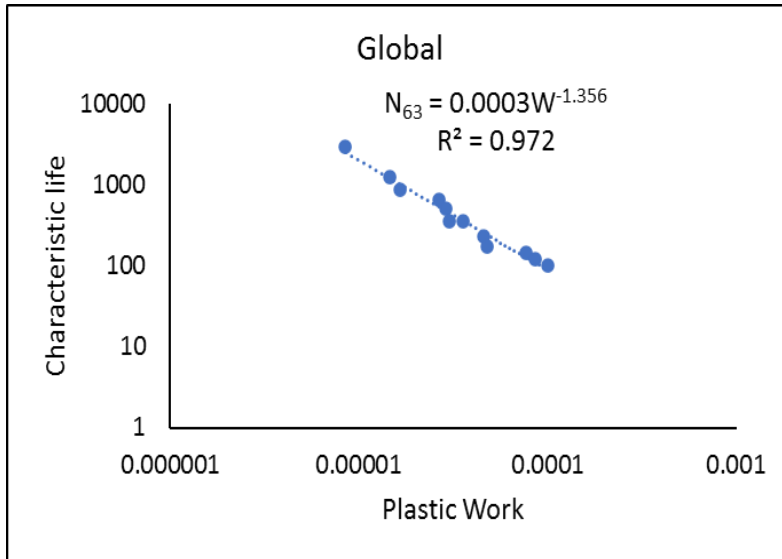


Figure 6.36: Characteristic life (Global Morrow Energy equation) vs. plastic work for SAC305 joints at various dwelling times on a log-log scale.

To generate the reliability model (Eq.6.1) as a function of inelastic work, the characteristic life equation as a function of plastic work (Eq.6.11) must be attained. Therefore, the characteristic life as a function of plastic work is developed from Figure 6.36 as shown in equation (6.12):

$$N_{63} = 0.0003W^{-1.356} \dots \dots \dots (6.12)$$

Finally, substituting equation 6.12 in the reliability equation (Eq.6.1) and considering the average shape parameter for all combinations as the defined shape parameter, the general reliability model is developed as shown in equation (6.13)

$$R(t) = e^{-\left(\frac{t}{0.0003*W^{-1.356}}\right)^{6.66}} \dots \dots \dots (6.13)$$

Where W is the Plastic work, t is the number of cycles.

6.4 Microstructure Analysis

The failure mode for samples at room temperature was determined by studying SEM images for tested joints after various dwelling times. This would provide an idea about the effect of dwelling on material evolution under various dwelling periods. Results show that failure is located within the bulk region among all cases of fatigue and creep-fatigue tests.

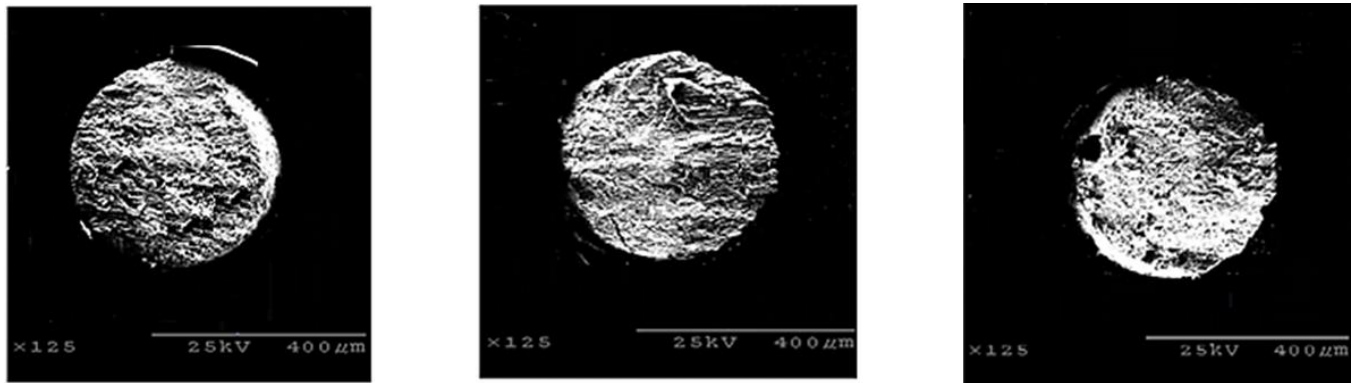


Figure 6.37: SEM images for tested joints under various dwelling periods compared to no dwelling condition (most left)

6.5 Summary

In this study, two-parameter Weibull plots were generated for each testing combination of dwell time and stress amplitude. Obvious relation is observed between accumulated damage or damage in term of plastic strain and inelastic work and stress amplitude and dwell time. Damage due to creep is quantified based on damage parameters values between corresponding testing conditions. Common formulas and models represented by Weibull distribution, stress-life equation, Coffin-Manson model, and Morrow Energy model are used to develop general reliability models. Reliability models were established as a function of dwellings, stress magnitude, plastic strain, and inelastic work per cycle to illustrate the behavior of individual SAC305 solder joints through its

fatigue life under accelerated conditions. Characteristic life (scale parameter) is the base of this work, and its extracted from the Weibull plots. However, the shape parameter is valued by averaging the values of shape parameters among corresponding tests since there was no defined pattern. Both Coffin-Manson and Morrow Energy models demonstrate robustness in assessing the characteristic life. Therefore, the reliability distribution of the solder joint can be predicted as a function of the plastic strain and inelastic work regardless of the dwell time.

Chapter 7: The Degradation Modeling of SAC305 Individual Solder Joints During Creep-Fatigue Loadings at Various Temperatures

7.1 Introduction

Thermal cycling is considered as a main cause of electronics failures among other triggers specially in harsh applications. It is characterized by multiple switching between on-off cycles of electronic devices in addition to exposure to elevated temperatures from surroundings. Solder joints are subjected to thermomechanical stresses due to the mismatch in the coefficients of thermal expansion (CTE) between printed circuit board and the component. Joint's behavior under thermal cycling is complicated and not very well-understood. It's primarily influenced by several factors of creep, fatigue, and combination of them. Creep is dominant during dwellings while fatigue is dominant between ramps. Creep is majorly activated at elevated temperature and this was the prime mover for this study.

The reliability of solder joints under both effects of both creep and fatigue at various elevated temperatures is investigated. Accelerated shear fatigue and combined creep-fatigue tests are utilized in this study. Effects of stress amplitude, dwell time, and temperature are explored. Each testing condition includes testing SAC305 individual solder joints with a certain stress magnitude, under dwell period, and at defined testing temperature. Two-parameters Weibull distribution is generated to describe the fatigue life of solder joints for testing combinations. A general reliability model based on Stress-Life equation as a function of those parameters is established by utilizing empirical and Arrhenius models. Also, the damage accumulation is examined by exploring the evolution in hysteresis loops with its both damage parameters of inelastic work and plastic strain. Hysteresis loops for related combination are compared and assessed. The relation between plastic strain and inelastic work with dwell time and testing temperatures is demonstrated. Coffin-Manson

and Morrow Energy models are utilized to correlate between plastic strain and plastic work respectively with fatigue life. Finally, general reliability models as a function of plastic strain and plastic work are constructed.

7.2 Test Matrix

In this study, the test includes cycling individual SAC305 solder joints at multiple combinations of stress magnitude, dwell period, and temperature level. Testing parameters involves three stress magnitudes of 16, 20, and 24 MPa with various dwelling periods of 0, 10, 60, and 180s, and three levels of temperature of 25, 60, 100°C. There are some deviations from original plan occurred in this study. 5s of dwelling was excluded from the dwelling periods since it is considered as a short period of dwell. At the conditions of room temperature and above, there are two mechanisms stored during the holds which are creep deformation and anelastic recovery [22]. Further details are revealed in the previous study. Deformation is initiated by anelastic strain, anelastic recovery during the relaxation time, followed by creep deformation. Therefore, hold time of below 10s is short enough and retard the creep mechanisms to be the influential damage mechanisms.

The other issue is the testing temperature levels. Cold temperature of -40°C is designed to be included in this study. Chamber could not achieve such temperature and instead (-10°C) is its minimum limit. Not all testing replicates are performed and, unfortunately, the testing chamber was damaged and requires long period of time for repair according to the manufacturer. However, mechanical fatigue only tests with various stress levels of 16, 20, 24 MPa were implemented, interpreted, and compared to results of fatigue tests at room temperatures at the end of this study. Also, the maximum elevated temperature proposed to be included in this study is +125°C, where 75°C is chosen to be in between room temperature and +125°C for correlation purposes. However, the initial results for +125°C was not promising. Results showed that only few cycles (around five

only) were obtained when cycling joints under mechanical fatigue conditions at +125°C. Less than one cycle is obtained when cycled joints under combined test with dwelling periods. With such number of cycles, it would be illegitimate to include such results for comparison purposes with results from other conditions due to absenteeism of variability compared to the modified testing temperature of 100°C. Therefore, testing at 60°C as an intermediate temperature is replaced 75°C. Finally, all replicates at 25°C are repeated since new setup is used. Seven individual solder joints are tested at each combination. Table 7.1 shows the modified test matrix for this study.

Table 7.1: The Test Matrix for Studying the Effect of Creep and Fatigue on Individual SAC305

Solder Joints Reliability at Elevated Temperature

Testing Temperature	Stress Amplitude (MPa)	Fatigue Only Test	Creep-Fatigue Test		
		0s dwell	10s dwell	60s dwell	180s dwell
25°C	16 MPa	7 samples	7 samples	7 samples	7 samples
	20 MPa	7 samples	7 samples	7 samples	7 samples
	24 MPa	7 samples	7 samples	7 samples	7 samples
60°C	16 MPa	7 samples	7 samples	7 samples	7 samples
	20 MPa	7 samples	7 samples	7 samples	7 samples
	24 MPa	7 samples	7 samples	7 samples	7 samples
100°C	16 MPa	7 samples	7 samples	7 samples	7 samples
	20 MPa	7 samples	7 samples	7 samples	7 samples
	24 MPa	7 samples	7 samples	7 samples	7 samples

7.3 Results and Analysis

In this study, the reliability of SAC305 solder joints under various conditions of stress magnitudes, dwell times, and testing temperatures are explored. First, two parameters Weibull plots are generated for all testing conditions and combinations. This would help in assessing the effect of several parameters on joints reliability under various conditions. Also, a general empirical model is generated to describe the reliability as a function dwell time, stress level and testing temperature. The second part includes a detailed analysis of stress-strain loops. Hysteresis loops evolution for each set of conditions are investigated for comparison purposes. This involves the examination of both damage parameters of inelastic work and plastic strain. Evolution of inelastic work as a function of life is obtained and justified for all results. Finally, general reliability models as a function of inelastic work and plastic strain are evaluated based on Morrow Energy and Coffin-Manson Models, respectively.

7.3.1 Weibull Plots Analysis and Prediction Modeling

This section discusses initially the Weibull plots for certain testing parameter of various levels while others are fixed to assess the effect of that parameter on fatigue life reliability. Weibull distribution plots were constructed using Minitab Software for each stress level, considering the maximum likelihood estimation method as the parametric estimation method. Furthermore, the two-parameter Weibull equation is applied to demonstrate the degradation effect on joints reliability as shown in equation (7.1)

$$R(t) = e^{-\left(\frac{t}{\theta}\right)^\beta} \dots\dots\dots(7.1)$$

Where R(t) is the reliability at time t (the probability of not fail), t' is the time or number of cycles, θ is the scale parameter or characteristic life and β is the shape parameter.

Figure 7.1 shows the Weibull plot for SAC305 joints cycled with several stress levels at room temperature under no dwelling conditions or mechanical fatigue only test. Significant reduction in fatigue life is observed with increasing stress level while factors remains constant according to scale parameter or characteristic life results. Almost 75% drop in characteristic life is noticed when rising the cycling stress from 16 to 24 MPa. The reason behind that is related to the extra damage accumulated when cycling with higher stress levels compared to lower ones. Identical trend is observed under all various dwellings at room temperature. Furthermore, data were examined at elevated temperatures of 60 and 100°C where similar trend is observed. Fatigue life is reduced drastically (with almost same percentages of 75%) with higher stress level. Figures 7.2 and 7.3 illustrate a severe drop in characteristic life at higher stress level when cycling during no dwelling conditions at testing temperature of 60°C and 100°C, respectively.

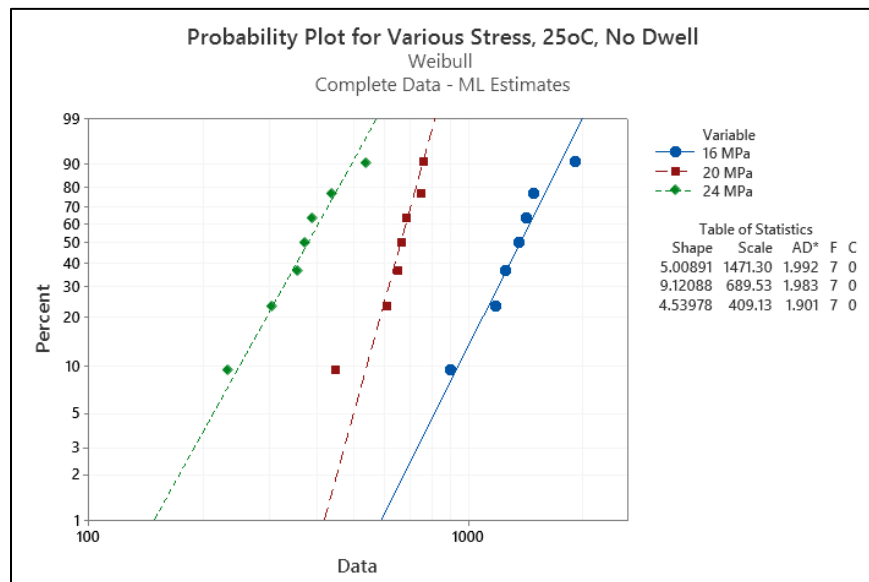


Figure 7.1: Weibull distributions for SAC305 joints cycled at different stress amplitudes under no dwelling at room temperature

The characteristic life characterizes the probability of failure with 63.2% among tested samples under certain conditions. Life-stress equation is one of the most common equation that describes the life as a function of stress amplitude. According to literature, characteristic life used to replace the averages of fatigue life results at certain condition in electronics. However, averages of fatigue life still utilized as well by some researchers. Equation 7.2 is the power equation used to describe the characteristic life as a function of stress amplitude as follows

$$N_{63} = C * P^{-n} \dots\dots\dots (7.2)$$

Where N_{63} is the characteristic life, P is cyclic stress value and C and n are the equation constants. The constant n (ductility index) shows the material ductility where higher n value means lower ductility. To interpret the life-stress relation, life as a function of stress amplitude is plotted and fitted to a power equation in a log-log scale as shown in Figure 7.4.

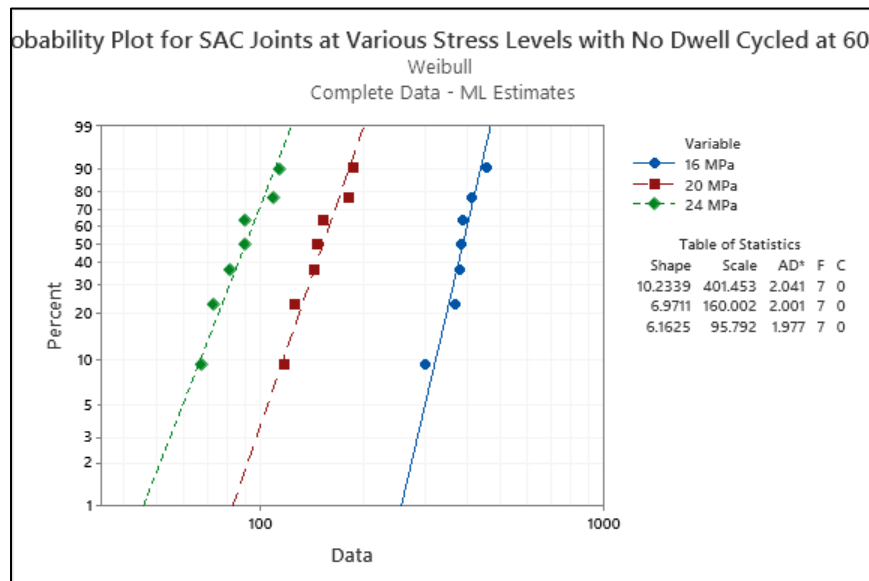


Figure 7.2: Weibull distributions for SAC305 joints cycled at different stress amplitudes under no dwelling at 60°C temperature

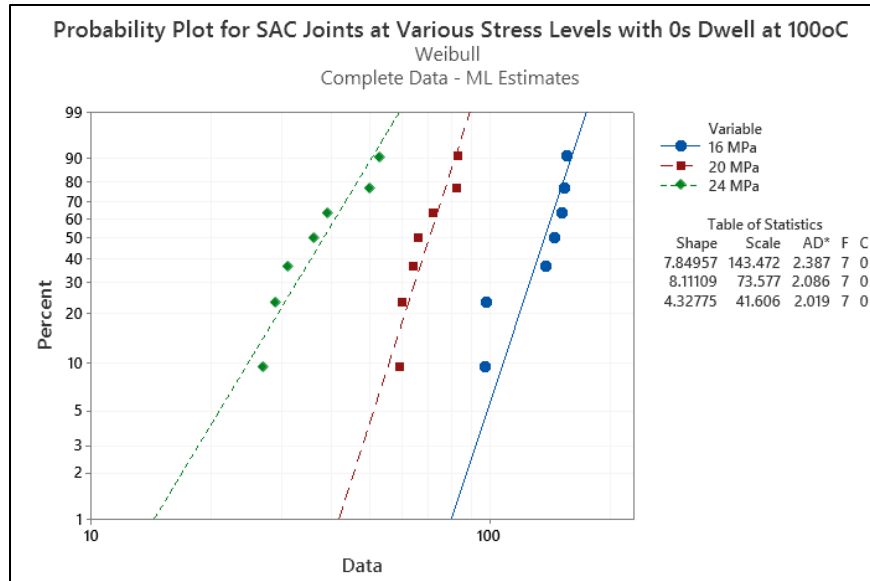


Figure 7.3: Weibull distributions for SAC305 joints cycled at different stress amplitudes under no dwelling at 100°C temperature

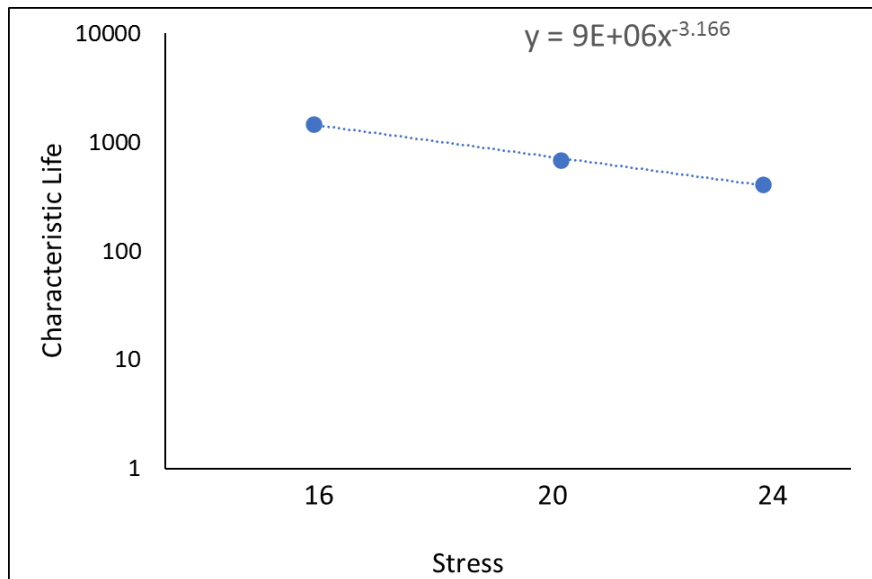


Figure 7.4: The relationship between the characteristic life and stress amplitude SAC305 solder joints in a log-log scale at no dwelling and room temperature

The second part is to investigate the effect of testing temperature while other parameters of dwell time and stress level are fixed. The general trend is that fatigue life is reduced substantially when switching the testing temperature from 25°C to 60°C. Also, drastic drop is still observed when switching between 60°C and 100°C at certain stress amplitude and dwell period in both cases. More damage due to creep is stored at higher temperature levels as creep is a main function of temperature. Room temperature is considered as elevated temperature since the homologous temperature is above 0.5 where creep is activated and keep increasing at higher levels. Figures 7.5 demonstrate such effect of temperature by comparing the characteristics life of joints in a combination of 10s of dwelling with 20MPa stress level as an example. Around 63% drop in fatigue life is noticed when increasing testing temperature between 25°C and 60°C, where almost same percentage of drop is noted between 60°C and 100°C.

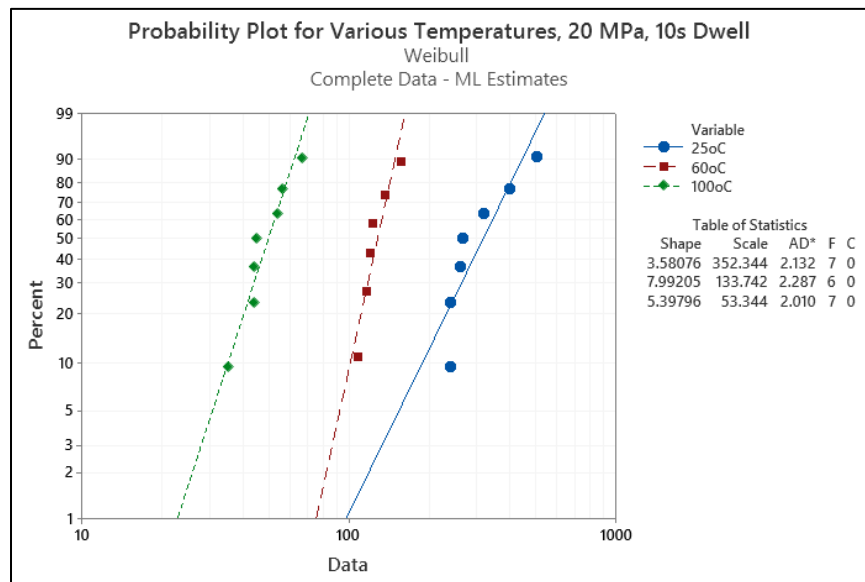


Figure 7.5: Weibull distributions for SAC305 joints cycled at different temperature levels with 10s of dwelling and 20 MPa stress level

The effect of various dwelling periods is the last parameter to be investigated while other parameters of temperature and stress level are fixed. It is concluded that cycling joints with longer dwellings would reduce the fatigue life specifically after 10s of dwelling compared to no dwell condition at defined stress level and testing temperature. Whereas this effect becomes less at longer dwellings beyond 10s as in 60s and 180s dwelling. The effect of dwelling is examined to be less at higher testing temperature even with longer dwelling periods. Damage due to creep effect is triggered at elevated temperature, and the effect of temperature becomes dominant compared to dwelling effect. Damage due to creep is stored during the dwelling period which causes the significant drop in life, while such effect becomes negligible but still exists after 180s of dwellings. Figures 7.10 and 7.11 illustrate the probability plots for joints cycled with several combinations of temperatures and stress levels under various dwellings. The combination includes distributions for joints cycled at 25°C with 20MPa, and 60°C with 24 MPa. A significant drop of almost 50% is noticed when cycling with longer dwelling time of 10s compared to no dwell condition, 40% when extending dwell time to 60s rather than 10s and reduced to around 15% when extending dwell time from 60s to 180s. However, the effect is elucidated to be less at higher testing temperature according to Figure 7.11. No drop more than 15% is observed among all dwelling times in the case of 100°C. All Weibull plots are listed in Appendix A.

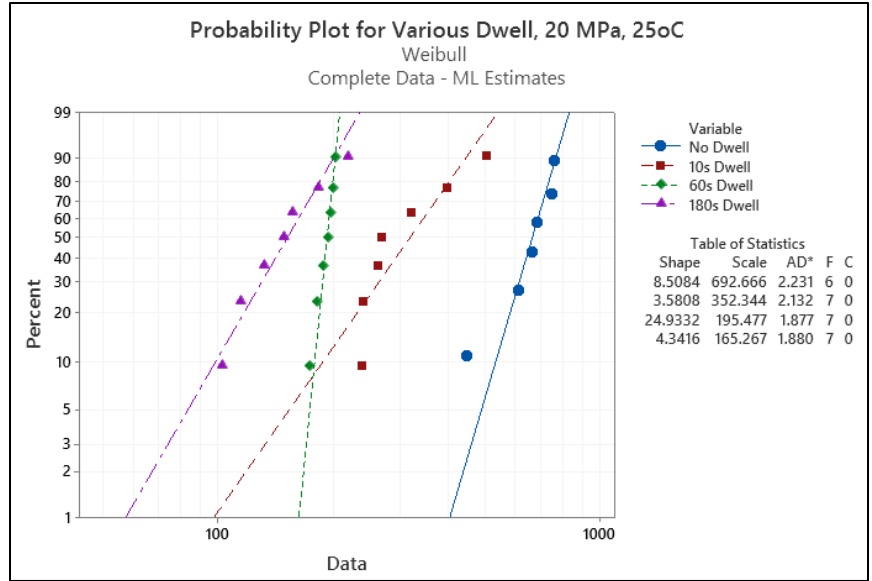


Figure 7.10: Weibull distributions for SAC305 joints cycled with different dwellings at 25°C and 20 MPa stress level

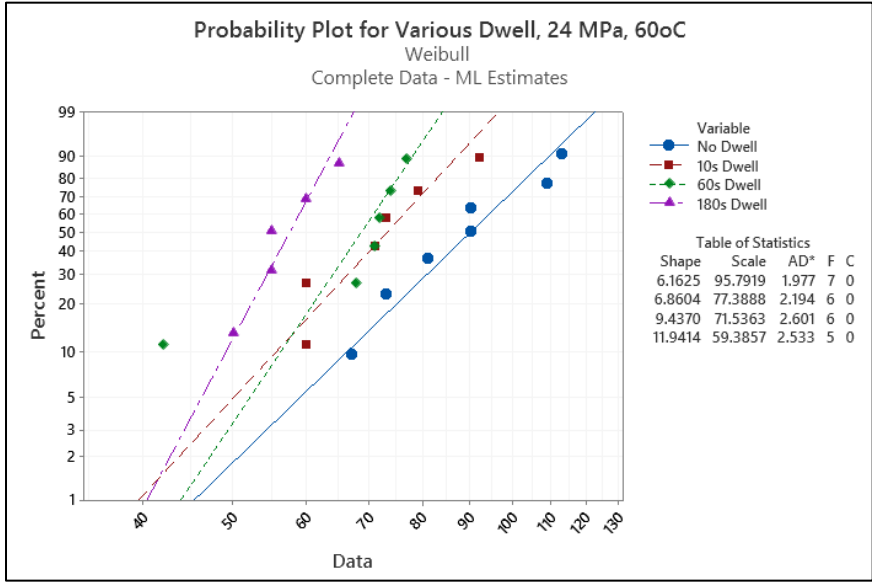


Figure 7.11: Weibull distributions for SAC305 joints cycled with different dwellings at 60°C and 24 MPa stress level

To illustrate the effect of dwell time, Figure 7.12 shows the correlation of characteristic life as a function of dwell time. It involves plot of characteristic life as a function of dwell time for various stress level at 60°C. Its concluded that increasing the dwell time from 0 to 10s would reduce the life significantly and this effect become less with longer dwellings. Also, for certain dwell time and testing temperature, cycling joints with higher stress level would cause drop in characteristic life. Similar trends are observed for room and 100°C temperature. The results of all combinations are summarized in Figure 7.13.

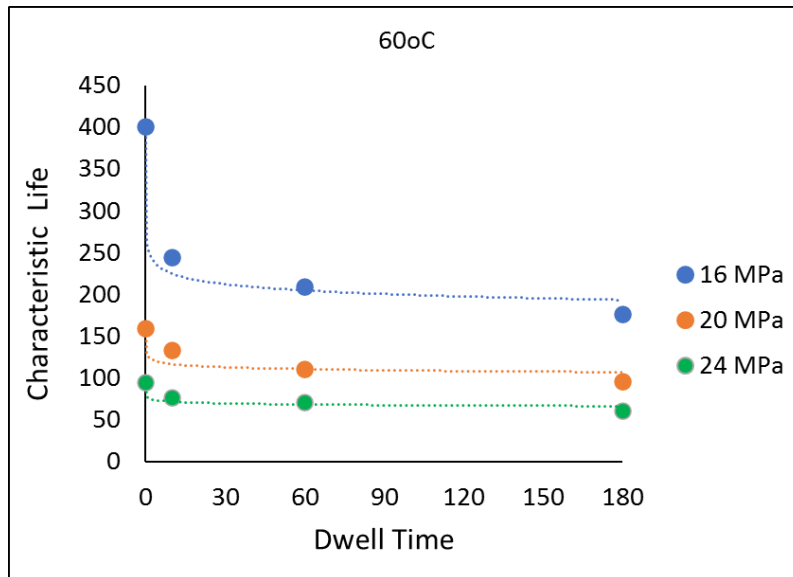


Figure 7.12: Characteristic life as a function of dwell time for SAC305 solder joints cycled with various stress level at 60°C

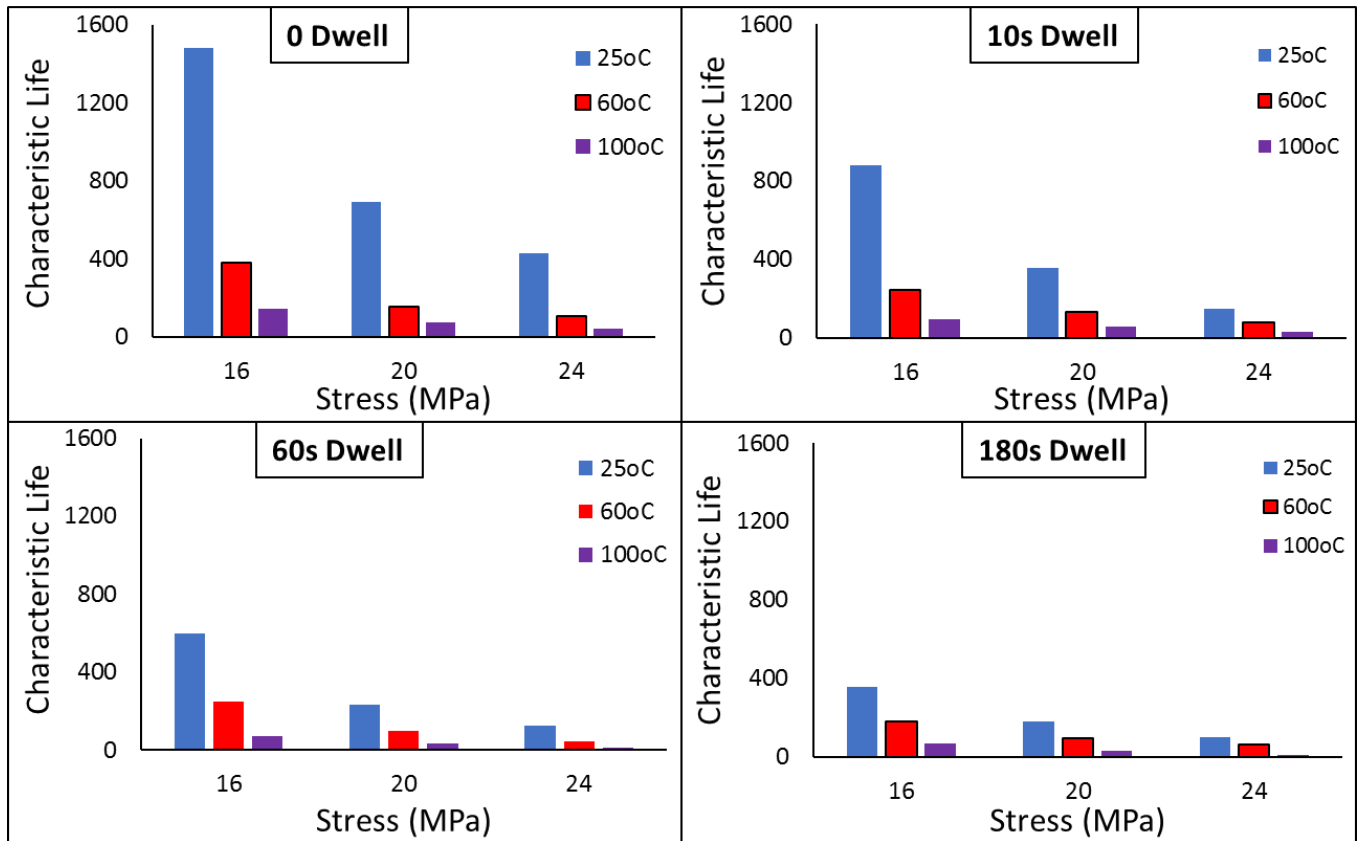


Figure 7.13: Summary of fatigue results for all combinations

Prediction Modeling

In order to generate a general empirical model as a function of stress level, dwell time and testing temperature, results in term of characteristic life as a function of stress amplitude under various conditions of dwell times and testing temperature should be correlated and interpreted. Figures 7.14 and 7.15 illustrate the relation of life-stress curve under various dwelling periods and temperature levels on a log-log scale, respectively. The effect of dwell time on life-stress curve is examined at 60°C as shown in Figure 7.14. Figure 7.15 illuminate the effect of various temperatures on life-stress equation with 10s dwelling. A power equation (fitted to equation 7.2) is generated for all conditions where constants (C and n) are defined for all conditions as shown in Table 7.2. All Weibull parameters of scale and shape in addition to degradation percentages among

several cases are summarized in Table 7.3. The trend in shape parameter is noticed among various testing conditions of dwell time, testing temperature, and stress magnitude with negligible change. Shape parameter represents the variability of testing replicates and they ranges between 3 and 20.

Table 7.2: Constant for stress-life equation at various testing conditions

Testing Temp	Dwell Time	Constants	
		C	n
25	0	9.00E+06	3.166
	10	701074	2.561
	60	2.00E+07	3.845
	180	837314	2.864
60	0	8.00E+06	3.573
	10	667860	2.85
	60	338131	2.669
	180	273804	2.651
100	0	731626	3.079
	10	928680	3.294
	60	1.00E+08	5.149
	180	7.00E+07	4.95

Table 7.3: Fatigue results summary

Testing Temp	Stress Amplitude	Weibull Parameters	Dwell Time			
			0	10	60	180
25	16	Characteristic Life	1479	558	501	376
		Shape parameter	4.7	7	5.1	5.2
		Drop		62%	10%	25%
	20	Characteristic Life	692.5	352.4	195.5	165
		Shape parameter	8.5	3.6	24.9	4.3
		Drop		49%	45%	16%
	24	Characteristic Life	409	176	126	99
		Shape parameter	4.5	4.5	13	6.1
		Drop		57%	28%	21%
60	16	Characteristic Life	401	245	209	177
		Shape parameter	10.2	13	4.2	6.2
		Drop		39%	15%	15%
	20	Characteristic Life	160	133	118	97
		Shape parameter	6.97	7.99	7.1	8
		Drop		17%	11%	18%
	24	Characteristic Life	95	77	71	59
		Shape parameter	6.1	7	9	12
		Drop		19%	8%	17%
100	16	Characteristic Life	143	96	82	69

		Shape parameter	7.8	5.9	5.4	20
		Drop		33%	15%	16%
		Characteristic Life	73	53	33	28
	20	Shape parameter	8.1	5.4	3	3.4
		Drop		27%	38%	15%
		Characteristic Life	38	23	15	10
	24	Shape parameter	4.3	7.7	3.4	2.9
		Drop		39%	35%	33%
		Characteristic Life	38	23	15	10

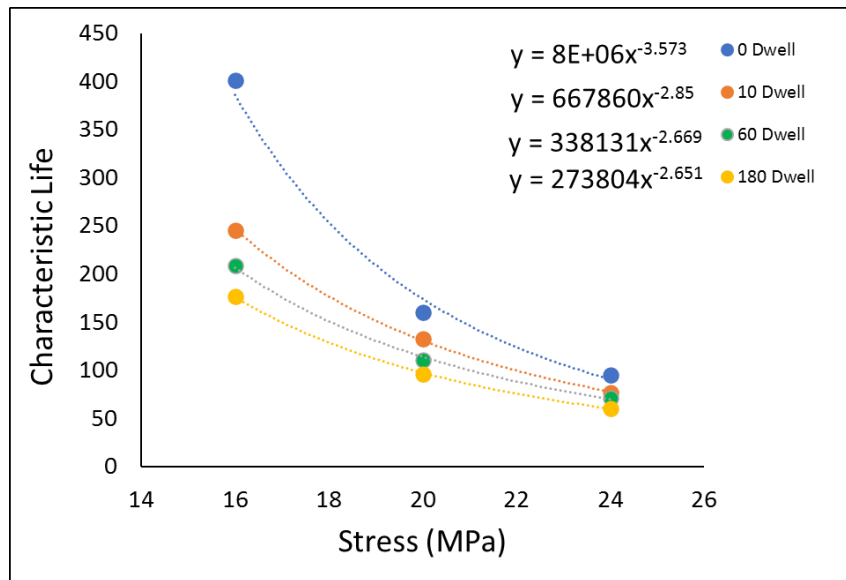


Figure 7.14 The characteristic life as a function of stress amplitude at different dwell times and at 60°C testing temperature

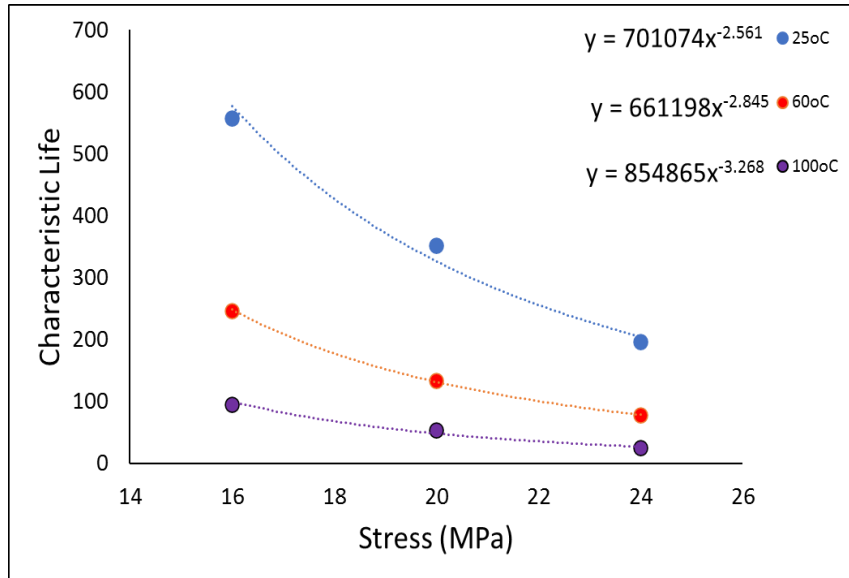


Figure 7.15 The characteristic life as a function of stress amplitude at different testing temperatures and at 10s of dwelling

To describe the effect of temperature, Arrhenius equation is the most common model used according to equation 7.3 below

$$r = A * e^{-\frac{B}{T}} \dots \dots \dots (7.3)$$

Where T is the testing temperature, r is the process rate and A, B are constants.

Based on above, the stress-life equation constant observed to be influenced by various parameters of dwelling times and testing temperatures. Therefore, a general prediction of characteristic life as a function of stress magnitude, dwell time, and testing temperature could be established. Essentially, such model is constructed based on stress-life equation considering that C and n constants are function of dwell time and testing temperature. Whereas, Arrhenius term is introduced to compromise for the temperature effect, terms in Equation 7.4 are used to describe the dwelling periods where t is the dwell time. $U1$ to $U3$ are the equation constants and H is the

stress-life equation constant (n or C). Equation 7.4 includes two terms; exponential and linear ones. The reason behind that is to represent the significant effect of dwell time at the first moments of dwelling, while the linear one is applied for longer dwelling periods where effect become less.

$$H = U_1 * e^{t*U^2} + t*U_3 \dots \dots \dots (7.4)$$

A general prediction model for the characteristic life as a function of stress amplitude and testing temperature is generated according to equation 7.5

$$N_{63} = \left(\overbrace{k_1 * e^{(k_2 * t)}}^{\text{Arrhenius term}} + \overbrace{k_3 * t + k_4 + k_5 * e^{-\left(\frac{k_6}{T}\right)}}^{\text{Dwell time term}} \right) * P \left(\overbrace{k_7 * e^{k_8 * t}}^{\text{Arrhenius term}} + \overbrace{k_9 * t + k_{10} + k_{11} * e^{-\left(\frac{k_{12}}{T}\right)}}^{\text{Dwell time term}} \right) \dots \dots (7.5)$$

Where N_{63} is the characteristic life, t is the dwell time, T is the testing temperature and K_1 to K_{12} are the equation constants. An excel solver was utilized to obtain the equation constant values, considering that the objective function used assures maximum R-squared. The final empirical model is shown in equation 7.6. where R-squared value found to be 98%.

$$N_{63} = 32206.5 + 91217.6 * t + 332647.1 + 1.6 E + 06 * e^{\left(\frac{36.7}{T}\right)} * P \left(0.3 * e^{-5733.8 * t} - 101.2 + 97.4 * e^{\left(\frac{0.1}{T}\right)} \right) \dots \dots \dots (7.6)$$

Finally, the general reliability model is constructed by substituting equation 7.5 in equation 7.1 as a replacement for scale parameter or the characteristic life. No defined trend noticed for the shape parameter with among various combinations of dwell time and testing temperature. As a result, the general reliability model could be found as a function of dwell time, testing temperature, and stress amplitude as shown in equation 7.7

$$R(t) = e^{-\left(\frac{t'}{32206.5+91217.6*t+332647.1+1.6 \text{ E}+06*e^{\left(\frac{36.7}{T}\right)} * P(0.3 * e^{-5733.8*t} - 101.2 + 97.4 * e^{\left(\frac{0.1}{T}\right)})\right)^{7.22}} \dots\dots\dots(7.7)$$

7.3.2 Stress-Strain Analysis

Evolution in stress-strain or hysteresis loop is used to characterize the damage accumulation during the fatigue life. Inelastic work per cycle and plastic strain are the parameters extracted from loops to identify the accumulated damage. Inelastic work per cycle is represented by the loop area which calculated numerically using a MATLAB code. Plastic strain is the change along x-axis during cycling. The evolution in loop elements of inelastic work and plastic strain indicates damage accumulation during the life. Figure 7.16 illustrates the parameters of inelastic work and plastic strain. Figure 7.17 illuminates the effects of stress amplitude on hysteresis loops for no dwell conditions at room temperature. Larger loops are obtained due to more storage of damage when cycling with higher stress amplitude. Greater inelastic work per cycle (loop area) and larger plastic strain (delta along x-axis) is noticed. Testing temperature has similar effect of stress level that rising the testing temperature would produce more creep damage. This effect is clearly shown when testing temperature switched between 25°C to 60°C, and from 60°C to 100°C in less manner. Figure 7.18 illustrates the evolution in stress-strain loops when cycling different joints at various temperatures levels with fixed dwell time and stress level of 10s and 16 MPa, respectively. The effect of dwell time on hysteresis loops evolution is explored as well. Figure 7.19 shows the enlargement in hysteresis loop for joints cycled with 20 MPa stress level under various dwelling times at room temperature. This is due to the accumulation of creep damage with longer dwellings compared to no dwell condition. However, the effect of dwell become less when cycling at higher temperature since the effect of temperature is dominant. Figure 7.20 shows the hysteresis loops for joints cycled under same conditions of dwelling periods and stress level (20 MPa), but at higher

temperature level of 100°C. Trends for effects on inelastic work per cycle and plastic strain by various testing parameters are obtained and found to be similar for the previously mentioned ones. Its concluded that the influence of temperature on both damage parameters of inelastic work per cycle and plastic strain is greater than dwell times. Plots for all combinations are mentioned in Appendix B.

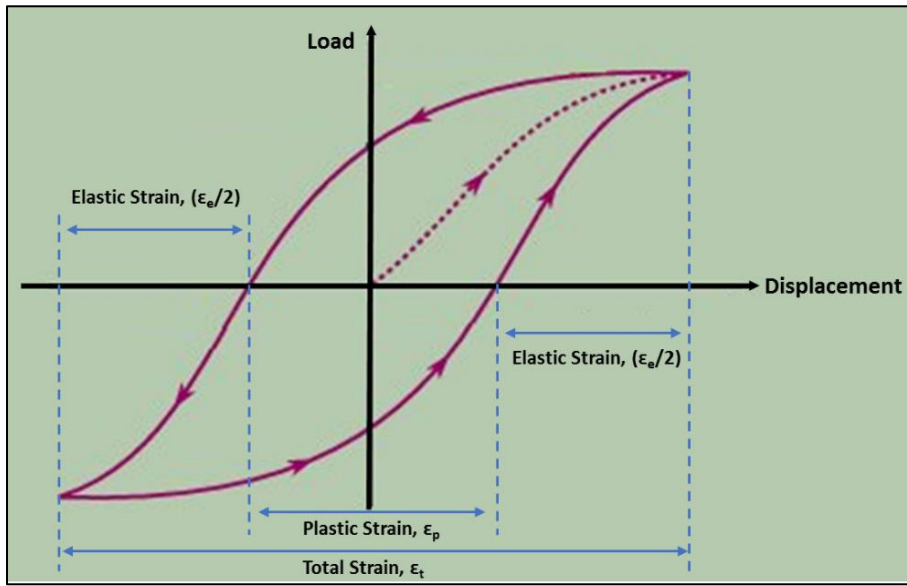


Figure 7.16: The full hysteresis loop for the SAC305 solder joints at certain stress amplitude

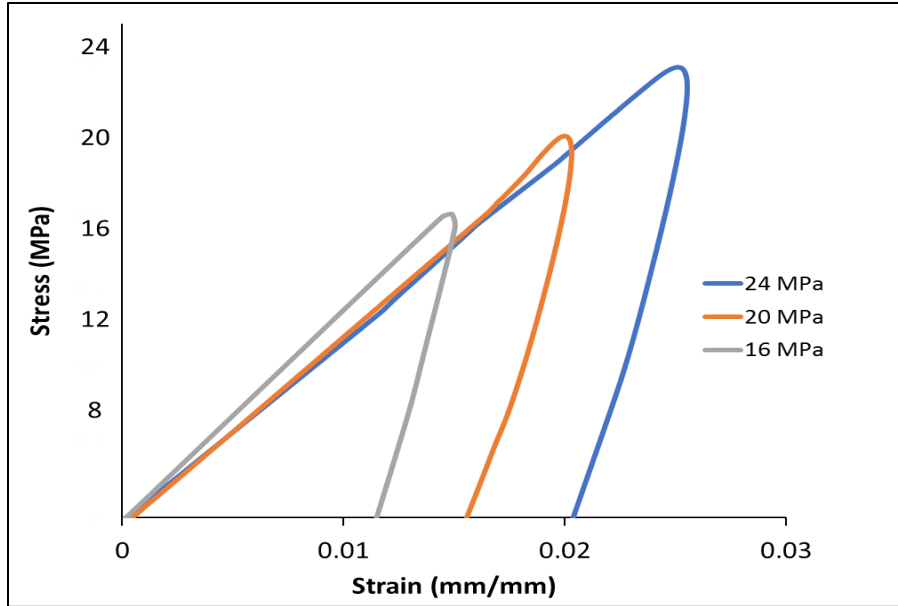


Figure 7.17: The evolutions in stress-strain loop for joints cycled with various stress amplitudes at room temperature with no dwelling condition

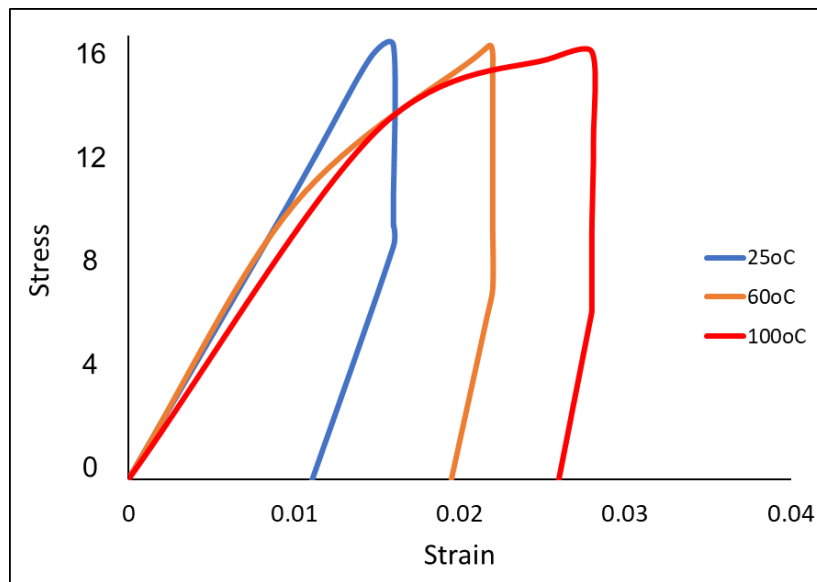


Figure 7.18: Stress-strain loop for joints cycled with various stress amplitudes at 60°C with 10s of dwelling condition

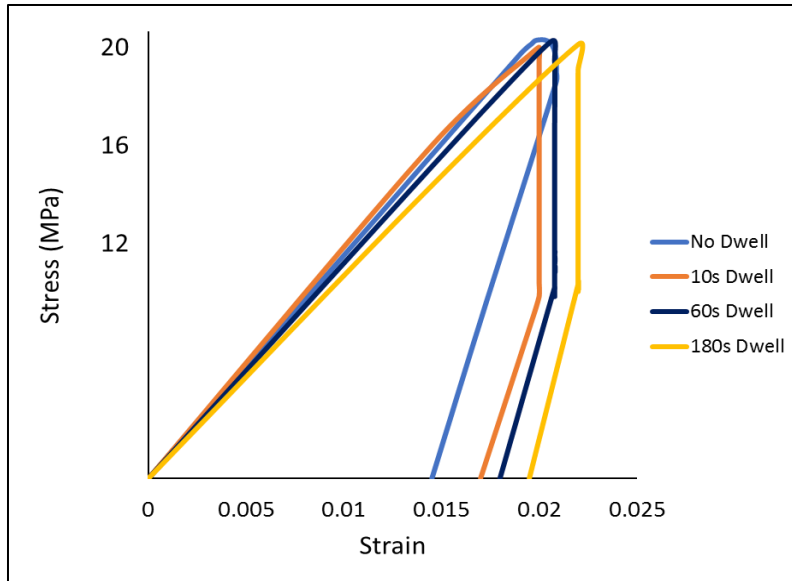


Figure 7.19: Stress-strain loop for joints cycled with 24 MPa stress amplitudes at 25°C with various dwelling periods

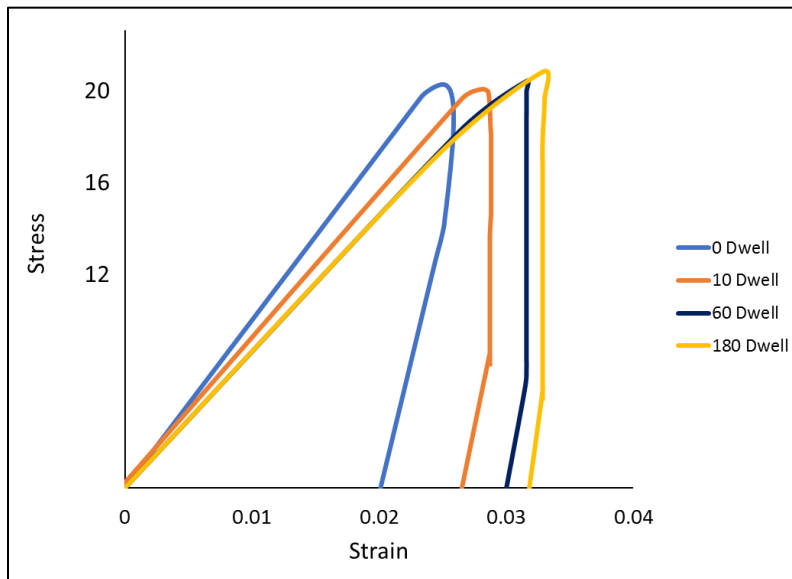


Figure 7.20: Stress-strain loop for joints cycled with 24 MPa stress amplitudes at 100°C with various dwelling periods

The evolution in inelastic work per cycle is determined and noticed to be of three stages; strain hardening, steady state, and crack initiation and propagation as shown in Figure 7.21 for joint cycled with 16 MPa at room temperature. Such behavior is demonstrated for all combination of stress amplitudes, dwell times, and temperatures levels which included in Appendix B. In FEA, average inelastic work per cycle is used which is the same as the steady state region for life prediction purposes. Such assumption facilitates providing prediction models. However, its not very accurate, since it doesn't consider the evolution with time. From Figures 7.22 to 7.24, effects of various parameters on the evolution of inelastic work among joints life are illustrated. Results show similar behaviors for various testing combinations.

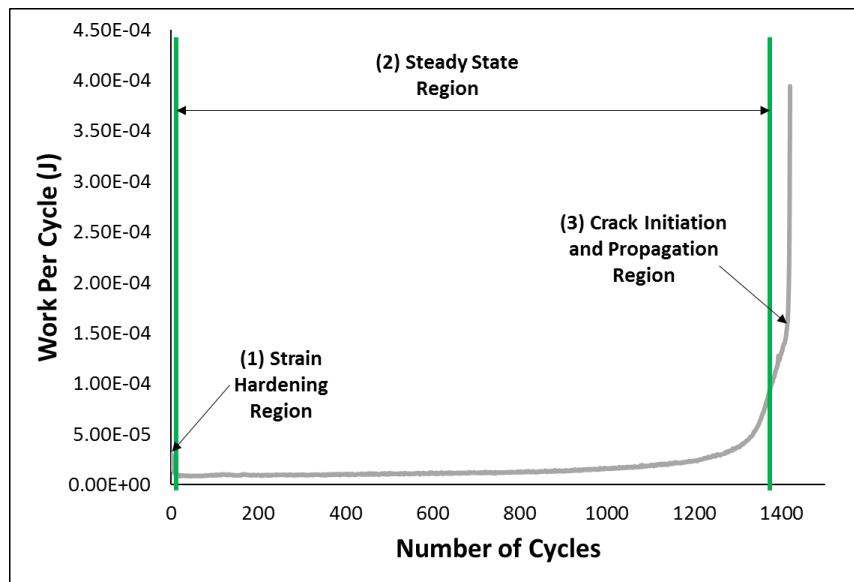


Figure 7.21: The evolution of inelastic work long the fatigue life of solder joint cycled with 16 MPa at room temperature

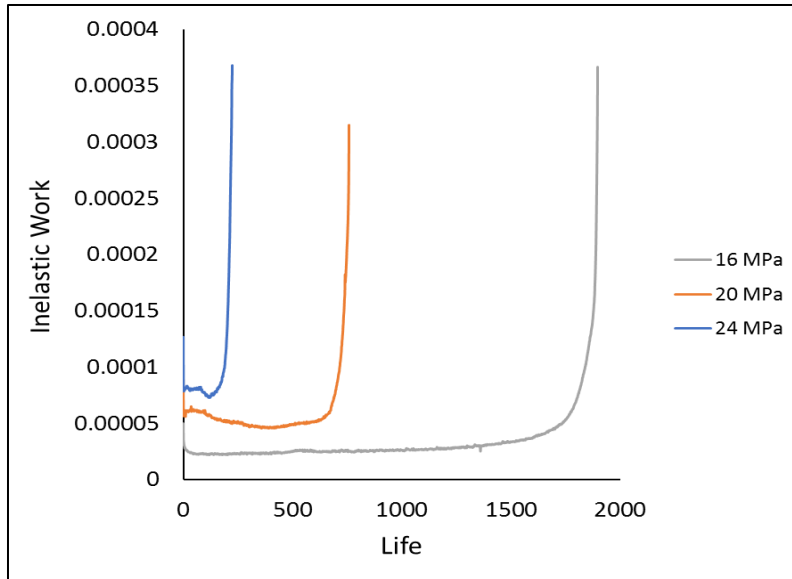


Figure 7.22: The effect of various stress amplitudes on inelastic work evolution during the joint life while other conditions of dwell time (0s) and temperature levels (25°C) are fixed

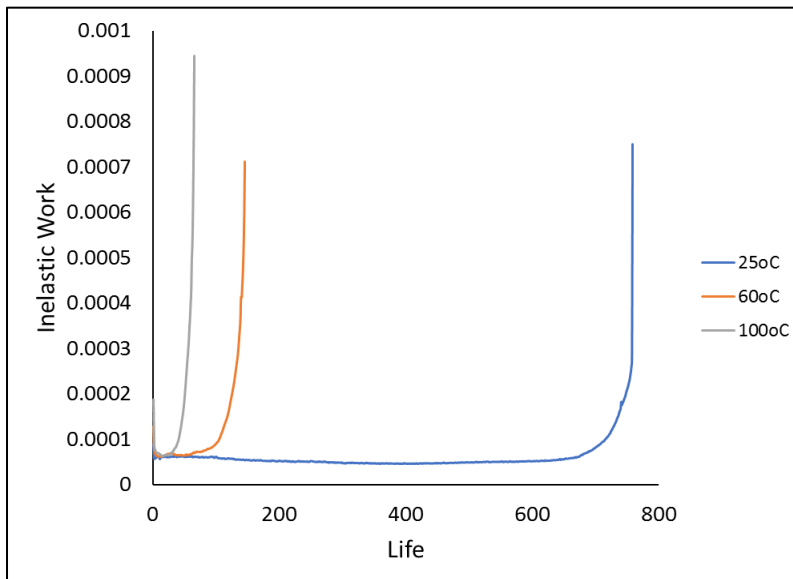


Figure 7.23: The effect of various temperatures levels on inelastic work evolution during the joint life while other conditions of dwell time (0s) and stress amplitude (20 MPa) are fixed

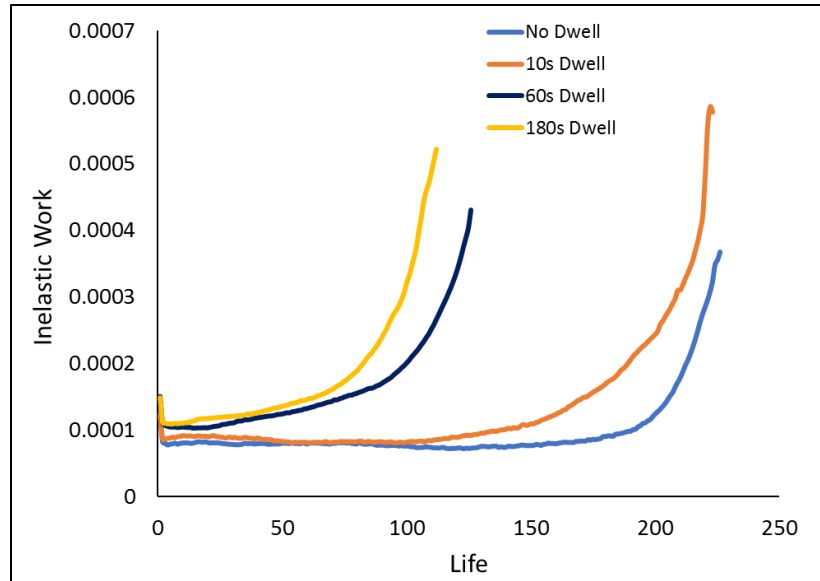


Figure 7.24: The effect of various dwell times on inelastic work evolution during the joint life while other conditions of temperature (60°C) and stress amplitude (24 MPa) are fixed

The last part discusses the relationship between the average work per cycle and plastic strain as a function of various testing parameters of dwell times, testing temperature, and various stress amplitudes. The results are interpreted by investigating and comparing the effect of two-testing parameter at a time on the average inelastic work per cycle and plastic strain while the third one kept constant. Basically, each point in the plots represents the average value of average work per cycle and plastic strain for seven tested joints at certain combination. Figure 7.25 illustrates both; the average work per cycle and plastic strain as a function of dwell time for joints tested with several stress levels at 100°C. At certain stress level, increasing the dwell time would increase the average inelastic work per cycle and plastic strain especially after 60s of dwelling. Similar trend is noticed for 60°C, while such parameters are growing significantly after only 10s of dwelling at 25°C. The effect of temperature on average work per cycle and plastic strain is also investigated for joints cycled with various stress levels with 10s of dwelling as shown in Figure 7.26. The

average work per cycle and plastic strain are increased exponentially when cycling at higher temperature levels for certain stress level. Moreover, the effect of temperature noticed to be dominant in some cases; both quantities of average inelastic work and plastic strain found to be greater when cycling with lower stress levels at higher temperature level compared to ones cycled with higher stress level at lower temperatures. Figure 7.27 shows average work per cycle and plastic strain as a function of dwell time at various temperature levels for 24 MPa stress level. It's clearly shown that cycling joints at higher temperatures with same dwell time cause large increment in average inelastic work per cycle and plastic strain. However, the dwell effect is less compared to temperature; only in few cases damage quantities noticed to be greater when cycling joints with longer dwellings at lower temperature in comparison to shorter dwellings at higher temperature. Also, increasing dwell time would cause an increment in damage quantities until certain point where negligible increment is observed beyond that dwell of 180s. This indicates that temperature influence is of greater importance compared to dwell time.

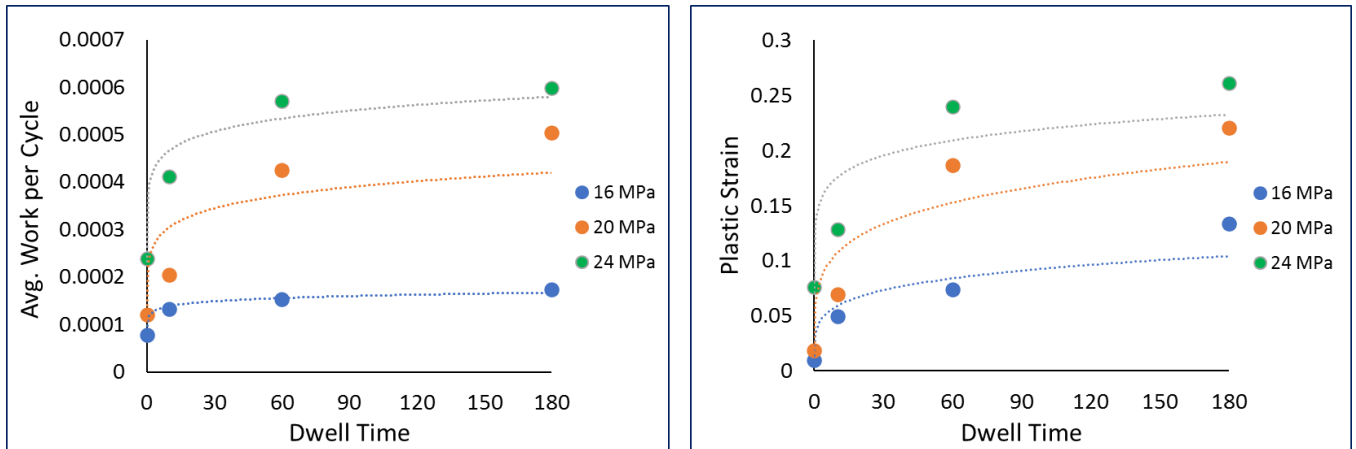


Figure 7.25: The effect of various dwell times on average inelastic work per cycle and plastic strain for joints tested under various stress magnitudes at 100°C

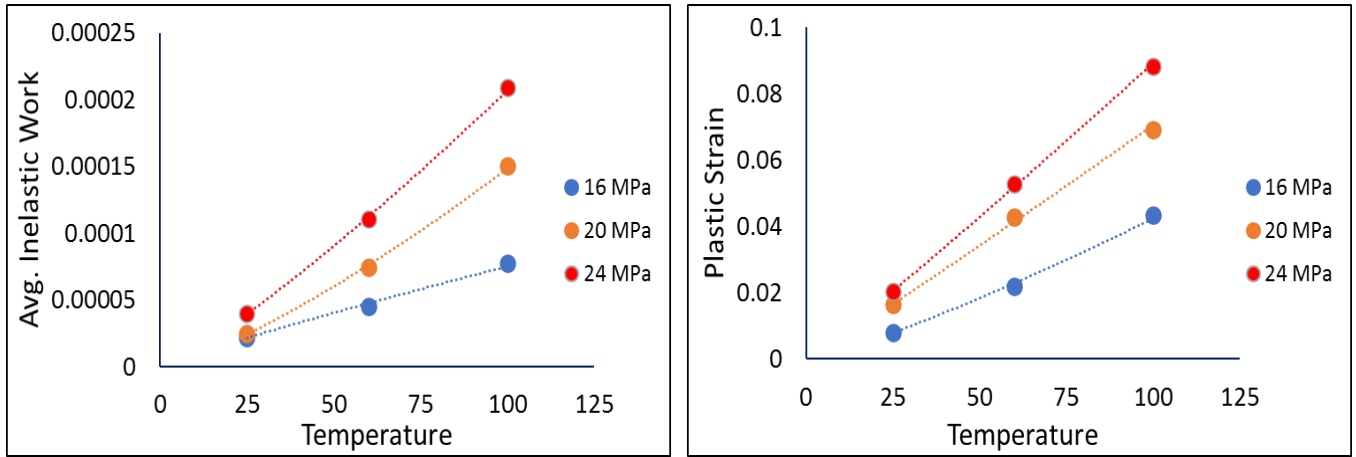


Figure 7.26: The effect of dwell time levels on average inelastic work per cycle and plastic strain for joints tested under various stress magnitudes with 10s of dwelling

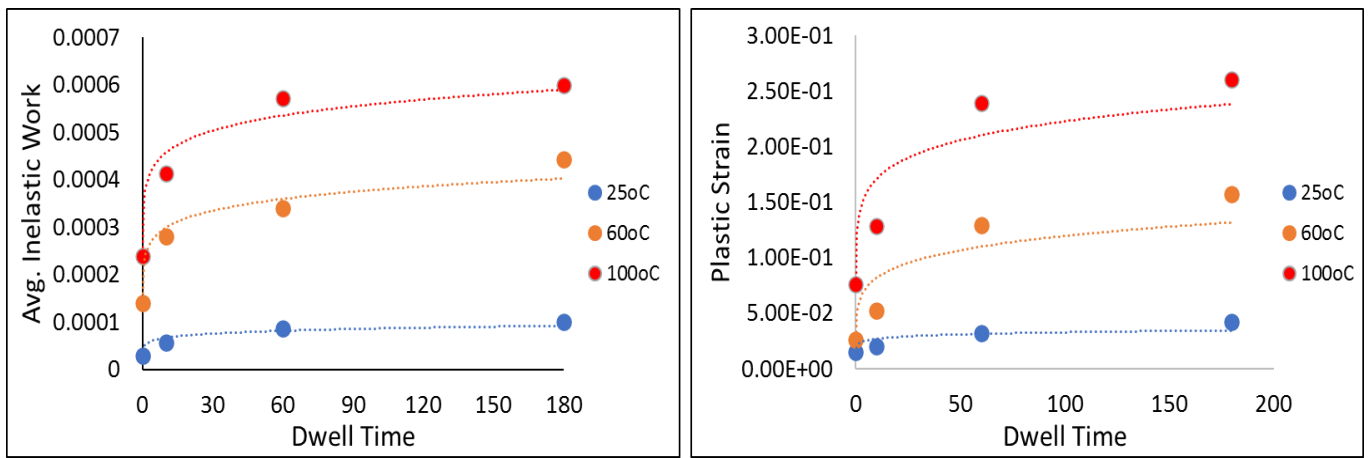


Figure 7.27: The effect of various temperature levels on average inelastic work per cycle and plastic strain for joints tested under various stress magnitudes with 10s of dwelling

7.3.3 Morrow Energy and Coffin-Manson Models

Morrow energy and Coffin-Manson models are common models applied to predict the characteristic life as a function of average inelastic work per cycle and plastic strain, respectively.

Morrow Energy Model

Morrow energy model is a power equation as shown in equation 7.8

$$N_{63} = C_m^{\frac{1}{m}} W_m^{-\frac{1}{m}} \dots\dots\dots (7.8)$$

Where N_{63} is the characteristic life, W is the inelastic work per cycle, C , m are material constants which represents fatigue ductility and fatigue exponent, respectively. To demonstrate Morrow model as a function of inelastic work, relation of characteristics life as a function of inelastic work is plotted for no dwelling conditions at room temperature as shown in Figure 7.28.

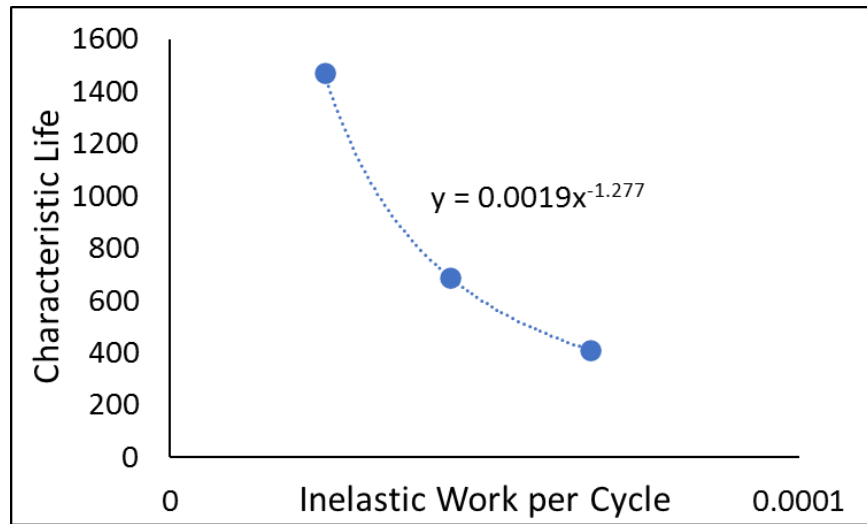


Figure 7.28: Morrow energy model for the SAC305 solder joints at room temperature with no dwelling

The effects of both testing parameters of dwell time and testing temperature on Morrow model are examined and summarized as shown in Table 7.4. No specific trend is observed for equation's constants with changing the dwelling conditions. Thus, a global Morrow model is generated to correlate the characteristic life as a function of inelastic work per cycle at each temperature level. So, three Morrow equations considering temperature levels were verified to predict the life as a function of inelastic work whatever the dwell time is as shown in Figure 7.29. The general model

defining the characteristic life as a function of inelastic work and testing temperature is constructed by correlating the global constants of the three Morrow equations and testing temperature using Arrhenius term as shown in Figure 7.30. Consequently, with high value of R-square, the final form of model to predict the life is established based on Morrow model and Arrhenius term as shown in equation 7.9.

$$N63 = (0.0048 * e^{\frac{16.649}{T}})^{-1.165 * e^{2.098/T}} * W^{1.165 * e^{2.098/T}} \dots\dots\dots (7.9)$$

A general reliability model as a function of temperature and inelastic work is obtained in equation 7.10 by substituting the equation 7.9 of characteristic life in equation 7.1 of reliability function. There was no trend found for shape parameter, so its estimated by considering the averages for all conditions.

$$R(t) = e^{-\left(\frac{t}{(0.0048 * e^{\frac{16.649}{T}})^{-1.165 * e^{2.098/T}} * W^{1.165 * e^{2.098/T}}}\right)^{7.2}} \dots\dots\dots(7.10)$$

Table 7.4: Summary of Morrow Energy constants at various dwell times and temperature levels

Testing Temp	Dwell time	Fatigue Exponent (m)	Fatigue Ductility (C)
25	0	0.783	0.0074
	10	0.95	0.017
	60	0.645	0.0041
	180	0.762	0.0073
	Global	0.79	.0095
60	0	0.797	0.00405
	10	0.829	0.0096
	60	0.767	0.0085
	180	0.567	0.0043
	Global	0.826	0.0059
100	0	0.956	0.0089
	10	0.826	0.0064

	60	0.626	0.0031
	180	0.504	0.0021
	Global	0.843	0.0061

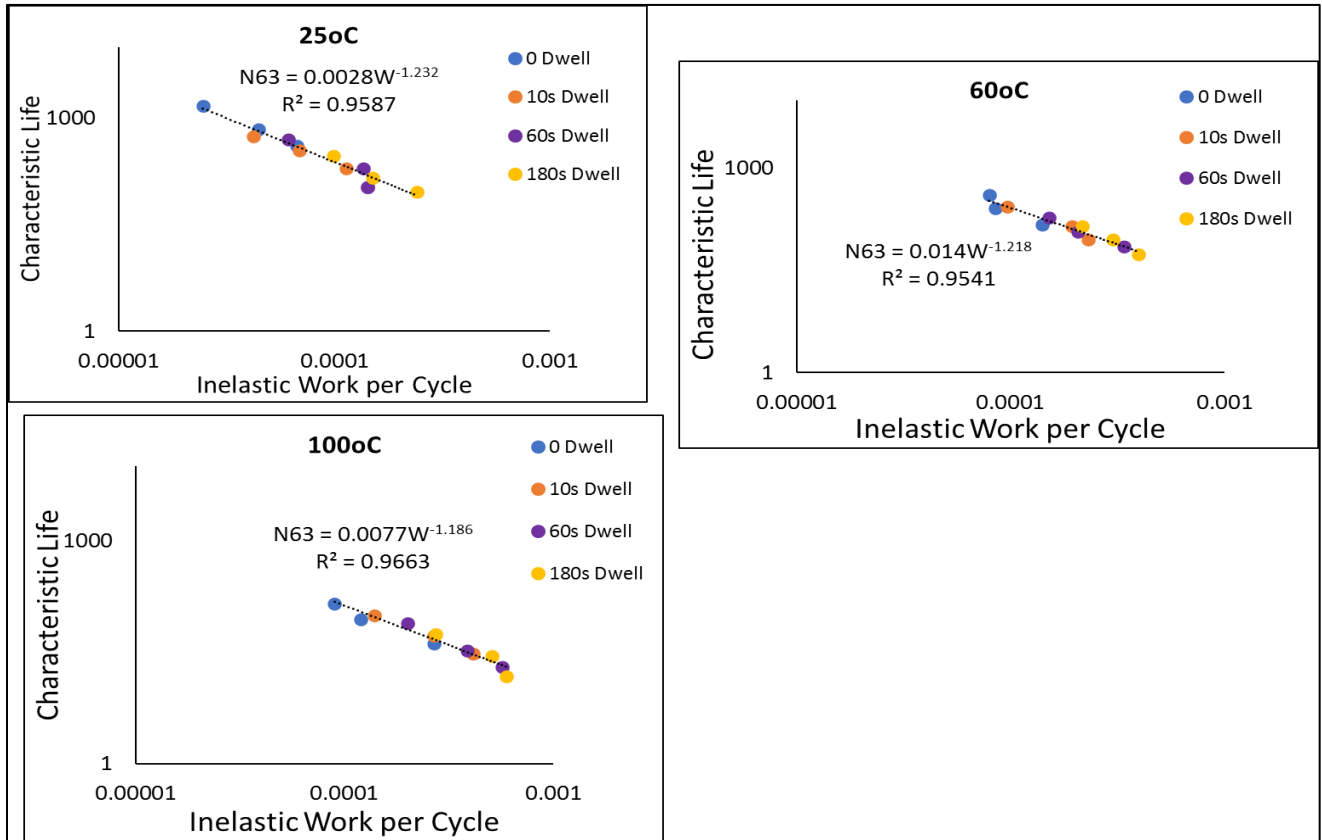


Figure 7.29: The characteristic life as a function of inelastic work per cycle at different testing temperatures with various dwellings.

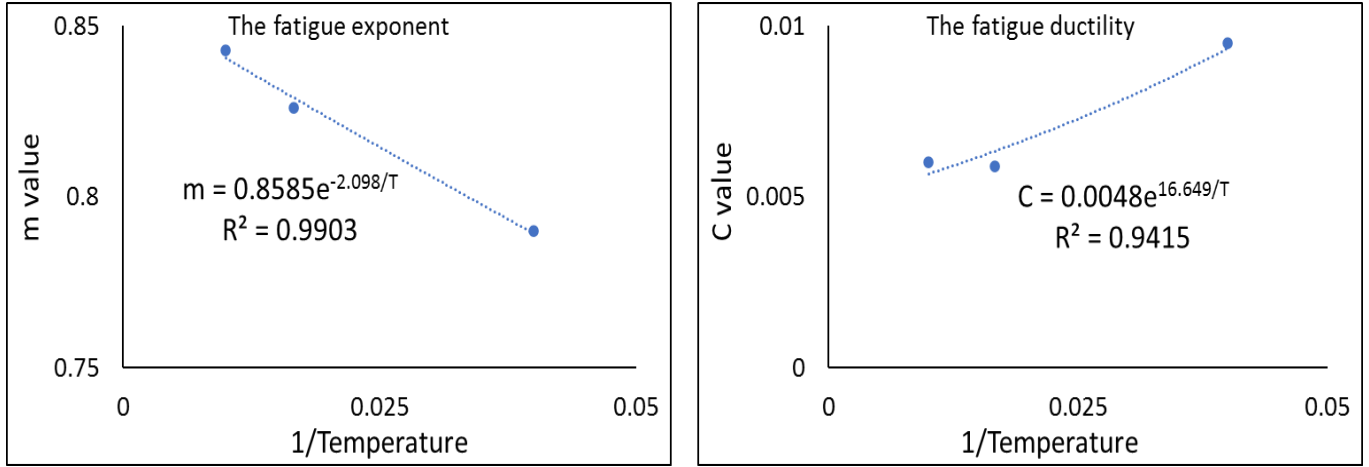


Figure 7.30: The correlation between the Morrow energy constants and the testing temperature utilizing Arrhenius model

Coffin-Manson Model

Coffin-Manson model utilizes plastic strain for life (characteristic life represents life) prediction purposes as shown in equation 7.11.

$$N_{63} = S^{-\frac{1}{\alpha}} \gamma^{\frac{1}{\alpha}} \dots\dots\dots (7.11)$$

Where N_{63} is the characteristic fatigue life, γ is the fatigue ductility coefficient, S is the plastic strain, and α is the fatigue exponent. Figure 7.31 illustrates the characteristic life as a function of plastic strain at our referenced conditions of no dwelling and room temperature, where results are fitted to a power equation. The way results are interpreted is similar to Morrow energy one. The effect of both dwell time and testing temperature on Coffin-Manson model is examined. Coffin-Manson equation constants for all combinations are determined and summarized as shown in Table 7.5. Therefore, a global Coffin-Manson model is generated to relate the characteristic life as a function of plastic strain at each temperature level. Consequently, three Coffin-Manson equations considering temperature levels were determined to predict the life as a function of plastic strain

whatever the dwell time is as shown in Figure 7.32. The general model that correlates the characteristic life as a function of plastic strain and testing temperature is constructed by relating the global constants of the three Coffin-Manson equations and testing temperature using Arrhenius term as shown in Figure 7.33. Consequently, with high value of R-square, the final model to predict the life is established based on Coffin-Manson model and Arrhenius term as shown in equation 7.12.

$$N63 = (354.21 * e^{-\frac{137.8}{T}})^{0.41 * e^{28.54/T}} S^{0.41 * e^{28.54/T}} \dots\dots\dots (7.12)$$

A general reliability model as a function of testing temperature and plastic strain is obtained in equation 7.13 by substituting the equation 7.12 of characteristic life in equation 7.1 of reliability function. There was no trend found for shape parameter, so its estimated by considering the averages for all conditions.

$$R(t) = e^{-\left(\frac{t}{(354.21 * e^{-\frac{137.8}{T}})^{0.41 * e^{28.54/T}} S^{0.41 * e^{28.54/T}}}\right)^{7.23}} \dots\dots\dots (7.13)$$

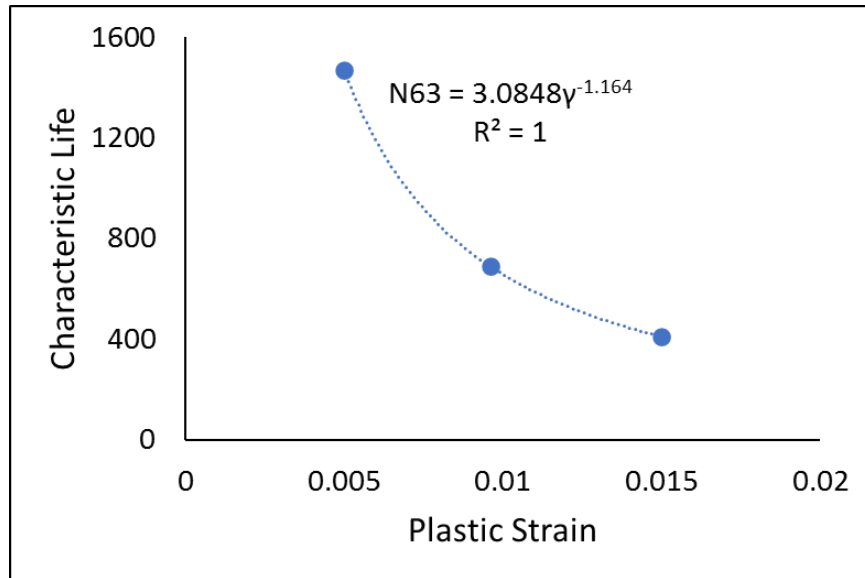


Figure 7.31: Characteristic life vs. plastic strain for joints with no dwelling condition at room temperature

Table 7.5: Summary of Coffin-Manson constants at various dwell times and temperature levels

Testing Temp	Dwell time	Fatigue Exponent (α)	Fatigue Ductility Coefficient (γ)
25	0	0.859	2.528
	10	0.997	4.57
	60	0.718	0.9
	180	0.802	1.53
	Global	0.757	1.21
60	0	0.928	2.812
	10	1.203	12.62
	60	1.612	105.3
	180	1.78	210.57
	Global	1.656	75.12
100	0	1.612	30.36
	10	0.967	3.45
	60	1.041	6.15
	180	0.862	3.39
	Global	1.69	50.04

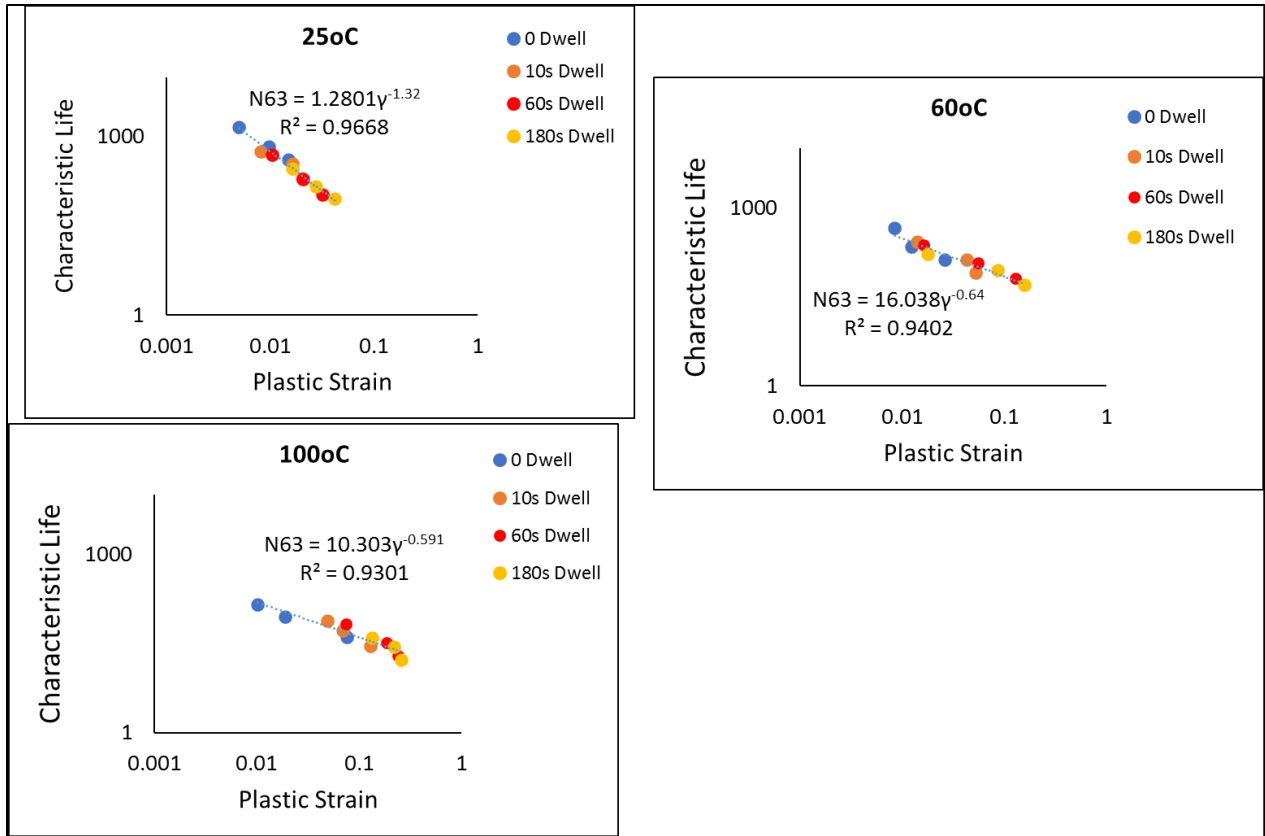


Figure 7.32: The characteristic life as a function of plastic strain at different testing temperatures with various dwellings.

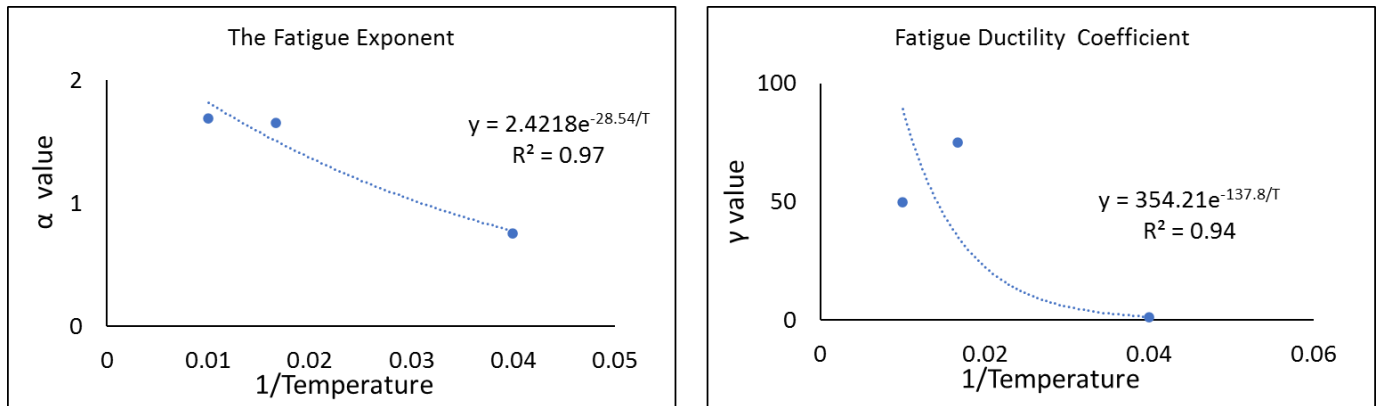


Figure 7.33: The correlation between the plastic strain constants and the testing temperature utilizing Arrhenius model

7.3.4 The Reliability of SAC305 Joints at Cold Temperature Under Fatigue Condition Compared to Room Temperature

The effect of creep on solder joints reliability is investigated under various testing parameters of dwell times and testing temperatures. Both concluded to enhance the creep damage where the effect of temperature is greater according to the evolution in average inelastic work per cycle and plastic strain results. Recent studies imply that room temperature is elevated one since it has large homologous temperature ratio of 0.5 for SAC305 alloy. However, other studies show that creep is still active at cold temperatures. Therefore, SAC305 solder joints were tested under fatigue conditions with various stress levels at -10°C and compared with room results. In this section, Weibull plots for both cases of -10°C and 25°C are examined and compared based on characteristics life data. S-N curve is plotted and a general model to predict the characteristic life is obtained as a function of stress level. A general reliability model as a function of stress level is generated as well. The second part discusses the hysteresis loops for both conditions including interpretation for inelastic work and plastic strain results. Also, evolution of inelastic work along the joint life is explored. Creep effect is investigated by comparing the average inelastic work per cycle as a damage parameter for both conditions under various stress levels. Also, accumulated inelastic work per cycle, average inelastic work per cycle, and plastic strain as a function of stress amplitude are investigated.

Weibull Analysis

Two-parameters Weibull distribution for SAC305 joints tested with various stress levels at -10°C is plotted in Figure 7.34. Results demonstrate that fatigue life is reduced significantly when cycling with higher stress levels. A drop in characteristic life with 50% is noticed when increasing stress between 16 and 20 MPa, whereas the drop in life almost was 70% when cycling at 24 MPa. More

damage is accumulated when cycling with higher stress level. Similar trend of life drop with increasing stress level is observed for room temperature. Figure 7.35 shows Weibull plots for joints cycled with same stress level of 16 MPa at both testing temperatures. Only around 10% drop is observed when cycling joints between -10°C and 25°C . This means that even -10°C is considered as high temperature for SAC305 alloys.

Characteristic life as a function of stress amplitude for both cases is illustrated in Figure 7.37. seven solder joints were studied at each condition. A drastic drop in fatigue life is obtained when increasing the stress amplitude. This plot shows the variability in life results for tested joints at each condition and found to be reasonable since variability among solder joints ranges between 3-5 according to literature [86, 96]. The characteristic life as a function of stress amplitude on a log-log scale is generated as shown in Figure 7.38. Data are fitted to a power equation with -3.14, and -3.17 as a power value for both cases of -10°C and 25°C , respectively. Such correlation used to predict the reliability of these joints under this condition. According to this equation, decreasing the stress value by a factor of 2 will lead to life reduction by a factor of 10. However, tiny difference in such power values means that these the behavior of joints in terms of life as function of stress levels are almost similar. The values of 3.14, and 3.17 represents the fatigue ductility exponent coefficient of the material where the lower the value, the higher the ductility. Results for both conditions are summarized in Table 7.6.

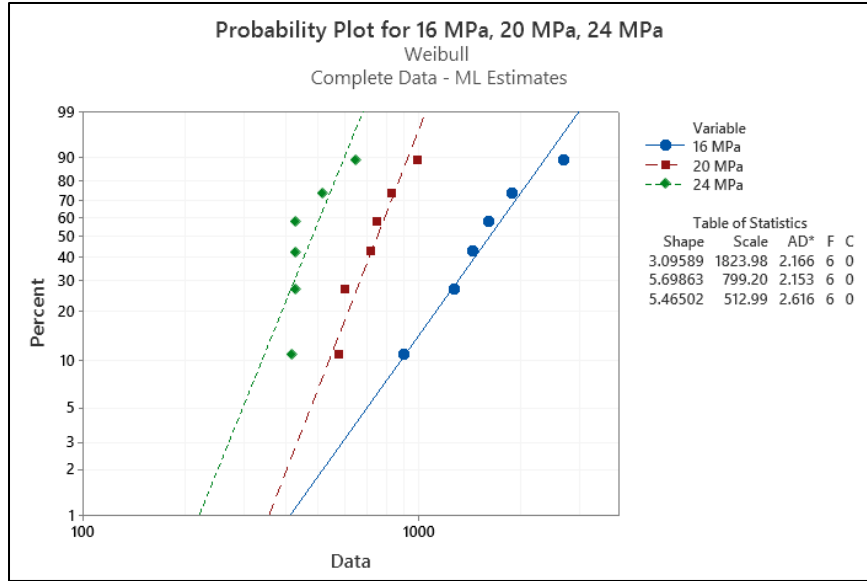


Figure 7.34: Weibull distributions for SAC305 joints cycled with various stress levels at -10°C

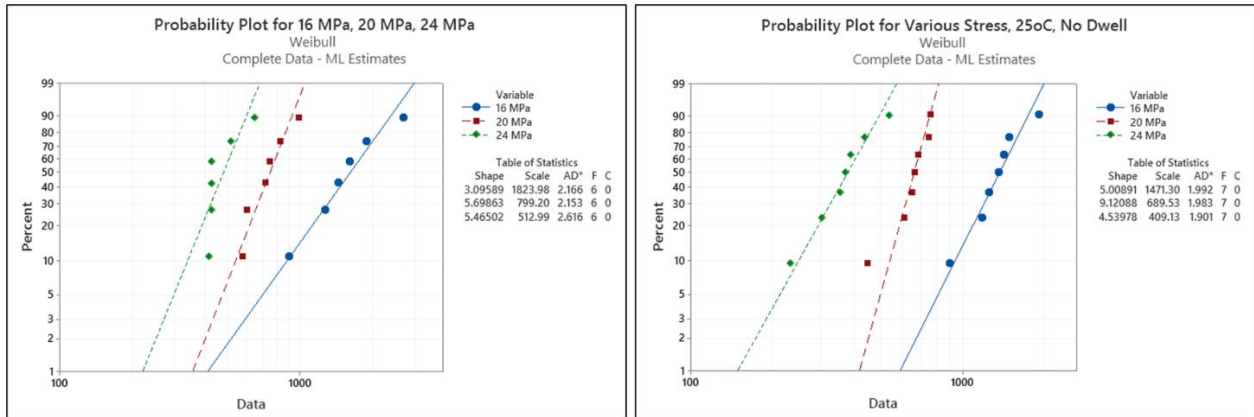


Figure 7.35: Weibull distributions for SAC305 joints cycled with various stress levels at -10°C and 25°C

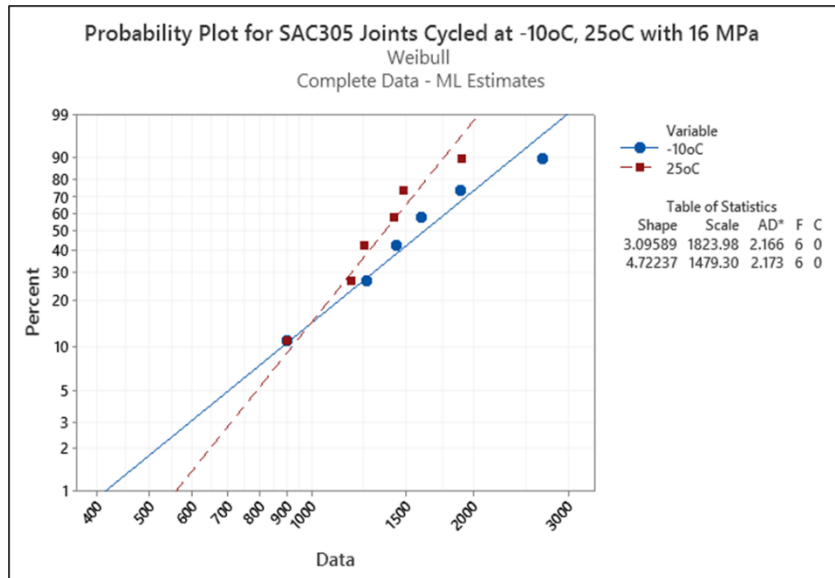


Figure 7.36: Weibull distributions for SAC305 joints cycled with 16 MPa stress level at -10°C and 25°C

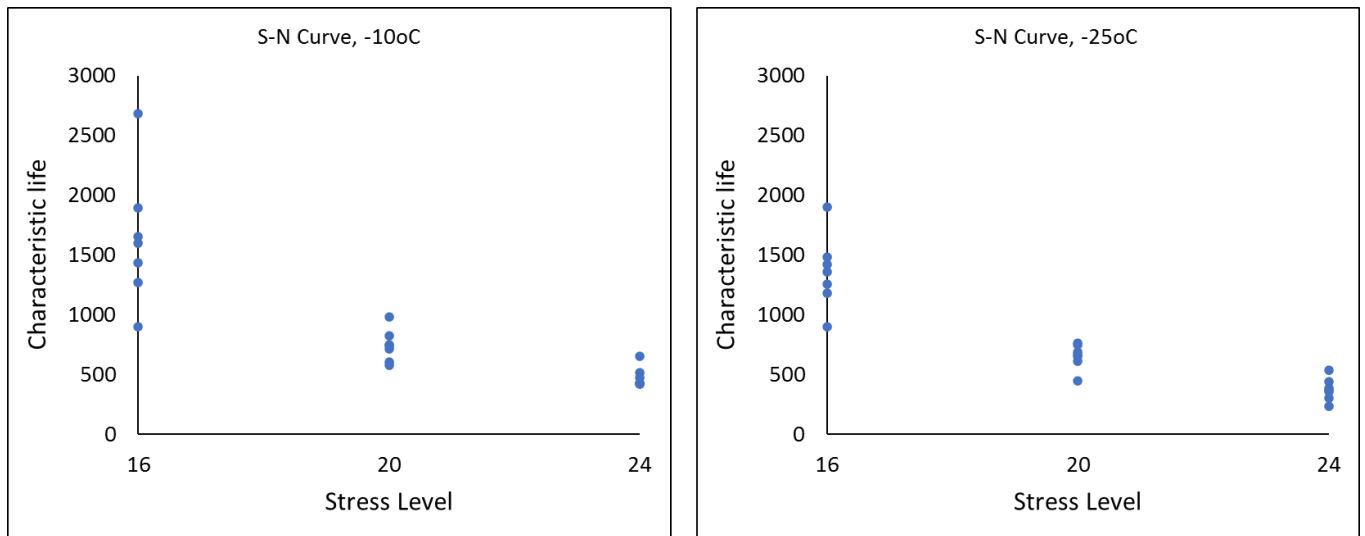


Figure 7.37: Characteristic life as a function of stress amplitude for both conditions of -10°C and 25°C

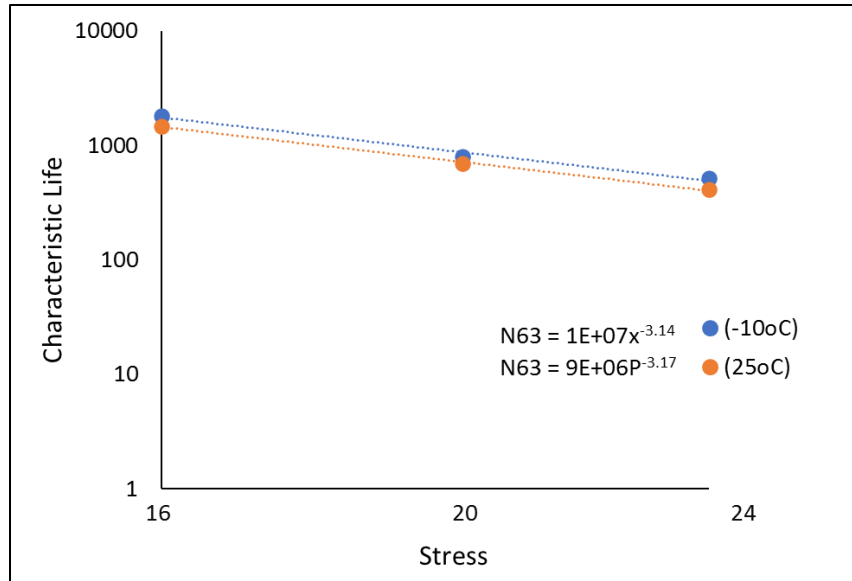


Figure 7.38: Characteristic life as a function of stress amplitude for both conditions of -10°C and 25°C on log-log scale

Table 7.6: Fatigue results summary

Stress amplitude (MPa)	Weibull parameters	Temperature	
		-10°C	+25°C
16	Characteristic life	1823	1479
	Shape parameter	3.3	4.7
20	Characteristic life	799	693
	Shape parameter	5.6	8.5
24	Characteristic life	513	429
	Shape parameter	5.4	5.5

Prediction Modeling

Equation 7.1 is utilized to predict the reliability as a function of stress amplitude for cold temperature of -10°C. First, the characteristic life as a function of stress amplitude is generated according to Figure 7.38 as shown in equation 7.14

$$N_{63} = 1E+07 * P^{-3.14} \dots\dots\dots(7.14)$$

Where N_{63} is the characteristic life, and P is the stress amplitude. By substituting equation 7.14 into equation 7.1 instead of characteristic life, and consider the average of shape parameters for various conditions since no trend is noticed, a general degradation in reliability is constructed as shown in equation 7.15

$$R(t) = e^{-\left(\frac{t}{1E+07P^{-3.148}}\right)^{5.5}} \dots\dots\dots(7.15)$$

Where P is the stress amplitude, t is the number of cycles.

Stress-Strain Analysis

Hysteresis loops are generated for various stress levels for both temperature conditions as shown in Figure 7.39. Similar trend is observed at cold temperature where larger loops are generated at higher stress levels. Slight increase in area is noticed when comparing areas of same stress levels and different temperatures of -10°C and 25°C. However, area is larger for 25°C temperature compared to -10°C due to more inelastic work and plastic strain correlated with higher creep damage at higher temperature. Also, Figure 7.40 shows full hysteresis loops for two individual joints cycled with 16 MPa stress level at -10°C and 25oC. The higher the testing temperature(25°C), the larger the area produced. Figure 7.41 (right side) shows hysteresis loops for joints cycled with 24 MPa stress level at -10°C and 25°C. The slight increase in area at 25oC

(the higher temperature) could be justified by comparing the average inelastic work per cycle in both cases. An increment of only 7% is noticed in room temperature case compared to cold one of -10°C. This amount of damage is accumulated at higher temperature due to more creep effect and other related weakness phenomena that joints suffer at room temperature as higher temperature compared to -10°C. The evolution in inelastic work is a vital parameter that observing the changing of the damaged work along the joints' life. Nevertheless, same behavior is obtained for joints cycled at various stress amplitudes at -10°C with three stages of strain hardening, steady state, and finally the crack initiation and propagation as shown in Figure 7.42.

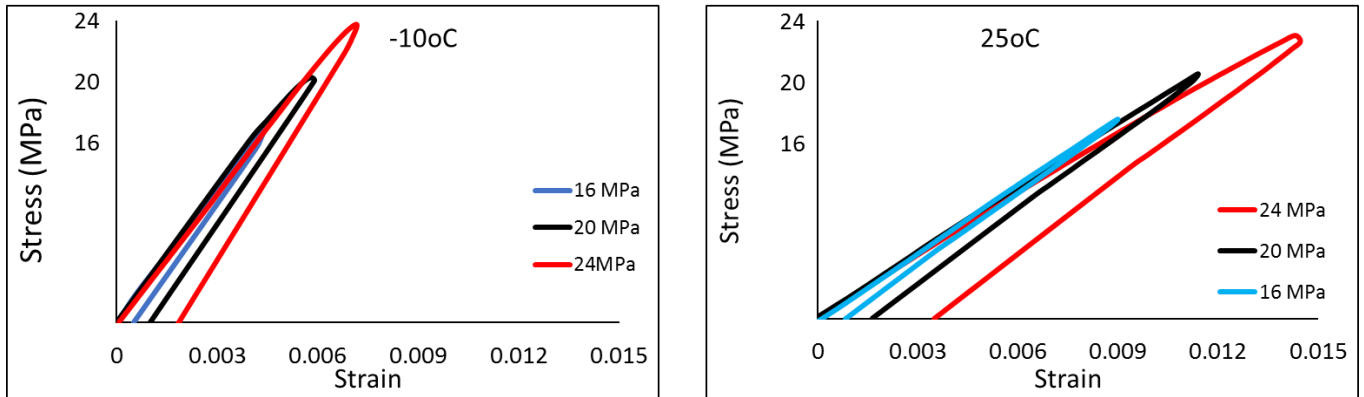


Figure 7.39: The evolutions in stress-strain loop for joints cycled with various stress amplitudes at room temperature with no dwelling condition

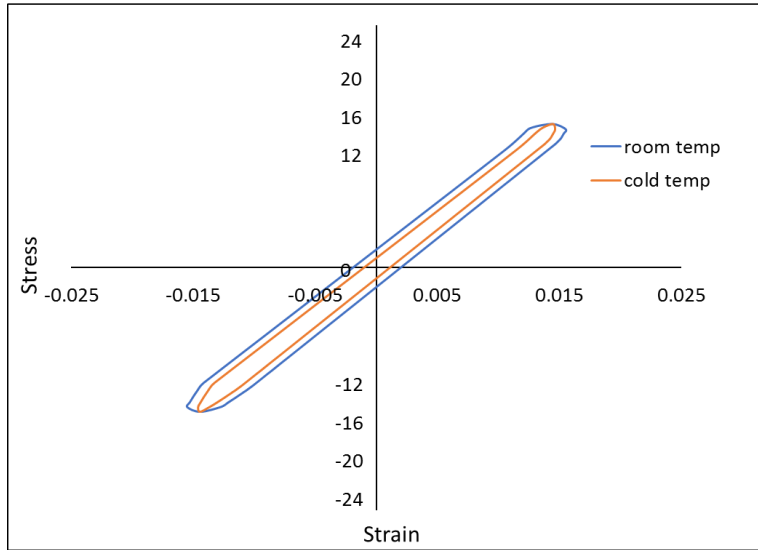


Figure 7.40: Full stress-strain loop for joints cycled with 16 MPa stress amplitudes at -10°C and 25°C

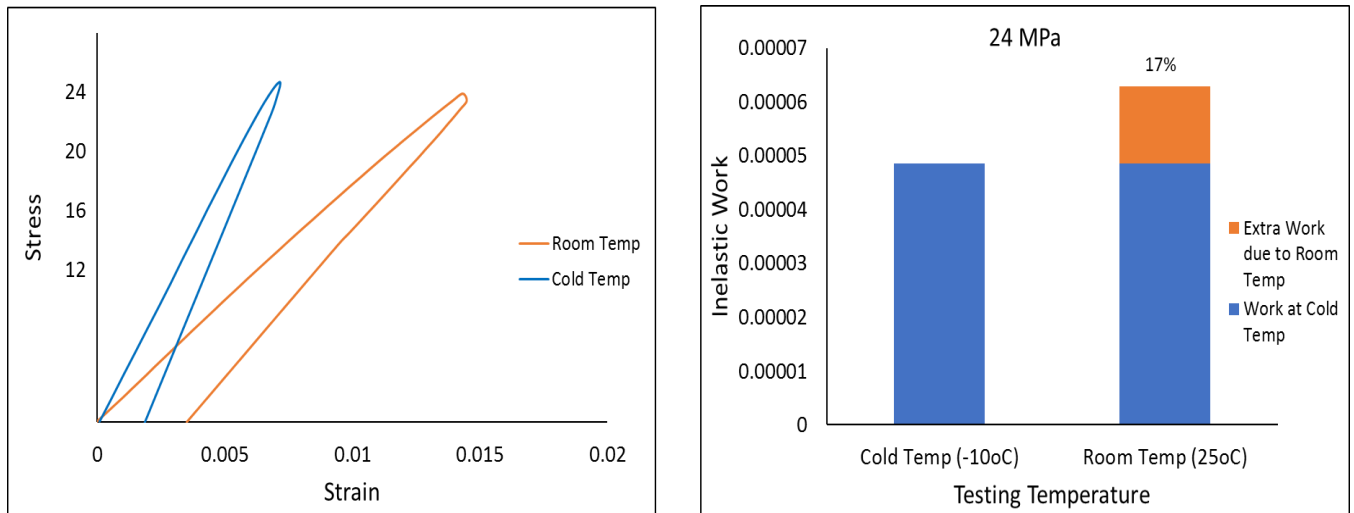


Figure 7.41: Hysteresis loops (right) with no dwelling and with 10s dwelling cycled at 24MPa, and bar chart for average inelastic work for both cases

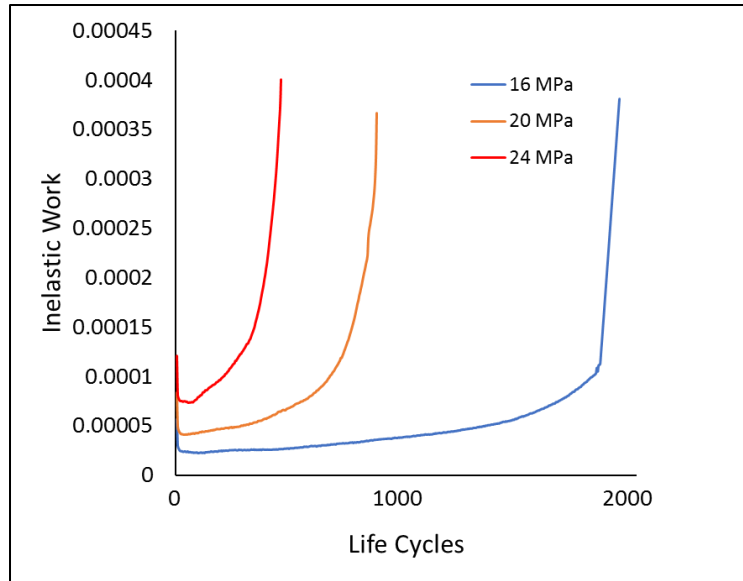


Figure 7.42: Evolution of inelastic work along SAC305 joints cycled at various stress level at -10°C

Inelastic Work per Cycle and Plastic Strain

Average inelastic work per cycle is critical parameter to demonstrate the related damage under fatigue test. Figure 7.43 illustrates the average inelastic work per cycle for both temperature cases. The average work per cycle noticed to be greater with higher stress levels when cycling joints at same temperature level. However, such increment amount of damage work is larger in room temperature case compared to the cold one of -10°C. Also, at certain stress level, increasing the testing temperature would increase the damage work per cycle. The effect of stress level on plastic strain for various testing temperatures is studied as shown in Figure 7.44. Similar trend is noticed of increasing the plastic strain with stress level at certain testing temperature. Moreover, at certain temperature level, increasing the stress level would increase the plastic strain per cycle.

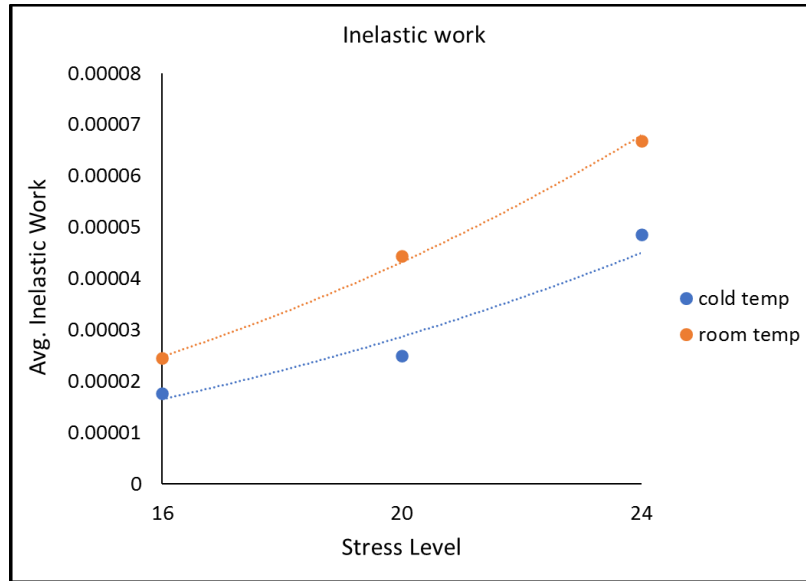


Figure 7.43: The effect of various stress levels on average inelastic work per cycle for joints tested at different temperature levels of 25°C and -10°C

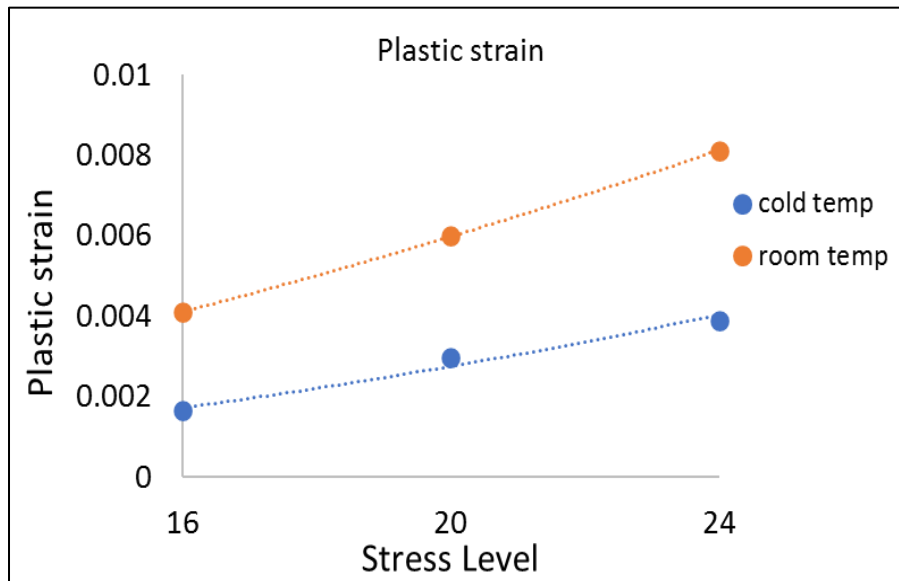


Figure 7.44: The effect of various stress levels on plastic strain for joints tested at different temperature levels of 25°C and -10°C

Morrow Energy Model

The general reliability model based on Morrow energy model is generated for -10oC as a function of inelastic work per cycle according to equation 7.8. Characteristic life as a function of inelastic work is plotted for various stress levels and fitted to a power equation as shown in Figure 7.45. Therefore, such results are fitted to a power equation and the characteristics life as a function of inelastic work cycle is obtained as shown in equation 7.16

$$N_{63} = 0.0038 * W^{-1.182} \dots\dots\dots(7.16)$$

Where N_{63} is the characteristic life, and W is the inelastic work per cycle. The fatigue ductility exponent (m) and fatigue ductility coefficient (C) are 0.853 and 0.0092, respectively. By substituting equation 7.16 into equation 7.1 instead of characteristic life, a general degradation in reliability is constructed as shown in equation 7.17

$$R(t) = e^{-\left(\frac{t}{0.0038 * W^{-1.182}}\right)^{5.5}} \dots\dots\dots(7.17)$$

Where W is the inelastic work per cycle, t is the number of cycles. The average of shape parameters for various conditions is considered of 5.5 since no trend is noticed among various conditions.

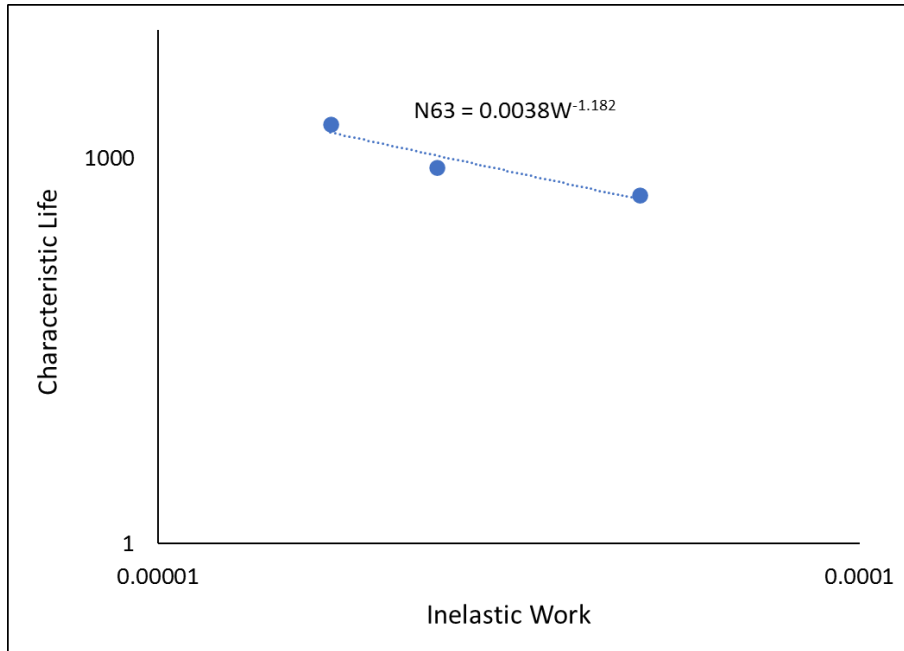


Figure 7.45: Characteristic life as a function of inelastic work per cycle for -10°C

Coffin-Mason Model

A general reliability model according to Coffin-Manson model is generated for -10oC conditions as a function of plastic strain according to equation 7.11. Therefore, the characteristic life as a function of plastic strain is plotted for various stress levels and fitted to a power equation as shown in Figure 7.46. Therefore, such results are fitted to a power equation and the characteristics life as a function of plastic strain is obtained as shown in equation 7.18

$$N_{63} = 0.1344 * S^{-1.488} \dots\dots\dots(7.18)$$

Where N_{63} is the characteristic life, and γ is the plastic strain. The fatigue ductility exponent (α) and fatigue ductility coefficient (γ) are 0.672 and 0.259, respectively. By substituting equation 7.18 into equation 7.1 instead of characteristic life, a general degradation in reliability is constructed as shown in equation 7.17

$$R(t) = e^{-\left(\frac{t}{0.1344 * \gamma^{-1.488}}\right)^{5.5}} \dots\dots\dots(7.17)$$

Where γ is the plastic strain, t is the number of cycles. The average of shape parameters for various conditions is considered of 5.5 since no trend is noticed among various conditions.

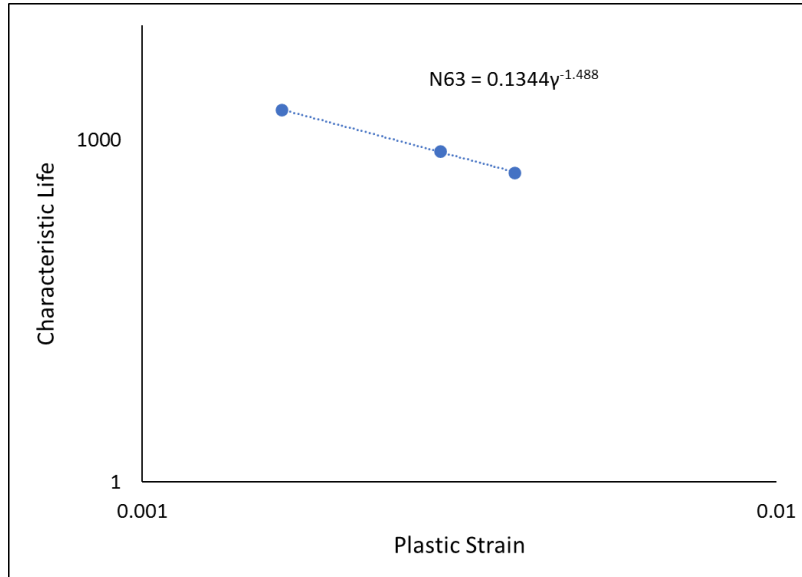


Figure 7.46: Characteristic life as a function of plastic strain for -10°C

7.4 Summary

In this study, Weibull distributions for each testing combinations of dwell time, stress level, and testing temperature are plotted. Results show that damage is enhanced by increasing the value of any testing parameters. Drop in characteristic life is a clear indication to be extracted from Weibull plots. Also, the changing in damage quantities of inelastic work and plastic strain when other parameters changeover is an obvious proof of the influence of these parameters. A general empirical model to predict the reliability is generated as a function of stress amplitude, dwell time and testing temperature based on S-N equation. Arrhenius term is utilized to compromise the temperature effect and a linear equation used to describe the dwell time effect. Moreover, general

models as a function plastic strain and inelastic work are constructed to predict the reliability based on Coffin-Manson and Morrow Energy Models, respectively. Both models were robust enough to predict reliability as a function testing temperature and average inelastic work per cycle and plastic strain. Finally, a comparison study is introduced to explore effect of very low temperature on life with room temperature. It concludes that even -10°C considered as low temperature, it's not for SAC305 alloy. Results show that cycling joints at such low temperature still produce damage but, in less manner, compared to room temperature.

Chapter 8: Conclusion and Future Works

8.1 Conclusions

First study discusses the effect of dwell time on SAC305 solder joint reliability. Accelerated shear fatigue tests were implemented to cycle individual joints under various dwell times (0, 10, 60, 180) and stress levels (16, 20, 24 MPa) at room temperature only. Two-parameter Weibull plots are generated for testing combination in order to observe the fatigue behavior under such conditions. Results show that life is reduced drastically with higher stress level at defined dwell time. However, similar trend is noticed for extending dwell time beyond 0s where such effect become less with longer dwellings. Consequently, a general model is constructed to describe the degradation in reliability for solder joints utilizing both dwell time and stress level. Hysteresis loop analysis are examined for all combination to investigate the influence of various testing parameters on damage quantities of inelastic work per cycle and plastic strain, since they calculated from stress-strain loops. Its concluded that increasing stress level or extending dwell period cause substantial increase in plastic strain or inelastic work per cycle. The reason is the creep damage that is activated due to dwell time and found to have great effect. It's pointless to extend dwell time beyond 180s since negligible drop in life and rise in damage quantities of plastic strain and inelastic work per cycle are noticed. The most common models to predict the life as a function of inelastic work and plastic strain are Morrow Energy and Coffin-Manson Model, respectively. Both models were robust in predicting the characteristic life as a function of dwell time and plastic astrain and inelastic work. Finally, general reliability models were generated accordingly based on inelastic work and plastic strain.

In the second study, temperature is introduced so that effects of various testing parameters; stress amplitude, dwell time, and testing temperatures are investigated. a slightly different fixture than

in first study is customized to fit with the chamber and offer testing individual joints as well. Weibull distribution for all conditions were plotted, examined, and compared for various testing combinations. As in previous study, results indicate that increasing dwell time and/or stress level would reduce the characteristic life radically. Furthermore, increasing the testing temperature found to have a great impact on fatigue life under constant dwellings and stress levels. Characteristic life is predicted as a function of stress level, dwell time, and testing temperature. The empirical model is generated considering the three parameters. Therefore, new terms are introduced to compromise for dwell time and temperature effect together. Arrhenius term is presented to accommodate for various temperature levels while an equation is utilized to represent the complexity of dwell time effect. Hysteresis loops evolution were studied for all combinations to investigate effects of various parameters on damage accumulation quantities of inelastic work and plastic strain. On the other hand, the evolution of inelastic work along the joint's life is analyzed to observe its behavior along its life. Increasing any of testing parameters would cause large raise in damage quantities of inelastic work and plastic strain. However, extending the dwell time at elevated temperature level would cause less effect on such damage quantities. This refers to greater creep damage related to elevated temperature compared to one related to dwellings. Finally, Morrow Energy and Coffin-Models were employed to investigate the performance of various testing conditions on reliability. Also, both were utilized to generate empirical models to predict the reliability as a function of plastic strain and inelastic work per cycle.

8.2 Future Works

This work might be extended by implementing combined creep-fatigue experiments with same dwellings at elevated temperature. Also, increasing the levels of stress amplitudes would be of great importance. It's good to correlate results of individual joints with one of the component levels

by performing thermal cycling tests involving same alloy of SAC305 and surface finish. No dedicated study was performed at Auburn University to investigate the reliability of SAC305 material only under various thermal cycling conditions and dwellings. The previous one's includes either doping alloy, different surface finish since OSP is not common in thermal cycling as ENIG is the most utilized one, different board types, or mismatch combination between solder paste and solder sphere. So, its highly recommended to explore such area with previously mentioned combination.

Introducing more stress levels, newly doped material, and most importantly various aging conditions of aging time and aging temperatures.

References:

- [1] Dally, James W., Pradeep Lall, and Jeffrey C. Suhling. Mechanical design of electronic systems. Knoxville, TN: College House Enterprises, 2008.
- [2] Prasad, Ray P Surface Mount Technology: Principles and Practice (2nd ed). Chapman & Hall, New York, 1997.
- [3] Puttlitz, Karl J., and Paul A. Totta, eds. Area array interconnection handbook. Springer Science & Business Media, 2012.
- [4] Rathore, H. S., Yih, R. C., and Edenfeld, A. R., "Fatigue Behavior of Solders Used in flip-Chip Technology," Journal of Testing and Evaluation, JTEVA, Vol. 1, No. 2, March 1973, pp. 170-178. DOI: [10.1520/JTE10895J](https://doi.org/10.1520/JTE10895J)
- [5] W. Engelmaier, "Fatigue Life of Leadless Chip Carrier Solder Joints During Power Cycling," in IEEE Transactions on Components, Hybrids, and Manufacturing technology, vol. 6, no. 3, pp. 232-237, September 1983. DOI: [10.1109/TCHMT.1983.1136183](https://doi.org/10.1109/TCHMT.1983.1136183).
- [6] Coombs, V. D., "An Investigation of Fatigue Life Performance in Lap-Type Solder Joints," Testing for Prediction of Material Performance in Structures and Components, ASTM STP 515, American Society for Testing and Materials, 1972, pp. 3-21. DOI: [10.1520/STP34675S](https://doi.org/10.1520/STP34675S)
- [7] Engelmaier, W., and Attarwala, A., 1989, "Surface-Mount Attachment Reliability of Clip Leaded Ceramic Chip Carriers on FR-4 Circuit Boards" IEEE Trans. Compon., Hybrids, Manuf. Technol.,12(2), pp. 284–296. DOI: [10.1109/33.31435](https://doi.org/10.1109/33.31435)
- [8] Murty, G. S., "Stress Relaxation In Superplastic Materials" J. Materials Sci., 1973, pp. 611-614. DOI: [10.1007/BF00550469](https://doi.org/10.1007/BF00550469)
- [9] J. H. Lau and Y.-H. Pao, "Solder Joint Reliability of BGA, CSP, Flip Chip, and Fine Pitch SMT Assemblies", McGraw-Hill New York, 1997.

- [10] R. A. Athamneh and S. Hamasha, "Fatigue Behavior of SAC-Bi and SAC305 Solder Joints with Aging," in IEEE Transactions on Components, Packaging and Manufacturing Technology. DOI: [10.1109/TCPMT.2019.2949719](https://doi.org/10.1109/TCPMT.2019.2949719)
- [11] Z. Hai, J. Zhang, C. Shen, J. L. Evans, M. J. Bozack, M. M. Basit, J. C. Suhling, "Reliability Comparison of Aged SAC Fine-Pitch Ball Grid Array Packages Versus Surface Finishes", vol. 5, no. 6, pp. 828-837, 2015. DOI: [10.1109/TCPMT.2015.2420566](https://doi.org/10.1109/TCPMT.2015.2420566)
- [12] S. Hamasha, S. Su, F. Akkara, P. Borgesen, "Effect of Cycling Amplitude Variations on SnAgCu Solder Joint Fatigue Life", IEEE Transactions CPMT, 2018. DOI: [10.1109/TCPMT.2018.2795347](https://doi.org/10.1109/TCPMT.2018.2795347)
- [13] R. A. Athamneh et al., "Effect of Aging on the Fatigue Life and Shear Strength of SAC305 Solder Joints in Actual Setting Conditions," 2019 18th IEEE Intersociety Conference on Thermal and Thermomechanical Phenomena in Electronic Systems (ITherm), Las Vegas, NV, USA, 2019, pp. 1146-1154.
- [14] S. Su et al., "Fatigue Properties of Lead-free Doped Solder Joints," 2018 17th IEEE Intersociety Conference on Thermal and Thermomechanical Phenomena in Electronic Systems (ITherm), San Diego, CA, 2018, pp. 1243-1248. DOI: [10.1109/ITHERM.2018.8419566](https://doi.org/10.1109/ITHERM.2018.8419566)
- [15] H. Ma, J. C. Suhling, "A review of mechanical properties of lead-free solders for electronic packaging", Journal of materials science, vol. 44, no. 5, pp. 1141-1158, 2009. DOI [10.1007/s10853-008-3125-9](https://doi.org/10.1007/s10853-008-3125-9)
- [16] M. S. Alam, J. C. Suhling and P. Lall, "High temperature tensile and creep behavior of lead free solders," 2017 16th IEEE Intersociety Conference on Thermal and Thermomechanical Phenomena in Electronic Systems (ITherm), Orlando, FL, 2017, pp. 1229-1237. DOI: [10.1109/ITHERM.2017.7992625](https://doi.org/10.1109/ITHERM.2017.7992625)

- [17] A. Fahim, S. Ahmed, J. C. Suhling and P. Lall, "Nanomechanical Characterization of Intermetallic Compounds in Lead Free Solder Joints," 2018 IEEE 68th Electronic Components and Technology Conference (ECTC), San Diego, CA, 2018, pp. 2359-2359. DOI: [10.1109/ECTC.2018.00355](https://doi.org/10.1109/ECTC.2018.00355)
- [18] C. Andersson, Z. Lai, J. Liu, H. Jiang, Y. Yu, "Comparison of isothermal mechanical fatigue properties of lead-free solder joints and bulk solders", Materials Science and Engineering: A , vol. 394, no. 1-2, pp. 20-27, 2005. DOI: [10.1016/j.msea.2004.10.043](https://doi.org/10.1016/j.msea.2004.10.043)
- [19] Korhonen, T.-M. K., Lehman, L. P., Korhonen, M. a, & Henderson, D. W. "Isothermal Fatigue Behavior of the Near-Eutectic Sn-Ag-Cu Alloy between -25°C and 125°C ". Journal "of Electronic Materials, 36(2), 173-178, 2001. DOI: [10.1007/s11664-006-0048-6](https://doi.org/10.1007/s11664-006-0048-6)
- [20] Dompierre, B., Aubin, V., Charkaluk, E., Maia Filho, W. C., & Brizoux, M. "Influence of Thermal Ageing on Cyclic Mechanical Properties of SnAgCu Alloys for Microelectronic Assemblies". Procedia Engineering, 2(1), 1477-1486 2010. DOI: [10.1016/j.proeng.2010.03.159](https://doi.org/10.1016/j.proeng.2010.03.159)
- [21] G. Paradee and A. Christou, "Stress Relaxation Behavior and Low Cycle Fatigue Behavior of Bulk SAC305," 2011 International Semiconductor Device Research Symposium (ISDRS), College Park, MD, 2011, pp. 1-2. DOI: [10.1007/s10854-014-2138-1](https://doi.org/10.1007/s10854-014-2138-1)
- [22] J. H. Lau, "Solder Joint Reliability: Theory and Applications", Springer Science & Business Media, 1991
- [23] Kariya, Y., & Suga, T. "Low-Cycle Fatigue Properties of Eutectic Solders at High Temperatures". Fatigue & Fracture of Engineering Materials and Structures, 30(5), 413-419, 2007. DOI: [10.1111/j.1460-2695.2006.01091.x](https://doi.org/10.1111/j.1460-2695.2006.01091.x)

- [24] Kanchanomai, Chaosuan, Miyashita, Y., & Mutoh, Yoshiharu. “Low-Cycle Fatigue Behavior of Sn-Ag, Sn-Ag-Cu, and Sn-Ag-Cu-Bi Lead-Free Solders”. *Journal of Electronic Materials*, 31(5), 456-465, 2007. DOI: [10.1007/s11664-002-0100-0](https://doi.org/10.1007/s11664-002-0100-0)
- [25] Pang, J. H. L., Xiong, B., & Low, T. “Creep and Fatigue Characterization of Lead Free 95.5 Sn-3.8 Ag-0.7 Cu Solder”. *Proceedings from the 54th Electronic Components and Technology Conference (Vol. 2, pp. 1333–1337)*, 2001. DOI: [10.1109/ECTC.2004.1320285](https://doi.org/10.1109/ECTC.2004.1320285)
- [26] Y. Zhang, K. Kurumaddali, J. C. Suhling, P. Lall, M. J. Bozack, "Analysis of The Mechanical Behavior Microstructure and Reliability of Mixed Formulation Solder Joints", *Proceedings of the 59th IEEE Electronic Components and Technology Conference*, pp. 759-770, May 27-29, 2009. DOI: [10.1109/ECTC.2009.5074098](https://doi.org/10.1109/ECTC.2009.5074098)
- [27] K. C. Norris and A. H. Landzberg, "Reliability of Controlled Collapse Interconnections," in *IBM Journal of Research and Development*, vol. 13, no. 3, pp. 266-271, May 1969. DOI: [10.1147/rd.133.0266](https://doi.org/10.1147/rd.133.0266)
- [28] Solomon, H., 1986, “Fatigue of 60/40 Solder”, *IEEE Trans. Compon., Hybrids,Manuf. Technol.*,9(4), pp. 423–432. DOI: [10.1109/TCHMT.1986.1136672](https://doi.org/10.1109/TCHMT.1986.1136672)
- [29] Kanchanomai, C., Mutoh, Y. Low-Cycle Fatigue Prediction Model for Pb-Free solder 96.5Sn-3.5Ag”, *Journal of Elec Materi* 33, 329–333 (2004). DOI: [10.1007/s11664-004-0139-1](https://doi.org/10.1007/s11664-004-0139-1)
- [30] Syed, A., 2001, “Predicting Solder Joint Reliability for Thermal, Power, and Bend Cycle Within 25% Accuracy,” *51st Electronic Components and Technol-ogy Conference, Orlando, FL, May 29–June 1*, pp. 255–263. DOI: [10.1109/ECTC.2001.927732](https://doi.org/10.1109/ECTC.2001.927732)
- [31] Syed, A., 2004, “Accumulated Creep Strain and Energy Density Based Thermal Fatigue Life Prediction Models for SnAgCu Solder Joints,” *54th Electronic Components and Technology Conference (ECTC), Las Vegas, NV, June 4*, pp.737–746. DOI: [10.1109/ECTC.2004.1319419](https://doi.org/10.1109/ECTC.2004.1319419)

- [32] Dalton, Eric, et al. "Accelerated Temperature Cycling Induced Strain and Failure Behaviour for BGA Assemblies of Third Generation High Ag Content Pb-Free Solder Alloys." *Materials & Design*, vol. 154, 2018, pp. 184–191. DOI: [10.1016/j.matdes.2018.05.030](https://doi.org/10.1016/j.matdes.2018.05.030)
- [33] W. Engelmaier, "The Use Environments of Electronic Assemblies and Their Impact On Surface Mount Solder Attachment Reliability," *InterSociety Conference on Thermal Phenomena in Electronic Systems*, Las Vegas, NV, USA, 1990, pp. 8-15. DOI: [10.1109/33.62538](https://doi.org/10.1109/33.62538)
- [34] N. Pan, "An Acceleration Model for Sn-Ag-Cu Solder Joint Reliability Under Various Thermal Cycle Conditions", *Proceeding of SMTAI*, 2006.
- [35] Weiping Liu, P. Bachorik and Ning-Cheng Lee, "The Superior Drop Test Performance of SAC-Ti Solders and Its Mechanism," 2008 33rd IEEE/CPMT International Electronics Manufacturing Technology Conference (IEMT), Penang, 2008, pp. 1-9. DOI: [10.1109/IEMT.2008.5507779](https://doi.org/10.1109/IEMT.2008.5507779)
- [36] M. Wu and J. Lan, "Prediction of Fatigue Resistance in Lead-Free Ni-Doped SAC 1205 Solder Alloys Using a Rate-Dependent Material Model and Subjected to Drop Tests," in *IEEE Transactions on Components, Packaging and Manufacturing Technology*, vol. 8, no. 10, pp. 1777-1787, Oct. 2018. DOI: [10.1109/TCPMT.2018.2869248](https://doi.org/10.1109/TCPMT.2018.2869248)
- [37] A. Syed, T. S. Kim, Y. M. Cho, C. W. Kim and M. Yoo, "Alloying Effect of Ni, Co, and Sb in SAC Solder for Improved Drop Performance of Chip Scale Packages with Cu OSP Pad Finish," 2006 8th Electronics Packaging Technology Conference, Singapore, 2006, pp. 404-411. DOI: [10.1109/EPTC.2006.342750](https://doi.org/10.1109/EPTC.2006.342750)
- [38] Mei, Z., Kaufmann, M., Eslambolchi, A., & Johnson, P. (1998, May). "Brittle Interfacial Fracture of PBGA Packages Soldered On Electroless Nickel/Immersion Gold", In *Electronic*

Components & Technology Conference, 1998. 48th IEEE (pp. 952-961). IEEE. DOI: [10.1109/ECTC.1998.678824](https://doi.org/10.1109/ECTC.1998.678824)

[39] N. Vijayakumar et al., "The Effect of Iso-Thermal Aging On Vibrational Performance of SAC 105 and 305 Alloys," 2013 IEEE International Symposium on Advanced Packaging Materials, Irvine, CA, 2013, pp. 69-81. DOI: [10.1109/ISAPM.2013.6510389](https://doi.org/10.1109/ISAPM.2013.6510389)

[40] P. Lall, V. Yadav, J. Suhling and D. Locker, "Reliability of Leadfree Solders in High Temperature Vibration in Automotive Environments," 2019 18th IEEE Intersociety Conference on Thermal and Thermomechanical Phenomena in Electronic Systems (ITherm), Las Vegas, NV, USA, 2019, pp. 566-585. DOI: [10.1109/ITHERM.2019.8757226](https://doi.org/10.1109/ITHERM.2019.8757226)

[41] D. Leslie, T. Heid, A. Dasgupta, "Effect of temperature on vibration fatigue of SAC105 solder material after extended room temperature aging", 2018 19th International Conference on Thermal Mechanical and Multi-Physics Simulation and Experiments in Microelectronics and Microsystems (EuroSimE), pp. 1-5, 2018. DOI: [10.1109/EuroSimE.2018.8369938](https://doi.org/10.1109/EuroSimE.2018.8369938)

[42] S. Steinberg, J. Wiley, "Preventing thermal cycling and vibration failures in electronic equipment", 9th Annual IEEE Dayton Chapter Symposium, 1988

[43] G. R. Henderson, A. G. Piersol, "Fatigue damage related descriptor for random vibration test environments", Sound and Vibration, vol. 29, no. 10, pp. 20-24, 1995

[44] J. Hu, "Life prediction and damage acceleration based on the power spectral density of random vibration", Journal of the IES, vol. 38, no. 1, pp. 34-40, 1995

[45] K. Upadhyayula, A. Dasgupta, "An incremental damage superposition approach for reliability of electronic interconnects under combined accelerated stresses", ASME International Mechanical Engineering Congress & Exposition, pp. 16-21, 1997

- [46] R. Li, "A Methodology for Fatigue Prediction of Electronic Components Under Random Vibration Load", *Journal of Electronic Packaging*, vol. 123, pp. 394-400, Dec. 2001. DOI: [10.1115/1.1372318](https://doi.org/10.1115/1.1372318)
- [47] H. Fu, P. Singh and J. Zhang, "Creep corrosion test in flowers of sulfur chamber," 2014 International Conference on Electronics Packaging (ICEP), Toyama, 2014, pp. 197-201. DOI: [10.1109/ICEP.2014.6826688](https://doi.org/10.1109/ICEP.2014.6826688)
- [48] M. Reid et al., "The Corrosion of Electronic Resistors," in *IEEE Transactions on Components and Packaging Technologies*, vol. 30, no. 4, pp. 666-672, Dec. 2007. DOI: [10.1109/TCAPT.2007.901749](https://doi.org/10.1109/TCAPT.2007.901749)
- [49] B. Medgyes, P. Tamási, G. Kósa, D. Rigler and L. Gál, "Morphological and composition study on lead-free micro-alloyed solders after corrosion test," 2016 39th International Spring Seminar on Electronics Technology (ISSE), Pilsen, 2016, pp. 245-248. DOI: [10.1109/ISSE.2016.7563198](https://doi.org/10.1109/ISSE.2016.7563198)
- [50] Comizzoli, R. B., Frankenthal, R. P., Milner, P. C., & Sinclair, J. D., "Corrosion of electronic materials and devices", *Science*, 234(4774), 340-345, (1986). DOI: [10.1126/science.234.4774.340](https://doi.org/10.1126/science.234.4774.340)
- [51] Z. Cai, Y. Zhang, J. C. Suhling, P. Lall, R. W. Johnson and M. J. Bozack, "Reduction of lead free solder aging effects using doped SAC alloys," 2010 Proceedings 60th Electronic Components and Technology Conference (ECTC), Las Vegas, NV, 2010, pp. 1493-1511. DOI: [10.1109/ECTC.2010.5490796](https://doi.org/10.1109/ECTC.2010.5490796)
- [52] J. Gu, Y. Lei, J. Lin, H. Fu, X. Xie and Z. Wu, "The study of Sn-0.3Ag-0.7Cu and Sn-1.0Ag-0.5Cu solder joint reliability under board level drop impact," 2015 16th International Conference on Electronic Packaging Technology (ICEPT), Changsha, 2015, pp. 491-496. DOI: [10.1109/ICEPT.2015.7236634](https://doi.org/10.1109/ICEPT.2015.7236634)

- [53] Kariya, Y. & Otsuka, M. *Journal of Elec Material* (1998) 27: 1229.
- [54] H. Xu, T. Lee and C. Kim, "Fatigue properties of lead-free solder joints in electronic packaging assembly investigated by isothermal cyclic shear fatigue," 2014 IEEE 64th Electronic Components and Technology Conference (ECTC), Orlando, FL, 2014, pp. 133-138. DOI: [10.1109/ECTC.2014.6897278](https://doi.org/10.1109/ECTC.2014.6897278)
- [55] Dompierre, B., Aubin, V., Charkaluk, E., Filho, W. C. M., & Brizoux, M. "Cyclic mechanical behaviour of Sn3.0Ag0.5Cu alloy under high temperature isothermal aging". *Materials Science and Engineering: A*, 528(13-14), 4812-4818 2011. DOI: [10.1016/j.msea.2011.03.001](https://doi.org/10.1016/j.msea.2011.03.001)
- [56] H. Pang, K. Tan, X. Shi, Z. Wang, "Microstructure and intermetallic growth effects on shear and fatigue strength of solder joints subjected to thermal cycling aging", *Materials Science and Engineering: A*, vol. 307, pp. 42-50, 2001. DOI: [10.1016/S0921-5093\(00\)01958-4](https://doi.org/10.1016/S0921-5093(00)01958-4)
- [57] A. El-Daly, A. El-Taher, T. Dalloul, "Enhanced ductility and mechanical strength of Ni-doped Sn–3.0 Ag–0.5 Cu lead-free solders", *Materials & Design*, vol. 55, pp. 309-318, 2014. DOI: [10.1016/j.matdes.2013.10.009](https://doi.org/10.1016/j.matdes.2013.10.009)
- [58] M. Wickham, J. Nottay, C. Hunt, "A review of mechanical test method standards for lead-free solders. National Physical Laboratory", 2001. DOI:
- [59] M. Mahmudur Chowdhury, M. A. Hoque, S. Ahmed, J. C. Suhling, S. Hamasha and P. Lall, "Effects of Mechanical Cycling on the Microstructure of SAC305 Lead Free Solder," 2018 17th IEEE Intersociety Conference on Thermal and Thermomechanical Phenomena in Electronic Systems (ITherm), San Diego, CA, 2018, pp. 1324-1332. DOI: [10.1109/ITHERM.2018.8419523](https://doi.org/10.1109/ITHERM.2018.8419523)
- [60] N. Fu, S. Ahmed, J. C. Suhling, P. Lall, "Visualization of Microstructural Evolution in Lead Free Solders During Isothermal Aging Using Time-Lapse Imagery", *Proceedings of the 67th*

Electronic Components and Technology Conference, pp. 429-440, May 30 - June 2, 2017. DOI: [10.1109/ECTC.2017.333](https://doi.org/10.1109/ECTC.2017.333)

[61] H. Ma, J. C. Suhling, P. Lall, M. J. Bozack, "Reliability of the Aging Lead-Free Solder Joint", Proceeding of the 56th IEEE Electronic Components and Technology Conference, pp. 849-864, 2006. DOI: [10.1109/ECTC.2006.1645757](https://doi.org/10.1109/ECTC.2006.1645757)

[62] H. Ma, J. C. Suhling, Y. Zhang, P. Lall, M. J. Bozack, "The Influence of Elevated Temperature Aging on Reliability of Lead Free Solder Joints", Proceedings of the 57th IEEE Electronic Components and Technology Conference, pp. 653-668, May 29-June 1, 2007. DOI: [10.1109/ECTC.2007.373867](https://doi.org/10.1109/ECTC.2007.373867)

[63] Z. Cai, Y. Zhang, J. C. Suhling, P. Lall, R. W. Johnson, M. J. Bozack, "Reduction of Lead Free Solder Aging Effects Using Doped SAC Alloys", Proceedings of the 60th IEEE Electronic Components and Technology Conference, pp. 1493-1511, June 2-4, 2010. DOI: [10.1109/ECTC.2010.5490796](https://doi.org/10.1109/ECTC.2010.5490796)

[64] M. Motalab, Z. Cai, J. C. Suhling, J. Zhang, J. L. Evans, M. J. Bozack, P. Lall, "Improved Predictions of Lead Free Solder Joint Reliability That Include Aging Effects", Proceedings of the 62nd IEEE Electronic Components and Technology Conference, pp. 513-531, May 30 - June 1, 2012. DOI: [10.1109/ECTC.2012.6248879](https://doi.org/10.1109/ECTC.2012.6248879)

[65] M. Motalab, Z. Cai, J. C. Suhling, J. Zhang, J. L. Evans, M. J. Bozack, P. Lall, "Improved Predictions of Lead Free Solder Joint Reliability That Include Aging Effects", Proceedings of the 62nd IEEE Electronic Components and Technology Conference, pp. 513-531, May 30 - June 1, 2012. DOI: [10.1109/ECTC.2012.6248879](https://doi.org/10.1109/ECTC.2012.6248879)

- [66] J. Zhang, Z. Hai, S. Thirugnanasambandam, J. L. Evans, M. J. Bozack, R. Sesek, Y. Zhang, J. C. Suhling, "Correlation of Aging Effects on Creep Rate and Reliability in Lead Free Solder Joints", SMTA Journal, vol. 25, no. 3, pp. 19-28, 2012. DOI: [10.1109/TCPMT.2013.2251932](https://doi.org/10.1109/TCPMT.2013.2251932)
- [67] Y. Zhang, K. Kurumaddali, J. C. Suhling, P. Lall, M. J. Bozack, "Analysis of the Mechanical Behavior Microstructure and Reliability of Mixed Formulation Solder Joints", Proceedings of the 59th IEEE Electronic Components and Technology Conference, pp. 759-770, May 27-29, 2009. DOI: [10.1109/ECTC.2009.5074098](https://doi.org/10.1109/ECTC.2009.5074098)
- [68] M. Mustafa, Z. Cai, J. C. Suhling, P. Lall, "The Effects of Aging on the Cyclic Stress-Strain Behavior and Hysteresis Loop Evolution of Lead Free Solders", Proceedings of the 61st IEEE Electronic Components and Technology Conference, pp. 927-939, June 1-3, 2011. DOI: [10.1109/ECTC.2011.5898623](https://doi.org/10.1109/ECTC.2011.5898623)
- [69] N. Fu, J. C. Suhling, P. Lall, "Cyclic Stress-Strain Behavior of SAC305 Lead Free Solder: Effects of Aging Temperature Strain Rate and Plastic Strain Range", Proceedings of the 66th IEEE Electronic Components and Technology Conference, pp. 1119-1127, May 31 - June 3, 2016. DOI: [10.1109/ECTC.2016.345](https://doi.org/10.1109/ECTC.2016.345)
- [70] M. M. R. Chowdhury, N. Fu, J. C. Suhling, P. Lall, "Evolution of the Cyclic Stress-Strain Behavior of Doped SAC Solder Materials Subjected to Isothermal Aging", Proceedings of ITherm 2017, pp. 1369-1379, May 30 – June 2, 2017. DOI: [10.1109/ITHERM.2017.7992641](https://doi.org/10.1109/ITHERM.2017.7992641)
- [71] C. Zhao, C. Shen, Z. Hai, M. M. Basit, J. Zhang, M. J. Bozack, J. L. Evans, J. C. Suhling, "Long Term Aging Effects on the Reliability of Lead Free Solder Joints in Ball Grid Array Packages with Various Pitch Sizes and Ball Arrangements", SMTA Journal, vol. 29, no. 2, pp. 37-46, 2016.

- [72] Z. Hai, J. Zhang, C. Shen, E. K. Snipes, J. C. Suhling, M. J. Bozack, J. L. Evans, "Reliability Degradation of SAC105 and SAC305 BGA Packages Under Long-Term High Temperature Aging", *SMTA Journal*, vol. 27, no. 2, pp. 11-18, 2014.
- [73] J. Zhang, Z. Hai, S. Thirugnanasambandam, J. L. Evans, M. J. Bozack, Y. Zhang, J. C. Suhling, "Thermal Aging Effects on Thermal Cycling Reliability of Lead-Free Fine Pitch Packages", *IEEE Transactions on Components Packaging and Manufacturing Technology*, vol. 3, no. 8, pp. 1348-1357, 2013. DOI: [10.1109/TCPMT.2013.2251932](https://doi.org/10.1109/TCPMT.2013.2251932)
- [74] M. Basit, M. Motalab, J. C. Suhling, Z. Hai, J. L. Evans, M. J. Bozack, P. Lall, "Thermal Cycling Reliability of Aged PBGA Assemblies - Comparison of Weibull Failure Data and Finite Element Model Predictions", *Proceedings of the 65th IEEE Electronic Components and Technology Conference*, pp. 106-117, May 27-29, 2015. DOI: [10.1109/ECTC.2015.7159579](https://doi.org/10.1109/ECTC.2015.7159579)
- [75] R. W. Evans and B. Wilshire, "Creep of Metals and Alloys," 1985
- [76] M. F. Ashby, "A First Report on Deformation-Mechanism Maps," *Acta Metallurgica*, vol. 20, no. 7, pp. 887-897, 1972. DOI: [10.1016/0001-6160\(72\)90082-X](https://doi.org/10.1016/0001-6160(72)90082-X)
- [77] J. Weertman, "Steady-State Creep through Dislocation Climb," *Journal of Applied Physics*, vol. 28, p. 362, 1957. DOI: [10.1063/1.1722747](https://doi.org/10.1063/1.1722747)
- [78] Weertman, J., "Theory of steady-state creep based on dislocation climb", *Journal of Applied Physics*, 26(10), 1213-1217., (1955). DOI: [10.1063/1.1721875](https://doi.org/10.1063/1.1721875)
- [79] R. L. Coble, "A Model for Boundary Diffusion Controlled Creep in Polycrystalline Materials," *Journal of Applied Physics*, vol. 34, p. 1679, 1963. DOI: [10.1063/1.1702656](https://doi.org/10.1063/1.1702656)
- [80] C. Herring, "Diffusional Viscosity of a Polycrystalline Solid," *Journal of Applied Physics*, vol. 21, pp. 437-445, 1950. DOI: [10.1063/1.1699681](https://doi.org/10.1063/1.1699681)

- [81] A. Fahim, S. Ahmed, J. C. Suhling and P. Lall, "Mechanical Characterization of Intermetallic Compounds in SAC Solder Joints at Elevated Temperatures," 2018 17th IEEE Intersociety Conference on Thermal and Thermomechanical Phenomena in Electronic Systems (ITherm), San Diego, CA, 2018, pp. 1081-1090. DOI: [10.1109/ITHERM.2018.8419525](https://doi.org/10.1109/ITHERM.2018.8419525)
- [82] S. Ahmed, M. Hasnine, J. C. Suhling and P. Lall, "Mechanical Characterization of SAC Solder Joints at High Temperature Using Nanoindentation," 2017 IEEE 67th Electronic Components and Technology Conference (ECTC), Orlando, FL, 2017, pp. 1128-1135. DOI: [10.1109/ECTC.2017.336](https://doi.org/10.1109/ECTC.2017.336)
- [83] J. Wu, N. Fu, S. Ahmed, J. C. Suhling and P. Lall, "Investigation of Microstructural Evolution in SAC Solders Exposed to Short-Term and Long-Term Aging," 2018 17th IEEE Intersociety Conference on Thermal and Thermomechanical Phenomena in Electronic Systems (ITherm), San Diego, CA, 2018, pp. 1234-1242. DOI: [10.1109/ITHERM.2018.8419474](https://doi.org/10.1109/ITHERM.2018.8419474)
- [84] A. Fahim, S. Ahmed, J. C. Suhling and P. Lall, "Nanomechanical characterization of IMCs formed in SAC solder joints subjected to isothermal aging," 2017 16th IEEE Intersociety Conference on Thermal and Thermomechanical Phenomena in Electronic Systems (ITherm), Orlando, FL, 2017, pp. 1398-1408. DOI: [10.1109/ITHERM.2017.7992645](https://doi.org/10.1109/ITHERM.2017.7992645)
- [85] Vayman, S., Fine, M.E. & Jeannotte, D.A. Isothermal fatigue of low tin lead based solder. MTA 19, 1051–1059 (1988).
- [86] X.Q. Shi, H.L.J. Pang, W. Zhou, and Z.P. Wang, Scripta Mater. 41, 289 (1999).
- [87] JSMS Standards, JSMS-SD-3-00: Standard Method for Low Cycle Fatigue Testing of Solder Materials (Kyoto: Japan: The Society of Material Science, 2000), pp. 1–51.
- [88] Monkman, F., 1956, "An Empirical Relationship Between Rupture Life and Minimum Creep Rate in Creep-Rupture Tests," Proc. ASTM,56, pp. 91–103.

[89] Miner, M., 1945, "Cumulative Damage in Fatigue," ASME J. Appl. Mech.,12(3), pp. A159–A164

[90] Osterman, Michael, Abhijit Dasgupta, and Bongtae Han. "A strain range based model for life assessment of Pb-free SAC solder interconnects." 56th Electronic Components and Technology Conference 2006. IEEE, 2006. DOI: [10.1109/ECTC.2006.1645760](https://doi.org/10.1109/ECTC.2006.1645760)

[91] Salmela, Olli. "Acceleration factors for lead-free solder materials." IEEE transactions on components and packaging technologies 30.4 (2007): 700-707. DOI: [10.1109/TCAPT.2007.900076](https://doi.org/10.1109/TCAPT.2007.900076)

[92] Maxim Serebreni¹, Nathan Blattau¹, Craig Hillman¹, Ravi Bhatkal², Gyan Dutt², Ranjit Pandher, "FATIGUE LIFE PREDICTION MODEL FOR LEDS ON METAL CORE PRINTED CIRCUIT BOARDS (MCPCBS) WITH PB-FREE SOLDER ALLOY".

[93] P. Lall, N. Singh, M. Strickland, J. Blanche and J. Suhling, "Decision-Support Models for Thermo-Mechanical Reliability of Leadfree Flip-Chip Electronics in Extreme Environments," Proceedings Electronic Components and Technology, 2005. ECTC '05., Lake Buena Vista, FL, 2005, pp. 127-136.

[94] Pierce, D. M., Sheppard, S. D., Vianco, P. T., Regent, J. A., & Grazier, J. M. (2008). Fatigue Life Prediction Methodology for Lead-Free Solder Alloy Interconnects: Development and Validation. ASME J. Electron. Packag., 130(1), 11003.

Appendices

Appendix A

Weibull Plots

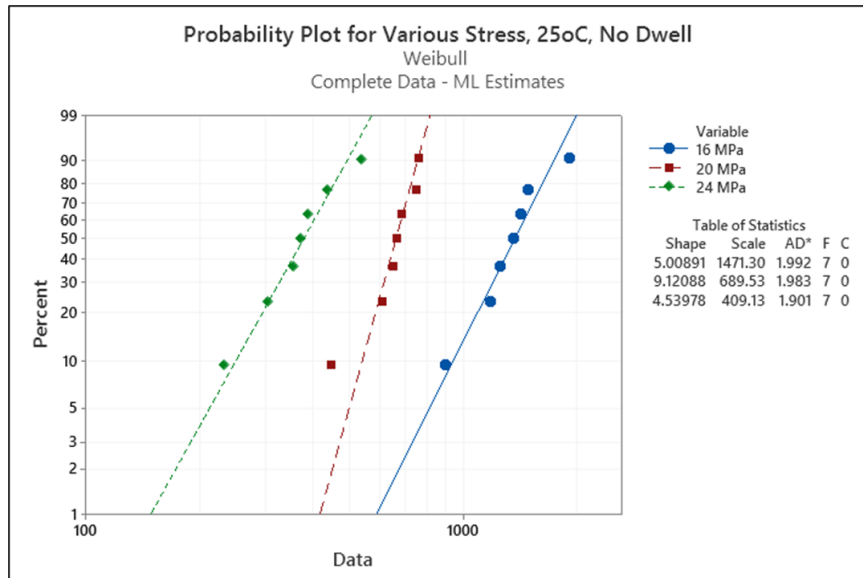


Figure A.1: Weibull Plot for joints cycled with various stress amplitudes at 25oC with 0s of dwelling condition

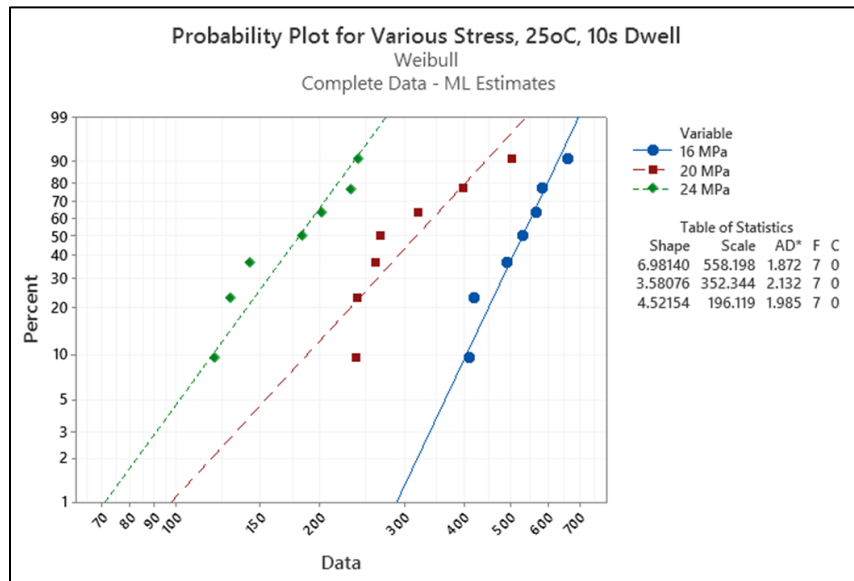


Figure A.2: Weibull Plot for joints cycled with various stress amplitudes at 25oC with 10s of dwelling condition

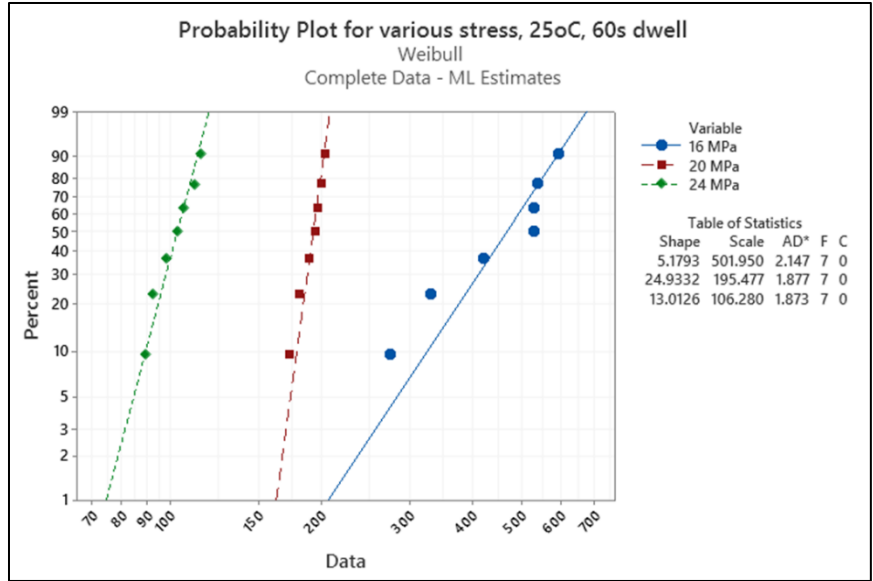


Figure A.3: Weibull Plot for joints cycled with various stress amplitudes at 25oC with 60s of dwelling condition

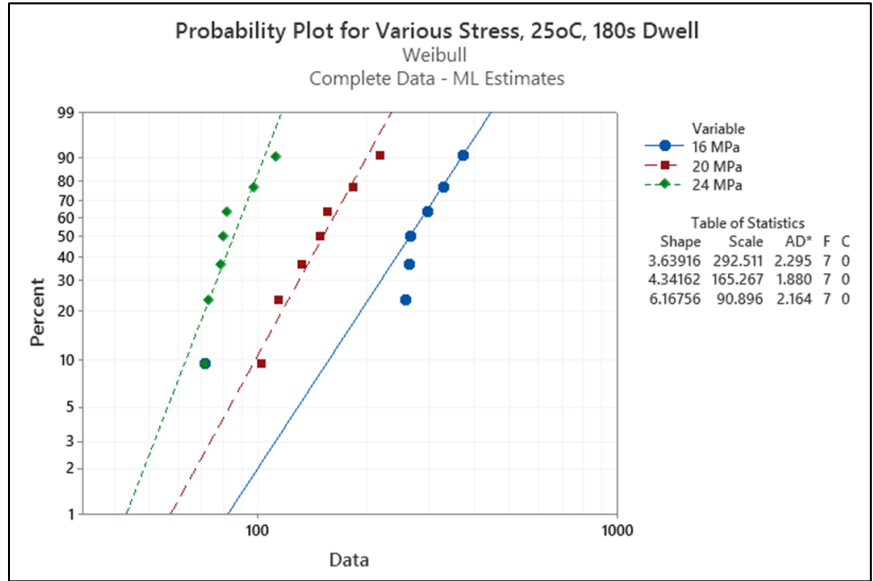


Figure A.4: Weibull Plot for joints cycled with various stress amplitudes at 25oC with 180s of dwelling condition

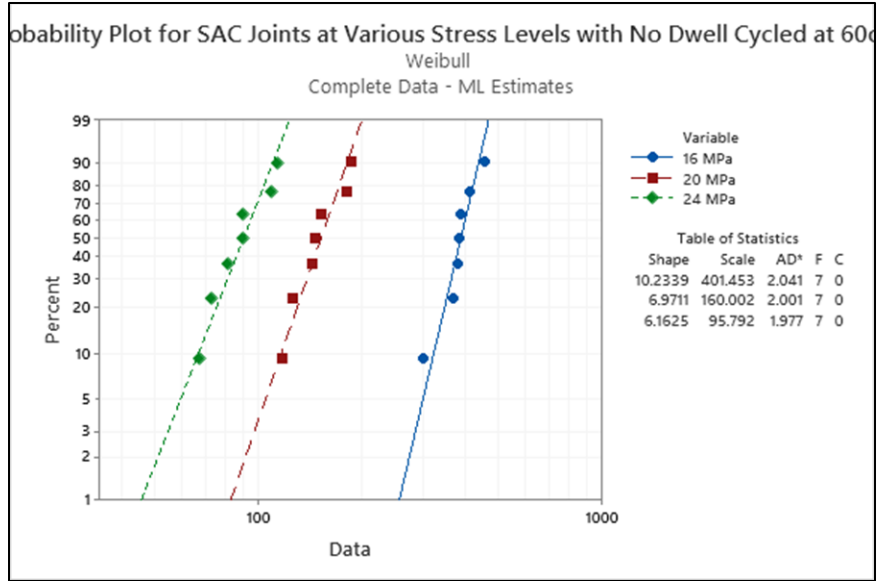


Figure A.5: Weibull Plot for joints cycled with various stress amplitudes at 60°C with 0s of dwelling condition

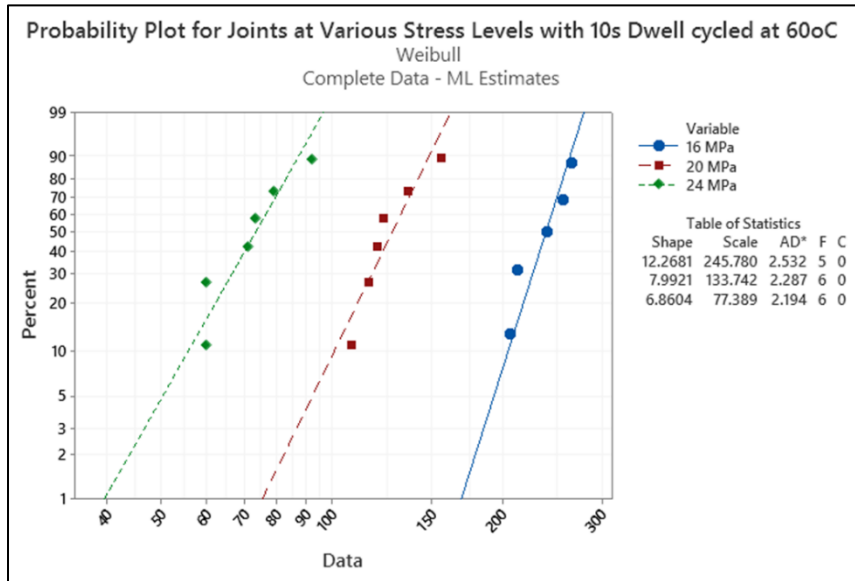


Figure A.6: Weibull Plot for joints cycled with various stress amplitudes at 60°C with 10s of dwelling condition

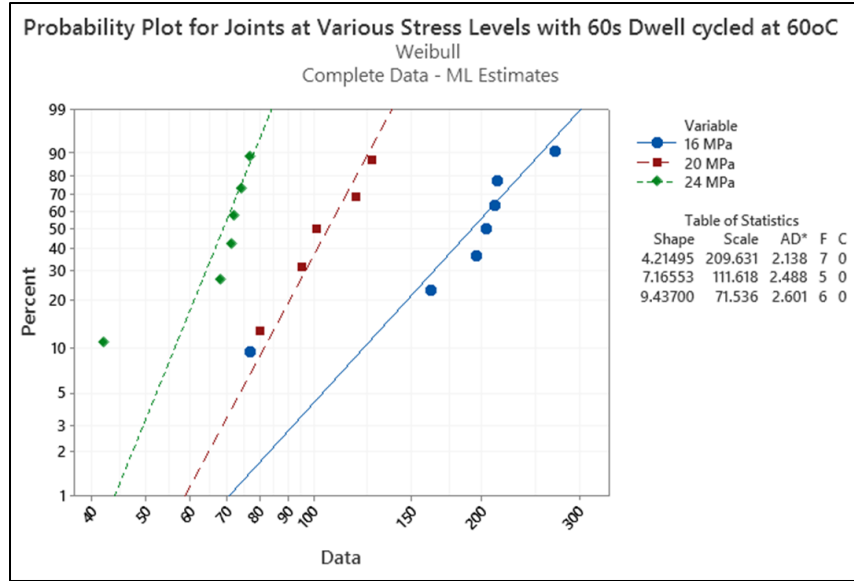


Figure A.7: Weibull Plot for joints cycled with various stress amplitudes at 60oC with 60s of dwelling condition

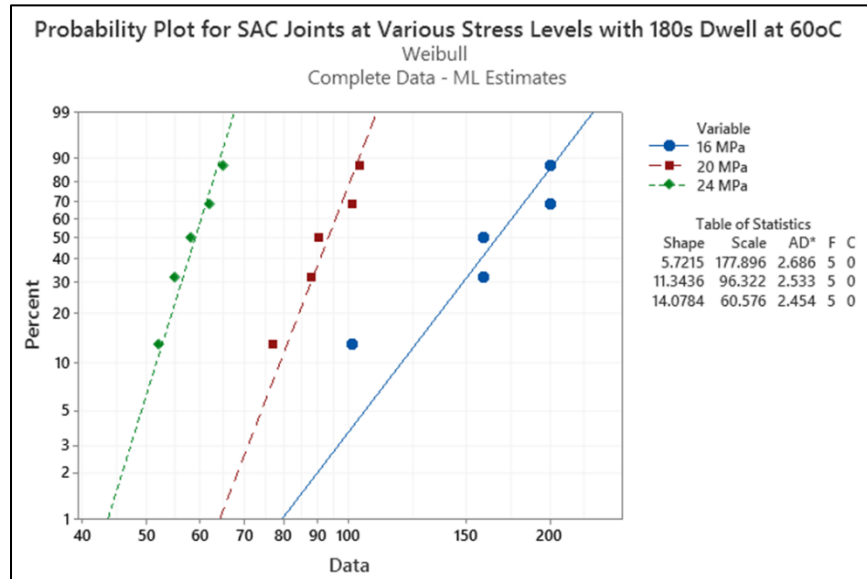


Figure A.8: Weibull Plot for joints cycled with various stress amplitudes at 60oC with 180s of dwelling condition

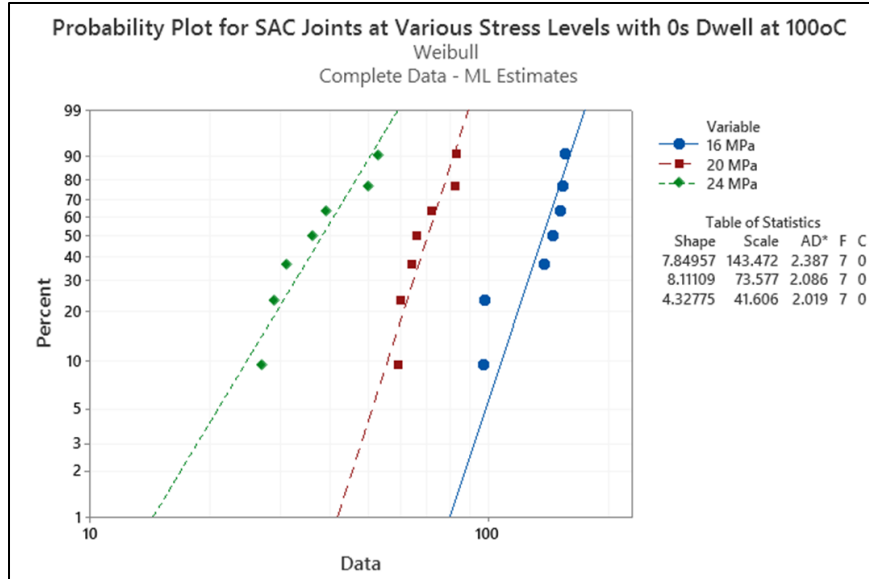


Figure A.9: Weibull Plot for joints cycled with various stress amplitudes at 100oC with 0s of dwelling condition

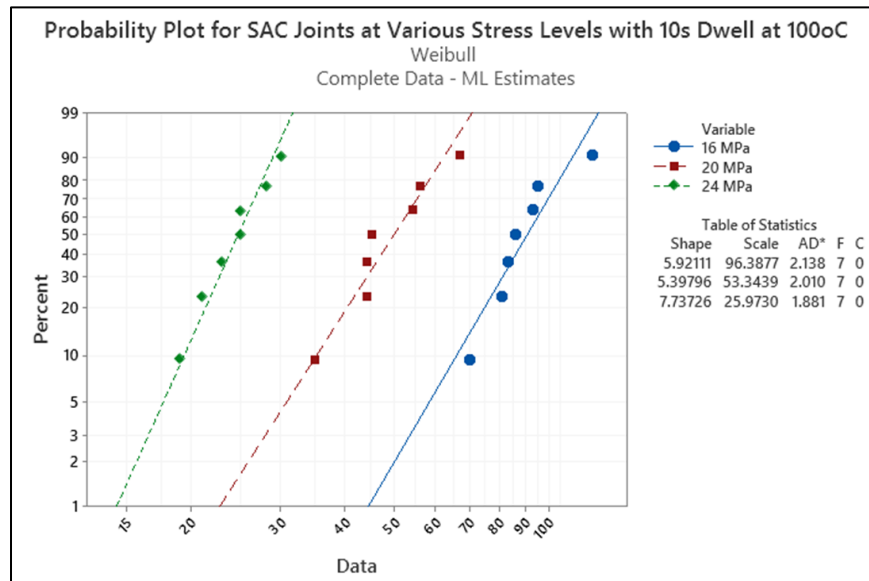


Figure A.10: Weibull Plot for joints cycled with various stress amplitudes at 100oC with 10s of dwelling condition

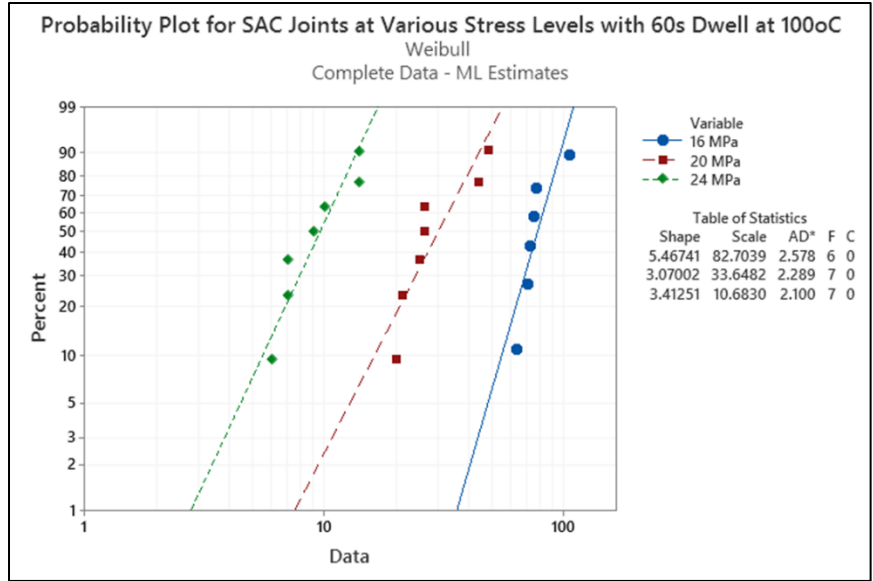


Figure A.11: Weibull Plot for joints cycled with various stress amplitudes at 100oC with 60s of dwelling condition

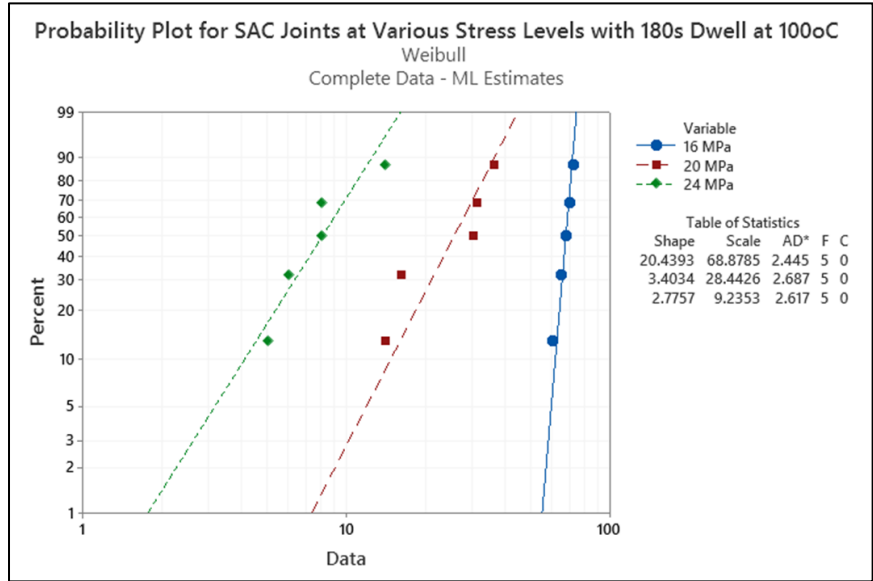


Figure A.12: Weibull Plot for joints cycled with various stress amplitudes at 100oC with 180s of dwelling condition

Appendix B

Hysteresis Loop and Work as a Function of Cycles Plots

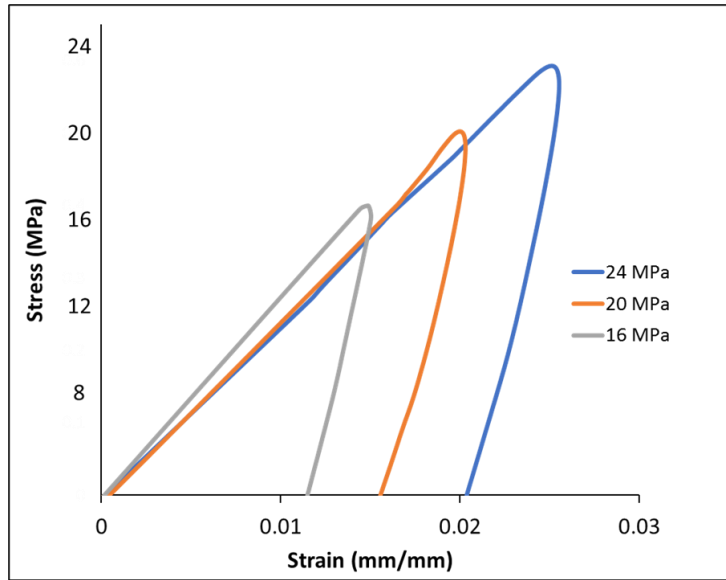


Figure B.1: Stress-strain loop for joints cycled with various stress amplitudes at 25°C with 0s of dwelling condition

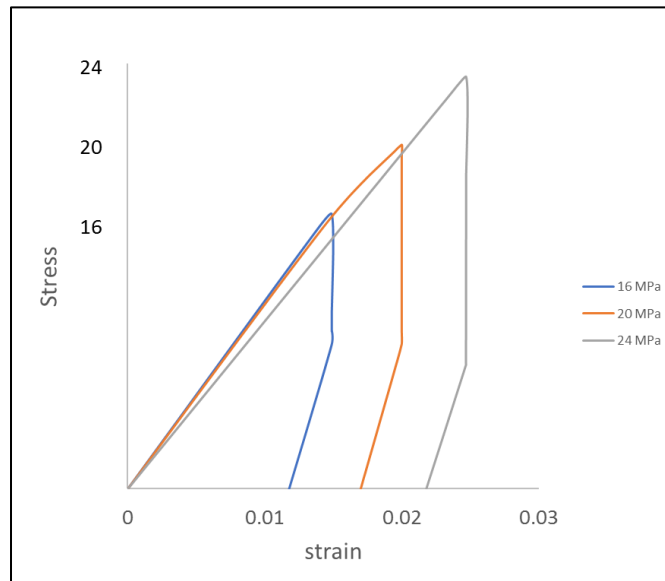


Figure B.2: Stress-strain loop for joints cycled with various stress amplitudes at 25°C with 10s of dwelling condition

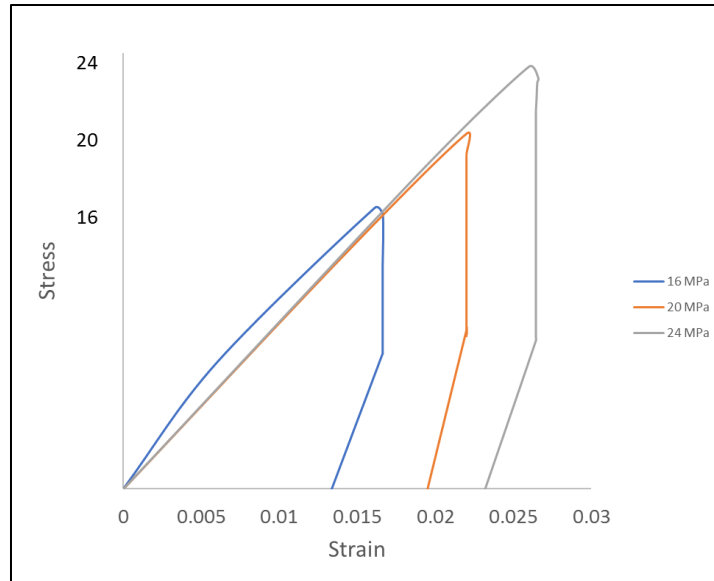


Figure B.3: Stress-strain loop for joints cycled with various stress amplitudes at 25°C with 60s of dwelling condition

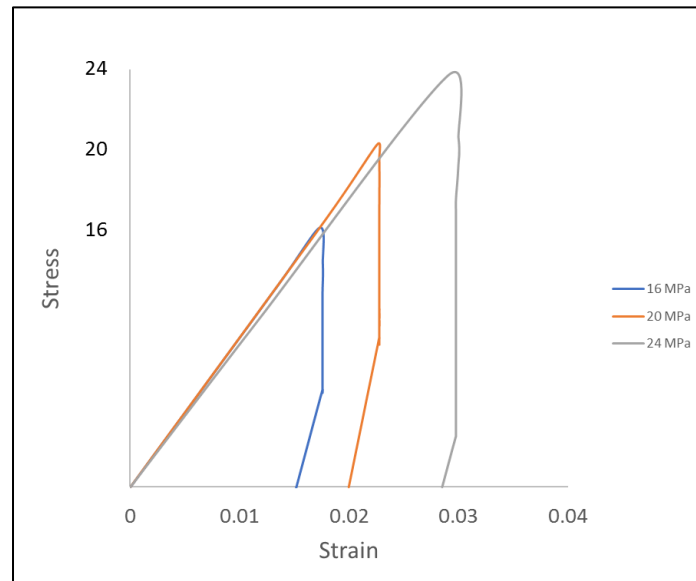


Figure B.4: Stress-strain loop for joints cycled with various stress amplitudes at 25°C with 180s of dwelling condition

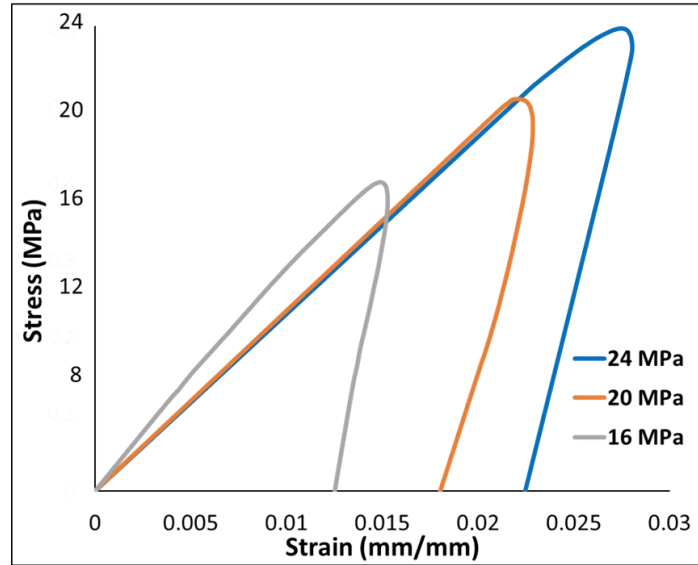


Figure B.5: Stress-strain loop for joints cycled with various stress amplitudes at 60°C with 0s of dwelling condition

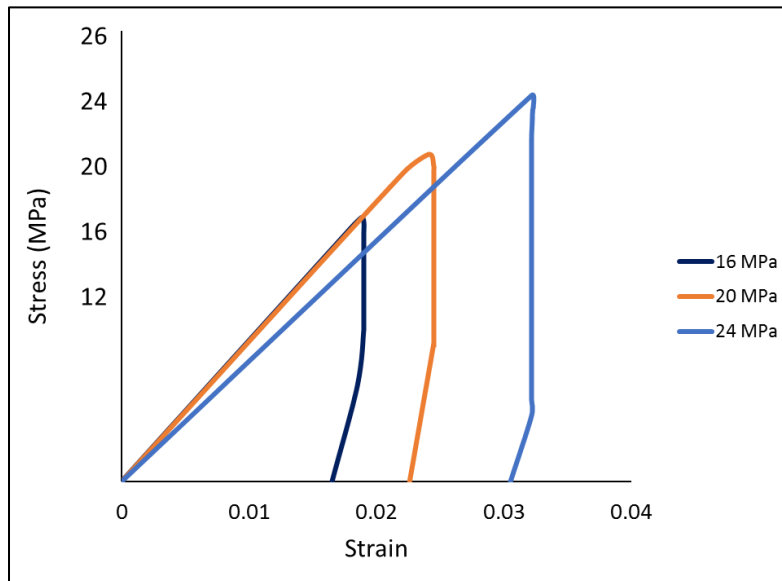


Figure B.6: Stress-strain loop for joints cycled with various stress amplitudes at 60°C with 10s of dwelling condition

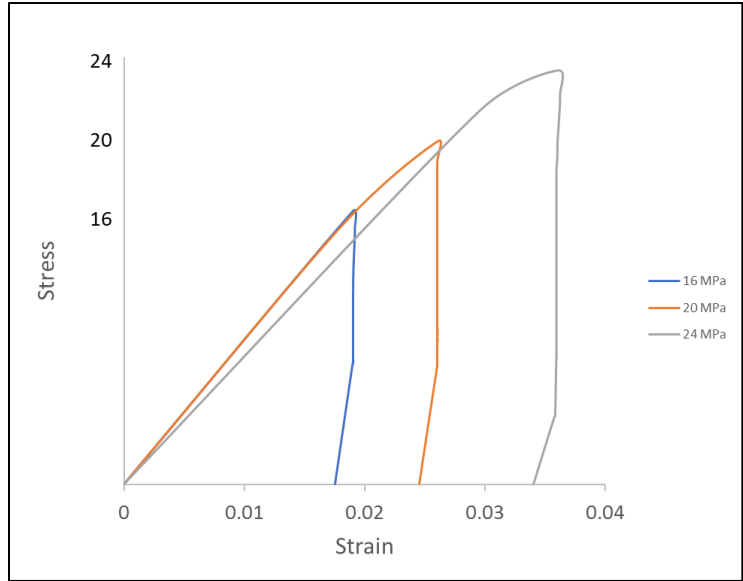


Figure B.7: Stress-strain loop for joints cycled with various stress amplitudes at 60°C with 60s of dwelling condition

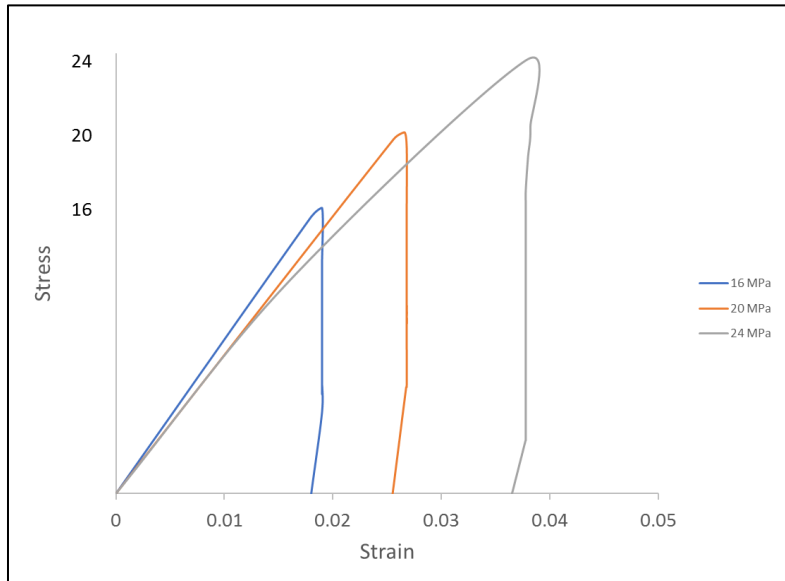


Figure B.8: Stress-strain loop for joints cycled with various stress amplitudes at 60°C with 180s of dwelling condition

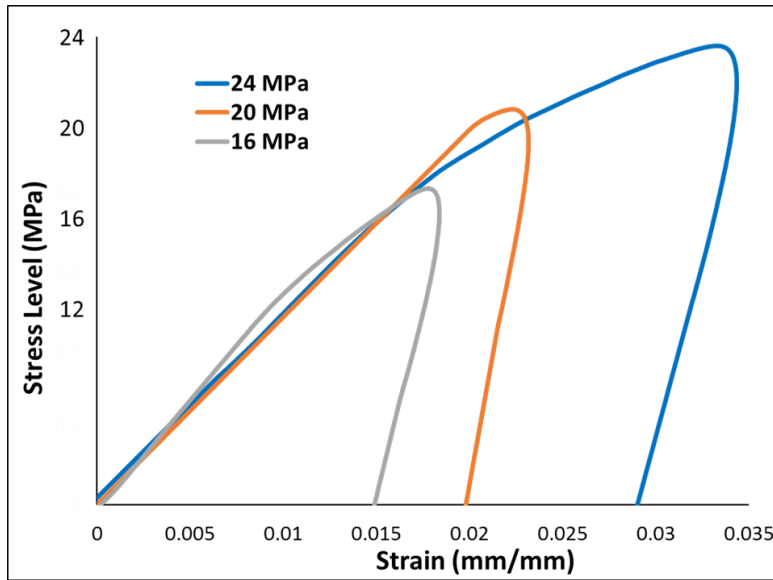


Figure B.9: Stress-strain loop for joints cycled with various stress amplitudes at 100°C with 0s of dwelling condition

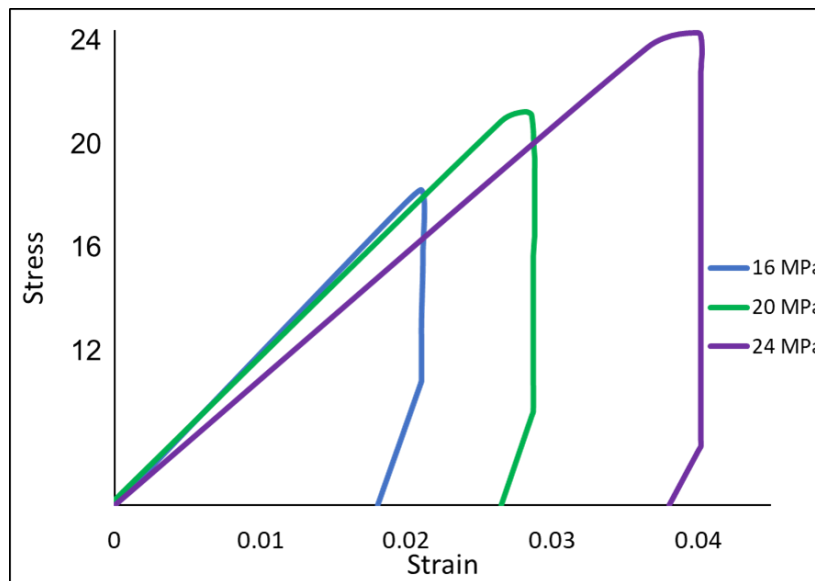


Figure B.10: Stress-strain loop for joints cycled with various stress amplitudes at 100°C with 10s of dwelling condition

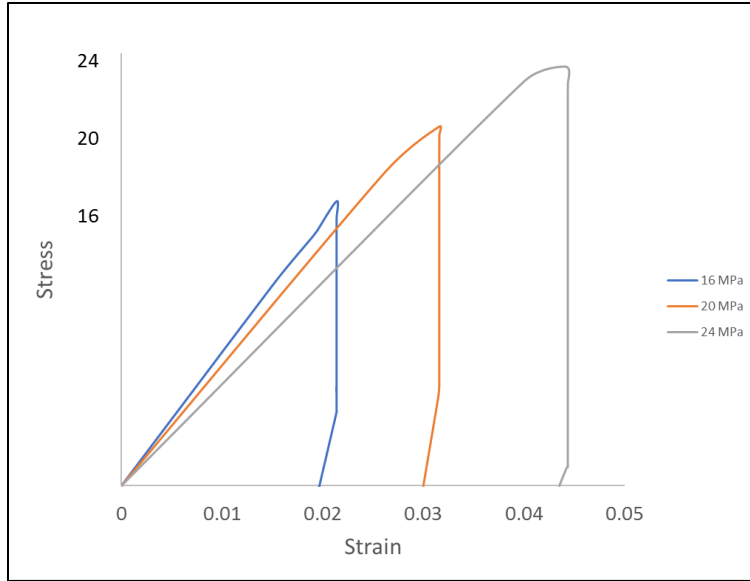


Figure B.11: Stress-strain loop for joints cycled with various stress amplitudes at 100°C with 60s of dwelling condition

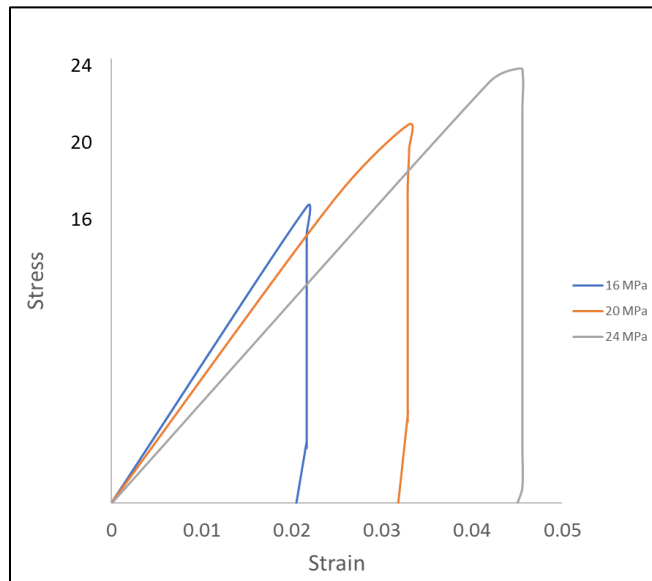


Figure B.12: Stress-strain loop for joints cycled with various stress amplitudes at 100°C with 180s of dwelling condition

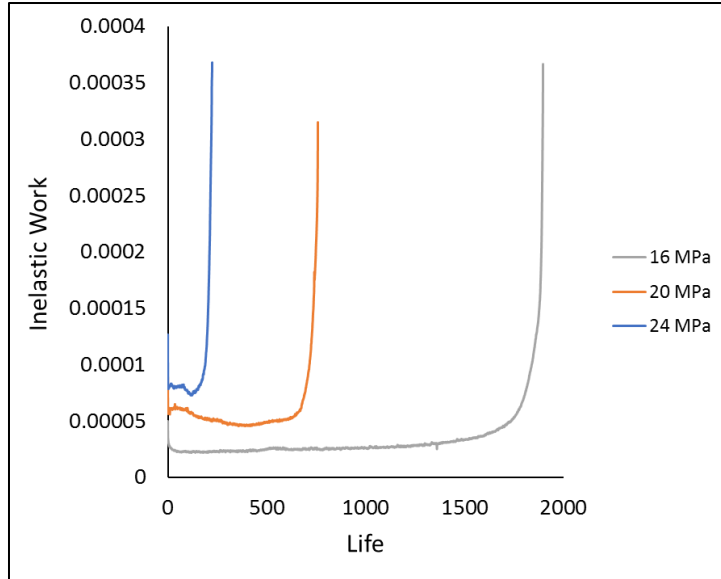


Figure B.13: Work as a function of life cycles for joints cycled with various stress amplitudes at 25oC with 0s of dwelling condition

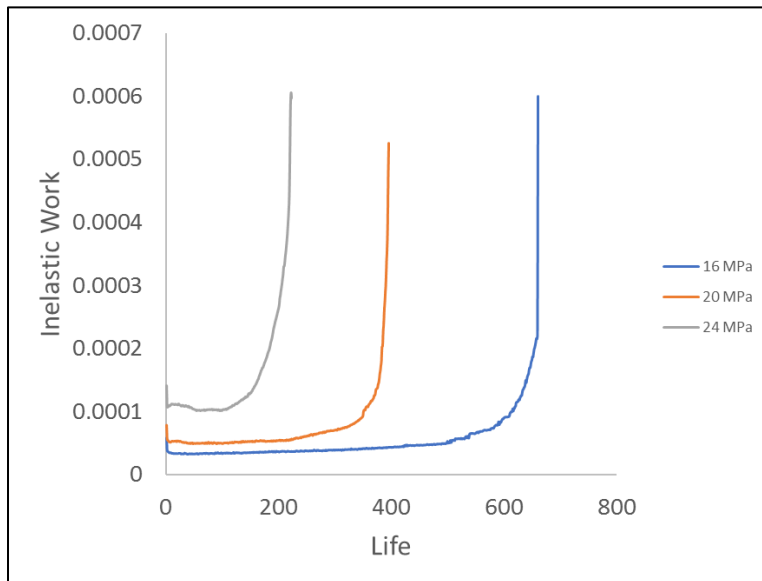


Figure B.14: Work as a function of life cycles for joints cycled with various stress amplitudes at 25oC with 10s of dwelling condition

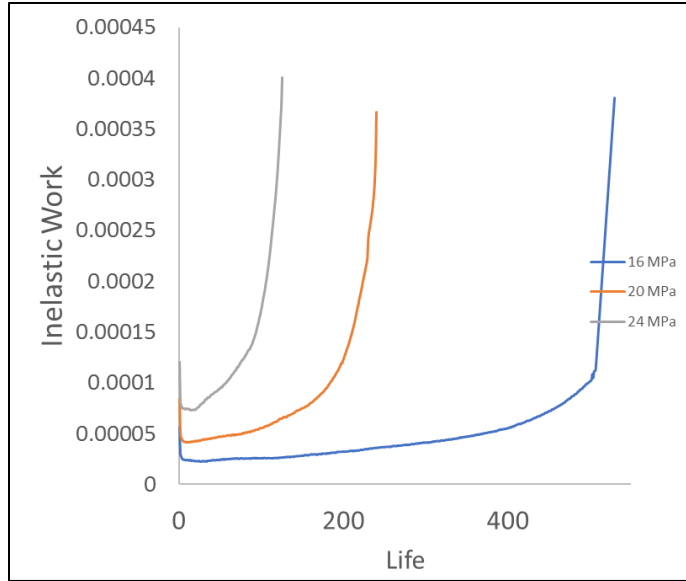


Figure B.15: Work as a function of life cycles for joints cycled with various stress amplitudes at 25oC with 60s of dwelling condition

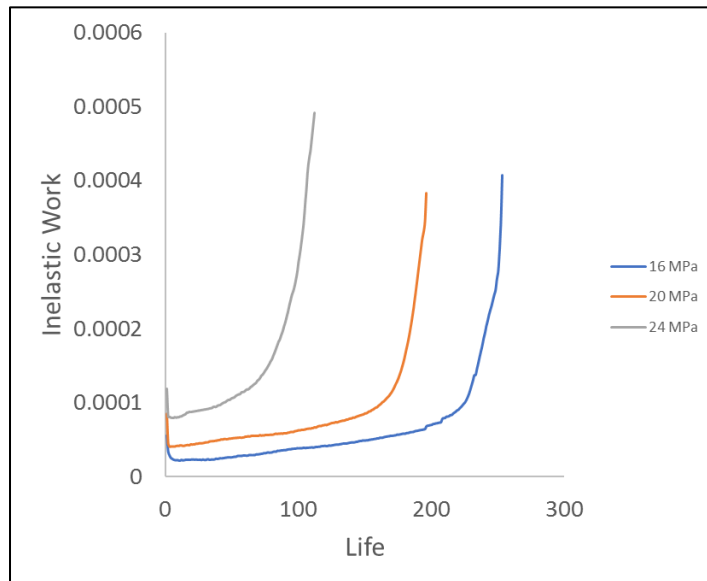


Figure B.16: Work as a function of life cycles for joints cycled with various stress amplitudes at 25oC with 180s of dwelling condition

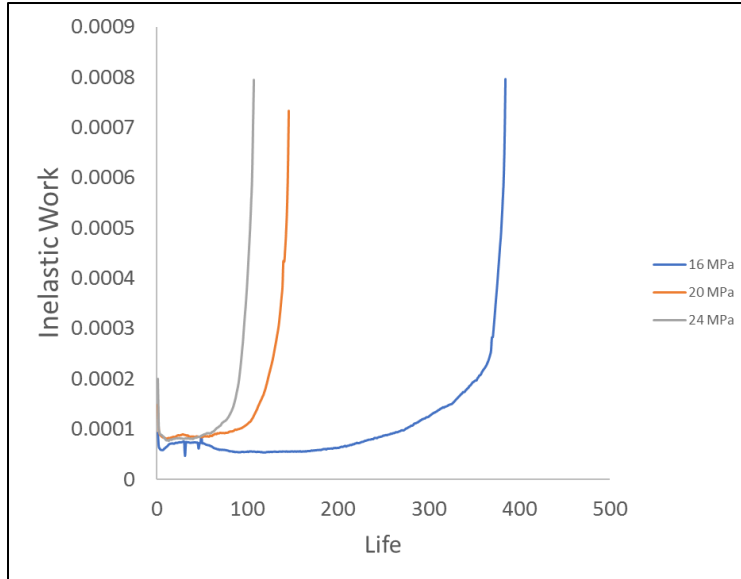


Figure B.17: Work as a function of life cycles for joints cycled with various stress amplitudes at 60°C with 0s of dwelling condition

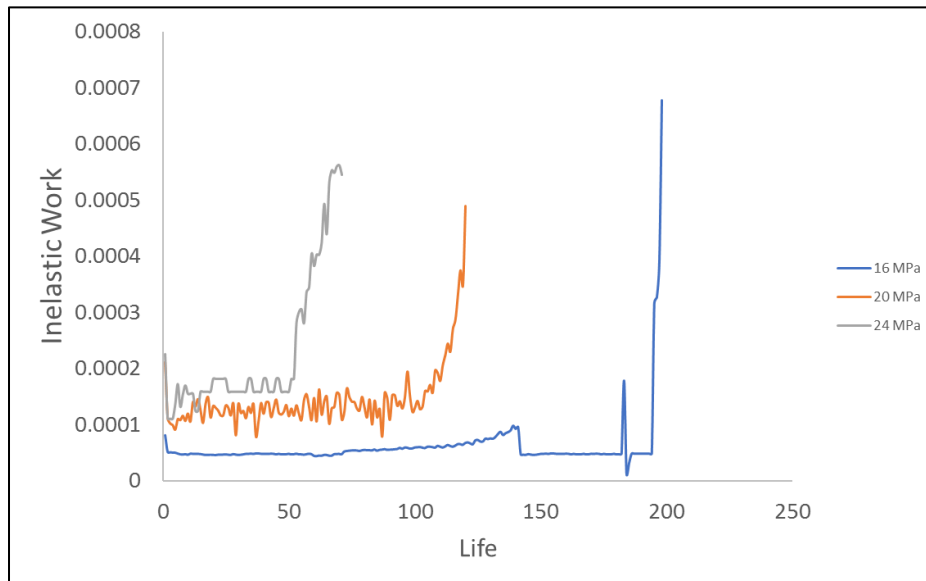


Figure B.18: Work as a function of life cycles for joints cycled with various stress amplitudes at 60°C with 10s of dwelling condition

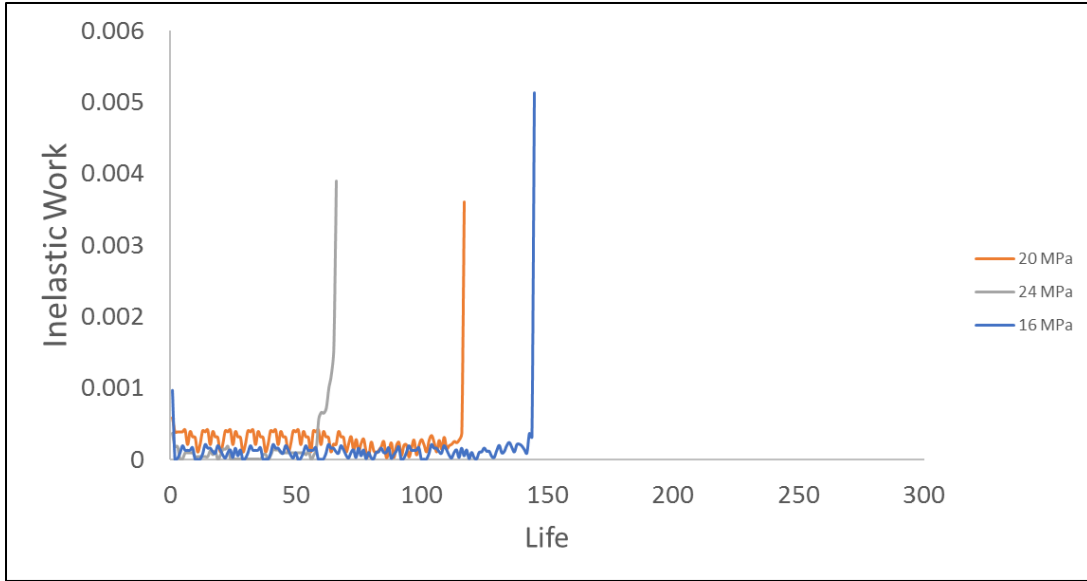


Figure B.19: Work as a function of life cycles for joints cycled with various stress amplitudes at 60°C with 60s of dwelling condition

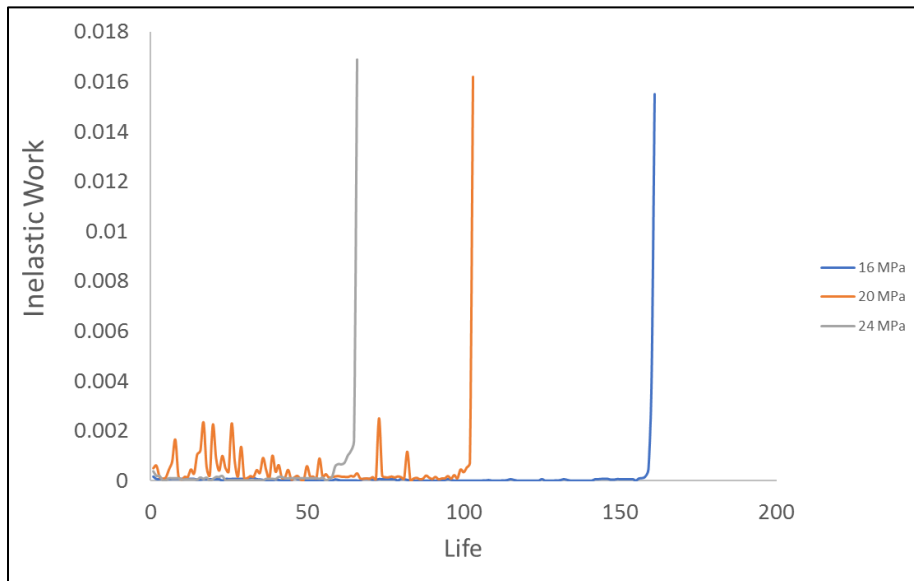


Figure B.20: Work as a function of life cycles for joints cycled with various stress amplitudes at 60°C with 180s of dwelling condition

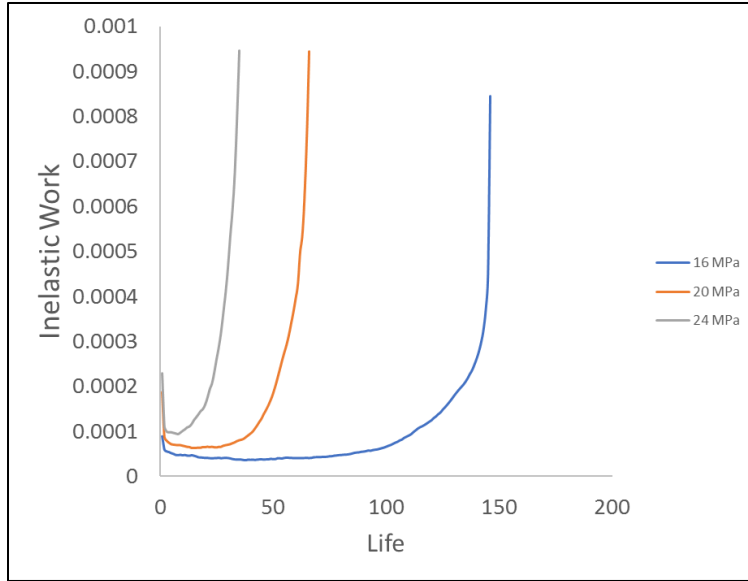


Figure B.21: Work as a function of life cycles for joints cycled with various stress amplitudes at 100°C with 0s of dwelling condition

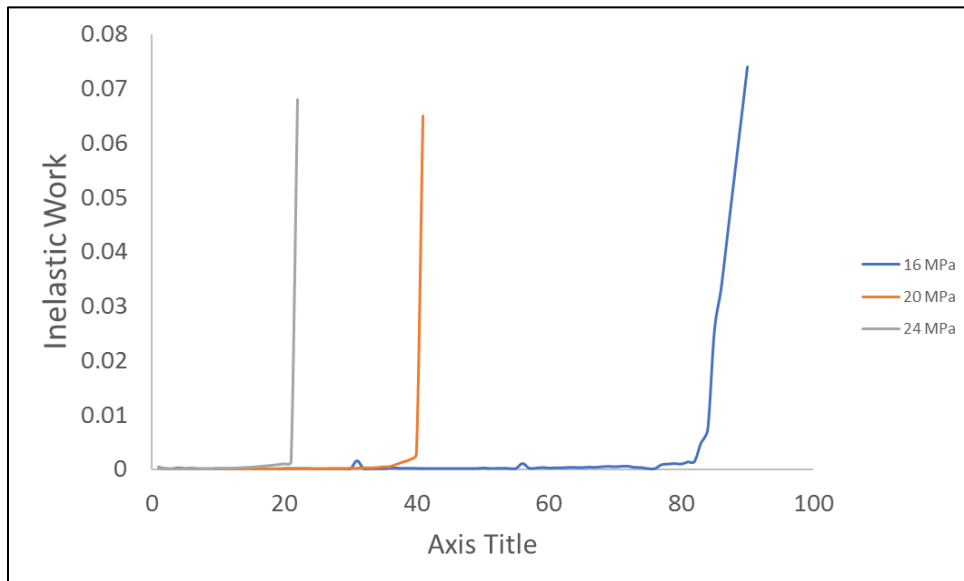


Figure B.22: Work as a function of life cycles for joints cycled with various stress amplitudes at 100°C with 10s of dwelling condition

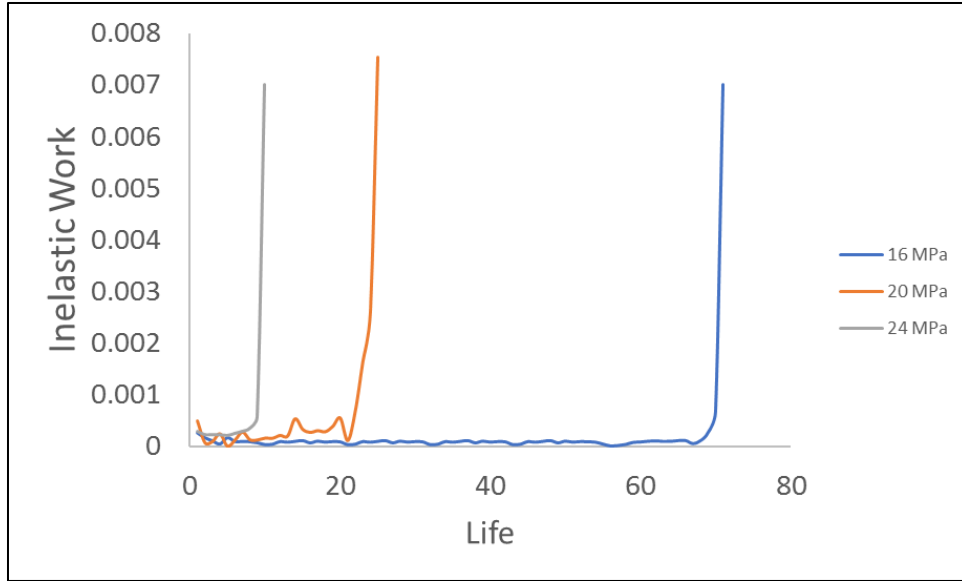


Figure B.23: Work as a function of life cycles for joints cycled with various stress amplitudes at 100oC with 60s of dwelling condition

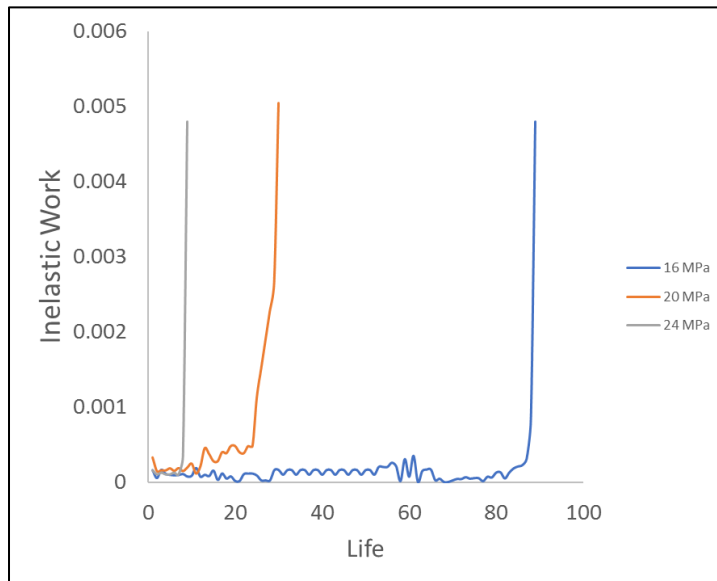


Figure B.24: Work as a function of life cycles for joints cycled with various stress amplitudes at 100oC with 180s of dwelling condition